

**POLYCYCLIC AROMATIC HYDROCARBON
SORPTION KINETICS IN
THREE IRON OXIDE-COATED AQUIFER SANDS**

by

Britt A. Holmén

B.A., Colby College, 1982
M.S., University of Washington, 1985

Submitted to the Department of Civil and Environmental Engineering
in partial fulfillment of the requirements for the degree of

Doctor of Philosophy

at the
Massachusetts Institute of Technology
February 1995

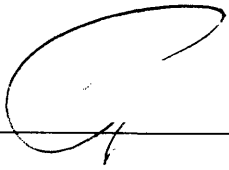
©1995 Massachusetts Institute of Technology

Author



Britt A. Holmén
Department of Civil and Environmental Engineering
February 1995

Certified by



Professor Philip M. Gschwend
Thesis Supervisor

Accepted by

Joseph M. Sussman
Chairman, Departmental Committee on Graduate Studies

Barker Eng

MASSACHUSETTS INSTITUTE OF TECHNOLOGY

MAR 07 1995

POLYCYCLIC AROMATIC HYDROCARBON SORPTION KINETICS IN THREE IRON OXIDE-COATED AQUIFER SANDS

by

BRITT A. HOLMÉN

Submitted to the Department of Civil and Environmental Engineering
in partial fulfillment of the requirements for the degree of
Doctor of Philosophy

Abstract

This work examined the rate of hydrophobic organic compound (HOC) sorption to low organic-carbon-content aquifer solids. Using column studies conducted at a range of flow velocities with a single well-characterized iron-oxide and kaolinite coated aquifer sand, we evaluated an average sorption rate constant for three relatively high molecular weight polycyclic aromatic hydrocarbons (PAHs), naphthalene, acenaphthene, and phenanthrene. We applied the method of moments to elution curves to deduce a single-site first-order sorption rate constant, and measured sorption rates that were comparable to small-scale (grain diameter) advection rates commonly observed under natural gradient conditions at many sandy aquifer localities. Therefore, a kinetic, rather than an equilibrium, description of aquifer sorption is more appropriate for successful mechanistic modeling of HOC subsurface transport. Comparison of the measured sorption rates among the three sorbates showed that sorption rate decreased with increasing hydrophobicity. This trend is consistent with an intrasorbent diffusion sorption mechanism. We examined the hypothesis that the organic matter-rich coatings on the quartz grains were the important diffusion media in this sand. Diffusion modeling based on measured sorbent properties over-predicted the sorption rates by two orders of magnitude.

In order to gain a better understanding of the mechanism of sorption in sandy aquifer materials, we compared the moment-derived first-order acenaphthene sorption rates among three aquifer sands after thorough characterization of sediment mineralogy and texture. We were able to identify two distinct types of sorption sites in the bulk sands we studied, using acetone as a conservative tracer. The two sites were zones of immobile water within fine-grained matrix between primary sand grains and organic matter in iron-oxide coatings on these grains. The study of three sands allowed us to identify some of the key sorbent properties which govern sorption rate. We found sorption rates decreased with (i) increasing fraction of immobile water, (ii) increasing proportion of surface iron, particularly amorphous iron oxides, and (iii) increasing intramineral porosity.

Thesis Supervisor: Dr. Philip M. Gschwend
Title: Professor

Acknowledgments

There's no greater satisfaction I can obtain, in completing such a phase in my life, than to acknowledge that my goal was attained with the assistance of many friends and colleagues. I offer the greatest thanks to the following people:

Phil Gschwend, for giving me the freedom to spend a few years learning about plumbing, electronics, and the "Ten Times Rule" (everything always takes ... longer than it should!); not to mention the opportunity to share in his excitement about science.

John MacFarlane, who provided continual help in getting things to work in the lab from day one to present. Thanks for all the wisdom you've shared with me! Thanks also for help with the sampling, ICP, HPLC, GC, ACAD...and every other acronym in the lab.

Allison Mackay and **Örjan Gustafsson** for thoughtful sorption discussions, help with presentations, reviews of manuscripts, and camaraderie. **Chris Swartz** for help with ICP, TiCEB, AOD and CHN samples, Aberjona sampling, early morning column comparisons, and helpful paper comments. **April Ulery** for analyzing my samples by XRD, sharing the secrets of AOD and Aberjona sampling help, not to mention some smile-breaking puns. **Peter Zeeb** for leading the way to Aberjona and **Sarah Herbelin** for help in digging the hole. **Mike Ernst** for being there at the critical moments when everything electronic was giving me fits. **Mike Collins** for keeping the columns going in the end and for (too many) last-minute batch tests. **Liz Kujawinski** for UROP help with CHN and ICP analyses, and with PB sediment digestions. **Trine Jensen** for thoughtful column modeling discussions and bringing her high spirits to the lab everyday. **Joe Ryan** for Pine Barrens discussions, helpful paper reviews and 'showing me the way'. **Lynn Roberts** for leading me to the method of moments.

I want to extend my appreciation to my other Committee members; **Harry Hemond** and **Lynn Gelhar**, for the time they invested in getting this thesis into its final shape.

I also greatly appreciated the moral support of the members of my 'Graduate Group': Thanks **Glenn, Jenny, Kaye, and Lisa!** I am also indebted to my squash friends who made the weeks go by a little smoother with their mid-week company on and off the courts: Thanks **Susan, Stacy, Kathryn, Beth, Margot, Doris and Sarah!**

Finally, thanks to Sue Meehan and my family who provided much-needed emotional support throughout my tenure at MIT.

Last but not least, thanks, but no thanks! to MIT Physical Plant for keeping the e⁻ going long enough for me to finish.

TABLE OF CONTENTS

Abstract	2
Acknowledgments	3
List of Tables	7
List of Figures	8
Chapter 1. INTRODUCTION	11
Motivation	11
Modeling Sorption Kinetics in Natural Sorbents	14
Experimental Approach	15
Literature Cited	16
Chapter 2. SORPTION KINETICS OF ACENAPHTHENE	19
Introduction	20
Background	20
Aquifer Solids Sorption Kinetics.	20
Modeling Approach	21
Experimental Methods	23
Sorbent	23
Chemicals and Solutions	26
Batch Experiments	26
Column Experiments	27
Experimental Moments	29
Results and Discussion	32
Batch Experiments	32
Column Experiments	32
Effective Column Length and Retardation Factor	37
Dispersivity and Reverse Sorption Rate Constant.	41
Process Relative Rates.	43
Field versus Laboratory Application of Results	44
Diffusion Model Interpretation.	46
Conclusions	47
Literature Cited	48

TABLE OF CONTENTS continued

Chapter 3. SORBATE HYDROPHOBICITY AND SORPTION RATE.....	52
Introduction.....	53
Background.....	53
Methods.....	54
Sorbent.....	54
Solutions.....	55
Sorption Experiments.....	56
Data Analysis.....	57
Results and Discussion.....	59
Batch Experiments.....	59
Column Experiments.....	65
Qualitative Evidence for Slow Sorption Kinetics.....	65
Retardation Factor.....	70
Sorption Rate, k_r	74
Sorption Rate Diffusion Modeling.....	80
Coating Properties.....	80
Effective Diffusivity Prediction.....	85
Moment-derived Effective Diffusivity.....	88
D_{eff} Divergence.....	89
Vicinal Water in Micropores.....	92
Intraorganic Matter Diffusion.....	96
Summary and Conclusions.....	97
Literature Cited.....	98
Chapter 4. SORBENT COMPOSITION EFFECTS.....	102
Introduction.....	103
Background.....	103
Methods.....	104
Sorbent Characterization.....	104
Solutions and Chemicals.....	106
Batch Experiments.....	106
Column Experiments.....	107
Data Analysis.....	108
Results and Discussion.....	110
Sorbent Properties.....	110
Grain Size and Organic Carbon.....	110
Iron Content.....	111
Mineralogy and Texture.....	114
Porosity.....	115
Summary.....	125
Batch Experiments.....	129
Georgetown.....	129
Aberjona.....	129

TABLE OF CONTENTS continued

Column Experiments.....	131
Georgetown.....	131
a. BTC shape and flow rate.....	131
b. Moment Curve Fits.....	136
Aberjona.....	139
a. BTC shape and flow rate.....	140
b. Moment Curve Fits.....	140
Summary.....	141
Sand Comparisons.....	145
Batch vs. Column Acenaphthene Partitioning.....	145
Acetone Retardation Factors.....	147
Acetone vs. Acenaphthene k_r	148
Sorption Time Constants.....	151
Measured Sorbent Properties and Sorption Rate.....	152
Peak Position and Flow Rate.....	153
Summary and Conclusions.....	155
Literature Cited.....	156
Chapter 5. CONCLUSIONS.....	161
Summary.....	161
Accomplishments.....	162
Implications.....	163
Modeling Solute Transport.....	163
Pump-and-Treat Remediation Schemes.....	164
Laboratory Sorption Studies.....	165
Future Work.....	165
Literature Cited.....	166
APPENDICES.....	167
Appendix A: Fortran Programs.....	167
Appendix B: Error Propagation Expressions.....	175
Appendix C: Breakthrough Curves.....	176

List of Tables

Table 2-1. Sorbent properties.....	25
Table 2-2. Natural groundwater velocities and advection rates in sandy aquifers.....	45
Table 3-1. Sorbate properties.....	55
Table 3-2. Batch isotherm model fits.....	61
Table 3-3. Column experiment results.....	70
Table 3-4. K_d and column truncation data.....	72
Table 3-5. Coating diffusion model and moment-derived effective diffusivities.....	85
Table 3-6. Literature vicinal water thicknesses.....	93
Table 4-1. Sorbent size fractions and organic carbon content.....	111
Table 4-2. Sorbent iron concentrations.....	113
Table 4-3. 250-1000 micron size fraction sorbent porosity.....	125
Table 4-4. Sorption regimes model summary for 3 sands.....	126
Table 4-5. Literature two-region model mass transfer rates and dispersivities.....	139
Table 4-6. Single-site first-order model parameters for 3 sands.....	141
Table 4-7. Acenaphthene partition coefficients.....	145
Table 4-8. Sorption process time constants.....	151

List of Figures

Figure 1-1. Illustration of effect slow sorption kinetics has on breakthrough curve shape and position as a function of pore velocity.	13
Figure 2-1. Simulation of sorption kinetics term contribution to second central moment as a function of k_r .	24
Figure 2-2. Continuous flow column experimental apparatus.	28
Figure 2-3. First-order model simulations of error in R and k_r due to truncation of acenaphthene peaks at 7.5 pore volumes.	31
Figure 2-4. Acenaphthene batch results.	33
Figure 2-5. Column experiment evidence for sorptive nonequilibrium.	35
Figure 2-6. Pore volume of peak maximum (PV_{cmax}) and pore volume of first absolute moment ($PV\mu_1$) as a function of velocity.	36
Figure 2-7. First absolute moment expression as a function of inverse velocity.	38
Figure 2-8. Sorption site exposure in an iron-oxide-coated sand.	40
Figure 2-9. Second central moments as a function of inverse velocity.	42
Figure 3-1. Batch sorption isotherms for naphthalene, acenaphthene and phenanthrene.	60
Figure 3-2. Batch kinetics experiments for acenaphthene and phenanthrene.	62
Figure 3-3. Comparison of batch and column K_d results with K_d s derived using two different $\log K_{oc}$ - $\log K_{ow}$ regressions from the literature.	64
Figure 3-4. Elution curves for naphthalene and phenanthrene at different flow rates.	67
Figure 3-5. Semi-logarithmic plot of pore volume to peak maximum (PV_{cmax}) vs. inverse velocity for four solutes as a function of flow rate.	68
Figure 3-6. Elution curves for the four solutes studied at a flow rate of approximately 0.4 mL/min ($v = 15$ to 18 cm/hr).	69
Figure 3-7. First absolute moments versus $1/v$ for four solutes.	71
Figure 3-8. Second central moments plotted against inverse velocity for four solutes.	77

List of Figures continued

Figure 3-9a. Evaluation of variation in R and k_r due to truncation of acenaphthene BTCs at 7.5 pore volumes.	78
Figure 3-9b. Evaluation of variation in R and k_r due to truncation of phenanthrene BTCs at 58 pore volumes.	79
Figure 3-10. Scanning electron micrographs of coatings on quartz grains in the Pine Barrens 250-1000 micron size fraction.	82
Figure 3-11. Pore size distribution for the coated and uncoated Pine Barrens 250-1000 micron sand fraction as determined by mercury porosimetry.	83
Figure 3-12. Constrictivity factors as a function of the ratio of molecular diameter to pore diameter, λ , based on empirical relationships in the literature.	87
Figure 3-13. Effect of coating porosity and coating thickness on the agreement between the predicted and moment-derived D_{eff} values	91
Figure 3-14. Comparison of the constrictivity factor in water versus organic solvents based on the data of Satterfield et al. [44] for diffusion out of 3.2 nm pores in silica-alumina catalysts pellets.	94
Figure 4-1. Pine Barrens 250-1000 micron fraction SEM micrographs.	117
Figure 4-2. Bulk Georgetown sand micrographs.	119
Figure 4-3. Bulk Aberjona sand micrographs.	121
Figure 4-4. X-ray diffraction patterns for < 53 micron wet-sieved size fraction for the PB, GT and AJ sands.	122
Figure 4-5. Mercury porosimetry data for the 250-1000 micron sieve fraction, sonicated 250-1000, and bulk samples of the PB, GT and AJ sands.	124
Figure 4-6. Aquifer Sand Sorption Regimes Model.	127
Figure 4-7. Iron and organic carbon relationships in three sands.	128
Figure 4-8. Georgetown batch kinetics and isotherm	130
Figure 4-9. Aberjona batch kinetics and isotherm.	132
Figure 4-10. GT-acetone elution curves at 5 flow rates.	133
Figure 4-11. GT-acenaphthene elution curves at four flow rates.	135
Figure 4-12. Georgetown moments versus $1/v$.	137

List of Figures continued

Figure 4-13. AJ-acetone elution curves at four flow rates.	138
Figure 4-14. Mercury porosimetry data for the three sand column sorbents	142
Figure 4-15. AJ-acenaphthene elution curves at four flow rates.	143
Figure 4-16. AJ moments versus $1/v$.	144
Figure 4-17. Pore volumes to peak maximum as a function of inverse velocity for three sands.	154

Chapter 1. INTRODUCTION

Motivation

Interest in the rate of hydrophobic organic compound (HOC) transport in groundwater has developed over the past decade due to the increasing number of identified sites with groundwater contamination problems, and the potential for toxic chemical plumes to affect water quality in drinking water wells and surface waters into which groundwater springs discharge. The transport of HOCs in groundwater depends on many physical and chemical processes, one of which is sorption. The extent and rate at which HOCs bind to the solid phase governs the fraction of their travel time which is spent in the flowing aqueous phase, and thus controls how quickly the compounds travel in the subsurface.

Many aquifers are composed of sandy materials with low organic carbon contents. Since much of the initial work in sorption research focused on soil sorbents, which have higher organic matter contents, we have only recently begun to understand the sorption process in aquifer materials which are important water-bearing strata. Furthermore, due to the difficulty of dissolving very hydrophobic organic compounds in water, most of the sorption kinetics studies to date have used relatively water-soluble organic compounds. Unfortunately, many of the organic pollutants that exist in groundwater today are highly hydrophobic. For instance, hundreds of town gas waste sites exist across the U.S. due to the abandonment of manufactured gas plants in the early 1950s [17]. The coal tars at these sites contain polycyclic aromatic hydrocarbons (PAHs) with a wide range in aqueous solubilities that are continually released into groundwater. It is important to identify whether or not sorption of such contaminants is rate-limited in order to determine how much of a risk these sites pose to human health. It is likely that the importance of sorption rate limitations is a function of solute hydrophobicity. Thus, we studied solutes of higher hydrophobicity than examined by previous workers in order to expand our understanding of the sorption mechanism and the conditions under which a kinetics description of sorption is required.

Another factor that affects whether or not organic solutes have enough time to reach equilibrium with the aquifer solids is the rate of groundwater advection. Many laboratory studies have been conducted at pore velocities in excess of 20 cm/hr for experimental convenience [2, 9, 13, 16, 25]. However, the determination that sorption kinetics significantly affects solute transport at such high flow rates does not translate directly into sorption kinetics being important at velocities close to natural gradient groundwater rates

(about 0.5 cm/hr). At lower flow rates, the solute may have sufficient time to interact with the sorbent such that an equilibrium description of sorption is sufficient.

Groundwater transport models are based on the advection-dispersion equation:

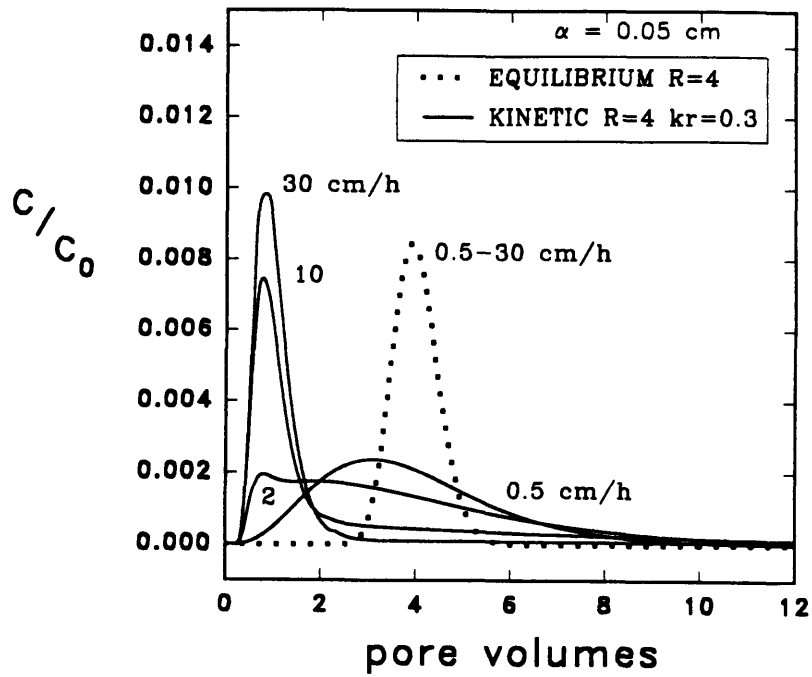
$$\theta \frac{\partial C}{\partial t} = \theta D \frac{\partial^2 C}{\partial x^2} - \theta v \frac{\partial C}{\partial x} - r_s \quad (1-1)$$

with θ = porosity, C = aqueous phase concentration (mol/mL), D = dispersion coefficient (cm²/sec) and v is the average pore water velocity (cm/sec). The source/sink term (r_s) on the right-hand side of equation (1-1) may include expressions for sorption, compound degradation (biological or chemical) and solute inputs along the flow path. We are interested in understanding the simplest formulation for r_s which accurately quantifies sorbing-solute transport. In addition the sorption model should include parameters which are amenable to *a priori* prediction using laboratory-based measurements of the properties of sorbate and sorbent.

The importance of correctly formulating the sorption expression is schematically depicted in **Figure 1-1**. Breakthrough curves (BTCs) for a pulse input of a slowly sorbing chemical (desorption rate = 0.3 hr⁻¹) with a retardation factor of 4 are plotted at four pore velocities. Also plotted is the BTC for a sorbing compound of the same retardation factor under conditions where the local equilibrium assumption (LEA) is valid. Three noticeable effects of slow sorption are evident in this simulation: (1) the BTCs for the kinetically-limited solute show significant tailing, especially at the higher velocities, (2) the BTCs for the kinetically-limited solute elute at earlier pore volumes as flow rate is increased, and (3) at pore velocities of 30 cm/h, similar to rates that would be used during pump-and-treat remediation, the bulk (about 90%) of the sorbing solute mass elutes with the conservative tracer at about one pore volume. In contrast, the LEA BTC shape and position are invariant with velocity. Clearly, an equilibrium sorption formulation would have overestimated the time of first arrival of this solute at a downgradient well, and would have predicted full elution (>99% of solute mass) of the pulse within only 8 pore volumes, rather than the 100 pore volumes required at the highest velocity! This simulation emphasizes that, in order to predict HOC subsurface transport, the sorption process must be accurately quantified.

The work reported in this thesis focused on the sorption of relatively hydrophobic PAHs in low f_{oc} aquifer solids in order to accomplish the following goals: (1) examine the

Figure 1-1. Illustration of effect slow sorption kinetics has on breakthrough curve shape and position as a function of pore velocity. Dotted lines show that the local equilibrium assumption (LEA) curves elute at the same pore volume for all velocities.



appropriateness of using an equilibrium sorption expression for r_s , (2) investigate the mechanisms that govern grain-scale sorption in aquifer material, and (3) identify the properties of the sorbent and sorbate which are critical for prediction of the rate of sorption.

Modeling Sorption Kinetics in Natural Sorbents

There has been a recent surge in research on sorption kinetics in aquifers since a 1982 field study was conducted at the Borden Site in Ontario, Canada [5]. As reported by Roberts et al. [23], the contaminant plumes of four hydrophobic organic compounds showed increasing retardation with travel distance, an observation attributed to slow sorption kinetics. Furthermore, many laboratory studies [10, 18, 19, 26, 30] have shown HOC sorption kinetics to be slow in sorbents with higher organic matter contents. Most of these studies were conducted using batch experiments and thus do not mimic groundwater conditions where the solid-to-water ratio is much higher, fluid dynamics are less energetic and soil aggregates remain intact. More relevant to aquifer conditions are column studies that have been carried out with soil sorbents and pesticide solutes for many years by soil scientists [3, 12, 27, 29]. These studies have culminated in a variety of mathematical models for describing the sorption term in equation (1-1).

Presently, the focus in sorption kinetics modeling for aquifer sorbents is on intraparticle diffusion models. These models derive from chromatography and chemical engineering applications [11, 15] and assume that the rate-limiting step in sorption is the rate of transfer (via diffusion) of the sorbate to the sorption sites (within adsorbent particles). Wu and Gschwend [30] employed a radial diffusion model to describe batch desorption data for contaminated river sediments and soils. This type of model had previously been successfully applied to packed column chromatography [14] and chemical engineering adsorption columns [24]. Soil scientists also incorporated a similar diffusion-based mechanism into their 2-region models for aggregated soils [22, 28]. Although there is no firm evidence to prove such a diffusion mechanism, the low activation energy for HOC partitioning into organic matter has been interpreted as evidence that the sorption "reaction" step is rapid. Thus, the slow step is believed to be transport to the sorption "sites". Batch desorption data have also been shown to fit the square-root of time dependency one expects for a diffusion process [6, 13, 26]. Furthermore, recent observations of increasing desorption rates with decreasing particle size [26, 30] and increased difficulty of extracting sorbates that have been incubated with sorbents for longer periods of time [10, 18, 20] are in agreement with a diffusion mechanism.

Such diffusion models contain physically-meaningful model parameters (i.e., particle diameter, solute aqueous diffusivity, solute intraparticle retardation factor) which may be quantified by independent measurements; thus the diffusion models offer the possibility of *a priori* prediction of sorption rate, although few such predictions have been made to date [21, 22, 28, 31]. Studies that have attempted to use the intraparticle diffusion model with aquifer materials have noted the difficulty of estimating the effective tortuosity (=tortuosity/constrictivity) of the intraparticle domain and the true diffusive length scale [1, 4, 7, 8]. Thus, it appears that sorption rate prediction, in the framework of the intraparticle diffusion model, requires quantification of the specific textural relationships within the sorbent. Textural relationships in this sense include description of the geometry of particles (size, shape), the total porosity of the particles and the pore size distribution, as well as the distribution of sorption sites (i.e., organic matter) within the particles (so diffusion path lengths may be estimated).

Work conducted to date leads us to believe that detailed characterization of the sorbent must be coupled with sorption rate measurements in order to understand the key properties controlling sorption rate. As natural sorbents are quite complex compared to the synthetic sorbents used by chemical engineers and chromatographers, it is incumbent upon us to illuminate the critical measurements that must be made on a given sorbent in order to calculate a sorption rate. The most successful and useful sorption rate predictor will be based on sorbent properties that are the most important variables and that are fairly easily measured.

Experimental Approach

To improve our understanding of the sorption process in aquifer materials, we conducted sorption studies using both batch and column methods. Since batch rates appeared to be instantaneous for the sorbents we studied, the column experiments were used to quantify sorption rate. The philosophy behind the column experiments was based on the understanding that sorption rate and advection rate are competing processes which control sorbate transport in the column. The advection rate can be controlled experimentally by varying the flow rate through the column; thus by changing the pore velocity, the degree to which sorptive equilibrium is approached varies. A moments technique [24] was used on short-pulse input breakthrough curves (BTCs) to quantify the sorption rate.

Techniques used to characterize the sorbent included mercury porosimetry, organic carbon determination, selective oxide extraction, scanning electron microscopy,

petrographic analysis and X-ray diffraction. Each of these methods aided in quantifying sorbent properties such as pore size distribution and sediment texture (i.e., distribution of organic carbon-rich phases; interrelationship of grain coatings and primary mineral grains); properties which we believed would affect the rate of sorption.

Chapter 2 addresses the question of whether or not the rate of sorption is fast compared to the natural advection rate in aquifers. This chapter is the basis for subsequent work in Chapter 3 where a series of polycyclic aromatic hydrocarbons (naphthalene, acenaphthene, and phenanthrene) was used to further define the mechanism of sorption to aquifer solids. Finally, Chapter 4 examines how the composition of the sorbent affects acenaphthene transport.

Literature Cited

1. Ball, W. P. and P. V. Roberts. (1991) Long-term sorption of halogenated organic chemicals by aquifer material. 2. Intraparticle diffusion. *Environ. Sci. Technol.*, 25: 1237-1249.
2. Bouchard, D. C., A. L. Wood, M. L. Campbell, P. Nkedi-Kizza and P. S. C. Rao. (1988) Sorption nonequilibrium during solute transport. *J. Contam. Hydrol.*, 2: 209-223.
3. Davidson, J. M., C. E. Rieck and P. W. Santelmann. (1968) Influence of water flux and porous material on the movement of selected herbicides. *Soil Sci. Soc. Am. J.*, 32: 629-633.
4. Farrell, J. and M. Reinhard. (1994) Desorption of halogenated organics from model solids, sediments and soil under unsaturated conditions. 2. Kinetics. *Environ. Sci. Technol.*, 28: 63-72.
5. Goltz, M. N. and P. V. Roberts. (1986) Interpreting organic solute transport data from a field experiment using physical nonequilibrium models. *J. Contam. Hydrol.*, 1: 77-93.
6. Grathwohl, P., W. Pyka and P. Merkel. (1994) Desorption of organic pollutants (PAHs) from contaminated aquifer material. In *Transport and Reactive Processes in Aquifers*. Dracos, Th. and F. Stauffer (Eds.) Balkema: Rotterdam; pp. 469-474.
7. Harmon, T. C. and B. K. D. Barre. (1994) The effect of temperature on the rate of desorption of halogenated alkenes from aquifer solids. 207th ACS National Meeting, San Diego, CA, 343-345.
8. Harmon, T. C., L. Semprini and P. V. Roberts. (1992) Simulating solute transport using laboratory-based sorption parameters. *J. Environ. Engineering.*, 118: 666-689.
9. Hutzler, N. J., J. C. Crittenden and J. S. Gierke. (1986) Transport of organic compounds with saturated groundwater flow: experimental results. *Water Resour. Res.*, 22: 285-295.

10. Karickhoff, S. W. (1980) Sorption kinetics of hydrophobic pollutants in natural sediments. In *Contaminants and Sediments*. Baker, R. A. (Ed.) Ann Arbor Science: Ann Arbor, MI; pp. 193-205.
11. Kasten, P. R., L. Lapidus and N. R. Amundson. (1952) Mathematics of adsorption in beds. V. Effect of intraparticle diffusion in flow systems in fixed beds. *J. Phys. Chem.*, 56: 683-688.
12. Kay, B. D. and D. E. Elrick. (1967) Adsorption and movement of lindane in soils. *Soil Sci.*, 104: 314-322.
13. Kookana, R. S., R. D. Schuller and L. A. G. Aylmore. (1993) Simulation of simazine transport through soil columns using time-dependent sorption data measured under flow conditions. *J. Contam. Hydrol.*, 14: 93-115.
14. Kucera, E. (1965) Contribution to the theory of chromatography: Linear non-equilibrium elution chromatography. *J. Chromat.*, 19: 237-248.
15. Lapidus, L. and N. R. Amundson. (1952) Mathematics of adsorption in beds. VI. The effect of longitudinal diffusion in ion exchange and chromatographic columns. *J. Phys. Chem.*, 56: 984-988.
16. Lee, L. S., P. S. C. Rao, M. L. Brusseau and R. A. Ogwada. (1988) Nonequilibrium sorption of organic contaminants during flow through columns of aquifer materials. *Environ. Tox. Chem.*, 7: 779-793.
17. Luthy, R. G., D. A. Dzombak, D. A. Peters, S. B. Roy, A. Ramaswami, D. V. Nakles and B. R. Nott. (1994) Remediation tar-contaminated soils at manufactured gas plant sites. *Environ. Sci. Technol.*, 28: 226A-276A.
18. Pavlostathis, S. G. and G. N. Mathavan. (1992) Desorption kinetics of selected volatile organic compounds from field contaminated soils. *Environ. Sci. Technol.*, 26: 532-538.
19. Pignatello, J. J. (1990) Slowly reversible sorption of aliphatic halocarbons in soils. II. Mechanistic aspects. *Environ. Tox. Chem.*, 9: 1117-1126.
20. Pignatello, J. J., F. J. Ferrandino and L. Q. Huang. (1993) Elution of aged and freshly added herbicides from a soil. *Environ. Sci. Technol.*, 27: 1563-1571.
21. Rao, P. S. C., R. E. Jessup, D. E. Rolston, J. M. Davidson and D. P. Kilcrease. (1980) Experimental and mathematical description of nonadsorbed solute transfer by diffusion in spherical aggregates. *Soil Sci. Soc. Am. J.*, 44: 684-688.
22. Rao, P. S. C., D. E. Rolston, R. E. Jessup and J. M. Davidson. (1980) Solute transport in aggregated porous media: theoretical and experimental evaluation. *Soil Sci. Soc. Am. J.*, 44: 1139-1146.
23. Roberts, P. V., M. N. Goltz and D. M. Mackay. (1986) A natural gradient experiment on solute transport in a sand aquifer 3. Retardation estimates and mass balances for organic solutes. *Water Resour. Res.*, 22: 2047-2058.
24. Schneider, P. and J. M. Smith. (1968) Adsorption rate constants from chromatography. *A.I.Ch.E. Journal.*, 14: 762-771.

25. Schwarzenbach, R. P. and J. Westall. (1981) Transport of nonpolar organic compounds from surface water to groundwater. Laboratory sorption studies. *Environ. Sci. Technol.*, 15: 1360-1367.
26. Steinberg, S. M., J. J. Pignatello and B. L. Sawhney. (1987) Persistence of 1,2-dibromoethane in soils: entrapment in intraparticle micropores. *Environ. Sci. Technol.*, 21: 1201-1208.
27. van Genuchten, M. T. (1981) Non-equilibrium transport parameters from miscible displacement experiments. 119, U.S. Salinity Laboratory, Riverside California.
28. van Genuchten, M. T. (1985) A general approach for modeling solute transport in structured soils. *Memoires IAH.*, 17: 513-526.
29. van Genuchten, M. T. and P. J. Wierenga. (1977) Mass transfer studies in sorbing porous media:II. Experimental evaluation with tritium. *Soil Sci. Soc. Am. J.*, 41: 272-278.
30. Wu, S.-C. and P. M. Gschwend. (1986) Sorption kinetics of hydrophobic organic compounds to natural sediments and soils. *Environ. Sci. Technol.*, 20: 717-725.
31. Wu, S.-C. and P. M. Gschwend. (1988) Numerical modeling of sorption kinetics of organic compounds to soil and sediment particles. *Water Resour. Res.*, 24: 1373-1383.

Chapter 2

SORPTION KINETICS OF ACENAPHTHENE IN AN ATLANTIC COASTAL PLAIN AQUIFER SAND

Submitted to
Environmental Science and Technology
May 27, 1994

Introduction

Recent field and laboratory evidence [9, 37] has challenged the assumption that hydrophobic organic compound (HOC) sorptive equilibrium prevails in the subsurface. The possibility of slow sorption kinetics has important implications for contaminant transport rates in groundwater and the required duration of pump-and-treat remediation schemes. In aquifers, the relative rates of the competing sorption and advection processes determine whether or not sorption kinetics affect HOC transport.

The focus in this paper is sorption of HOCs to low organic-carbon-content sandy aquifer materials. These solids are ubiquitous in aquifers which serve as sources of groundwater, a fact which heightens the importance of understanding how hydrophobic contaminants are transported within them. Our objective was to determine an average time scale for sorption that can be compared to the advection time scale under natural gradient flow conditions in order to assess whether a kinetics description of sorption is required in aquifers.

Our approach was to perform a series of column experiments at different flow rates which would allow a range of contact times between the HOC sorbate and the quartz sand sorbent. In contrast to other studies, the experiments were conducted using short pulse inputs over a range of flow rates that extended from natural gradient to pumping conditions. Elution peaks were analyzed using the method of moments and a first-order sorption model to extract a single kinetic sorption parameter. The appropriateness of using batch techniques to quantify the sorption capacity of the sand, as defined by the equilibrium partition coefficient, K_d , was tested by comparing the partitioning behavior observed for the sand column studies with traditional batch experiments.

Background

Aquifer Solids Sorption Kinetics. Evidence for slow sorption kinetics in low- f_{oc} (fraction organic carbon) sorbents comes from field studies as well as batch and column laboratory experiments. Batch methods have shown that long incubation times (weeks to months) are required to reach equilibrium for some sorbent/sorbate pairs [3, 42], and that the time required for complete desorption from field-contaminated soil or sediment increases with longer sorptive incubation times [32, 43]. Researchers using laboratory column studies have generally attributed early compound breakthrough and increased tailing of breakthrough curves (BTCs) to nonequilibrium sorption when sorbing compounds show these asymmetric traits, but conservative tracer BTCs are symmetric [10].

The magnitude of the sorption rate constant is often estimated by fitting column breakthrough curves to a two-site model with the widely available computer program, CXTFIT [29]. This model assumes two types of sorption "sites" (one type always at equilibrium, and the other exhibiting first-order kinetic limitations), and therefore requires three sorption fitting parameters to model experimental data: the equilibrium sorption coefficient, K_d , the fraction of sites for which equilibrium prevails, F , and the first-order desorption rate constant, k_2 . This approach also assumes that the K_d which applies to the equilibrium sites is the same as would ultimately apply to the kinetic sites.

Early solute breakthrough and increased BTC asymmetry with increasing velocity has been observed in column laboratory studies conducted with aquifer material at flow velocities that ranged from 2 to 60 times the natural groundwater velocity [5, 9, 23], and these investigators attributed these observations to slow sorption kinetics. Both field [1, 17, 33, 45] and laboratory studies [6, 9, 21] have concluded that the improved curve-fits achieved with the 2-sorption site model for experiments conducted at high pore velocity indicate that sorption kinetics is important even though the local equilibrium model (which assumes a single type of sorption site) has only one sorption fitting parameter, K_d . Others have noted a dependence of the applicability of the local equilibrium model on the magnitude of a compound's retardation factor [5, 21]. Researchers utilizing the 2-site model have also noted a positive correlation between the desorption rate constant (k_2) and pore velocity [6, 19, 23, 45], an observation that suggests k_2 is a lumped parameter [6, 19].

Roberts et al. [37] observed an increase in solute retardation with time over a two-year sampling program at the Borden site (Ontario, Canada) under natural-gradient conditions and attributed this result to slow sorption kinetics. Another Borden field study examined the influence of pore velocity and found retardation factors to increase as velocity decreased [33]. Field studies comparing natural gradient and pumping conditions suggest that a kinetics description for sorption may be needed under forced-gradient conditions, but models based on local equilibrium may be adequate to describe sorbate transport at natural flow rates [1, 45]. Although these studies have concluded that sorption kinetics may be important in aquifers, we still lack a mechanistically-meaningful model for predicting sorption rate and capacity that can be used to assess HOC transport rates under both natural gradient and pumping conditions.

Modeling Approach. The subsurface HOC partitioning process is analogous to that of column chromatography. In both systems, the transport time of a pulse input is governed by the affinity the chemical has for the solid phase (i.e., K_d) as well as the transport

distance (i.e., column length). The width of a chromatographic peak is determined by sorbent grain size and shape, column length, partition coefficient, sorption rate and hydrodynamic dispersion coefficient [20]. Schneider and Smith [41] demonstrated how moments of gas chromatography peaks could be used to evaluate sorption rate constants for those analytical systems. Here, we use the same method of moments to analyze sand column elution curves and to extract values of sorption rate constants *assuming only a single-site sorption model*. For our columns, the following governing equations are assumed to apply:

$$\frac{\partial C}{\partial t} = -v \frac{\partial C}{\partial x} + D \frac{\partial^2 C}{\partial x^2} - r_{sw} \frac{\partial S}{\partial t} \quad (2-1)$$

$$\frac{\partial S}{\partial t} = k_f C - k_r S \quad (2-2)$$

where C = aqueous concentration (mol/mL), S = sorbed concentration (mol/g), v = pore water velocity (cm/sec), D = dispersion coefficient (cm²/sec), r_{sw} = solid-to-water ratio (g/mL), k_f = first-order sorption rate constant (mL/g-sec), and k_r = first-order desorption rate constant (sec⁻¹). We have chosen a single-site, first-order model for sorption kinetics because there is currently no evidence for chemically distinct sorption sites in aquifer solids. The one-site first-order model is also amenable to interpretation as a mass-transfer type of model [8, 16, 17, 49], and requires the minimum number (i.e., one) of independent kinetic fitting parameters to characterize sorption. At steady state, $\frac{\partial S}{\partial t} = 0$ and equation (2-2) can be rearranged to define the equilibrium partition coefficient, K_d (mL/g):

$$\frac{S}{C} = \frac{k_f}{k_r} \equiv K_d \quad (2-3)$$

K_d is defined by equation (2-3) as long as k_f and k_r are true *constants*. The model also assumes that the sorption isotherm is linear.

Valocchi [47] solved the above equations for a Dirac delta-function input in a semi-infinite domain and reported the time-moment formulas in terms of pore volumes. In our study, Valocchi's dimensionless moment expressions were restored to dimensional form by using the factor (L/v) to convert from pore volumes to time in seconds. The resulting expressions, modified for a non-Dirac pulse of finite width, for the first absolute moment (μ'_1) and second central moment (μ_2) are:

$$\mu'_1 = \frac{L}{v} R + \frac{t_0}{2} \quad (2-4)$$

$$\mu_2 = \frac{2LDR^2}{v^3} + \frac{2L(R-1)}{k_r v} + \frac{t_0^2}{12} \quad (2-5)$$

where L is the column length in cm, R is the retardation factor ($= 1 + r_{sw} K_d$), and t_0 is the pulse duration in seconds. This conversion allows one to see the dependence of the

individual moments on pore velocity, our experimental variable. Since the retardation factor in equations (2-4) and (2-5) is defined by the ratio of the forward and reverse rate constants, the R value obtained from first moments is the equilibrium R value. That the first absolute moment is independent of kinetic influences has also been noted by previous authors [9, 15]. Equation (2-5) can be further simplified by assuming that hydrodynamic dispersion varied linearly with velocity, an assumption we found to be valid over the range of velocities studied. Thus, we set $D=\alpha v$ in equation (2-5) where α is defined as the dispersivity in cm:

$$\mu_2 = \frac{2L\alpha R^2}{v^2} + \frac{2L(R-1)}{k_r v} + \frac{t_0^2}{12} \quad (2-5')$$

The second central moment describes the peak width relative to the peak's center of mass ($=\mu_1'$) and is composed of three terms. The first term accounts for longitudinal dispersion, the second term reflects sorption kinetics, and the third term describes the input pulse width contribution to elution peak width. In order to evaluate k_r , the parameter of interest in this study, experimental velocities must fall within a range such that the sorption kinetics term is important. In general, the dispersion term dominates at very low pore velocities and the input pulse width will govern μ_2 at very high velocities. The sorption kinetics term in equation (2-5') will be important over a range of velocities that depends on the magnitude of the sorption rate constant. For parameter values anticipated for our column experiments (a dispersivity value corresponding to the geometric mean grain diameter, 0.05 cm; a column length of 7 cm, and $R=3.5$), one can see that the sorption kinetics term will dominate μ_2 over a wider range of velocities for $k_r = 5 \times 10^{-4} \text{ sec}^{-1}$ than for $k_r = 10^{-3} \text{ sec}^{-1}$ (**Figure 2-1**). For $k_r \geq 5 \times 10^{-3} \text{ sec}^{-1}$, the dispersion term dominates over the entire velocity range considered (0.36 to 18 cm/hr) in this simulation.

Experimental Methods

Sorbent. Aquifer sand was collected from the coastal plain aquifer in the New Jersey Pine Barrens from the auger flights at 13.5 meters depth. The sand was thoroughly characterized [40] as an iron-oxide- and kaolinite-coated, medium-grained beach deposit sand. The sand is predominantly quartz with goethite (FeOOH) and kaolinite accounting for ~3 wt %, and heavy minerals (chiefly ilmenite, FeTiO₃) comprising 1 wt% of the sediment. The sand was separated by dry sieving into five size fractions: >1000, 250-1000, 105-250, 53-105 and <53 microns. Another bulk sample was sonicated in distilled water for 2 min in an 81-watt bath and then wet-sieved into five size fractions (**Table 2-1**). The organic carbon content of each fraction was determined using a Perkin-Elmer Model 2400 CHN analyzer. Bulk f_{oc} was also calculated as the sum of each fraction's

Figure 2-1. Simulation of sorption kinetics term (B/v) contribution to second central moment as a function of k_r . Dashed line indicates range of velocity over which sorption kinetics term dominates. Solid line indicates dispersion term dominates magnitude of μ_2 . Note that for the conditions considered, the pulse input term is never dominant. $A=2L\alpha R^2$; $B=2L(R-1)/k_r$ (see equation 2-5' in text).

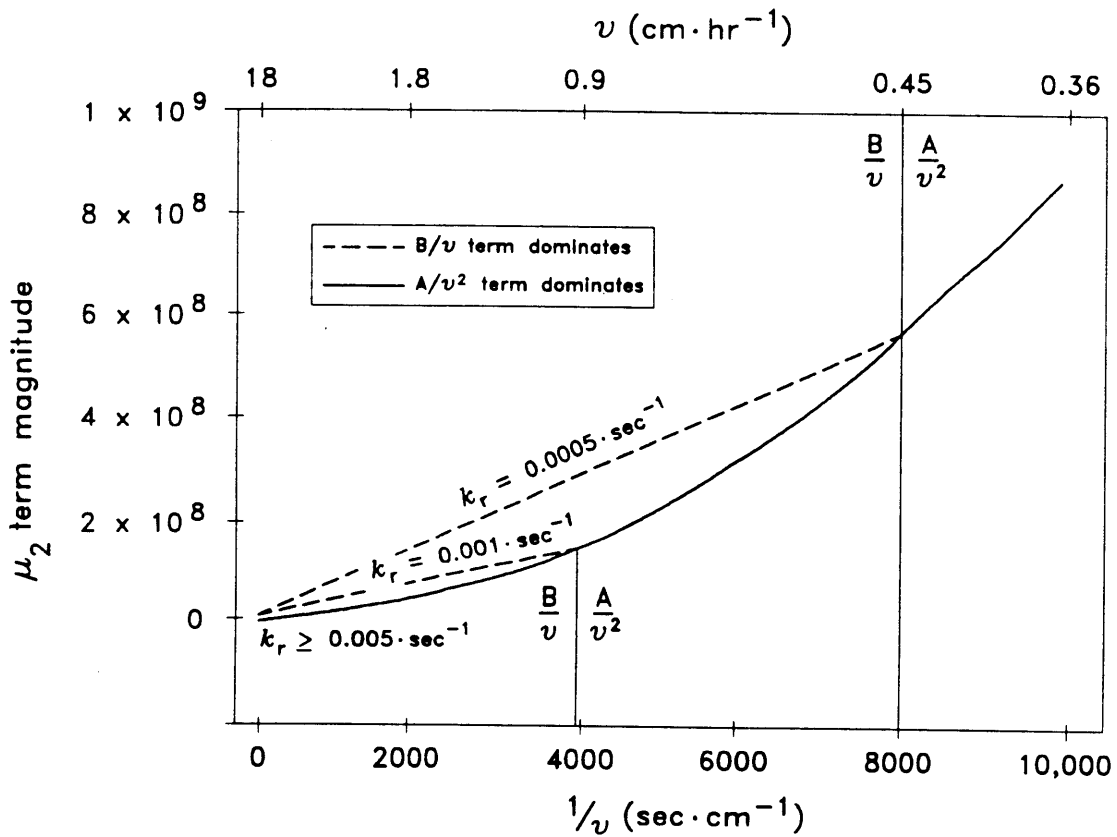


Table 2-1
Sorbent Properties

Size Fraction (μm)	Weight %	f_{oc} (%)	f_{oc} weight fraction* (%)
<i>unsonicated sediment</i>		(1 σ)	
>1000	21.5	0.061 (0.009)	21.2
250-1000**	66.45	0.048 (0.003)	51.2
105-250	11.34	0.111 (0.012)	20.2
53-105	0.42	0.528 (0.005)	3.6
<53	0.31	0.784 (0.096)	3.9
bulk measured		0.057 (0.005)	
bulk calculated‡		0.062	
<i>sonicated sediment</i>			
>1000	21.2	0.026 (0.002)	8.6
210-1000	64.2	0.020 (0.004)	20.1
105-210	11.58	0.061 (0.008)	11.1
53-105	0.99	0.223 (0.024)	3.5
<53	2.12	1.708 (0.121)	56.8
bulk calculated‡		0.064	

** fraction used in column experiments.

‡ calculated bulk $f_{oc} = \sum(\text{wt}\%)(\%f_{oc})$

* f_{oc} weight fraction = $(\text{wt}\%)(\%f_{oc})/\text{calculated bulk } f_{oc}$

organic carbon contribution ($=\sum(\%f_{oc})_i*(wt\ \%)_i$). Two 250-1000 micron subsamples were sent to Porous Materials, Inc. (Ithaca, NY) for mercury porosimetry analysis. One subsample had iron-oxide coatings on the quartz grains and the second subsample had the coatings removed by sonication followed by 250 micron wet sieving. The porosimetry data provided information on intraparticle and coating pore size distribution.

Chemicals and Solutions. Acenaphthene (Aldrich, 99%), acetone (EM Science, omnisolv[®]), methanol (EM Science, omnisolv[®]), and sodium nitrate (Johnson Matthey) were used in the sorption experiments. The log K_{ow} value for acenaphthene is 3.92, and its aqueous solubility is 25 μ M [27].

Distilled water was 0.2 micron-filtered, prior to adding sodium acetate and glacial acetic acid (final concentrations of 10^{-4} M) to buffer the pH near the ambient groundwater value of 4.8. The buffer also contained mercuric chloride at 10 mg/L to limit biological activity. Standard epifluorescence techniques [12] were unable to detect bacteria in both the column effluent and in slurries of column material in buffer.

For the batch and column experiments, acenaphthene solutions were made up directly from the solid PAH and were mixed with a stirrer for 1 week prior to use. Care was taken to avoid sub-sampling the bottom of the solution flasks where solid compound may have been present, although none was observed visually.

Batch Experiments. All batch tests were designed to achieve final equilibrium aqueous concentrations equal to approximately 50% of the initial aqueous concentration using calculations based on $K_{oc}f_{oc}$. Wheaton v-vials (4.5 mL capacity) with foil-lined screw caps were used for the batch kinetics experiment with acenaphthene. Two grams of the 250-1000 μ m size fraction of the Pine Barrens sediment were tumbled end-over-end at ~2 rpm with a 2.6 μ M acenaphthene solution made up in the acetate/HgCl₂ buffer (solid/water ratio = 0.55). The vials were removed from the tumbler at elapsed times ranging from 0 to 43,000 min (30 days) and centrifuged for 20 min at 1400g. The supernatant was then pipetted into a quartz cuvet for fluorescence measurement (290 nm excitation/322 nm emission). Time of contact was recorded as ending when the cuvet was filled. Positive controls (acenaphthene solution without sand) were analyzed with each time point. One negative control was tumbled for the entire 43,000 min in buffer (no acenaphthene added). Apparent K_d was calculated for each time point as:

$$K_d^{app} = \frac{(F_{ctrl} - F_{samp})V_{samp}}{F_{samp}V_{samp} r_{sw}} \quad (2-6)$$

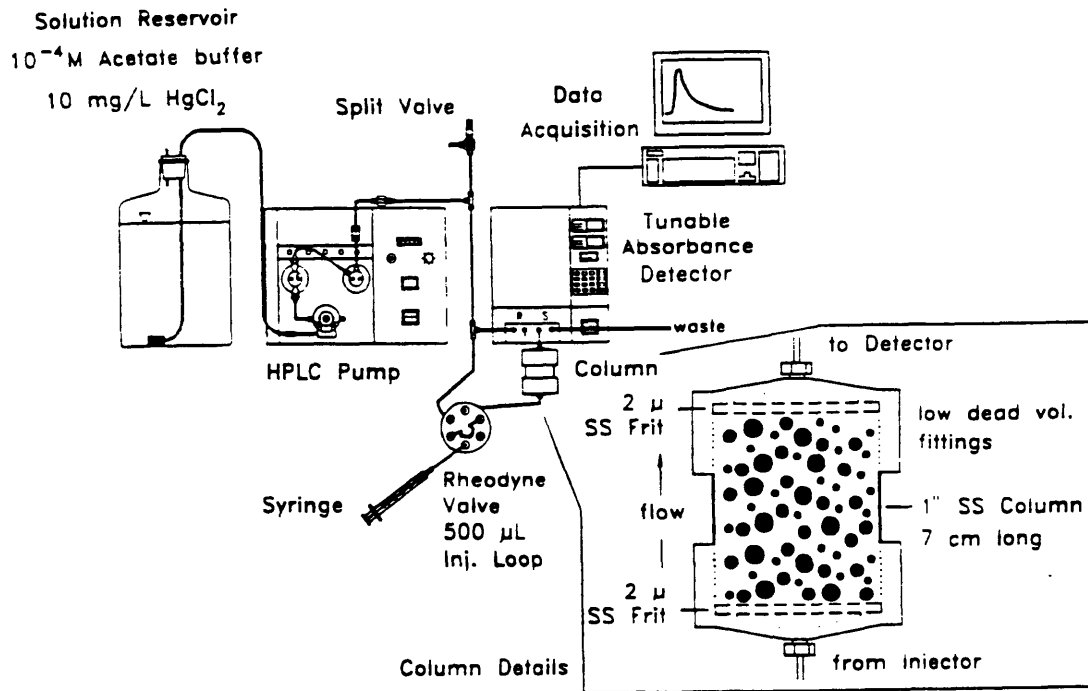
where F_i is the fluorescence of the control or sample (F.U., fluorescence units), V_i is volume of solution tested (mL), and r_{sw} is the solid/water ratio (g/mL). Fluorescence readings, made using a Perkin-Elmer LS-5 fluorescence spectrophotometer, were averaged over 16 sec for each sample. All experiments were conducted at room temperature (22 ± 4 °C). Loss to vial walls was evaluated in controls and found to be insignificant compared to the fraction of compound lost from the aqueous phase.

At the end of the batch kinetics experiment, the sediment at the final time point was extracted with methanol in order to check for mass balance. After tumbling the sample and control vials with methanol for 24 hr, the methanol was analyzed for acenaphthene via fluorescence. Recoveries were calculated by comparison with fluorescence measurements made on three subsamples of the initial acenaphthene solution analyzed at the beginning of the experiment. The two positive control samples gave 100.2 and 105% recoveries and the two sample vials gave 109% recoveries. These results confirmed that no appreciable losses occurred over the month-long experiment.

A batch isotherm experiment was performed using five acenaphthene solutions at initial concentrations ranging from 0.3 to 16 μM (about 10 to 60% of solubility). This range encompassed the concentrations used in the column experiments and the batch kinetics experiment. Isotherm vials had $r_{sw} = 0.55$ g/mL, as for the kinetics experiment, and incubation times of 4 days were used. Sorbed concentrations were calculated by difference, based on fluorescence measurements, as described above.

Column Experiments. The experimental setup used for column experiments was assembled from high-pressure liquid chromatography (HPLC) components and a specially designed sediment column (**Figure 2-2**). Acetate/mercuric chloride buffer, as used in batch experiments, was contained in a glass or stainless steel reservoir and was continuously pushed through the aquifer material by a Waters Model 501 pump. All tubing was stainless steel and precautions were taken to ensure that test compounds contacted only glass or stainless steel surfaces to minimize sorptive losses to teflon [24]. The column was a 7 cm length of 22 mm i.d. (3.8 cm^2 cross-section) stainless steel mirror-finish tubing supplied by Alltech Associates (Deerfield, IL). Column end fittings were Alltech low-dead-volume HPLC fittings. The column was packed both wet and dry with no observed difference in tracer breakthrough behavior. The column porosity ($n = 0.42$) and solid-to-water ratio ($r_{sw} = 3.7$) were calculated based on a gravimetrically-determined column bulk density value of 1.55 g/cm^3 and an assumed solid density of 2.65 g/cm^3 (quartz). The 250-1000 micron Pine Barrens sand fraction was used in all column experiments to constrain grain-scale heterogeneity as well as because it was the most abundant size fraction

Figure 2-2. Continuous flow column experimental apparatus.



and accounted for about half of the sand's organic carbon content. The column was initially saturated from the bottom at a flow rate of 0.05 mL/minute. Effluent turbidity was monitored during the initial column flushing, and experiments were commenced after turbidity measurements stabilized at flow rates greater than the highest experimental rate. (A rough estimate of colloid losses due to initial column flushing was ~0.005% of the column solids or 0.2 % of the column fines, based on turbidity and assuming 1 NTU = 1 mg/L colloids [39]). Experimental flow rates ranged from 0.007 to 3.0 mL/min which corresponds to linear velocities of 0.3 to 113 cm/hr. This range of velocities allowed us to evaluate the sorption kinetics term in equation 5' while operating under realistic aquifer flow conditions. The slow flow rates were obtained by shunting some of the flow to waste using the split valve in the experimental setup.

A Rheodyne injection valve was used to make pulse injections of the compound of interest using both 200 and 500 microliter sample loops. The Waters Model 484 UV absorbance detector was operated in difference mode as buffer was also pumped through the reference cell. The detector monochromator was set to various wavelengths for each analyte: acenaphthene (226 nm), acetone (226 or 264 nm), and nitrate (226 nm). Millivolt output from the UV detector was collected by a data acquisition system (12 bit, A/D converter ADALAB-PC board, Interactive Microware, Inc., State College, PA) and Labtech Notebook software (Laboratory Technologies, Inc., Wilmington, MA).

Effluent pH and conductivity were monitored throughout the experiments with flow-through cells and meters. No change in pH (4.8) or conductivity (0.01 micromhos) was observed throughout the study.

The absorbance output of the detector was occasionally checked by fluorescence analysis of column effluent during peak elution to confirm the presence of acenaphthene. Mass balance was also monitored on a few experiments by collecting column effluent fractions and analyzing them with the Perkin-Elmer spectrofluorimeter. Recoveries were consistently greater than ~85% but were generally higher for the higher velocity experiments. This dependence on flow rate was attributed to acenaphthene volatilization losses from the effluent reservoir over the longer duration, slow velocity experiments.

Experimental Moments. Experimental moments were calculated using the trapezoidal rule based on the following definitions:

$$k^{\text{th}} \text{ original moment: } m_k = \int_0^{\infty} Ct^k dt \quad (2-7)$$

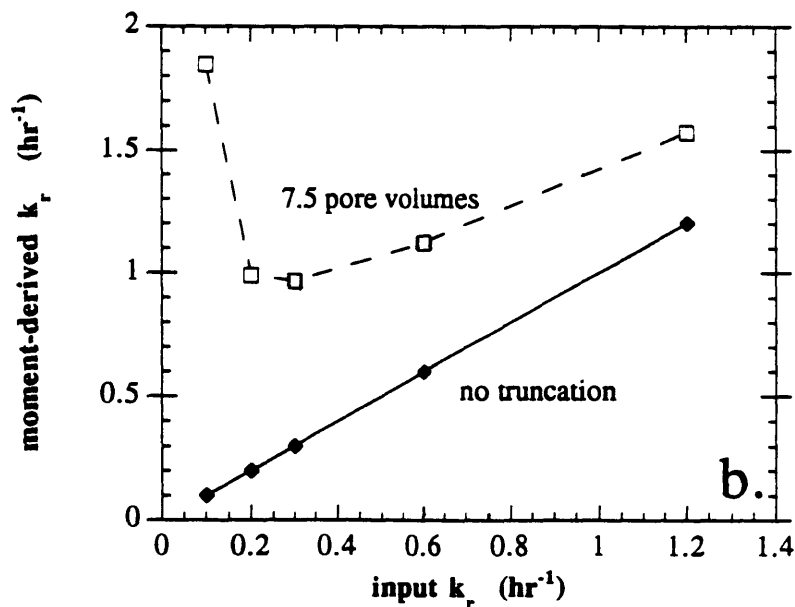
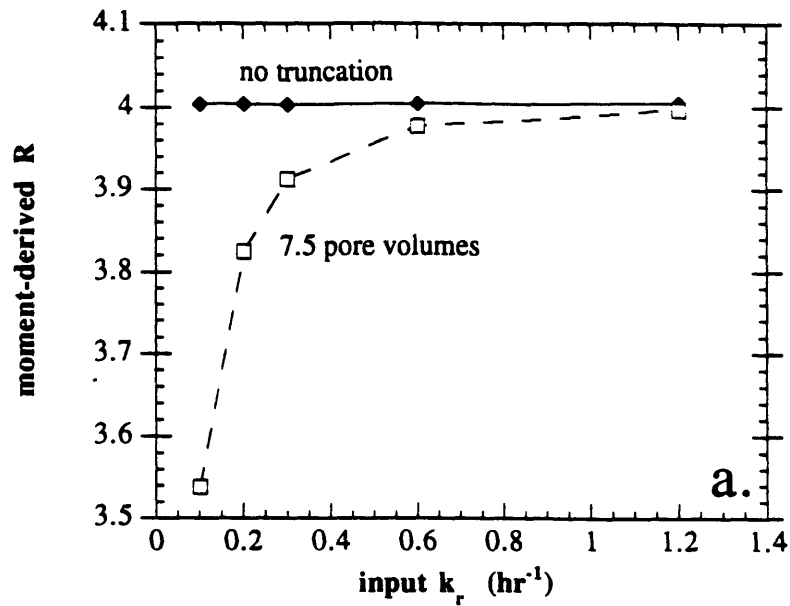
$$\text{first absolute moment: } \mu_1' = \frac{m_1}{m_0} = \frac{\int_0^{\infty} Ctdt}{\int_0^{\infty} Cdt} \quad (2-8)$$

$$\text{second central moment: } \mu_2 = \frac{1}{m_0} \int_0^{\infty} C(t - \mu_1')^2 dt \quad (2-9)$$

Prior to calculating experimental moments, the elution curves obtained at different velocities were truncated at times corresponding to the same number of pore volumes in order to minimize artifacts in the calculated moments due to differences in recorded peak tailing. Truncation corresponded to 2.7 pore volumes for nitrate and 7.5 pore volumes for acenaphthene. In addition, sloping baselines were subtracted from the raw data prior to moment calculation in order to account for detector drift (especially over the 5- to 8-day experiments).

The moments of elution curves generated at different flow velocities were fitted using the statistical capabilities of SigmaPlot (Jandel Scientific; Corte Madera, CA) to the theoretical expressions, equations (2-4) and (2-5'), to determine the model parameters L , R , α and k_r . The moments method was tested with simulated elution curves generated using the computer program CXTFIT [29] operated as a one-site, first-order kinetic model (i.e., $\beta=1/R$). The simulations showed that the moment fitting method recovered the input parameter values for ideal elution curves when the entire elution curve was accounted for (i.e., 124 pore volumes). Since experimental moment calculations are sensitive to the low concentration tails on the BTCs which are difficult to measure accurately (due to detector noise and drift), we made estimates of the error expected in our sorption parameters due to BTC truncation. Using reasonable values of α (0.05 cm), L (7 cm) and R (4.0), we varied k_r from 0.1 to 1.2 hr⁻¹ and velocity from 0.5 to 30 cm/hr in CXTFIT model simulations. The numerical experiments were treated by the method of moments for both the truncated (7.5 pore volumes) and full BTC cases. The simulations indicated that R is decreased by 2 to 12% from the true value (**Figure 2-3a**) and k_r is increased by a factor of 2 to 18 (**Figure 2-3b**) due to truncation. For both sorption parameters, the error increases dramatically as the input k_r value is decreased because of the increasing importance of long tails with slower desorption rate. From these simulations, we conclude that our moment-derived R value will not be significantly affected by the truncation, but the k_r value we calculate will be higher than the true k_r due to truncation. Thus, our sorption rate will be a conservative minimum estimate and sorption kinetics will have a greater impact on acenaphthene transport than our calculations below indicate.

Figure 2-3. First-order model simulations of error in (a) R and (b) k_r due to truncation of acenaphthene peaks at 7.5 pore volumes. The error for both parameters is a strong inverse function of the sorption rate parameter. See text for assumed parameter values. The R value obtained for our acenaphthene experiments was not significantly affected by truncation, but the k_r value we obtained is too high by a factor of approximately 4.



Errors reported below for the best-fit model parameters were calculated from SigmaPlot curve fit standard errors (SE) and error propagation techniques. The reported precisions are not corrected for truncation-derived inaccuracy.

Results and Discussion

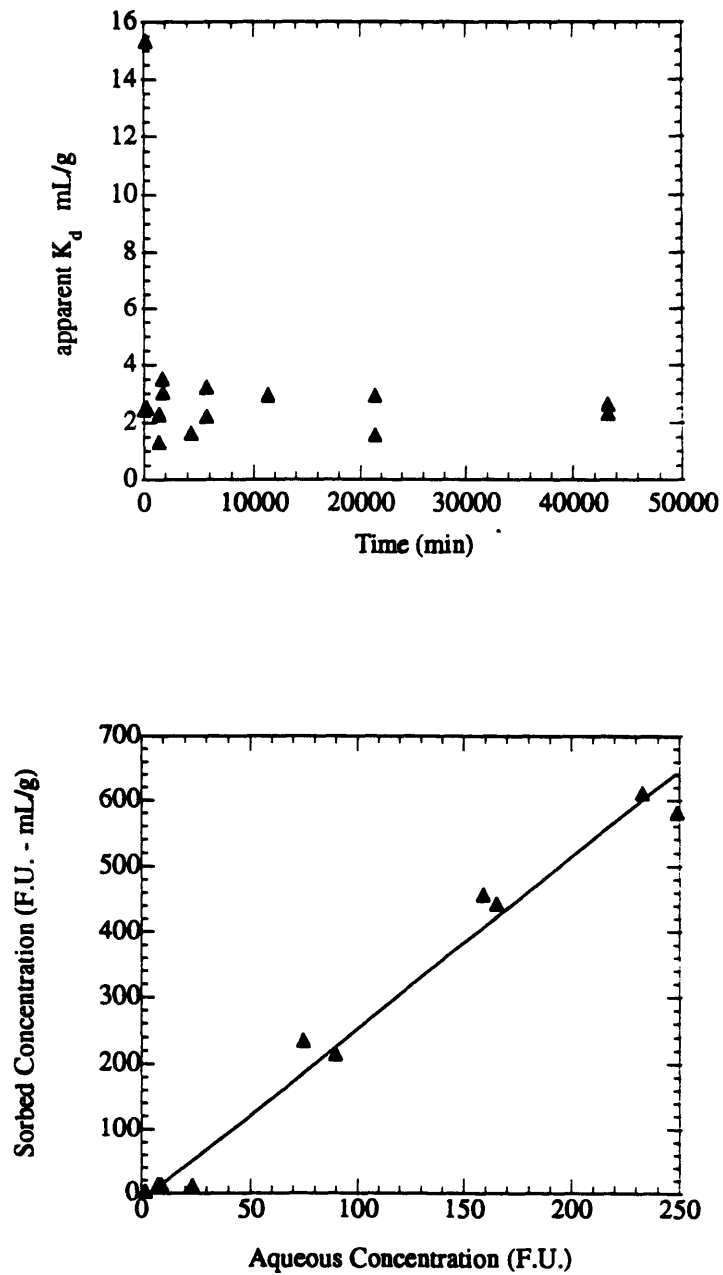
Batch Experiments. In the acenaphthene batch kinetic experiment, equilibrium was apparently reached within 24 min, the time of the first observation (**Figure 2-4a**). This was confirmed by the near-zero slope obtained for regression of the data without considering the single data point with a large apparent K_d . The average K_d value calculated from the kinetics data was 2.5 ± 0.63 (1σ) mL/g. The batch isotherm results (**Figure 2-4b**) confirmed the K_d value obtained in the kinetics experiment with a measured slope of 2.56 ± 0.08 (S.E.; standard error). The Freundlich model was also fit to the data and resulted in a K_d value of 2.94 ± 1.5 (S.E.) mL/g and an exponent value of 0.97 ± 0.09 (S.E.). Since the exponent value is not significantly different from 1.0, the linear isotherm model is appropriate.

The measured K_d value is approximately two times the value one would predict ($K_d^{\text{predict}} = 1.6$ mL/g) using the $K_{oc}f_{oc}$ relationship when K_{oc} is calculated using the log K_{oc} - log K_{ow} regression of Karickhoff [18] and f_{oc} of the 250-1000 μm size fraction. The predicted K_d value is close to the lower 2σ limit on the measured value, suggesting that $K_{oc}f_{oc}$ can be used to obtain a reasonable estimate of K_d for this system. The higher measured K_d value may also indicate mineral surface contributions to K_d . Other studies that reported agreement between measured K_d and $K_{oc}f_{oc}$ in aquifer sands include Ball and Roberts [2] and Larsen et al. [21].

The batch K_d value can be used to estimate the expected retardation factor for the column experiments. Given the column's bulk density of 1.55 g/cm^3 and porosity of 0.42, the expected R value for acenaphthene is 10 ± 0.09 (1σ , based on kinetics data).

Column Experiments. The elution pulses for nitrate and acetone did not show variations in peak position with pore velocity and eluted at one pore volume, confirming the assumption that these compounds did not sorb (**Figure 2-5a**). The nitrate peaks were symmetrical at the various flow rates, indicating there was little physical nonequilibrium (i.e., no appreciable immobile water) in this sandy aquifer material which would manifest itself as peak shifts and increased peak asymmetry with increasing velocity [35]. In addition, experiments at a given velocity (not shown) revealed that acetone and nitrate peaks coincided,

Figure 2-4. Acenaphthene batch results. (a) 30-day kinetics time course. K_d calculated based on equation (2-6) in text. (b) isotherm. Concentrations expressed in fluorescence units (F.U.). Sorbed concentrations were calculated by difference.



indicating that anion exclusion was not important in controlling nitrate transport through the column.

Acenaphthene elution curves, however, showed increasingly earlier breakthrough as pore velocity increased (**Figure 2-5b**). This was true for both the peak maximum and the center of mass (**Figure 2-6**). The observation that sorbing compounds are affected by pore velocity, while nonsorbing compounds are not, has been interpreted by many authors as evidence of sorption nonequilibrium affecting transport of the sorbing compound [5, 9, 23]. We conclude that sorptive nonequilibrium is indicated by shifts in the pore volume of the peak maximum (PV_{cmax}) with flow rate for sorbing compounds while conservative tracer peaks do not shift. This nonequilibrium condition is indicated by the acenaphthene and nitrate data for our column (**Figure 2-6a**). In contrast, the shifts in the center of mass with velocity (**Figure 2-6b**) was probably due to truncation. The rationale for these interpretations follows.

Under true equilibrium sorption conditions, the degree of sorbate retention by the column solids should be independent of flow rate because the sorption “reaction” is infinitely fast. Thus, for all compounds which achieve equilibrium with the sand, the sorbate peak should elute at the same number of pore volumes at all flow rates. Similarly, the peak for a conservative tracer should elute at one pore volume under all flow rates. In contrast, the elution peaks of kinetically-limited sorbing compounds will shift to lower pore volumes with increasing flow rate because the inverse relationship between contact time and flow rate allows less of the sorbate to complete the sorption “reaction”. In the limit of an infinitely fast flow rate, the sorbate-sorbent contact time would be too short to allow any sorption and sorbing compound peaks would elute with the conservative tracer at one pore volume.

Theoretically, the pore volume at which the first absolute moment elutes ($PV_{\mu 1}$) should be invariant with velocity as can be seen from manipulation of equation (4) to obtain a dimensionless expression (multiply both sides by v/L). $PV_{\mu 1}$ (center of mass) differs from PV_{cmax} (peak maximum) due to BTC tailing caused by slow desorption kinetics which increases the column residence time of some solute molecules. The long tails are difficult to quantify experimentally because tail concentrations approach the limits of compound detection. We observed an unexpected shift in $PV_{\mu 1}$ with velocity for acenaphthene (**Figure 2-6b**) which we attribute to poor resolution of the elution tails for the high velocity acenaphthene experiments and to our truncation of acenaphthene peaks at 7.5 pore volumes.

Although the tail truncation affected our $PV_{\mu 1}$ values for individual experiments, the higher velocity data are affected more than the low velocity runs. Since the moment

Figure 2-5. Column experiment evidence for sorptive nonequilibrium: (a) nitrate and (b) acenaphthene elution curves at three flow rates. Pore volumes were calculated assuming $L=6.2$ cm, $n=0.42$ and column cross-sectional area = 3.8 cm². Arrows indicate pore volume of first absolute moment.

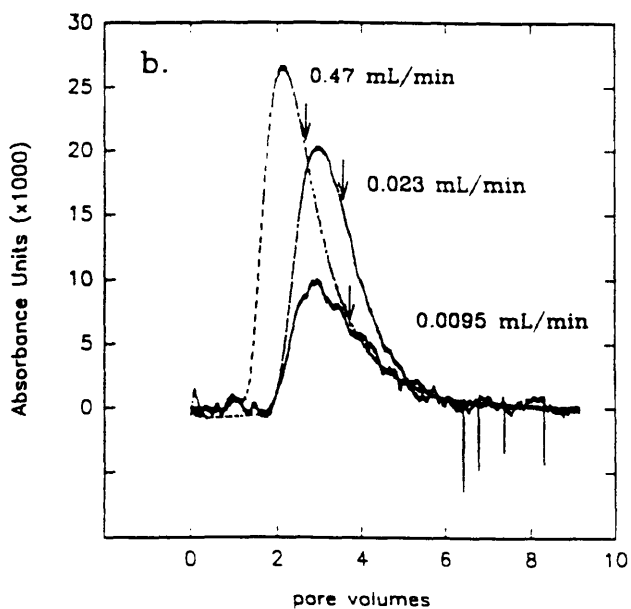
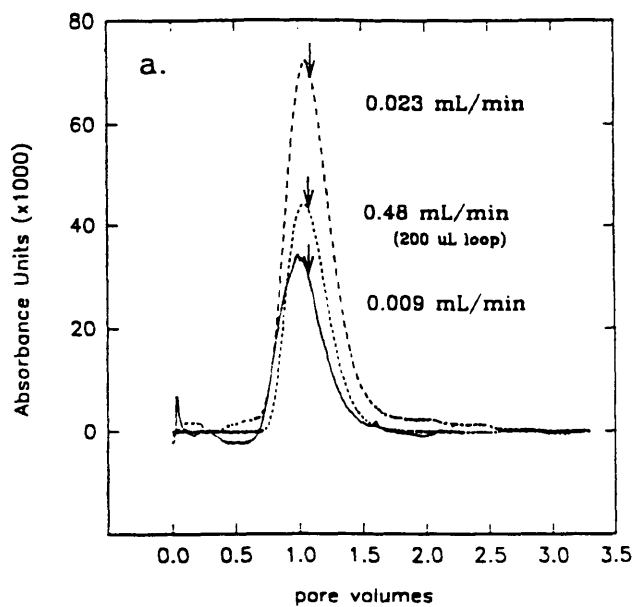
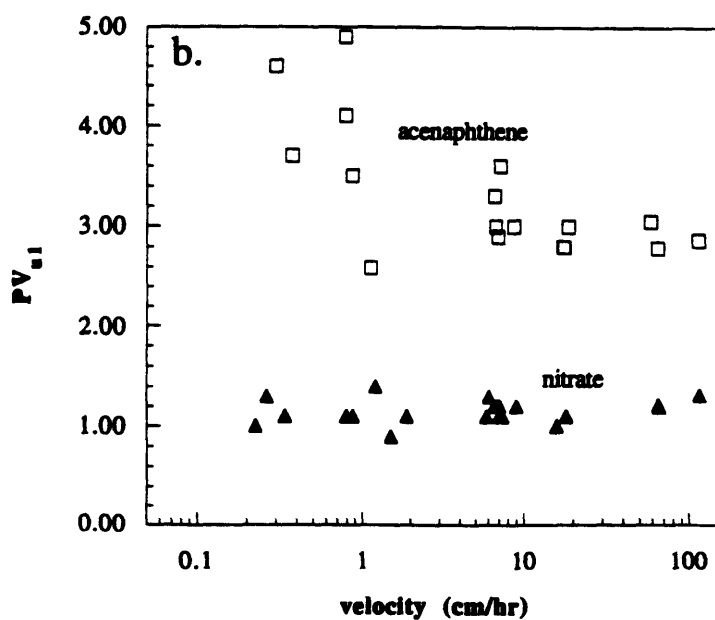
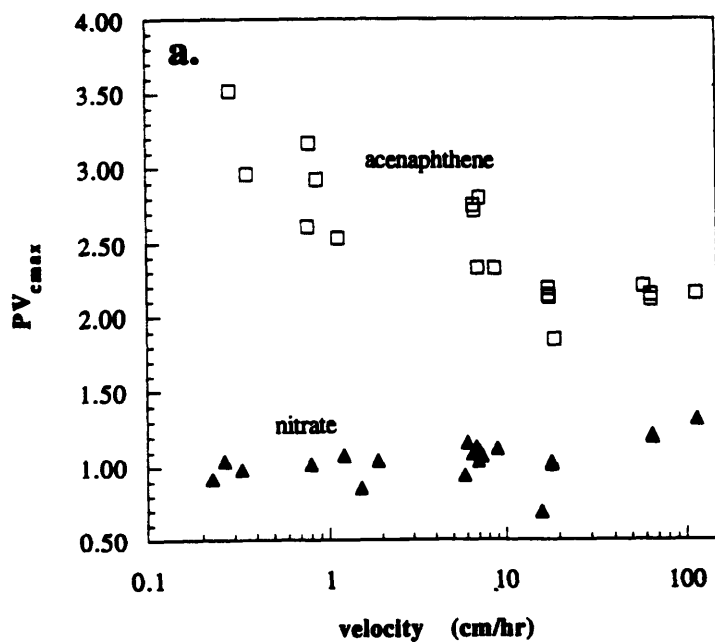


Figure 2-6. (a) Pore volume of peak maximum (PV_{cmax}) and (b) pore volume of first absolute moment (PV_{u1}) as a function of velocity. Experimental runs conducted at velocities greater than 20 cm/hr had additional tubing between column outlet and detector, possibly accounting for the slight increase in PV values.



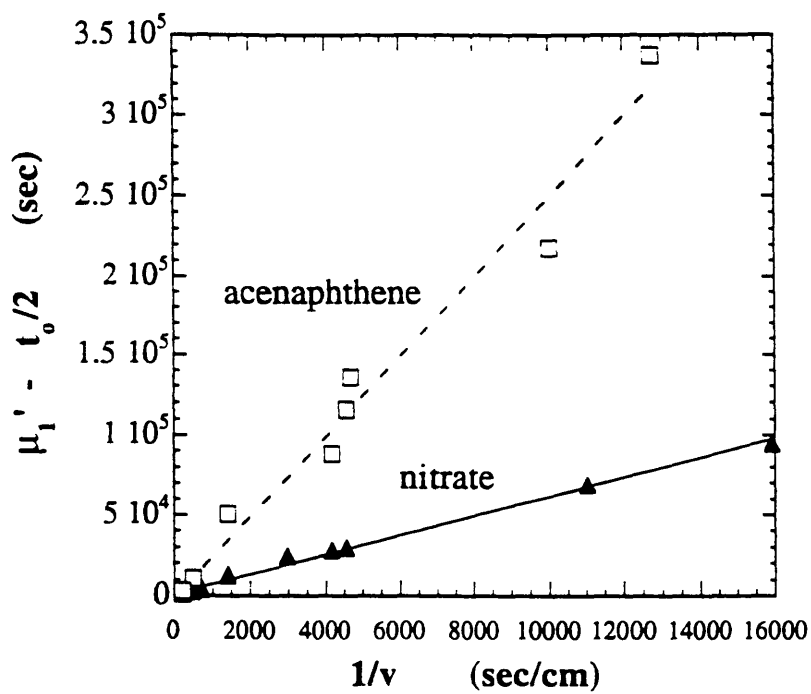
technique utilizes graphical plots versus inverse velocity (**Figures 2-7 and 2-9** below) which are insensitive to the individual high velocity experiments, the $PV_{\mu 1}$ value determined by the slowest velocity will govern the value of R. Thus, the truncations will not greatly impair our determination of R and k_r below.

Effective Column Length and Retardation Factor. The first moments of the elution peaks for nitrate and acenaphthene were used to calculate the effective column length, L, and the acenaphthene retardation factor, R, based on the assumption that nitrate behaved conservatively ($R_{NO_3} = 1$). The slope of the nitrate first absolute moment versus inverse velocity plot (**Figure 2-7**) indicates that $L = 6.18 \pm 0.1$ cm (1σ) for these experiments. This value is close to the actual packed column length of 7 cm giving us confidence in our data analysis technique. The retardation factor for acenaphthene, determined from first moments is 4.04 ± 0.14 (1σ), a value considerably less than that expected based on the batch K_d and column r_{sw} ($R_{expect} = 10 \pm 0.09$). The column R value determined from curve fits to equation (2-4) should be the true equilibrium value. Our column R indicates that acenaphthene was transported through the sand 3 times faster than one would predict based on batch results.

Possible explanations for this discrepancy between batch and column partitioning behavior are: (a) organic matter (or other significantly sorptive material) was lost from the column during initial column flushing, and (b) sorbate-sorbent contact times in the column were too short to allow equilibration. Alternative (a) can be ruled out because the organic carbon content of the column material before and after months of flushing showed no significant difference. (A 50% decrease in f_{oc} would be required to explain the observed discrepancy). There remains the possibility that the acenaphthene was not able to contact the same amount of sorptive material in the batch and column experiments. This explanation implies that some of the organic matter that is available for sorption in the batch tubes is essentially inaccessible in the column.

The texture of the Pine Barrens sediment lends itself to this interpretation. The quartz framework grains are coated with iron-oxide and kaolinite [40]. In addition, removal of the coatings by sonication resulted in a higher weight fraction of < 53 micron solids, a significant increase in the f_{oc} of this size fraction (see **Table 2-1**), and grey-white quartz grains instead of the natural orange-brown color. Furthermore, a preliminary experiment showed that supernatant turbidity increased dramatically (1000 NTU) immediately after tumbling commenced, but showed no further increase with tumbling time over a 2 week period. Assuming 1 NTU ~ 1 mg/L [39], the jump of approximately 1000 NTU represents ~ 2 wt % of the sediment used in this batch experiment ($r_{sw} = 0.09$: 3g sediment, 54 mL buffer).

Figure 2-7. First absolute moment expression (equation 2-4) as a function of inverse velocity. The nitrate best fit slope is 6.18 ± 0.11 (S.E.) and acenaphthene data slope is 24.97 ± 0.71 (S.E.). Assuming $R = 1.0$ for nitrate, the model parameters are $L = 6.2$ cm and $R = 4.04$ for acenaphthene.



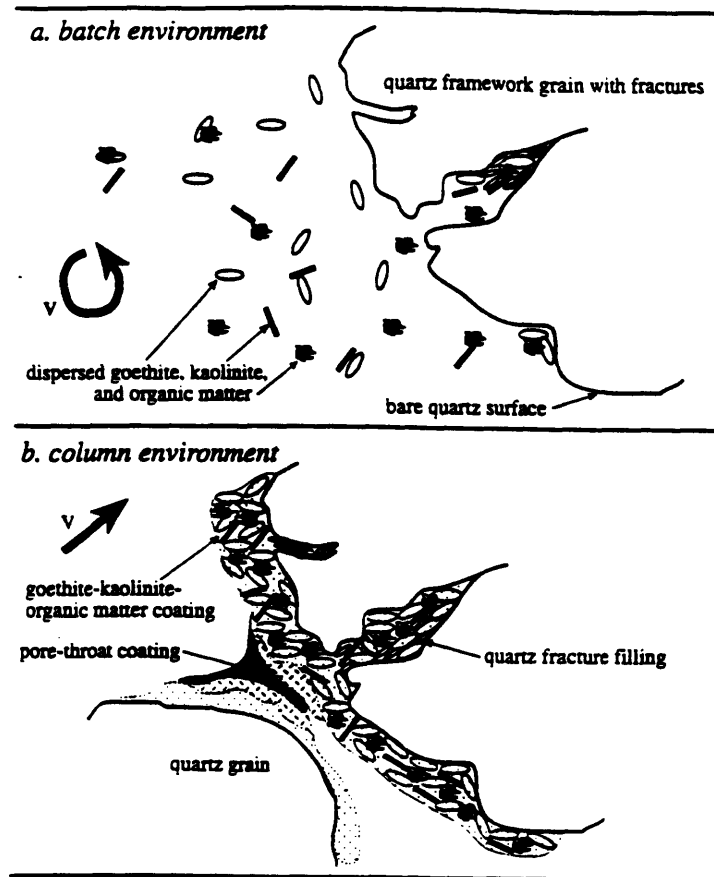
This weight fraction represents all of the available coatings, assuming that the sonicated <53 μm fraction chiefly represents grain coatings (**Table 2-1**). For the acenaphthene batch conditions at an r_{sw} of 0.55, the aqueous phase in the tumbled vials turned an exceedingly turbid, orange-brown color, indicating that iron oxide coatings were dispersed during the batch test. These tumbling and sonication data highlight the sensitivity of the Pine Barren sand's texture to high energy experimental conditions. Other studies have noted a dependence of sorption capacity and rate on tumbling dynamics or sorbent pulverization [2, 3, 28, 36].

Given these observations, we propose that organic matter is associated with the iron-oxide and kaolinite coatings in this sand and that these coatings become dispersed when the sand is immersed in water. The association of organic matter with the coatings is also consistent with the expected surface charge of organic matter (-), goethite (+) and kaolinite edges (+) at pH 4.8 based on the zero points of charge of these minerals [30, 31]. The association of organic matter with iron-bearing minerals in an aquifer sand was also noted by Barber et al. [4] for Cape Cod aquifer material.

The dispersion of the coatings is probably a function of r_{sw} and the dynamics of mixing as well as the solution pH and ionic strength which control particle surface charge and electrostatic double layer thickness. Certainly, the higher energy environment of the batch experiment must release more colloids into solution than for the column tests, and therefore the batch conditions must expose more of the colloid-associated organic matter to the sorbate. Dispersion of the coatings is also consistent with the nearly instantaneous uptake observed in the batch kinetic experiment.

An additional hypothesis is that removal of the iron-oxide and kaolinite coatings during batch mixing exposed additional sorption sites that remained inaccessible in the lower-energy column environment. These sites may be either bare mineral surfaces or pores and cracks in the quartz grains that contain diagenetic iron oxide and associated organic matter. The retardation factor observed for the column may delimit the accessibility between distinctly different types of sites: easily-dispersed exterior coatings on quartz grains (column-accessible) versus more-cohesive inner coatings and fracture fillings (batch-accessible) (**Figure 2-8**). In reality, there is a continuum of sorption sites with different degrees of accessibility in a given sorbent (i.e., organic matter located different distances from flowing water zones). The degree of sediment disaggregation that occurs under different experimental conditions probably controls which sites become available for a given experimental technique. The column/batch K_d discrepancy we observe has important implications for predictions of HOC transport in this sand based on batch tests alone. Since field conditions are more closely approximated by column experimental conditions, we

Figure 2-8. Sorption site exposure in an iron-oxide-coated sand. Variations in sediment texture for the batch and column experiments are interpreted as controlling the observed retardation factor or partition coefficient in these diverse hydrodynamic environments.



expect the column K_d rather than the batch K_d to be more representative of sorption behavior in the field. Use of the batch K_d value in this case would result in overprediction of compound retardation in the field by a factor of 3.

In contrast to our observations, numerous literature studies using aquifer sorbents and sorbates with $\log K_{OW}$'s that ranged from 1.8 to 3.6 have found agreement between batch and column K_d values [5, 23, 25, 33]. Fewer studies have noted large discrepancies between batch and column partition coefficients, although Miller and Weber [26] found column K_d 's that were 5 times lower than batch K_d 's for Ann Arbor aquifer material and lindane. Thus, batch-column K_d agreement cannot be attributed to low sorbent f_{OC} or low sorbate K_{OW} and is more likely dependent on column flow rate, batch dynamics and sorbent composition and texture, factors that are difficult to compare between different studies.

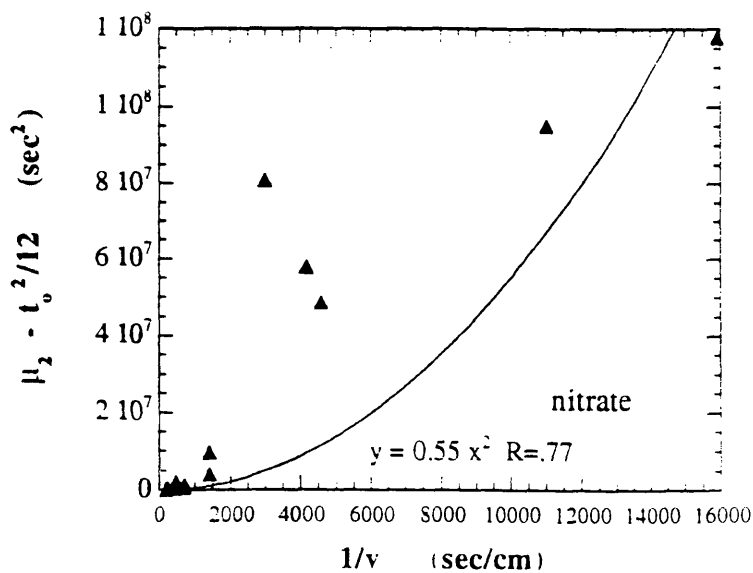
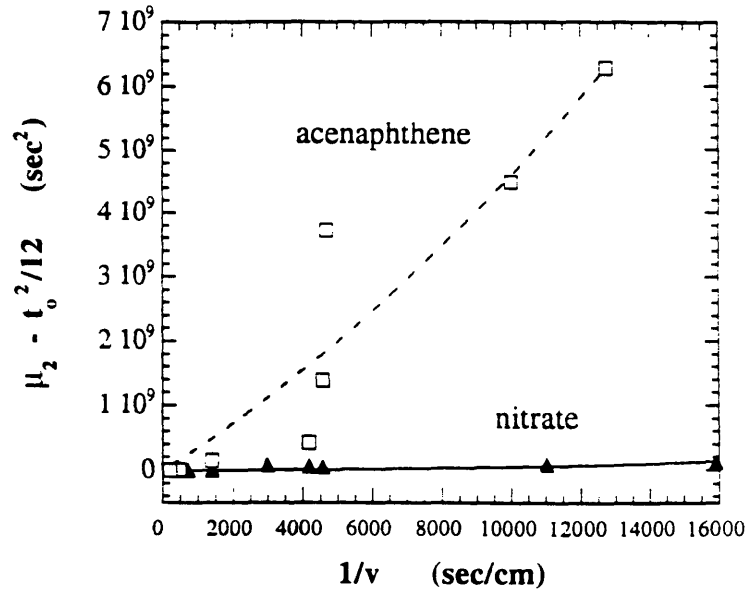
Dispersivity and Reverse Sorption Rate Constant. Hydrodynamic dispersion and sorption kinetics both contribute to peak width. As discussed above, equation (2-5') can be used to evaluate the hydrodynamic dispersivity, α , and the reverse rate constant for sorption, k_r . The nitrate data (**Figure 2-9**) gave a dispersivity for this column of 0.045 ± 0.007 cm (1σ), a value that is comparable to literature values for aquifer sands. For example, Lee et al. [23] calculated dispersivities of 0.05 and 0.06 cm for laboratory columns of Lula and Borden aquifer materials, respectively, using tritium BTCs fit to an equilibrium model. Brusseau [7] fit pentafluorobenzoic acid BTCs using dispersivities of 0.05 cm (Tampa) and 0.11 cm (Borden) at flow velocities of 83 and 5 cm/hr. Generally, one expects dispersivity to be on the order of the particle size [14] and the result we obtained is in excellent agreement with the geometric mean grain diameter of the column material, 0.05 cm.

The reverse sorption rate constant, k_r , calculated using the acenaphthene second central moment is $0.4 \pm 0.15 \text{ hr}^{-1}$. Recalling the inaccuracy due to BTC truncation, the true value of this desorption rate constant must be about 0.1 hr^{-1} . This first-order rate constant is based on a wide range of experimental sorbate-sorbent contact times that encompass the natural groundwater velocity, and it is therefore considered to be representative of the sorption process under natural flow conditions. Given this k_r , we calculate k_f' , the forward rate constant with inverse time units, using equation (2-3) as:

$$\begin{aligned} k_f' &= k_f r_{sw} = (K_d^{column} k_r) r_{sw} = (R - 1) k_r \\ &\approx 0.3 \text{ hr}^{-1} \end{aligned} \quad (2-10)$$

For any reversible first-order process, the time constant governing the response of the system is calculated from the sum of the forward and reverse rate constants [44]. The

Figure 2-9. Second central moment expression (equation 2-5') as a function of inverse velocity. Upper graph shows both compounds and lower plot shows nitrate only. Curve fits assuming $R = 1.0$ for nitrate, $L = 6.2$ cm and $R = 4.04$ for acenaphthene are as follows: dispersion term coefficient for nitrate = 0.55 ± 0.08 (S.E.) and for acenaphthene = 12.46 ± 11.3 (S.E.). Sorption kinetics term coefficient for nitrate = 0 (conservative assumption) and for acenaphthene = $3.4 \times 10^5 \pm 1.2 \times 10^5$ (S.E.). These curve fits give first-order model parameter values of $\alpha = 0.06$ cm and $k_r = 0.40$ hr⁻¹.



characteristic time scale for the sorption process is therefore equal to $(k_f' + k_r)^{-1}$, or 3 hr for our column experiments.

Process Relative Rates. In order to assess the importance of sorption kinetics in describing contaminant transport on the scale of a laboratory column, we must quantify the relative rates of the competing sorption and advection processes. We determined a Peclet number ($= \frac{vL}{D}$) of 40-60 for our column by fitting an equilibrium model to individual nitrate BTCs. (This is equivalent to saying that the column length is about 40 times the value of the sand's dispersivity). Thus, advective transport dominates over dispersive transport in our sand column and therefore advection is the appropriate hydrodynamic process with which sorption should be compared. The rate of advection, r_{adv} , is quantified by pore velocity and the distance over which the processes are to be compared. Thus,

$$r_{adv} \left[\frac{l}{v} \right] = \frac{v}{l} \quad (2-11)$$

The dimensionless Damkohler number is generally used to compare the rate of a chemical reaction to a physical transport rate. Here we define the Damkohler number as:

$$D_{klr} = \frac{r_{adv}}{r_{sorp}} = \frac{v}{l(k_f' + k_r)} \quad (2-12)$$

When $D_{klr} \gg 1$, advection rates dominate and contaminants are transported through the sorbent too quickly to allow completion of the sorption "reaction". In this case, a kinetics description for sorption is necessary to accurately model compound transport. On the other extreme, when $D_{klr} \ll 1$ the rate of sorption is very fast relative to the physical transport rate and an equilibrium description of sorption is sufficient to quantify HOC transport.

The advection and sorption rates must be calculated based on an appropriate length scale for both physical processes. Since the competition is between transport of solute passed a sorbing grain versus retardation of the solute via sorption to the grain, it is reasonable to choose a length scale on the order of the size of sand grains in our system. Thus, we have chosen the geometric mean particle diameter as the appropriate value of l in equation (2-12). Other authors have used the column length in their definitions of Damkohler number [6, 8, 9, 47], a practice which seems appropriate only when the column can be viewed as a well-mixed batch reactor. For our pulse-input experiments, the particle scale determines the appropriate sorbate-sorbent contact time for comparison with the time constant for sorption.

D_{klr} , calculated for velocities that span our range of experimental values, range from 10 to 5000, values which suggest that on the grain-scale, relatively fast advection would not

allow the sorption process for HOCs like acenaphthene to proceed to equilibrium under all of the flow rates studied. These Damkohler numbers based on the geometric mean grain diameter corroborate our other experimental observations (i.e., peak shifts with velocity; see **Figure 2-5**) which indicate that nonequilibrium conditions prevailed in the column.

The use of the grain diameter as the advection length scale has important implications for interpreting our results in terms of field transport of PAHs such as acenaphthene. Since the grain size length scale is invariant from the laboratory to the field (for unsieved materials), we can apply our results directly to the field as long as we have information on average groundwater velocity and particle size.

Field versus Laboratory Application of Results. In the field, several factors which contribute to solute transport may outweigh the importance of small-scale sorption kinetic limitations on transport. For example, aquifer heterogeneity at the field scale will be important in determining the spatial variability of both advection rates and sorptive capacity [17]. Thus, knowledge of the sorptive properties of all the subsets of aquifer material that make up the whole transport regime is essential to predicting contaminant transport on a large-scale. Burr et al. [11] showed that, under certain conditions, aquifer-scale heterogeneity in hydraulic conductivity and K_d can outweigh the importance of small-scale nonequilibrium processes such as physical nonequilibrium (intraparticle diffusion) or sorption kinetics. However, the column studies reported here can help us understand the grain-scale importance of sorption kinetics and lead to greater understanding of the mechanism of sorption. If the sorption mechanism can be determined, we can better identify the field-scale conditions under which sorption kinetics will have an important influence on solute transport.

Natural groundwater velocities at a few sandy aquifer sites were examined in order to determine whether advection rates greatly exceed the acenaphthene sorption rate determined in this study. This comparison assumes that the sorption rate measured in the Pine Barrens column is comparable to that which would be measured for other sandy aquifer materials. The advection rates, calculated on the basis of a particle diameter length scale (500 microns), exceed the sorption process rate of 0.4 hr^{-1} for all of the aquifers under natural flow conditions (**Table 2-2**). This calculation implies that *a kinetic description of sorption will be required at these sites*. Furthermore, we would expect pumping conditions to exacerbate the departure from sorptive equilibrium as noted by Bahr [1].

Table 2-2
Natural groundwater velocities and advection rates in sandy aquifers

Location	Aquifer Type	f_{oc}	v (cm/day)	Γ_{adv}[*] (hr⁻¹)	Ref
Gloucester Landfill Ontario	confined, stratified sand and gravel (glacial outwash) <i>[hazardous waste plume ~350 m long]</i>	NR	5-7	4.17- 5.8	[1]
Borden Ontario	unconfined, sandy (glaciofluvial) <i>[~20 meter plume dimensions]</i>	0.02%	9	7.5	[37]
Pine Barrens New Jersey	unconfined, iron-oxide-coated quartz sand (marine sheet sands) <i>[uncontaminated site]</i>	0.2%	8.5	7.1	[39]
Moffett Field California	confined, sand and gravel (alluvial) <i>[organic solutes contamination]</i>	0.11%	100-200	83-167	[38]
Cape Cod Massachusetts	unconfined, stratified sand and gravel (outwash) <i>[sewage plume ~2 km long]</i>	NR	40	33	[22]

NR = not reported

*advection rates based on particle length scale of 500 microns and equation (2-11).

Diffusion Model Interpretation. The first-order rate constant obtained in this study can be interpreted in terms of an intrasorbent diffusion model [3, 49] if k_r in equation (2-2) is considered to be a lumped mass transfer parameter:

$$k_r' = \Omega \frac{D_{eff}}{\delta^2} \quad (2-13)$$

where D_{eff} is the effective diffusion coefficient (cm^2/sec), δ is the length scale over which diffusion occurs, and Ω accounts for both differences in the analytical solutions to the first-order and radial diffusion models [34, 48, 49] and for solid-to-water ratio in the column system relative to the single sphere analytical solution (i.e., Crank [13]). This model allows one to interpret the sorption rate we measured for acenaphthene in terms of meaningful physico-chemical properties of the sorbate and sorbent.

We propose that the relatively high- f_{oc} , kaolinite-goethite coatings on the quartz framework grains are the primary sorption sites in this aquifer material. Slow sorption kinetics can therefore be interpreted as slow diffusion within these fine-grained coatings of randomly-oriented grains which Ryan and Gschwend [40] report to be up to 10 μm thick. Assuming that diffusion occurs in the pore spaces of the coatings, an effective diffusivity can be defined as:

$$D_{eff} = \frac{D_{aq}}{R_{coat} \tau} \quad (2-14)$$

where D_{aq} = molecular diffusivity of acenaphthene, τ = coating tortuosity, and R_{coat} = coating retardation factor. We evaluate R_{coat} from estimates of coating K_d and solid-to-water ratio. Coating K_d may be estimated from K_{oc} and the f_{oc} of the fine fraction (< 53 μm) mobilized by sonication of the Pine Barrens sand (~2 %, see **Table 2-1**). Assuming a coating porosity value of 0.5, a solid density of 2.5 cm^3/g , and $\log K_{oc} = 3.5$, we calculate a coating retardation factor of 130. Finally, we use the inverse porosity relationship of Ullman and Aller [46] for tortuosity. Assuming an acenaphthene aqueous diffusivity of $8 \times 10^{-6} \text{ cm}^2/\text{sec}$, D_{eff} based on equation (2-14) is $3 \times 10^{-8} \text{ cm}^2/\text{sec}$. Combining this estimate of effective diffusivity with our observed desorption rate constant of 0.1 hr^{-1} (taking truncation into account), and a range of Ω of 10-100 (covering the range of contact times in our column), we calculate an average diffusion distance, δ , of approximately 1000 to 3000 microns using equation (2-13).

Our calculated diffusion length is 100 times larger than the coating thickness reported by Ryan and Gschwend [40] and is closer to the diameter of the largest quartz grains in our column. However, in contrast to other studies with calcareous sands [3, 42], we can rule out diffusion within the quartz grains based on mercury porosimetry data for the uncoated quartz

grains which showed no intraparticle micropores less than approximately 10 microns diameter. It is more likely that we have not correctly accounted for a coating transport parameter such as tortuosity or pore constrictivity in equation (2-14). The range of coating pore diameters we measure (5 nm - 1 μm) suggests that coating tortuosity and constrictivity may require a more complex model than we have employed. Alternatively, we may not be modeling the right rate-limiting step in the sorption process (i.e., intraorganic matter diffusion; [8]). Further work is required to develop a method for estimating HOC sorption kinetics in sands based on measurable sorbent properties.

Conclusions

Moments analysis using a first-order sorption model was applied to breakthrough curves measured at a range of realistic (natural gradient to pumping conditions) pore velocities to give a sorption process rate constant (sum of forward and reverse rates) of 0.4hr^{-1} for acenaphthene sorption onto an iron-oxide and kaolinite coated sand. This translates into a characteristic time scale for sorption of a few hours. Sorption rates of this order of magnitude are comparable to small-scale (grain diameter) advection rates commonly observed under natural gradient conditions at many sandy aquifer localities. Thus, our results indicate that a kinetic sorption model rather than an equilibrium one is required to assess acenaphthene transport in these aquifers at natural groundwater flow rates. We suspect that at the higher pore velocities induced by groundwater pumping, sorption kinetics will play an increasingly important role in acenaphthene transport.

We found a discrepancy between batch and column K_d which we attribute to an increase in accessibility of sorption sites in the batch tests. In batch experiments, dispersion of organic-matter-rich, iron-oxide and kaolinite coatings on quartz grains, and possibly disaggregation of more-cohesive diagenetic mantles on the framework quartz grains, allowed acenaphthene interaction with sorption sites that were inaccessible or even nonexistent in the column experiments. These results emphasize that factors such as r_{sw} , column flow rate, batch incubation time, sediment composition and texture, as well as batch mixing dynamics will have an impact on sorption parameters quantified in the laboratory. It is important to take these experimental factors into account when applying batch K_d values to diverse environmental conditions. As we observed, for some sorbents, batch K_d values may not apply to laboratory column experiments with the same material.

Literature Cited

1. Bahr, J. M. (1989) Analysis of nonequilibrium desorption of volatile organics during field test of aquifer decontamination. *J. Contam. Hydrol.*, 4: 205-222.
2. Ball, W. P. and P. V. Roberts. (1991) Long-term sorption of halogenated organic chemicals by aquifer material. 1. Equilibrium. *Environ. Sci. Technol.*, 25: 1223-1237.
3. Ball, W. P. and P. V. Roberts. (1991) Long-term sorption of halogenated organic chemicals by aquifer material. 2. Intraparticle diffusion. *Environ. Sci. Technol.*, 25: 1237-1249.
4. Barber, L. B., II, E. M. Thurman and D. D. Runnells. (1992) Geochemical heterogeneity in a sand and gravel aquifer: Effect of sediment mineralogy and particle size on the sorption of chlorobenzenes. *J. Contam. Hydrol.*, 9: 35-54.
5. Bouchard, D. C., A. L. Wood, M. L. Campbell, P. Nkedi-Kizza and P. S. C. Rao. (1988) Sorption nonequilibrium during solute transport. *J. Contam. Hydrol.*, 2: 209-223.
6. Brusseau, M. L. (1992) Nonequilibrium transport of organic chemicals: the impact of pore-water velocity. *J. Contam. Hydrol.*, 9: 353-368.
7. Brusseau, M. L. (1993) The influence of solute size, pore water velocity and intraparticle porosity on solute dispersion and transport in soil. *Water Resour. Res.*, 29: 1071-1080.
8. Brusseau, M. L., R. E. Jessup and P. S. C. Rao. (1991) Nonequilibrium sorption of organic chemicals: elucidation of rate-limiting processes. *Environ. Sci. Technol.*, 25: 134-142.
9. Brusseau, M. L., T. Larsen and T. H. Christensen. (1991) Rate-limited sorption and nonequilibrium transport of organic chemicals in low organic carbon aquifer materials. *Water Resour. Res.*, 27: 1137-1145.
10. Brusseau, M. L. and P. S. C. Rao. (1989) Sorption nonideality during organic contaminant transport in porous media. *CRC Crit. Rev. Environ. Control.*, 19: 33-99.
11. Burr, D. T., E. A. Sudicky and R. L. Naff. (1994) Nonreactive and reactive solute transport in three-dimensional heterogeneous porous media: Mean displacement, plume spreading, and uncertainty. *Water Resour. Res.*, 30: 791-815.
12. Coleman, A. (1980) Enhanced detection of bacteria in natural environments by fluorochrome staining of DNA. *Limnol. Oceanogr.*, 25: 948-951.
13. Crank, J. (1975) The Mathematics of Diffusion. Oxford University Press: Oxford; 414 pp.
14. Freeze, R. A. and J. A. Cherry. (1979) Groundwater. Prentice-Hall, Inc.: Englewood Cliffs, NJ; 604 pp.

15. Galan, M. A., M. Suzuki and J. M. Smith. (1975) Effect of adsorption characteristics on pulse retention times. *Ind. Eng. Chem., Fundam.*, 14: 273-275.
16. Goltz, M. N. and P. V. Roberts. (1986) Interpreting organic solute transport data from a field experiment using physical nonequilibrium models. *J. Contam. Hydrol.*, 1: 77-93.
17. Harmon, T. C., L. Semprini and P. V. Roberts. (1992) Simulating solute transport using laboratory-based sorption parameters. *J. Environ. Engineering.*, 118: 666-689.
18. Karickhoff, S. W. (1981) Semi-empirical estimation of sorption of hydrophobic pollutants on natural sediments and soils. *Chemosphere.*, 10: 833-846.
19. Kookana, R. S., R. D. Schuller and L. A. G. Aylmore. (1993) Simulation of simazine transport through soil columns using time-dependent sorption data measured under flow conditions. *J. Contam. Hydrol.*, 14: 93-115.
20. Kucera, E. (1965) Contribution to the theory of chromatography: Linear non-equilibrium elution chromatography. *J. Chromat.*, 19: 237-248.
21. Larsen, T., P. Kjeldsen and T. H. Christensen. (1992) Sorption of hydrophobic hydrocarbons on three aquifer materials in a flow through system. *Chemosphere.*, 24: 439-451.
22. LeBlanc, D. R., S. P. Garabedian, K. M. Hess, L. W. Gelhar, R. D. Quadri, K. G. Stollenwerk and W. W. Wood. (1991) Large-scale natural gradient tracer test in sand and gravel, Cape Cod, Massachusetts 1. Experimental design and observed tracer movement. *Water Resour. Res.*, 27: 895-910.
23. Lee, L. S., P. S. C. Rao, M. L. Brusseau and R. A. Ogwada. (1988) Nonequilibrium sorption of organic contaminants during flow through columns of aquifer materials. *Environ. Tox. Chem.*, 7: 779-793.
24. Lion, L. W., T. B. Stauffer and W. G. MacIntyre. (1990) Sorption of hydrophobic compounds on aquifer materials: Analysis methods and the effect of organic carbon. *J. Contam. Hydrol.*, 5: 215-234.
25. MacIntyre, W. G., T. B. Stauffer and C. P. Antworth. (1991) A comparison of sorption coefficients determined by batch, column, and box methods on a low organic carbon aquifer material. *Ground Water.*, 29: 908-913.
26. Miller, C. T. and W. J. Weber Jr. (1986) Sorption of hydrophobic organic pollutants in saturated soil systems. *J. Contam. Hydrol.*, 1: 243-261.
27. Miller, M. M., S. P. Wasik, G.-L. Huang, W.-Y. Shiu and D. Mackay. (1985) Relationships between octanol-water partition coefficient and aqueous solubility. *Environ. Sci. Technol.*, 19: 522-529.
28. Ogwada, R. A. and D. L. Sparks. (1986) Kinetics of ion exchange on clay minerals and soil: I. Evaluation of methods. *Soil Sci. Soc. Am. J.*, 50: 1158-1162.
29. Parker, J. C. and M. T. van Genuchten. (1984) Determining transport parameters from laboratory and field tracer experiments. Bulletin 84-3, Virginia Agricultural Experimental Station.

30. Parks, G. A. (1965) The isoelectric points of solid oxides, solid hydroxides and aqueous hydroxo complex systems. *Chem. Rev.*, 65: 177-198.
31. Parks, G. A. (1967) Aqueous surface chemistry of oxides and complex oxide minerals. Isoelectric point and zero point of charge. In *Equilibrium Concepts in Natural Water Systems*. Stumm, W. (Ed.) A.C.S.: Washington, D.C.; pp. 121-160.
32. Pavlostathis, S. G. and G. N. Mathavan. (1992) Desorption kinetics of selected volatile organic compounds from field contaminated soils. *Environ. Sci. Technol.*, 26: 532-538.
33. Ptacek, C. J. and R. W. Gillham. (1992) Laboratory and field measurements of non-equilibrium transport in the Borden aquifer, Ontario, Canada. *J. Contam. Hydrol.*, 10: 119-158.
34. Rao, P. S. C., R. E. Jessup, D. E. Rolston, J. M. Davidson and D. P. Kilcrease. (1980) Experimental and mathematical description of nonadsorbed solute transfer by diffusion in spherical aggregates. *Soil Sci. Soc. Am. J.*, 44: 684-688.
35. Rao, P. S. C., D. E. Rolston, R. E. Jessup and J. M. Davidson. (1980) Solute transport in aggregated porous media: theoretical and experimental evaluation. *Soil Sci. Soc. Am. J.*, 44: 1139-1146.
36. Rijnaarts, H. H. M., A. Bachmann, J. C. Jumelet and A. J. B. Zehnder. (1990) Effect of desorption and intraparticle mass transfer on the aerobic biomineralization of a-hexachlorocyclohexane in a contaminated calcareous soil. *Environ. Sci. Technol.*, 24: 1349-1354.
37. Roberts, P. V., M. N. Goltz and D. M. Mackay. (1986) A natural gradient experiment on solute transport in a sand aquifer 3. Retardation estimates and mass balances for organic solutes. *Water Resour. Res.*, 22: 2047-2058.
38. Roberts, P. V., G. D. Hopkins, D. M. Mackay and L. Semprini. (1990) A field evaluation of in-situ biodegradation of chlorinated ethenes: Part 1, methodology and field site characterization. *Ground water.*, 28: 591-604.
39. Ryan, J. N. (1988) Colloid mobilization in two Atlantic Coastal Plain aquifers: colloid formation and stability. M.S. thesis, Massachusetts Institute of Technology.
40. Ryan, J. N. and P. M. Gschwend. (1992) Effect of iron diagenesis on the transport of colloidal clay in an unconfined sand aquifer. *Geochim. Cosmochim. Acta.*, 56: 1507-1521.
41. Schneider, P. and J. M. Smith. (1968) Adsorption rate constants from chromatography. *A.I.Ch.E. Journal.*, 14: 762-771.
42. Schuth, C. and P. Grathwohl. (1994) Nonequilibrium transport of PAHs: A comparison of column and batch experiments. In *Transport and Reactive Processes in Aquifers*. Dracos, Th. and F. Stauffer (Eds.) Balkema: Rotterdam; pp. 143-148.
43. Steinberg, S. M., J. J. Pignatello and B. L. Sawhney. (1987) Persistence of 1,2-dibromoethane in soils: entrapment in intraparticle micropores. *Environ. Sci. Technol.*, 21: 1201-1208.

44. Stone, A. T. and J. J. Morgan. (1990) Kinetics of chemical transformations in the environment. In *Aquatic Chemical Kinetics*, Stumm, W. (Ed.) John Wiley and Sons, Inc.: New York; pp. 1-41.
45. Thorbjarnarson, K. W. (1990) Evaluation of sorption nonequilibrium in forced-gradient tracer tests. Ph.D. thesis, University of California, Los Angeles.
46. Ullman, W. J. and R. C. Aller. (1982) Diffusion coefficients in nearshore marine sediments. *Limnol. Oceanogr.*, 27: 552-556.
47. Valocchi, A. J. (1985) Validity of the local equilibrium assumption for modeling sorbing solute transport through homogeneous soils. *Water Resour. Res.*, 21: 808-820.
48. van Genuchten, M. T. (1985) A general approach for modeling solute transport in structured soils. *Memoires IAH.*, 17: 513-526.
49. Wu, S.-C. and P. M. Gschwend. (1988) Numerical modeling of sorption kinetics of organic compounds to soil and sediment particles. *Water Resour. Res.*, 24: 1373-1383.

Chapter 3

SORBATE HYDROPHOBICITY AND SORPTION RATE IN AN AQUIFER SAND

Introduction

Numerous recent studies have examined the rate of sorption to natural solids and concluded that diffusive transport limitations control the rate of solute uptake and release [1, 15, 20, 37, 38]. However, many questions remain concerning the mechanism of hydrophobic organic compound sorption. For example, there are two possible diffusion media - intraparticle/mineral pores and sediment organic matter [6] - and no method to distinguish the two using current analytical techniques. Furthermore, regardless of the actual mechanism, there is presently no consensus as to how one can predict the rate of sorption from solute and sorbent properties. Elucidating the mechanism of sorption will help pinpoint the key measurements required for sorption rate prediction. Conversely, identifying the sorbate and sorbent properties required to estimate the rate of sorption will help delineate the sorption mechanism. Here we focus on how sorbate hydrophobicity affects the rate of sorption and develop a conceptual framework for predicting sorption rate for three polycyclic aromatic hydrocarbons (PAHs).

Background

A few recent studies have used a series of organic compounds to test the diffusion model, chiefly using batch tests to quantify the intraparticle diffusivity [1, 20]. Hutzler et al. [23] modeled column breakthrough curves (BTCs) with a diffusion-based model and estimated many of the seven fitting parameters using empirical correlations from the chemical engineering literature. They were unsuccessful in fitting the dispersion coefficient with available correlations and found best-fit particle radii (i.e., diffusion path lengths) to vary for different compounds. Pignatello et al. [38] fit column desorption data for two polar organic compounds to a "2-site" diffusion model (i.e., one fast sorption component and one that is kinetically controlled) and concluded that because particle size had little influence on desorption rate, the "slow" compartment diffusion medium was microparticles that existed in all the size fractions. Earlier, Pignatello [37] had concluded that slow diffusion in organic matter was controlling the sorption rate for a series of halogenated compounds based on batch desorption tests which showed increased residual sorbed compound with increasing soil organic matter content and appreciable residual in a sorbent size fraction with significant plant detritus. Pignatello [37] also pointed out the importance of mineral phases in affecting sorption rate chiefly through the shielding and aggregating effects iron- and aluminum-oxyhydroxide and clay minerals have on organic matter in soils and sediments. Farrell and Reinhard [15] examined trichloroethylene (TCE) sorption kinetics under 100% relative humidity conditions with silica gel and aquifer sand sorbents

and concluded that adsorption in micropores (which are on the order of the solute diameter) controlled the rate of sorption. These authors showed that the commonly-employed retarded pore diffusion model based on particle diameter diffusion lengths was unable to successfully fit both the fast and slowly desorbing elution profiles. Farrell and Reinhard [15] also noted that the slowly desorbing TCE fraction correlated with the Freundlich isotherm exponent and surface area of the silica gel, but did not correlate with internal porosity, organic matter content, pore diameter or particle size. Further, they attributed slow desorption to "microporosity" but failed to mechanistically model what was meant by such a term. Brusseau et al. [6] examined the sorption mechanism for a series of aromatic compounds in aquifer sands, and found that a slow diffusion step, rather than a slow chemical reaction or physical nonequilibrium, provided the best explanation of their data. They pointed out that in order for retarded intraparticle (i.e., mineral) diffusion to be the rate-limiting process, a significant fraction of mineral pores with diameters less than 25 nm are required (assuming solute diameters of approximately 1 nm). These authors also observed a molecular weight dependence of sorption rates determined by curve-fitting breakthrough curves with the computer model CXTFIT [36] and concluded that intraorganic matter diffusion was responsible for the slow sorption rates they observed.

We carried out sorption kinetics column and batch experiments using three sorbates with well-known physico-chemical properties: naphthalene, acenaphthene and phenanthrene and a single well-characterized sorbent, Pine Barrens sand [43]. By comparing the relative sorption rates of these chemicals with a single sorbent material using the same experimental techniques as described by Holmén and Gschwend [22], and estimating sorbent properties such as diffusion path length, tortuosity and constrictivity from empirical correlations and detailed observation of sorbent textural properties, we further constrain the key sorbate and sorbent properties required to predict diffusion model parameters in this low organic carbon aquifer material. Our objective was to understand the key sorbate parameters required to successfully estimate the sorption rate in this sand which previous work [22] with acenaphthene showed to be critical for accurate estimation of acenaphthene transport under natural flow conditions.

Methods

Sorbent. The aquifer sand used in all sorption experiments was a subfraction of the Pine Barrens, New Jersey, iron-oxide- and kaolinite-coated quartz sand previously characterized by Ryan and Gschwend [43]. As described in detail in Chapter 2, the coatings on the

quartz grains have organic matter contents 30 times higher than the bulk sand and are believed to be the primary source of sorption capacity. After air-drying, the 250-1000 micron size fraction was stored in glass jars. Organic carbon content was determined to be 0.048% (± 0.003 , 1σ) for this size fraction based on CHN analysis of four replicate 50 mg pulverized sand samples using a Perkin-Elmer Model 2400 instrument. The pore size distribution and total surface area of the sorbent were determined by mercury intrusion by Porous Materials Inc. (Ithaca, NY) assuming cylindrical pores, a mercury surface tension of 480 dynes/cm and contact angle of 140 degrees. Scanning Electron Microscopy (SEM) and Energy Dispersive X-ray (EDX) analysis using a Cambridge Instruments model 240 StereoScan were used to identify sorbent texture and coating morphology. Sand samples were prepared either by mounting dry sediment on aluminum stubs with double-sided tape, or as polished thin sections after the dry sand was impregnated with Spurr's® low-viscosity resin.

Solutions. Acetate buffer (10^{-4} M) was used in all experiments to maintain a pH close to the natural groundwater value of 4.8. Mercuric chloride was added to the buffer at 10 mg/L concentration in order to inhibit microbial activity. In addition, the distilled water used to make the buffer was 0.2 micron filtered prior to adding the acetate and HgCl_2 .

Acenaphthene, naphthalene and phenanthrene solutions were made up in buffer from the solid PAH and were magnetically mixed for at least one week prior to use. Sorbate properties (**Table 3-1**) are based on data of Miller et al. [31] and K_{oc} was calculated from Karickhoff's [26] regression for PAH sorption to soils: $\text{Log } K_{oc} = 0.989 \text{ Log } K_{ow} - 0.346$.

Table 3-1
Sorbate Properties

compound	MW [g/mole]	Log K_{ow}	Log K_{oc}	Molar Volume [cm ³ /mole]
naphthalene	128.2	3.35	2.97	148
acenaphthene	154.2	3.92	3.53	173
phenanthrene	178.2	4.57	4.17	199

Sorption Experiments. Batch and column sorption experiments were conducted with the 250-1000 micron Pine Barrens sand size fraction. This sand is predominantly quartz with goethite and kaolinite coatings on the surfaces of the quartz grains [43]. Batch isotherm experiments were conducted independently for naphthalene and phenanthrene using fluorescence analysis of the aqueous phase, and sorbed phase concentrations were calculated by difference. Positive controls (without sediment) were analyzed at each concentration to check for losses to vial walls and a single negative control (no PAH) was analyzed for each compound. Both tests were carried out for 4 days in 4.5 mL Wheaton vials at solid-to-water ratios (r_{sw}) calculated to give 50% sorbate uptake at equilibrium, based on K_d estimates using the organic partitioning model, $K_d = K_{oc}f_{oc}$. The resulting r_{sw} for naphthalene was 0.62 g/mL and for phenanthrene was 0.14 g/mL. Naphthalene was measured at excitation/emission wavelengths of 275/335 and phenanthrene at 250/365 nm using a Perkin-Elmer LS-5 Spectrofluorimeter. A time course was not carried out for naphthalene since the acenaphthene batch kinetics test [22] showed equilibrium was reached within tens of minutes, probably because the sorbent was rapidly disaggregated in the batch tubes. We did conduct a batch kinetics test with the larger PAH, phenanthrene, with sorbate-sorbent contact times ranging from 1 to 482 hours. Previous results [22] for acenaphthene batch kinetics and isotherm were obtained using the same methods and are reported again here for comparison.

Methanol extractions (24 hr) of the sediment phase from the phenanthrene kinetics test gave sample recoveries of 82 and 83% with positive controls showing 98% recovery. Mass balance calculations for two sets of naphthalene batch vials had recoveries of 96 and 74% with positive control recoveries of 82 and 95%.

Column experiments with naphthalene and phenanthrene were similar to those reported for acenaphthene [22], with the exception of using a Waters model 470 fluorescence detector to monitor phenanthrene elution from the column using excitation and emission wavelengths of 250 and 356, respectively, and setting the absorbance detector (Waters model 484) wavelength to 275 nm for naphthalene elutions. Briefly, the column (7 cm long and 22 mm i.d.) was mirror-finished stainless steel tubing (Alltech, Associates; Deerfield, IL) fitted with low-dead-volume high-pressure liquid chromatography (HPLC) end caps. The sand was contained in the column between two 2-micron stainless steel frits and the column solid-to-water ratio and porosity were 3.7 g/mL and 0.42, respectively. A stainless steel buffer reservoir was sampled using a Waters model 501 HPLC pump which pumped buffer to an injection valve located below the column. The injection port enabled 500 microliter pulse injections of the PAH of interest to be fed into the column inlet. Flow to the column was upwards and all tubing (1/16", 0.020" i.d.) in the column setup was

stainless steel in order to minimize PAH sorptive losses. The detector was located as close to the column outlet as possible (approximately 2.5 cm and 5 μL) in order to minimize apparatus dispersion. After passing through the detector cell, the column effluent was collected in tared flasks to monitor flow rate gravimetrically.

Column experiments were carried out over a range of pore velocities (0.5 to 115 cm/hr) in order to evaluate the rate of sorption from the first two moments of the pulse-input elution curves. To facilitate data processing, the output of the detectors was sent to a data acquisition system (12 bit, A/D converter ADALAB-PC board, Interactive Microware, Inc., State College, PA and LABTECH NOTEBOOK software, Wilmington, MA). The moments of the elution pulses were calculated using a Fortran program employing the trapezoidal rule for integrations (see Appendix).

Mass balances were carried out on a few column experiments by analyzing the effluent concentration via fluorescence. Recoveries were consistently between 88 and 110 percent for all three PAH compounds.

Data Analysis. The method of moments was used to analyze our sand column elution curves. The model equations were originally based on a diffusion model developed for gas-solid chromatography which examines intraparticle diffusion in porous packings with impermeable core regions [45]. This model is appropriate for the Pine Barrens sorbent since the primary quartz grains are rimmed by a porous, high f_{oc} , iron-oxide and kaolinite coating. For our column, we assumed spherical particles and the following governing equations (after [45]):

$$\frac{\partial C}{\partial t} = -v \frac{\partial C}{\partial x} + E \frac{\partial^2 C}{\partial x^2} - \frac{3}{R_p} \frac{\gamma}{\beta} D \frac{\partial C'}{\partial t} \quad (3-1)$$

$$\frac{\partial C'}{\partial t} = \frac{D}{\beta} \left[\frac{\partial^2 C'}{\partial r^2} + \frac{2}{r} \frac{\partial C'}{\partial r} \right] - \frac{\rho_p}{\beta} \frac{\partial S'}{\partial t} \quad (3-2)$$

where C = aqueous concentration in column pore space (mol/mL), C' = aqueous concentration in pores of coating (mol/mL), S' = sorbed concentration inside porous coating (mol/g), v = pore water velocity (cm/sec), E = dispersion coefficient (cm^2/sec), D = diffusion coefficient in the porous coating (cm^2/sec), ρ_p = particle bulk density (g/mL), R_p = particle radius including porous coating (cm), γ = ratio of intraparticle pore volume to column void volume, and β = porosity of coating. Using reasonable boundary conditions, Schneider [45] solved the above equations in the Laplace domain and reported the time-moment formulas for the first absolute moment (μ'_1) and second central moment (μ_2). By analogy with the moment expressions of Valocchi [50] used previously (Chapter 2), the diffusion model parameter $1+\gamma^*(1+K)$ found in Schneider's first moment expression can be

regarded as a column retardation factor, R_f , and Schneider's moment expressions reduce to:

$$\mu_1' = \frac{L}{v} R_f + \frac{t_0}{2} \quad (3-3)$$

$$\mu_2' = \frac{2L\alpha R_f^2}{v^2} + \frac{2L\Delta^2\beta[R_f - 1]^2}{v D \gamma^* \vartheta^*} + \frac{t_0^2}{12} \quad (3-4)$$

where L is the column length in cm, t_0 is the pulse duration in seconds, α is the dispersivity in cm (we assumed $E = \alpha v$), γ^* is γ modified for the thickness of the coating layer:

$$\gamma^* = (1 - n)\beta^* / n \quad \beta^* = \beta(1 - \chi) \quad \chi = R_p^* / R_p \quad (3-5)$$

n is the column porosity, R_p^* is the radius of the impermeable particle core (i.e., quartz grain), Δ is the coating thickness ($= R_p - R_p^*$) and ϑ^* is a numerical coefficient dependent on χ and particle geometry. For spherical particles the following definition applies [45]:

$$\vartheta^* = \frac{15(1-\chi)^2}{1-\chi^3(4+4\chi-5\chi^2)/(1+\chi+\chi^2)} \quad (3-6)$$

By equating the second central moment expressions for the single-site first order model used previously (equation 2-5') [22] and the diffusion model (equation 3-4), an equivalent first-order model sorption rate constant is defined as:

$$k_r = \frac{D \gamma^* \vartheta^*}{\Delta^2 \beta (R_f - 1)} = \frac{D \vartheta^*}{\Delta^2 \beta (1 + K)} \quad (3-7)$$

where K is the dimensionless partition coefficient ($= \frac{\rho_p S'}{\beta C'}$) and $1+K$ for our sorbent describes the intra-coating retardation factor, R_{coat} .

The diffusion model has more fitting parameters than the first-order model we used previously ([22];Chapter 2) because sorbent geometry factors must be specified such as the coating thickness, particle radius and coating porosity. Our approach was to first fit the first-order model to the data in order to quantify L , R , α and k_r , and then assess whether or not a coating diffusion model based on independent estimates of the diffusion model parameters could predict the moment-derived effective diffusivity. The first-order model parameters were quantified by curve-fitting experimental moments to equations 2-4 and 2-5' (Chapter 2) as functions of inverse velocity. One standard deviation errors for each model parameter were calculated using propagation-of-error techniques based on the standard errors (S.E.) obtained from the curve-fits.

The breakthrough curves (BTCs) for each individual compound were truncated at the same number of pore volumes to minimize artifacts due to detector noise and drift. Truncation bias was quantified using simulated breakthrough curves generated with the computer program CXTFIT [36] operated as a single-site model for a range of pore

velocities (0.5 to 20 cm/hr). For various values of the model parameter, k_r , the moments of these simulated BTCs were calculated for both the full data files (i.e., sufficient pore volumes such that $C/C_0 = 0$; to 7 decimal place accuracy) and for data files truncated at a given pore volume. The model parameter k_r was adjusted until the truncated simulation output approached the experimental k_r value. When the simulation output k_r value for the truncated data set matched the experimental value (within a factor of 2) for a given compound, the iteration procedure was halted. In this way we were able to estimate the true reverse sorption rate (i.e., assuming accurate quantitation of the BTC tails) from our truncated data sets. Iteration was performed using k_r because it is more sensitive to truncation than the retardation factor.

Results and Discussion

Batch Experiments

Isotherms (**Figure 3-1**) for naphthalene, acenaphthene and phenanthrene were linear with Freundlich model ($S = K_f C^n$) exponents that were not significantly different from 1.0 (**Table 3-2**). The K_d values determined for naphthalene and acenaphthene were respectively 3 and 2 times higher than the partition coefficient one would predict using the organic matter partitioning model ($K_d = K_{oc} f_{oc}$), but the measured K_d for phenanthrene showed excellent agreement with the model. The previously-reported batch kinetics test with acenaphthene indicated a K_d of 2.51 (0.63, 1σ), in good agreement with the isotherm value. The phenanthrene kinetics experiment mean apparent K_d (5.54; 1.76 1σ) also agreed with the isotherm K_d . The organic partitioning model gave acceptable estimates of K_d (within a factor of 4) for all three compounds and thus can be used to predict K_d for sorption of other compounds to the Pine Barrens sand. However, there is no obvious reason why the most hydrophobic compound, phenanthrene, showed the best agreement with the $K_{oc} f_{oc}$ model. Possible explanations for these data are explored below.

The discrepancy between measured K_d and the partitioning model for naphthalene and acenaphthene could be due to (1) volatile or biodegradation losses of these compounds which were attributed to sorption in the difference calculation of sorbed mass, (2) calculated K_{oc} s which are incorrect for these sorbates due to the nature of the Pine Barrens organic matter, (3) differences in batch mixing dynamics among the three compounds due to experimental conditions, (4) significant mineral surface sorption in this sand, or (5) any combination of these hypotheses. We do not believe losses of the smaller PAHs explains the data because mass balances performed using methanol extraction of the sand after a 30-

Figure 3-1. Batch sorption isotherms for naphthalene, acenaphthene and phenanthrene. Sorbed concentrations were calculated by difference and all concentrations are expressed in fluorescence units (F.U.). The range of aqueous concentrations encompasses the concentrations used in all batch and column experiments. Lines are best-fit linear and Freundlich isotherm models.

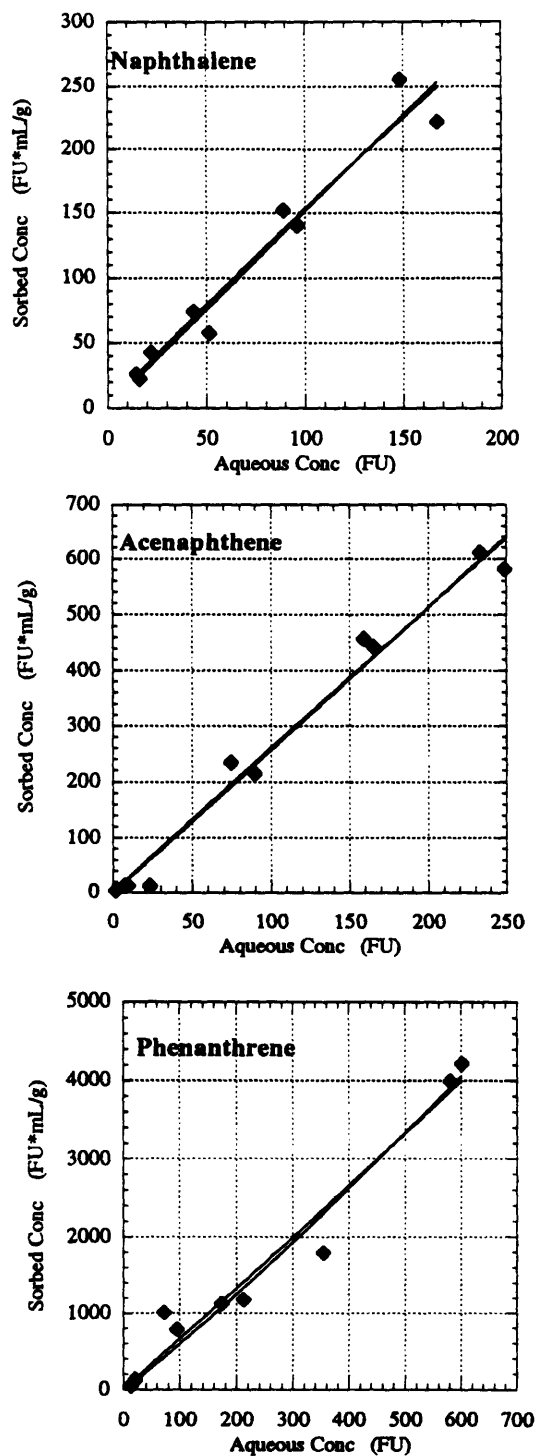


Table 3-2
Batch Isotherm Model Fits

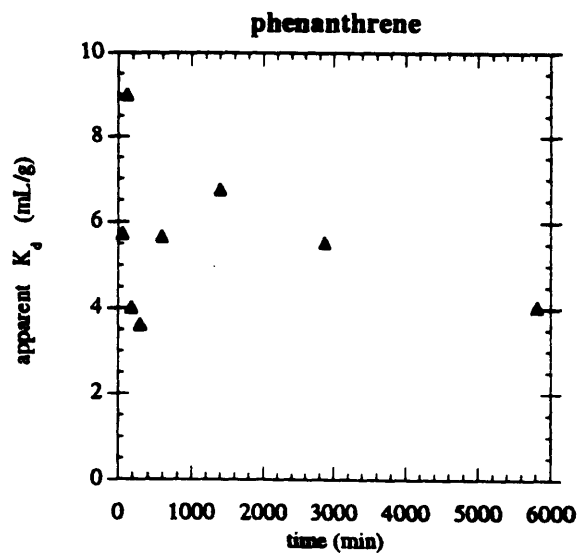
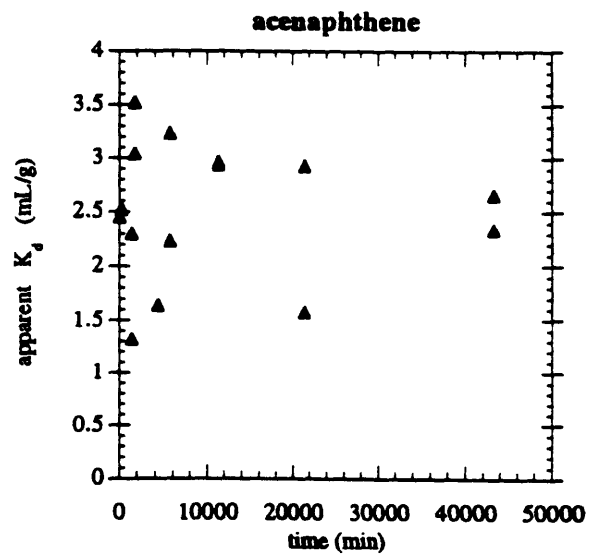
compound	<i>Linear</i>	<i>Freundlich</i>		<i>Partitioning Model</i>
	K_d	K_f	n	$K_{oc}f_{oc}$
naphthalene	1.5 (0.07)	1.95 (1.06)	0.95 (0.11)	0.45
acenaphthene	2.6 (0.08)	2.94 (1.46)	0.97 (0.09)	1.63
phenanthrene	6.65 (0.29)	4.31 (3.10)	1.07 (0.12)	7.1

Errors in parentheses are standard errors.

day acenaphthene batch kinetics test indicated 109% recovery in two sample vials (Chapter 2), thus indicating no significant volatile or biodegradation losses of acenaphthene. Mass balances on naphthalene batch vials similarly showed recoveries of 96 and 74% on samples and 82 and 95 % on positive controls. These potential losses of about 15% are too small to explain the measured discrepancy between K_d and $K_{oc}f_{oc}$.

Another possibility is that the K_{oc} values we calculated from K_{ow} are too low, possibly because the Pine Barrens organic matter is a better sorbent for PAHs than the soil organic matter upon which Karickhoff's [26] regression is based. If K_{oc} values are adjusted (increase K_{oc} by a factor of 2.4) to account for the naphthalene batch K_d , the acenaphthene and phenanthrene measured K_d s will be lower than $K_{oc}f_{oc}$ by factors of 2 and 4, respectively. This result implies that either (a) the larger PAH had insufficient time to reach equilibrium in the isotherm experiments, a requirement that is not borne out by batch kinetics data for these two compounds (**Figure 3-2**), or (b) the sediment organic matter was located in regions inaccessible to acenaphthene and phenanthrene in the batch tests. It is possible that the distribution of organic matter varied among the three batch tests due to the fact that different amounts of sediment were used with each compound in order to achieve 50% uptake at equilibrium. Varying the mass of sediment may have resulted in different degrees of coating dispersal within the batch tubes. Naphthalene tests employed 2.2 grams of sand, and acenaphthene and phenanthrene tests used 2 and 0.6 grams, respectively. It is difficult to imagine differences in sorbent disaggregation between the naphthalene and acenaphthene experimental conditions, but the phenanthrene experimental conditions were significantly different from the other two compounds. The phenanthrene

Figure 3-2. Batch kinetics experiments for acenaphthene and phenanthrene. Apparent K_d was calculated using equation 2-6 (Chapter 2) based on by-difference quantification of sorbed concentrations.



solid-to-water ratio was about 0.15 g/mL while that for the two smaller PAHs was about 0.6 g/mL. It is conceivable that the sorbent in the phenanthrene tests was not disaggregated as much as the sorbent used with the other compounds (although this is difficult to quantify) and this could explain the larger discrepancy (4 times) for phenanthrene from the adjusted organic partitioning model K_d value relative to the other compounds.

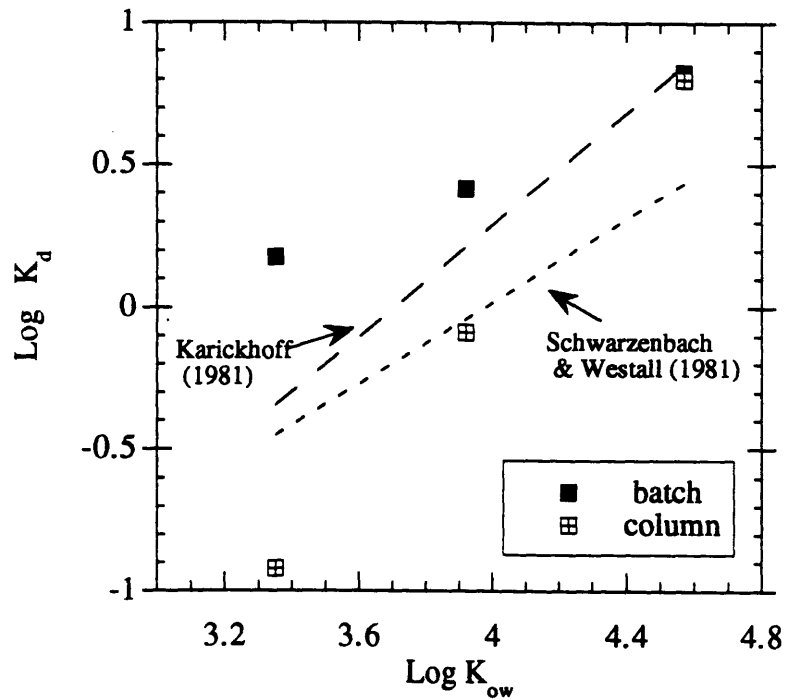
Alternatively, the observed agreement between batch K_d and the unadjusted $K_{oc}f_{oc}$ values for phenanthrene may reflect the reduced availability of mineral surfaces in the phenanthrene vials relative to naphthalene and acenaphthene vials due to less sorbent breakup at lower r_{sw} . Invoking mineral sorption to explain the batch vs. $K_{oc}f_{oc}$ data is not supported by the fact that the most hydrophobic compound, phenanthrene, which one would expect to sorb more strongly to mineral surfaces, showed excellent agreement with the partitioning model. However, if there were significant differences in the proportions of mineral surfaces available due to experimental conditions such as r_{sw} , we might expect to see differences in the dominant sorption mechanism for the different compounds. At present we have no way to quantify the relative amounts of mineral surface that were exposed at the different solid-to-water ratios in the batch tests.

Sorption to mineral surfaces could also explain the batch data if the K_{oc} calculated from Karickhoff's [26] $\log K_{oc}$ - $\log K_{ow}$ regression is too high for this low f_{oc} sorbent due to differences in organic matter composition between soils and aquifer sand (i.e., [16, 17]). For example, use of Schwarzenbach and Westall's [47] $\log K_{oc}$ - $\log K_{ow}$ regression based on aquifer materials and chlorobenzenes results in measured batch K_d s that are 3-4 times higher than $K_{oc}f_{oc}$ for all three PAH compounds (**Figure 3-3**). The Schwarzenbach and Westall [47] regression results in a discrepancy between batch K_d and calculated $K_{oc}f_{oc}$ that can be attributed to mineral sorption of the PAHs assuming the overall K_d is a linear combination of individual sorbing component contributions [30]:

$$K_d = K_{oc}f_{oc} + K_{min}f_{min} \quad (3-8)$$

If the mineral sorption coefficient, K_{min} [mL/g_{min}], as defined by Schwarzenbach and Westall's [47] regression for sorption to kaolin, $\log K_{min} = 0.43 \log K_{ow} - 1.37$, represents sorption to both the kaolinite and goethite of the dispersed coatings, and this K_{min} value is converted to area-based units [mL/m²_{min}] using the reported kaolin surface area of 12 m²/g, then the fraction of mineral surfaces, f_{min} [m²_{min}/g_{sed}], required to match the observed K_d values can be calculated using equation (3-8). The f_{min} values are 11.4, 9.3 and 11.4 m²/g_{sed} for naphthalene, acenaphthene and phenanthrene, respectively, with an average value of 10.7 m²/g_{sed}. This f_{min} value is the specific surface area required for mineral sorption to explain the discrepancy between $K_{oc}f_{oc}$ and measured K_d assuming Schwarzenbach and Westall's [47] K_{oc} - K_{ow} regression and their kaolin K_{min} regression

Figure 3-3. Comparison of batch and column K_d results with K_d s derived using two different $\log K_{oc}$ - $\log K_{ow}$ regression from the literature. The regression of Karickhoff [26] was developed using seventeen high f_{oc} soils (0.11 to 2.38 %) and five aromatic hydrocarbons (benzene to pyrene). Schwarzenbach and Westall's [47] regression is based on sorption of a series of chlorobenzenes to aquifer, lake and river sediments with f_{oc} ranging from 0.04 to 5.8%.



applies to the Pine Barrens sand. We can compare this f_{\min} value with the total surface area (TSA) determined for the Pine Barrens sand using mercury porosimetry ($1.94 \text{ m}^2/\text{g}_{\text{sed}}$). This measured value is about 6 times lower than necessary to account for the K_d - $K_{oc}f_{oc}$ discrepancy. However, the measured surface area was obtained for air-dried material such that the coatings remained intact on the quartz grains. The measured TSA for dried material may not be representative of the batch test surface area where coatings were dispersed. In addition, sorption to goethite may be more important in our sand than sorption to kaolinite. If K_{\min} for goethite is significantly higher than that for kaolin, the corresponding f_{\min} would be lower. At present we have no data to quantify the importance of sorption to goethite mineral surfaces in our sand.

The interpretation of the batch K_d data for the three PAH compounds is complex. The simplest explanation is that of differences in exposure of kaolinite and goethite mineral surfaces in the batch vials due to varying r_{sw} . This explanation implies that the two smaller PAH were sorbed significantly by mineral surfaces as well as organic matter, but phenanthrene test conditions did not make a similar amount of mineral surface area available to this compound thus resulting in a K_d value equal to $K_{oc}f_{oc}$ using Karickhoff's regression for PAH. More complicated explanations require invoking more than two factors to explain the data. Since K_d calculated using organic partitioning models can vary up to an order of magnitude due to differences in organic matter composition [17], it is not worthwhile to further belabor the discrepancy between batch and organic partitioning model K_d values. The discussion above highlights the importance of choosing the appropriate log K_{oc} -log K_{ow} regression equation for the sorbate and sorbent pair of interest when using the organic partitioning model and emphasizes that mineral sorption may be significant in batch tests with low organic carbon content aquifer materials. It is also important to reiterate that use of either regression with the $K_{oc}f_{oc}$ model gave acceptable estimates (within a factor of 4) of the sorption partition coefficient to the Pine Barrens sand for all three PAH compounds. Therefore, use of the organic partitioning model with this low f_{oc} sand would provide a reasonable estimate of the batch K_d value without having to quantify the mineral contribution to sorption, a task that is not currently straightforward.

Column Experiments.

Qualitative Evidence for Slow Sorption Kinetics. For pulse input experiments, the pore volume at which the maximum concentration elutes, PV_{cmax} , should be invariant with velocity for experimental conditions with Peclet Numbers ($Pe = \frac{vL}{E}$) greater than about 40 [27]. Therefore, when this criterion is met, we can qualitatively attribute peak shifts with

pore velocity to another process such as slow sorption kinetics or slow mass transfer to stagnant water zones (physical nonequilibrium). Since the conservative tracer, nitrate, did not show BTC asymmetry or significant peak shifts with pore velocity (**Figure 2-5a**), we presume that physical nonequilibrium did not affect the BTCs for the sorbing compounds (see Chapter 2). Furthermore, the nitrate peak shape did not vary with pore velocity, indicating that P_e did not vary significantly over the range of velocities studied. To check that P_e was high, CXTFIT was used to model a few nitrate BTCs assuming $R=1.0$ and using the local equilibrium model. The best-fit P_e values were between 40 and 60, confirming that advection governed solute transport in the column.

Elution curves for phenanthrene shifted left (to shorter retention times) with increasing flow rate, but those for naphthalene did not show significant shift (**Figure 3-4**). The BTCs for both compounds showed tailing similar to that previously observed for acenaphthene transport in this sand (**Figure 2-5b**). For the three PAH compounds we studied, the pore volume at which the peak maximum eluted varied with velocity for acenaphthene and phenanthrene, but the naphthalene data did not show a similar trend (**Figure 3-5**). As discussed further below, the constant PV_{cmax} for naphthalene and lack of BTC shift may reflect the difficulty of discerning small deviations from one pore volume due to scatter in the data for a compound with a retardation factor close to 1. For acenaphthene and phenanthrene, with retardation factors of 4 and 24, respectively, we observed PV_{cmax} changes of 1.7 pore volumes for acenaphthene and 8.2 pore volumes for phenanthrene, while naphthalene and nitrate PV_{cmax} values varied by only 0.6 and 0.4 pore volumes, respectively, over the range of pore velocities studied.

The BTCs for all three PAH compounds were asymmetrical, while the nitrate trace peaks were symmetrical (see Figure 2-5; Chapter 2). Furthermore, the order of solute elution correlated with increasing hydrophobicity for a given flow rate (**Figure 3-6**). The tailing on the PAH BTCs is due to both dispersion and sorption kinetics. We used the moments of the nitrate elution curves to quantify the effective column length (6.2 cm) and dispersivity (0.05 cm) in the Pine Barrens column [22] (see Chapter 2) and the remaining contribution to the second central moment was attributed to sorption kinetics.

Figure 3-4. Elution curves for naphthalene and phenanthrene at different flow rates. Pore volumes were calculated using the column porosity of 0.42, a column length of 6.18 cm and column cross-sectional area of 3.8 cm².

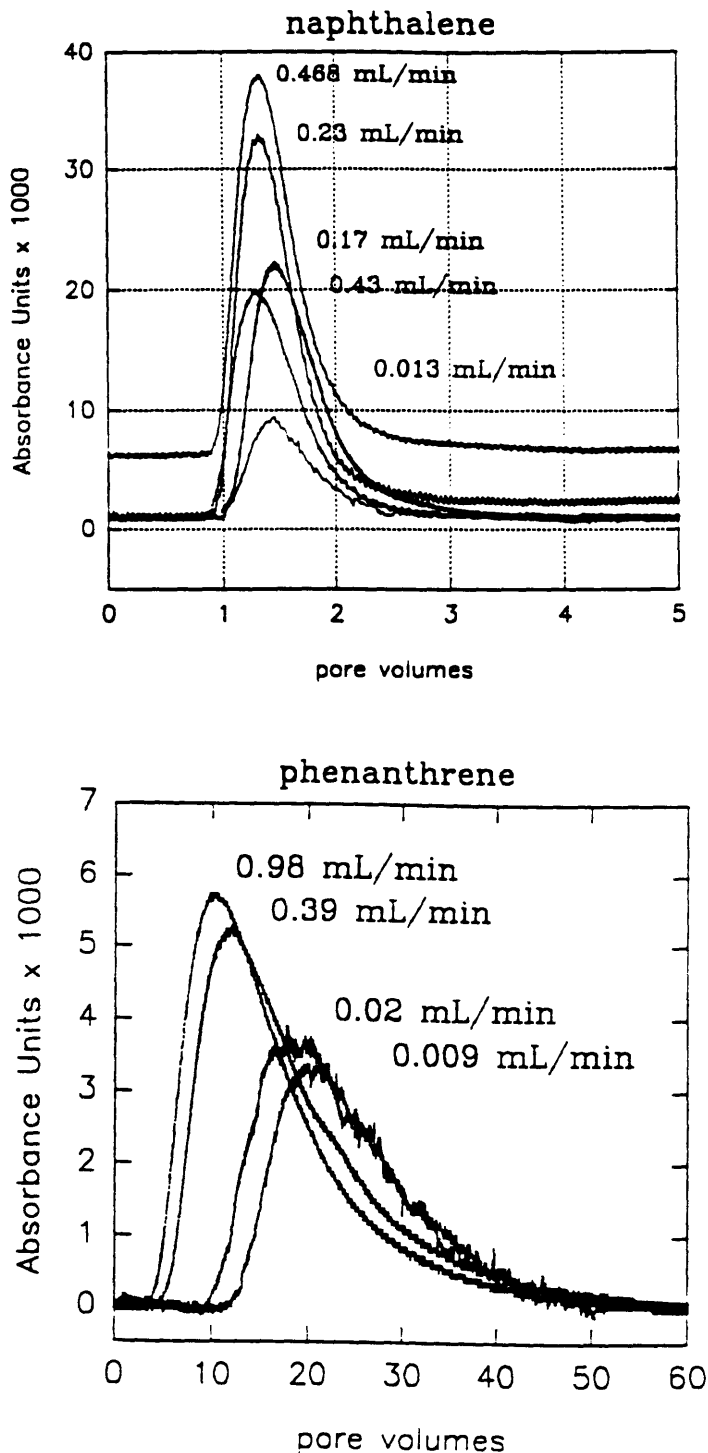


Figure 3-5. Semi-logarithmic plot of pore volume to peak maximum (PV_{cmax}) vs. inverse velocity for four solutes as a function of flow rate for the column experiments with Pine Barrens sand.

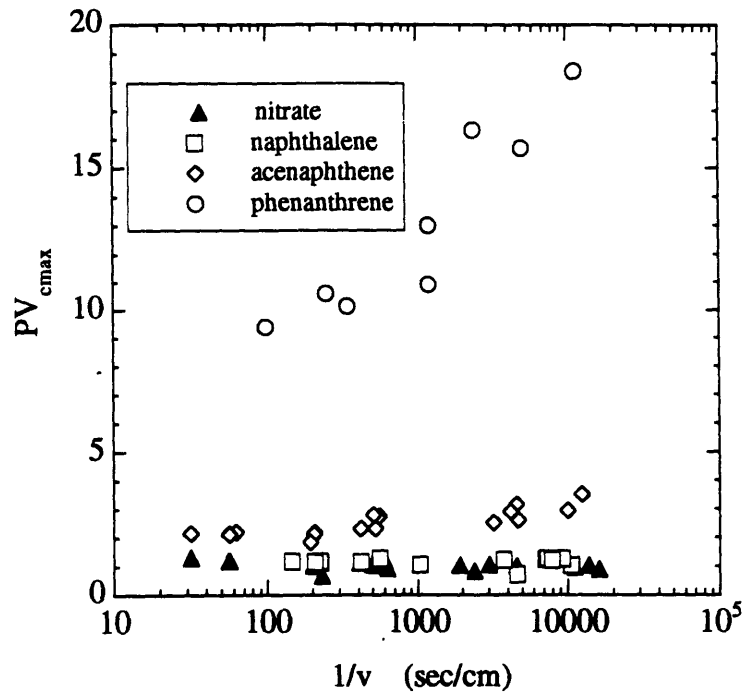
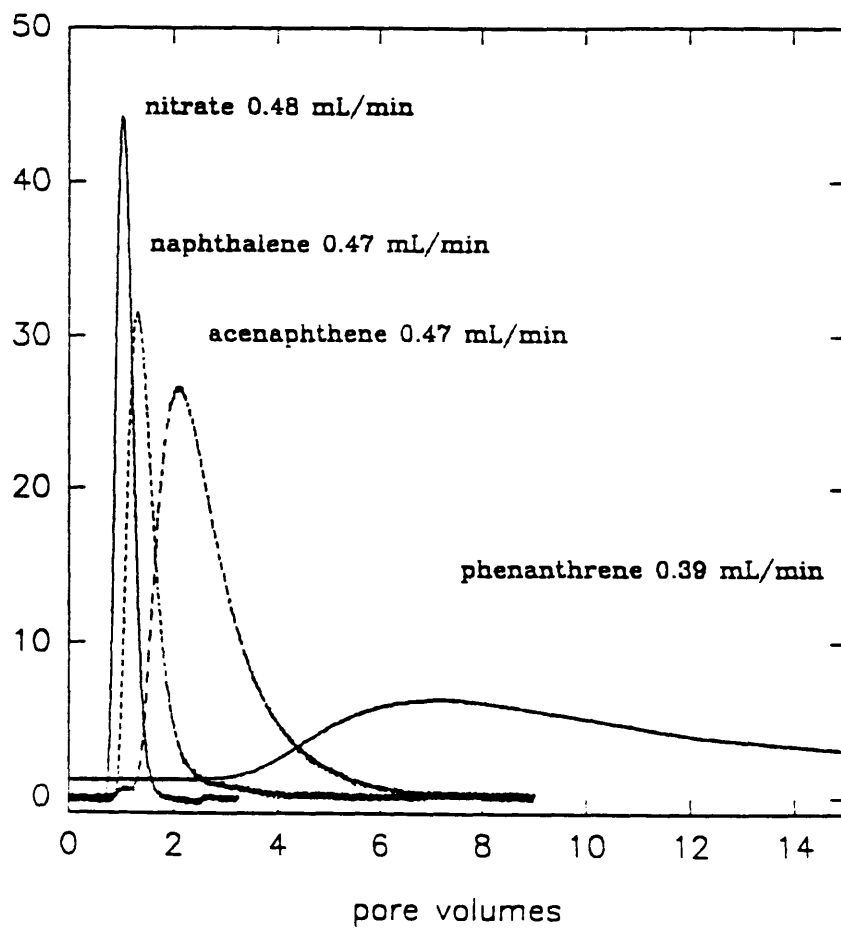


Figure 3-6. Elution curves for the four solutes studied at a flow rate of approximately 0.4 mL/min ($v = 15$ to 18 cm/hr).



Retardation Factor. Fitting the first absolute and second central moment expressions to the data as a function of inverse velocity allows determination of the retardation factor and desorption rate constant for each of the PAH compounds. The results of curve fitting and the reported one standard deviation errors for each compound (**Table 3-3**) show a trend of increasing retardation factor and decreasing sorption rate (k_r) with increasing hydrophobicity as one would expect for diffusion-limited sorption.

Table 3-3
Column Experiment Results

compound	v range [cm/hr]	R_{col}	$\alpha^{(1)}$ [cm]	$k_r^{(2)}$ [hr ⁻¹]
nitrate	0.4 - 25	assumed 1.0	0.05 ± 0.01	undefined
naphthalene	0.3 - 25	1.46 ± 0.05	0.02 ± 0.08	1.3 ± 0.3
acenaphthene	0.3 - 110	4.04 ± 0.14	0.06 ± 0.06	0.4 ± 0.2
phenanthrene	0.3 - 37	24.5 ± 0.5	0.2 ± 0.04	0.06 ± 0.03

(1) dispersivity for independent fit to second central moment. (2) the reported k_r values were based on curve fits with the dispersivity set equal to the value determined for the conservative tracer, nitrate, 0.05 cm. The reported R and k_r values were not corrected for truncation.

The first absolute moments as a function of inverse velocity (**Figure 3-7**) give retardation factors of 1.46, 4.04 and 24.5 for naphthalene, acenaphthene and phenanthrene, respectively. Column K_d values calculated from these retardation factors using the column r_{sw} value of 3.7 (**Table 3-4**) show considerable discrepancy between the batch and column partitioning for the two lower molecular weight PAH, naphthalene and acenaphthene, but the column and batch results agree for phenanthrene. The higher K_d values in the batch for naphthalene and acenaphthene relative to the column (factors of 12 and 3, respectively) could solely reflect differences in mixing dynamics and solid-to-water ratio that resulted in different degrees of sorbent disaggregation between the batch and column conditions, as discussed previously [22]. However, the equivalence of the phenanthrene sorption capacity under both test conditions indicates that another factor must be affecting the extent of agreement between batch and column K_d . Possible explanations for the phenanthrene data are discussed separately from the smaller PAHs below.

Figure 3-7. First absolute moments versus $1/v$ for four solutes. The slope of each line is used to calculate the retardation factor for each compound using equation 2-4 (Chapter 2).

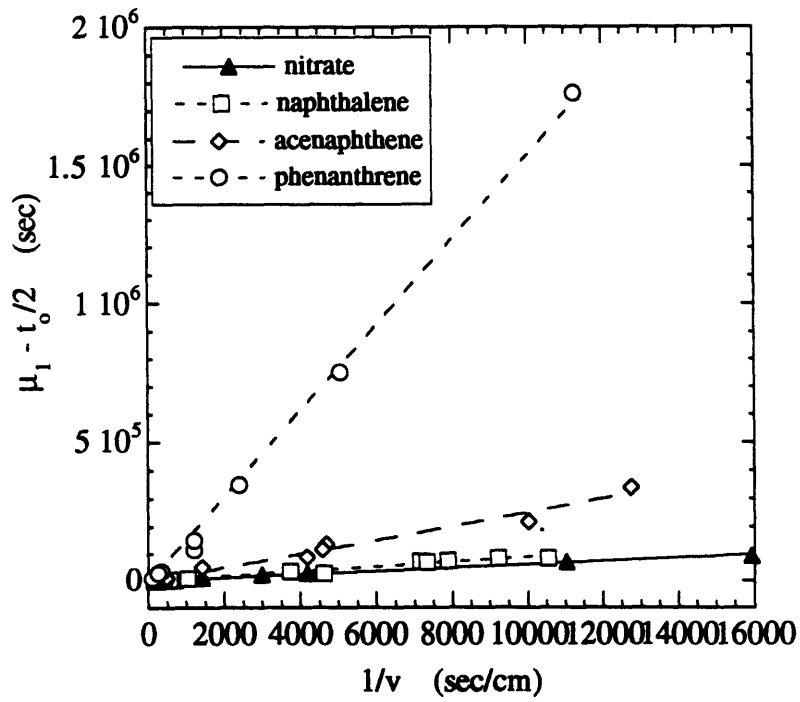


Table 3-4
 K_d and Column Truncation Data

	Batch K_d	Column K_d	PV_{trunc}	PV_{trunc}/R
naphthalene	1.5	0.12	5	3.4
acenaphthene	2.6	0.82	7.5	1.9
phenanthrene	6.7	6.4	58	2.4

Four possible explanations for the batch/column K_d data for naphthalene and acenaphthene are (1) significant volatile or microbial degradation losses of these smaller PAH compounds in the batch test which were incorrectly attributed to sorption; (2) higher batch partition coefficients resulted from significant sorption to mineral surfaces which were not available in the more quiescent column (and these mineral sites are not accessible to phenanthrene in either the column or the batch tests); (3) contact times in the column were too short to achieve equilibrium sorption capacity, and (4) BTC truncation resulted in column K_d s that were too low.

As discussed above, we can rule out losses in the batch tests based on mass balance data and, as discussed in more detail below, truncation of BTCs has only a minor effect (within 20%) on the column retardation factor. The fact that acenaphthene batch and column data agreed more closely than the naphthalene data seems to rule out hypothesis (3) because the rate of naphthalene sorption in the column is faster than that for acenaphthene (see below) and both compounds were tested over similar ranges of column contact times. One remaining possibility is that mineral sorption in the batch tests caused a significant increase in batch K_d and further that these mineral sites were not available in the column test. The fact that naphthalene showed a significantly larger batch K_d /column K_d ratio than acenaphthene is consistent with mineral sorption sites being more available to smaller molecules and suggests that the additional sorption sites available to naphthalene in the batch still remained somewhat inaccessible to acenaphthene. Following this same trend, the phenanthrene batch data show even further inaccessibility from these sorption sites. Alternatively, the trend in batch/column K_d ratios among the three compound may reflect different degrees of sorbent degradation due to tumbling. In other words, either all three compounds were exposed to sorbent that had the same amount of mineral sites but the

PAHs had different abilities to reach those sites, or the three PAHs were exposed to sorbent of varying degrees of disaggregation (and number of sorption sites) due to r_{sw} variation among the batch tests. These scenarios lead us to additional hypotheses for the agreement between batch and column K_d for phenanthrene: (5) slow sorption in the batch for phenanthrene such that the batch K_d is an apparent, not an equilibrium, value; (6) no differences in availability of sorption sites from batch to column (but the smaller PAH had different site availability in each test); (7) evolution of the column sediment with time exposed more organic matter sorption sites to phenanthrene in the column such that there was no difference in organic matter exposure for this compound between the two experimental techniques; and (8) different batch fractional uptakes of the three PAHs due to experimental design.

We can rule out rate-limited phenanthrene uptake in the batch (hypothesis 5) based on the batch kinetics experiment with this solute that showed equilibrium was reached rapidly (within 1 hour) (see **Figure 3-2**). Furthermore, the phenanthrene batch tests showed no differences in $r_{sw}K_d$ from the naphthalene and acenaphthene tests, thus ruling out differences in the degree of approach to equilibrium by the different compounds (hypothesis 8).

Hypothesis (6) is consistent with the explanation made previously to address the batch vs. $K_{oc}f_{oc}$ discrepancies for the two smaller PAH: if phenanthrene batch conditions maintained the integrity of the coatings on the quartz grains, but naphthalene and acenaphthene batch conditions (due to higher r_{sw}) resulted in disaggregation of the coatings, we would expect both batch/column agreement of phenanthrene K_d and lower column K_d s for naphthalene and acenaphthene (relative to batch) provided the coatings are intact in the column (see below). On the other hand, due to the larger size of the phenanthrene molecule, mineral sorption sites may not be available to this compound in either the column or the batch tests. To address the accessibility issue further, we estimated the sizes of the three PAH molecules assuming spherical molecular geometry and the following equation for average solute radius [39]:

$$r_s = \left(\frac{3\bar{V}}{4\pi N_a} \right)^{1/3} \quad (3-9)$$

Using the molar volume (\bar{V}) data (**Table 3-1**) and Avogadro's number (N_a), solute radii of 3.9, 4.1 and 4.3 Å were calculated for naphthalene, acenaphthene and phenanthrene, respectively. Since the relative sizes of these three PAH compounds are within 40% of one another, it is not likely that phenanthrene sorption will be significantly hindered relative to the smaller PAH.

An increase in organic matter exposure (hypothesis 7) in the column could result if the iron-oxide and kaolinite coatings on quartz were removed from the quartz and redeposited elsewhere in the column (i.e., at end frits or between grain contacts) over long periods of column flushing. Since the phenanthrene column experiments were conducted approx. 14 months after the column was initially flushed, and 2 months after the last acenaphthene experiment, it is conceivable that the column would evolve over such a long period of time. If such reorganization of the column fines has occurred, the retardation of both naphthalene and acenaphthene in the Pine Barrens column should increase accordingly and should now approach the predicted batch R value. We tested for column reorganization using naphthalene injections at 0.49 and 0.2 mL/min and saw no significant increase in retardation (expected change from 1.5 to 6 would easily be quantified). Therefore, column reorganization cannot explain why the column K_d agrees with the batch value only for phenanthrene.

At present, the reason for batch-column K_d agreement only for the largest compound we tested, phenanthrene, is unresolved. We do not suspect use of the fluorescence detector for phenanthrene BTCs is responsible for the observed result because some experiments with the fluorescence detector were performed with acenaphthene and showed the equivalence of moments obtained with the two detectors. The most consistent explanation for both the batch $K_d/K_{oc}f_{oc}$ and batch K_d /column K_d data for all three compounds is that batch mixing affected the degree of sorption to mineral surfaces for the three PAHs to a different extent due to differences in r_{sw} among the batch experiments. We suspect that the higher r_{sw} for naphthalene experiments resulted in increased disaggregation of the sorbent, thus exposing more mineral surface area for batch uptake. With increasing compound hydrophobicity, the experiments were conducted with smaller r_{sw} in order to obtain 50% fractional aqueous concentrations at equilibrium. The breakup of the sorbent may have been correspondingly lower when less sediment was in a tube and could have resulted in less sorption to mineral surfaces. This hypothesis could be tested by thoroughly assessing K_d variability as a function of r_{sw} for a single compound. Literature data on such a topic would not be directly applicable to this study due to sorbent-specific responses to mixing dynamics.

Sorption Rate, k_r . The second central moment fits to inverse velocity were used to calculate k_r for each compound (**Figure 3-8**). The sorption rates reported previously in **Table 3-3** have not been corrected for truncation bias. Truncation error was evaluated using CXTFIT simulations with the single-site first-order model (i.e., fix $\beta=1/R$) assuming a dispersivity value of 0.05 cm, a column length of 7 cm and pulse input of 0.05 pore

volumes duration. In addition, we assumed D was a linear function of pore velocity and carried out simulations at five velocities : 0.5, 2, 5, 10 and 20 cm/hr. The method of moments was applied to the simulated BTCs to evaluate R and k_r . We examined different ranges of input k_r values for the three PAH compounds based on the experimentally-derived k_r . For naphthalene, simulations at 1.3 and 0.6 hr^{-1} gave output k_r values of 1.5 and 0.8 hr^{-1} , respectively, showing little truncation error for this compound.

Acenaphthene truncation at 7.5 pore volumes had more of an effect on k_r with relative errors between 1.5% and 120% for k_r values from 1.2 to 0.05 hr^{-1} and the error increased with decreasing k_r value (**Figure 3-9a**). Phenanthrene BTCs were truncated at 58 pore volumes and simulations showed errors increased from 0.5 % to 61% as k_r decreased from 0.2 to 0.01 hr^{-1} (**Figure 3-9b**). Retardation factors showed less variation (up to 23%) due to truncation than observed for k_r and truncation generally decreased the R values.

From the truncation simulations, we conclude that the best-fit moment-derived reverse sorption rate constants reported in **Table 3-3** are within a factor of 2 of the "true" k_r value for each compound. We estimate that the bias due to truncation is most significant for acenaphthene, probably because of the fact that the acenaphthene BTCs were truncated at a pore volume less than 2 times R while the other two compounds had truncation 2-3 times greater than R (**Table 3-4**).

It is important to recognize that the truncation analysis conducted here differs from that of Holmén and Gschwend [22] (Chapter 2) in that the dispersivity was held constant at 0.05 cm for the moments analysis done here. Comparison of **Figure 3-9a** with **Figure 2-3b** indicates that the earlier acenaphthene moments calculations, where dispersivity was allowed to vary, resulted in more truncation error because two parameters, α and k_r , were allowed to vary. When both variables change, the best-fit k_r behavior was counterintuitive in that at very low values of input k_r the best-fit k_r suddenly increased greatly (i.e., input $k_r = 0.1 \text{ hr}^{-1}$ in **Figure 2-3b**) and the moment-derived k_r that we measured (0.4 hr^{-1}) was never approached. In contrast, holding α constant resulted in a smooth increase in error as input k_r was decreased and a truncated best-fit k_r value equal to what we measured was achieved for an input k_r of about 0.35 hr^{-1} . Note that the lower bias estimates reported here do not affect the conclusions made previously [22].

For the phenanthrene data reported in **Table 3-3** it is important to note that the k_r value derived without holding α constant ($0.18 \pm 0.09 \text{ hr}^{-1}$) is based on a dispersivity value (0.2 cm) that is four times the value measured for nitrate (0.05 cm). This large dispersivity indicates that truncation at 58 pore volumes resulted in some bias in k_r . However, as **Figure 3-9b** shows, when α is held constant at the nitrate value, the error due to truncation is insignificant. In summary, the k_r values reported in **Table 3-3** are based on

the assumption that the PAH compounds and nitrate have the same hydrodynamic dispersivities. Brusseau [5] showed that for porous media with low intraparticle porosities (such as the Pine Barrens sand), solute size does not greatly affect hydrodynamic dispersion, thus this assumption is valid. Furthermore, our data suggest that, in general, the measurement of large dispersivities for reactive solutes relative to conservative tracers may indicate a truncation-related bias that results in a sorption rate constant that is biased high by approximately the same factor that the dispersivity is high.

The sorption rate in inverse time units (k'_f) can be calculated from R and k_r (see equation 2-10) for each compound. Assuming reversible first-order sorption, the characteristic time for sorption is calculated as $(k_r + k'_f)^{-1}$. These characteristic times are 0.5 hr for naphthalene, 0.6 hr for acenaphthene and 0.7 hr for phenanthrene. Thus, over the range of velocities studied for each compound, sorption rate was significantly slower than the particle-scale advection rate; this is reflected in calculated Damkohler numbers of 9 to 3500 for all three compounds (see equation 2-12).

The slow sorption rates we measured for these three sorbates indicates that use of a kinetic sorption model is warranted for accurate estimation of subsurface transport of these PAHs. The use of an equilibrium model in transport codes will generally predict later breakthrough (i.e., pore volume at which $C/C_{\max} = 0.5$) and fewer total pore volumes for solute removal from the porous medium than a kinetic model. The magnitude of the error due to inappropriate use of an equilibrium sorption model under kinetically-limited sorption conditions is dependent on flow velocity and sorption rate. For example, using both equilibrium and kinetic CXTFIT simulations of the three solutes we studied, the equilibrium model predicted breakthrough pore volume was 3 to 25 times later than the kinetic model breakthrough at high velocities (20 cm/hr), and 2 to 10 times earlier breakthrough at low velocity (0.5 cm/hr) for these three compounds. Also, the error in the pore volume of breakthrough at a given pore velocity will be greater for more hydrophobic compounds. The degree of tailing on a BTC due to slow kinetic processes such as sorption affects the remediation time for a contaminated aquifer. CXTFIT simulations for the conditions we studied showed the equilibrium sorption model underestimated the number of pore volumes required to remove the solute by up to a factor of 10 relative to a single-site kinetic sorption model. Again, the error was greater for higher velocities and more hydrophobic compounds. Thus, at natural groundwater velocities, use of an equilibrium model could result in predicted transport errors up to an order of magnitude for a compound such as phenanthrene. If one is interested in preventing contaminant arrival at a nearby drinking water well, use of a kinetic sorption model is required to accurately predict phenanthrene arrival downgradient.

Figure 3-8. Second central moments plotted against inverse velocity for four solutes. Phenanthrene data were plotted separately because the moments were orders of magnitude higher than for the other compounds. Curve fits to these data were used to derive the dispersivity and k_r values reported in Table 3-3 based on equation 2-5'.

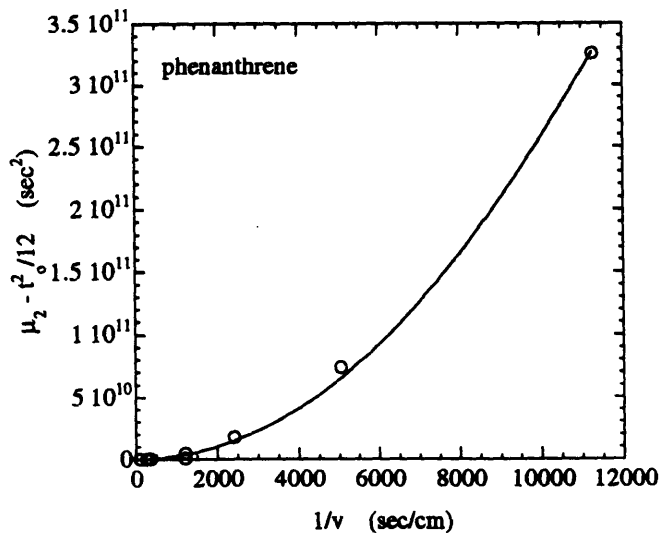
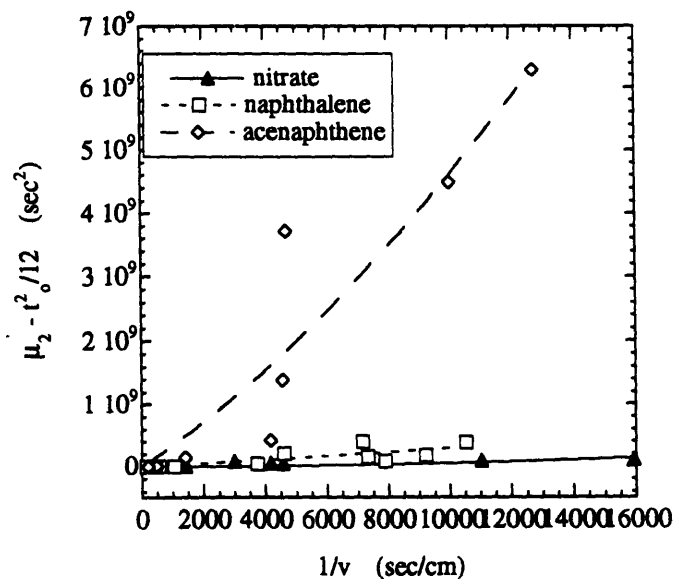


Figure 3-9a. Evaluation of variation in R and k_r due to truncation of acenaphthene BTCs at 7.5 pore volumes. The dispersivity was held constant in these CXTFIT simulations at 0.05 cm thus resulting in less truncation bias than previously estimated (Figure 2-3; Chapter 2).

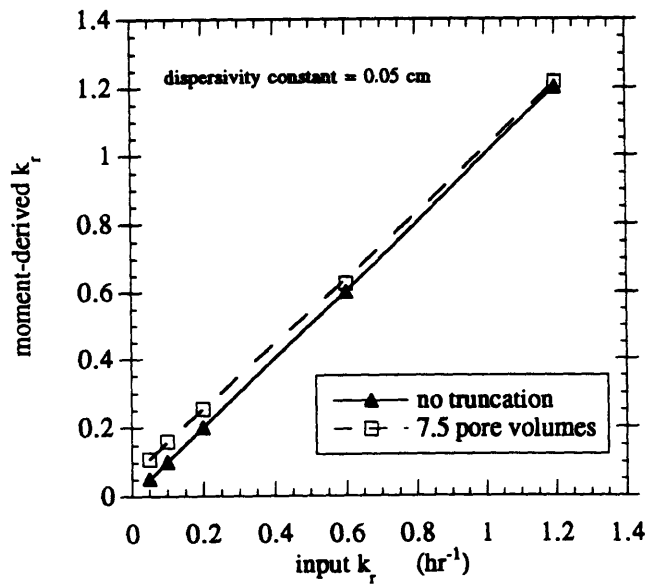
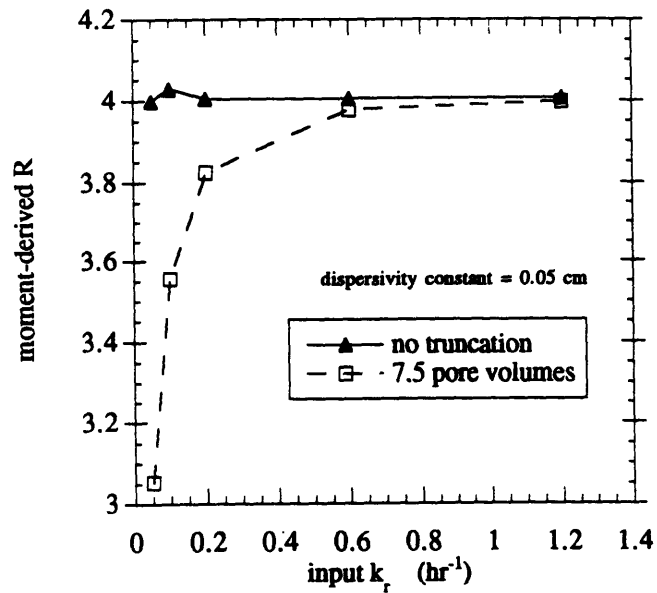
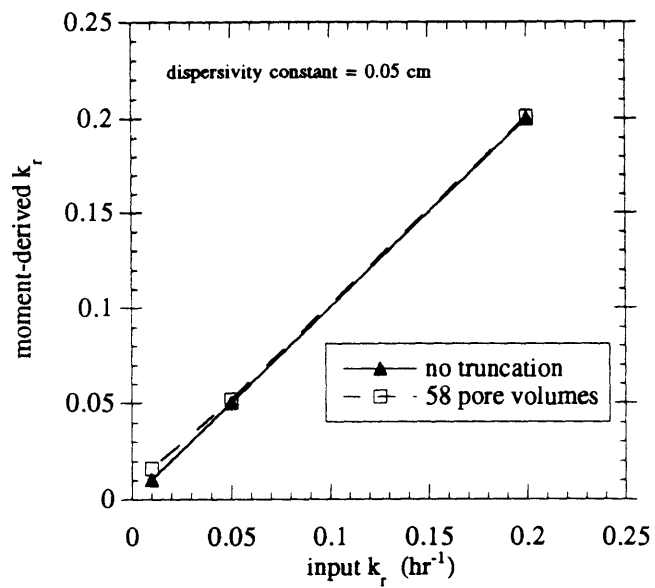
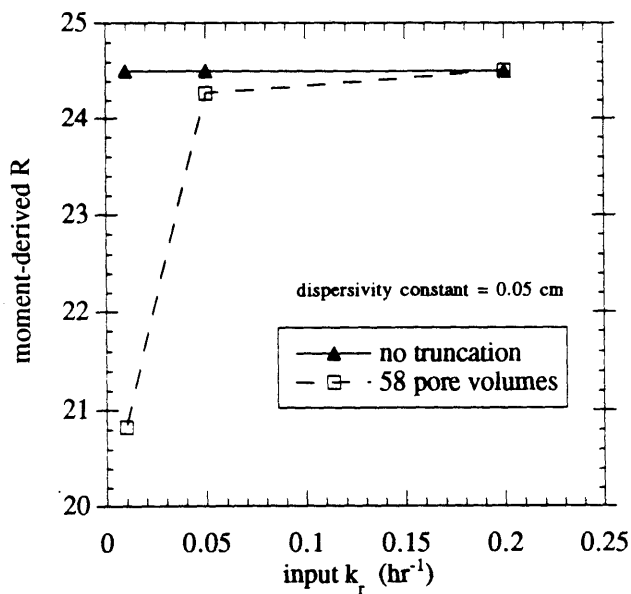


Figure 3-9b. Evaluation of variation in R and k_r due to truncation of phenanthrene BTCs at 58 pore volumes. The dispersivity was held constant in these CXTFIT simulations at 0.05 cm.



Sorption Rate Diffusion Modeling.

The first-order model we employed for our moment fits lacks physically-meaningful sorption parameters; but, as shown by many authors, the first-order model can be converted into an equivalent spherical diffusion model either by equating the second moment expressions [35] or by matching the analytical solutions for batch systems at the 50% fractional uptake point [40, 51, 53]. The diffusion model contains parameters that can be estimated independently in order to develop a predictive tool for sorption rate. Previous research has shown that particle diameter, sorbate intraparticle diffusivity, and sorbent effective tortuosity are critical parameters that must be estimated in order to predict effective diffusivities [1, 20, 41, 52]. These studies have had varying degrees of success in matching measured and predicted effective diffusivities, a fact that highlights our incomplete grasp of the sorption mechanism.

For the Pine Barrens sorbent, we propose that sorption is rate-limited by diffusion to the organic matter located within the fine-grained coatings on the quartz grains. As discussed above, Schneider [45] has defined a diffusion model for such a system of particles with a porous exterior shell (**equations 3-1 to 3-7**). Based on the properties of the Pine Barrens sand and empirical correlations, we will first develop a predictive model for the effective diffusivity of the PAH sorbates and then, using **equation 3-7**, compare the predicted effective diffusivity to that calculated from the column experiment moments. Agreement between the two effective diffusivities will indicate that the predictor includes all of the parameters necessary to describe the rate of sorption in this sand.

Coating Properties. The clay-oxide coatings on the Pine Barrens quartz grains are composed of both lath-shaped grains (presumably kaolinite) and rounded grains (iron oxide, high Fe content) with a very fine-grained (<1 micron) matrix between these grains (**Figure 3-10**). Coating thicknesses vary and were reported by Ryan and Gschwend [43] to range up to 10 microns; but coatings between adjacent grains can be up to 50 microns thick. On average, we estimate the coating thickness to be approximately 10 microns.

Mercury porosimetry analyses of the coated 250-1000 micron size fraction were compared to mercury porosimetry measurements made on the same sand fraction after it had been subjected to sonication in distilled water using an 81 watt bath for 30 minutes, followed by wet sieving through a 250 micron screen. After sonication and wet-sieving, the sand color changed from orange-brown to grey-white due to removal of the iron-oxide-

Figure 3-10 (next page). Scanning electron micrographs of coatings on quartz grains (Q) in the Pine Barrens 250-1000 micron size fraction. Scale bars are 20 microns. Note the lath-shaped grains in (a) and the fine-grained nature of the coatings (C). EDX analysis on the coatings gave Si, Al and Fe peaks which we attribute to kaolinite and goethite. There are also pieces of quartz within the coatings (larger smooth grains) and iron-rich rounded grains (Fe in (b)). These samples were prepared by impregnating the sand with low viscosity Spurr's epoxy and grinding and polishing flat specimens. The chatter marks in the quartz surfaces in (b) are due to grinding and do not represent primary porosity.

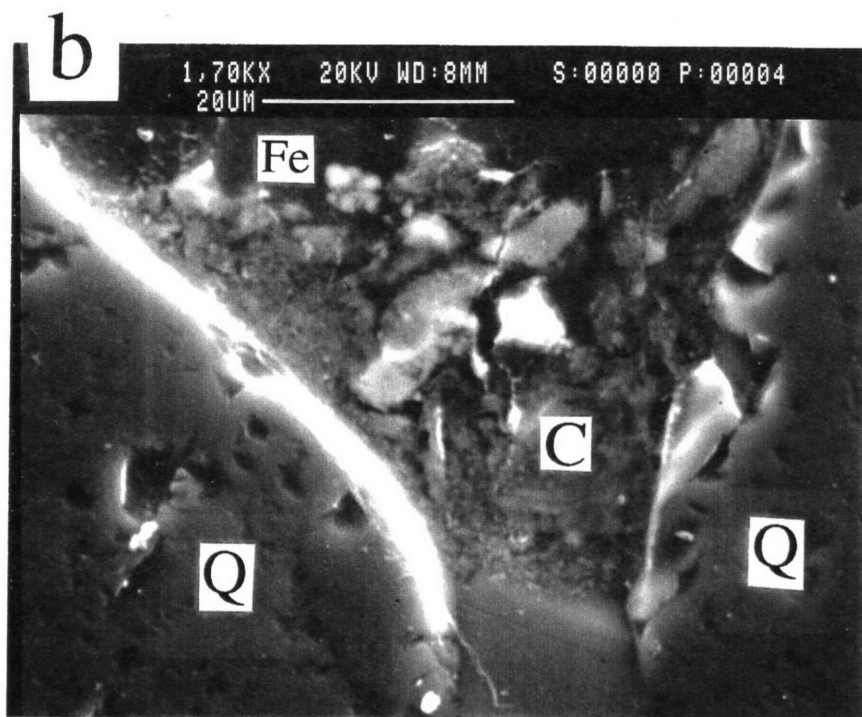
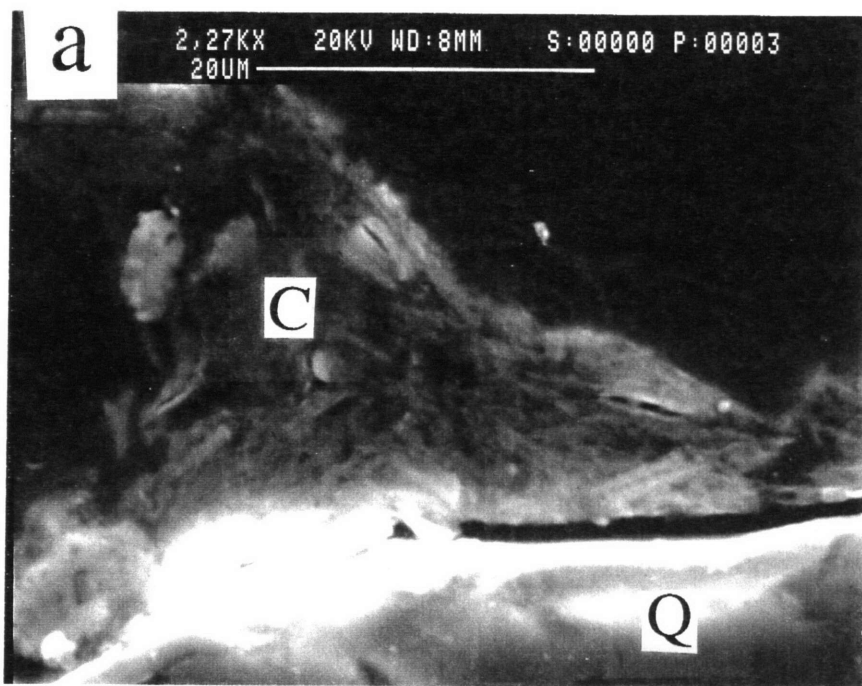
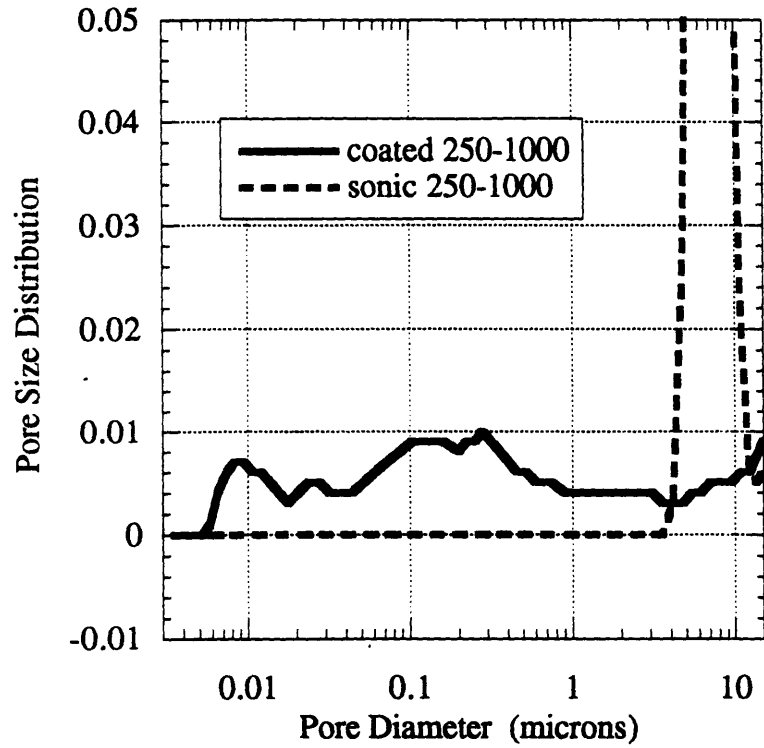


Figure 3-11. Pore size distribution for the coated (solid line) and uncoated (dashed line) Pine Barrens 250-1000 micron sand fraction as determined by mercury porosimetry.



rich coatings. Thus, the sonicated porosimetry sample indicates the porosity of the quartz grains only. The porosimetry data (**Figure 3-11**) clearly indicate that the Pine Barrens quartz grains lack internal porosity since the sonicated sample had no detectable pores less than 4 microns in diameter. The abundance of pores of approximately 8 microns diameter was attributed to external quartz surface pores which are apparently filled by coating material in the coated sample (note disappearance of 8 micron peak in coated sample, **Figure 3-11**). There is an obvious difference between the coated and uncoated distribution of pore sizes which can be interpreted as the coating porosity. The coatings are made up of pores which range in size from about 5 nm to 1000 nm with significant populations of 8 nm, 25 nm and 170 nm size. Strictly speaking, the mercury intrusion data give information regarding the diameter of the pore necks rather than the pore bodies because the necks control the pressure required for mercury entry into a pore [10, 18]. Furthermore, mercury porosimetry data become increasingly prone to error at the lower limit of the technique (about 3.5 nm for 60,000 psi). Total surface area calculations from the mercury intrusion tests showed that the coated sand had a significantly higher surface area (1.94 m²/g) than the uncoated sand (0.049 m²/g) as one would expect due to the addition of fine-grained materials that comprise the coatings.

The porosity of the coating was calculated to be 43% based on the cumulative pore volume of pores between 3 and 50 nm (0.0045 cm³/g) and iron and aluminum concentrations of the <53 micron fraction obtained by HF/HCl/HNO₃ digestion:

$$n_{coat} = \frac{V_{void}}{V_{void} + V_{kaol} + V_{goeth}}$$

$$V_{void} \left[\frac{cm^3}{g_{coat}} \right] = \frac{.0045 cm^3}{g_{250-1000}} \frac{64.2 g_{250-1000}}{100 g_{sed}} \frac{g_{sed}}{0.02 g_{coat}}$$

$$V_{kaol} \left[\frac{cm_{kaol}^3}{g_{coat}} \right] = \frac{2880 \times 10^{-6} mol Al}{g_{coat}} \frac{mol_{kaol}}{2 mol Al} \frac{258 g_{kaol}}{mol kaol} \frac{cm^3_{kaol}}{2.6 g kaol}$$

$$V_{goeth} \left[\frac{cm_{goeth}^3}{g_{coat}} \right] = \frac{1640 \times 10^{-6} mol Fe}{g_{coat}} \frac{mol_{goeth}}{mol Fe} \frac{89 g_{goeth}}{mol goeth} \frac{cm^3_{goeth}}{3.3 g goeth}$$

In making this calculation we assumed: (1) the coatings were composed of voids, goethite and kaolinite and were compositionally similar to the < 53 micron size fraction, (2) all Fe (1640 μmol/g) was goethite with a solid density of 3.3 g/cm³ and all Al (2880 μmol/g) was kaolinite with a density of 2.6 g/cm³, (3) heavy mineral oxides do not contribute significantly to the measured Fe values, and (4) coating pores are <0.05 microns in diameter. This porosity is similar to values one would see in natural clay deposits, 0.32-0.6 [25, 33, 48].

Effective Diffusivity Prediction. For the coating diffusion model we propose for this sorbent, the effective diffusivity within the coatings can be defined as:

$$D_{eff} = \frac{D_{aq} n_{coat} \kappa_{coat}}{R_{coat} \tau_{coat}} \quad (3-10)$$

where, D_{aq} is the aqueous diffusivity, n_{coat} is the coating porosity, κ_{coat} is the coating constrictivity, R_{coat} is the coating retardation factor, and τ_{coat} is the tortuosity of the coating. The n_{coat} factor in the numerator accounts for the reduced available cross-section for diffusion due to the presence of coating particles and R_{coat} accounts for retardation along the diffusion path within the coating. Aqueous diffusivities (**Table 3-5**) were calculated using the expression of Hayduk and Laudie [21] based on the molar volumes (\bar{V} ; cm³/mol) found in **Table 3-1** and an assumed water viscosity (μ) of 0.894 centipoise at 25°C [29]:

$$D_{aq} [\frac{cm^2}{sec}] = \frac{13.26 \times 10^{-5}}{\mu^{1.14} \bar{V}^{0.589}} \quad (3-11)$$

Table 3-5
Coating Diffusion Model and Moment-Derived Effective Diffusivities

	Predictor Model				Moments
	D_{aq} [cm ² /sec]	R_{coat}	D_{eff} [cm ² /sec]	D_{pore} [cm ² /sec]	$D/(1+K)$ [cm ² /sec]
naphthalene	7.9 x 10 ⁻⁶	71	7.2 x 10 ⁻⁹	5.1 x 10 ⁻⁷	4.7 x 10 ⁻¹¹
acenaphthene	7.2 x 10 ⁻⁶	255	1.8 x 10 ⁻⁹	4.6 x 10 ⁻⁷	1.4 x 10 ⁻¹¹
phenanthrene	6.7 x 10 ⁻⁶	1110	3.8 x 10 ⁻¹⁰	4.3 x 10 ⁻⁷	2.2 x 10 ⁻¹²

Aqueous diffusivity calculated based on equation 3-11. R_{coat} assumes a coating r_{sw} of 3.8 and coating f_{oc} of 2% (Table 2-1, <53 μm). D_{eff} calculated from equation 3-10. $D_{pore} = D_{eff} * R_{coat}$. $D/(1+K)$ calculated from equation 3-14 assuming 10 micron coating thickness.

The remaining parameters we must estimate are coating retardation factor, tortuosity and constrictivity. Since batch K_d values were reasonably well estimated from the organic partitioning model (within a factor of 4), we similarly estimate the coating retardation factor from the coating solid-to-water ratio and coating f_{oc} . Again assuming that the <53 micron

wet-sieve size fraction is representative of the coating properties, the coating f_{oc} is 2% (Table 2-1). Assuming an average coating solid density of 2.5 g/cm^3 , and $n_{coat} = 0.4$, the coating r_{sw} is calculated as:

$$r_{sw}^{coat} = \frac{\rho_s(1 - n_{coat})}{n_{coat}} = 3.8 \text{ g/cm}^3 \quad (3-12)$$

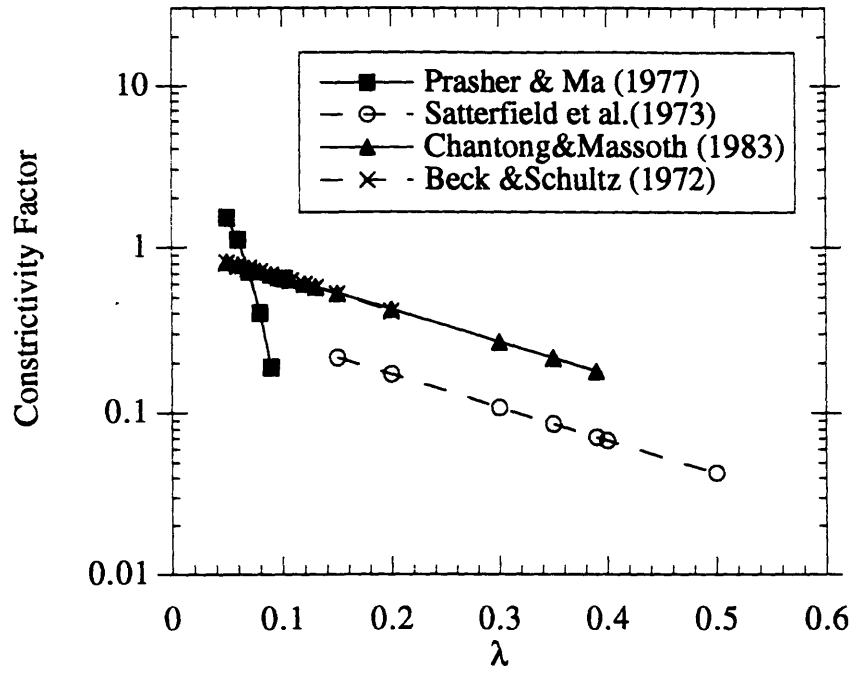
and the coating retardation factors for the three PAH compounds are 71, 255 and 1110 for naphthalene, acenaphthene and phenanthrene, respectively (Table 3-5). Coating tortuosity can be estimated using available empirical correlations between formation factors and porosity (see summary in Iversen and Jorgensen, [24]). We chose the correlation with inverse porosity (n) of Ullman and Aller [49] which applies to marine sediments over a wide range of porosities:

$$\tau = \frac{1}{n^{(m-1)}} \quad (3-13)$$

Values of m range from 2.5 to 5.4 for clays [49] and we chose a value of 3 for the fine-grained coatings to give a tortuosity factor of 6. Thus, the only remaining parameter is coating constrictivity. Constrictivity describes the decrease in diffusivity due to solute interactions with the walls in small pores. Chemical engineers have developed empirical correlations based on batch desorption experiments with porous silica and alumina catalyst particles [7, 39, 44]. These studies had the benefit of well-defined and relatively homogeneous sorbent pore size distributions. Most of these studies were conducted using organic solvents as the diffusion medium; thus, due to the anomalous properties of water in confined pore spaces (i.e., on the order of 5 nm diameter: [9, 11, 29]), these relationships may not be directly applicable to aqueous systems. Other studies with mica membranes [3] and cellulose [8] were conducted in aqueous media and yield approximately the same relationship between the constrictive factor and the parameter λ , the ratio of solute diameter to pore diameter, although these latter studies used relatively large pore diameters (9-60 nm). Various studies examined different ranges of λ , but in general the empirical relationships show an exponential dependence of constrictivity factor on λ over a range of $0.05 \leq \lambda \leq 0.5$ (Figure 3-12).

For the PAH solutes we used (equivalent spherical diameters of 7.8 to 8.6 Å) and the pore size distribution determined by mercury porosimetry (smallest pores were 5 nm diameter), we calculate λ values of less than 0.17 for diffusion within the Pine Barrens coatings. Based on the empirical relationships plotted in Figure 3-12, constrictivity factors range from 0.2 to 1.0 for our system depending on which correlation one chooses. (The data of Prasher and Ma [39] are significantly different from other researchers and constrictivity values exceed 1.0 at small values of λ . This implies that solute diffusivities

Figure 3-12. Constrictivity factors as a function of the ratio of molecular diameter to pore diameter, λ , based on empirical relationships in the literature.



exceeded the aqueous diffusivity in larger diameter pores and suggests that surface diffusion was significant in their study for certain solute-solvent pairs, although the authors did not address this possibility).

As a first approximation, we assume $\kappa_{\text{coat}} = 1$ since the majority of coating pores are significantly larger than the solute diameters we used. With these parameter estimates, the effective diffusivities were calculated from **equation 3-10** as 7.2×10^{-9} , 1.8×10^{-9} and 3.8×10^{-10} cm²/sec for naphthalene, acenaphthene and phenanthrene, respectively.

Moment-derived Effective Diffusivity. We also calculated D_{eff} from the moment-derived k_r value using the following relationship (rearrange **equation 3-7**):

$$\frac{D}{(1+K)} = \frac{k_r \Delta^2 \beta}{\vartheta^*} \quad (3-14)$$

Since $(1+K)$ is equivalent to a retardation factor, and Schneider's [45] model assumes sorption only occurs within the porous portion of the particle, the left hand side of equation 3-14 is equivalent to an effective diffusivity for the coating. Choosing the coating thickness as 10 microns, ($=\Delta$) and the particle radius as 500 microns (our measured geometric mean column particle diameter), then χ in **equation 3-6** is 0.98 and $\vartheta^* = 3.06$. Note that this numerical correction factor differs from the value of 15 obtained by Parker and Valocchi [35] for spheres that are completely permeable, and agrees with the limiting values of 3 to 15 for spherical geometry shape factors (see Figure 5, ref. [45]).

The resulting moment-derived effective diffusivities (**Table 3-5**) are two orders of magnitude smaller than the values we predict using the coating model (**equation 3-10**). It is conceivable that we overestimated the effective coating diffusivities by assuming a constrictivity of unity. However, as discussed above, the empirical relationships derived by chemical engineers for constrictivity effects would decrease our predicted D_{eff} by a factor of 0.2 at most. Our coating diffusion model has either failed to account for an important factor that decreased diffusivity or our model parameter estimates are in error. Below we explore some possible explanations for error in our predictive model.

It is important to note, however, that the qualitative trends of the moment-derived effective diffusivities are reproduced by the coating model predictions. Since the 3 compounds showed the same deviation between measured and predicted D_{eff} (a factor of 150), we conclude that the PAHs had similar diffusion path lengths, in contrast to the work of others [23]. Furthermore, we expect that compounds of similar molecular size would have similar pore diffusivities ($D_{\text{pore}} = D_{\text{eff}} * R_{\text{coat}}$), and this is supported by our moment-

derived pore diffusivities ($= \frac{D}{(1+K)} * R_{coat}$) which agreed within about 30% among the three compounds (see **Table 3-5**).

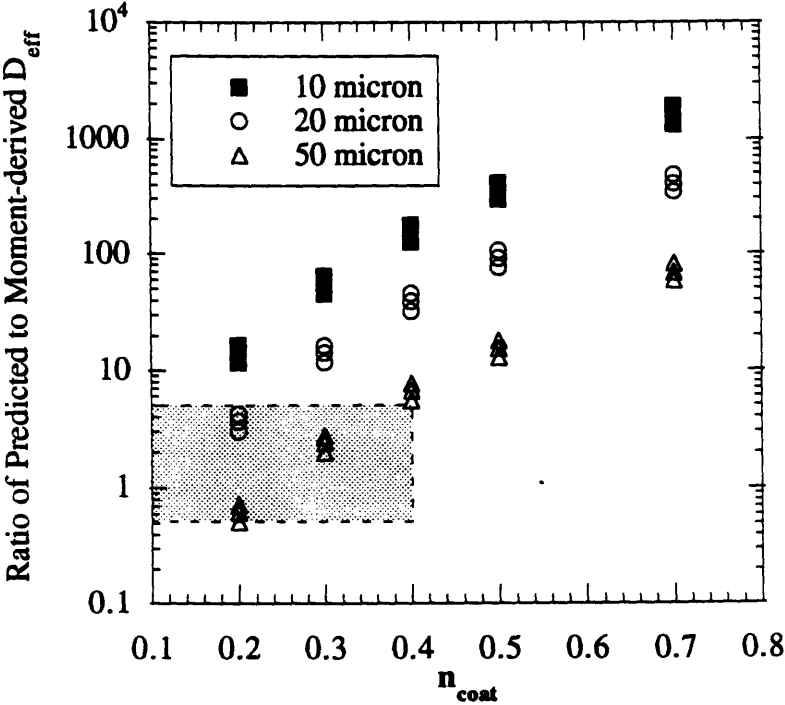
D_{eff} Divergence. The most obvious explanation for the estimated D_{eff} being 150 times higher than that derived from moments is that we have incorrectly quantified one of the coating model parameters. We may also have incorrectly estimated a parameter in Schneider's diffusion model that was used to convert the moment-derived k_r to an effective diffusivity (e.g., Δ or ϑ*). The coating model parameters include D_{aq}, coating tortuosity and coating retardation factor. It is unlikely that we have miscalculated D_{aq} by more than 10%, but coating tortuosity and retardation factor are dependent on properties of the sorbent that are not easily measured or verified. Both coating tortuosity and R_{coat} depend on coating porosity and the porosity value we calculated for the coatings is within the range measured for clay deposits. Thus, assuming macroscopic clay deposits are the appropriate analog for the microscopic Pine Barrens coatings, we do not expect that our tortuosity value explains the observed discrepancy. However, it is possible that clay beds are not an appropriate model for the coatings due to the way the coatings were formed as proposed by Ryan and Gschwend [43]. In their view, the iron oxide in the coatings was derived from Fe⁺³ produced by weathering of ilmenite grains in the sand matrix. The Fe⁺³ was transported to the surfaces of the quartz grains where it complexed to silica surface hydroxyl groups; and after sufficient iron concentrations built up on the quartz surfaces, crystallization of iron oxides began. Further, Ryan and Gschwend [43] presumed that colloidal kaolinite particles released from weathered feldspars were electrostatically attracted to the positively charged iron-oxide particles coating the quartz. The coatings were thus envisioned to be the result of repetitive Fe complexation-kaolinite deposition cycles as the sand deposit weathered over the 5 million years since it emerged from its marine depositional environment. Ryan and Gschwend [43] also report that the Pine Barrens goethite crystals are extremely small (<<1 micron) and contain a significant amount of aluminum (up to 20 mole %, possibly from weathered feldspar). This mode of formation may have resulted in a much more compact and tortuous "sandwich" coating structure than one might expect for a clay deposit, or the pore shapes and orientations may be such that their interconnectivity is low (i.e., the effective coating porosity is much lower than the total coating porosity). We attempted to evaluate the microscale structure of the Pine Barrens coatings with transmission electron microscopy, but were unsuccessful in producing an electron-transparent section of the coating/quartz boundary suitable for TEM observation.

We examined the dependence coating porosity had on our estimates of D_{eff} . We found that n_{coat} can change D_{eff} by more than two orders of magnitude over the porosity range of 0.2 to 0.7. The significant increase in D_{eff} as n_{coat} increases is due to the inverse squared dependence of tortuosity on n_{coat} (**Figure 3-13**). The dependence of predicted/moment-derived D_{eff} ratio on the estimate of coating thickness used in Schneider's [45] model is also shown in **Figure 3-13** as a function of coating porosity. As the coating thickness increases from 10 to 50 microns, the deviation between predicted and moment-derived D_{eff} decreases from a factor of 150 to a factor of 5 at $n_{\text{coat}} = 0.4$ and, at n_{coat} values of 0.2, the agreement is within a factor of 5 for more reasonable coating thicknesses of about 20 microns (shaded area in **Figure 3-13**). Thus, we suspect that the most critical properties to estimate for this sorbent are coating porosity and coating thickness as they both affect D_{eff} by at least an order of magnitude for changes of 2 and 4 times in porosity and thickness, respectively.

Coating retardation factor depends on both coating porosity and coating K_d . The changes in R_{coat} due to varying n_{coat} were included in the calculations above (i.e., **Figure 3-13**) but variations in coating K_d could also explain the discrepancy between predicted and observed D_{eff} . It is conceivable that we have underestimated the coating partition factor by only considering organic partitioning. As inferred from the batch K_d data, significant mineral sorption may have occurred in this sorbent. However, since batch and column phenanthrene partition coefficients indicated little sorption to mineral surfaces, including mineral sorption in the coating model results in an inconsistency in pore diffusivities among the three compounds that does not make intuitive sense (using batch K_{ds} , D_{pore} varied by factor of 5 among the three PAHs; compared to 30% variation using $K_{oc}f_{oc}$). Thus, due to the high organic matter content of the coatings ($f_{oc} \sim 2\%$) we believe that sorption is chiefly controlled by partitioning with organic matter. Furthermore, the magnitude of the changes in D_{eff} due to increasing R_{coat} are only about a factor of 3, which alone is not enough to explain the observed disagreement in D_{eff} .

Other possible explanations for the disagreement between measured and predicted effective diffusivities are: (1) constrictivity is greatly underestimated because mercury porosimetry data is unable to probe the micropores which may be present in the coatings, (2) the behavior of water in micropores may substantially decrease solute diffusivity due to changes in structuring of water adjacent to solid surfaces, and (3) the diffusion model we have chosen for calculating an effective diffusivity from the moments data is inappropriate for our system. In other words, the diffusion medium could be organic matter such that polymer diffusivities are more appropriate than aqueous diffusivities in equation 3-10. We

Figure 3-13. Effect of coating porosity and coating thickness on the agreement between the predicted and moment-derived D_{eff} values. The shaded area shows the region of acceptable agreement between the coating model and the measured D_{eff} which results at low n_{coat} (0.2 - 0.3) and relatively large coating thicknesses (20-50 microns).



briefly examine the micropore/ vicinal water and intraorganic matter diffusion hypotheses below.

Vicinal Water in Micropores. The more-structured properties of water near solid surfaces ("vicinal" water) may explain the discrepancy between our measured and predicted effective diffusivities. If vicinal water extends out to 5 nm [11] from pore walls, then pores of 10 nm diameter will be filled with structured water and we'd expect solute diffusivity to be lower than the diffusivity in bulk water. Pores of 10 nm diameter are present in the coatings and a rough estimate of the decrease in solute diffusivity that can be expected in such pores can be derived from changes in fluid properties between bulk water and vicinal water.

We first examined the potential contribution vicinal water could have on PAH diffusivities by comparing the constrictivity factors obtained by Satterfield et al. [44] in water with those they obtained in organic solvents. The 2.8-3.5 nm pore diameters used by Satterfield et al. [44] should have been filled with structured water if the estimates for vicinal water thicknesses on solid surfaces of about 5 nm are correct (**Table 3-6**). Although the data are few and show some scatter (**Figure 3-14**), there is a significant difference in the best-fit exponential relationships between water and organic solvents, but the diffusivity in vicinal water was not orders of magnitude lower than that in organic solvents. One problem in making the above comparison however is that different solutes were used in the aqueous and organic solvent tests of Satterfield et al. [44]. Their aqueous data was for very water soluble compounds such as NaCl, glucose, sucrose and cyclohexaamylose, while nonpolar organic solutes (alkanes) were tested in hexane and 2,2,4-trimethylpentane. It is likely that restrictive factors and sorption coefficients will be enhanced for more hydrophobic compounds in water because of the higher potential energy gain from transference of hydrophobic compounds to vicinal water than for transfer of polar compounds which have higher aqueous solubilities (i.e.,[46]). At present, there is no data available to provide empirical estimates of the magnitude of this hydrophobic effect. Literature data on the changes in water properties at solid surfaces can however give us an idea of the potential magnitude of changes in diffusivity due to vicinal water.

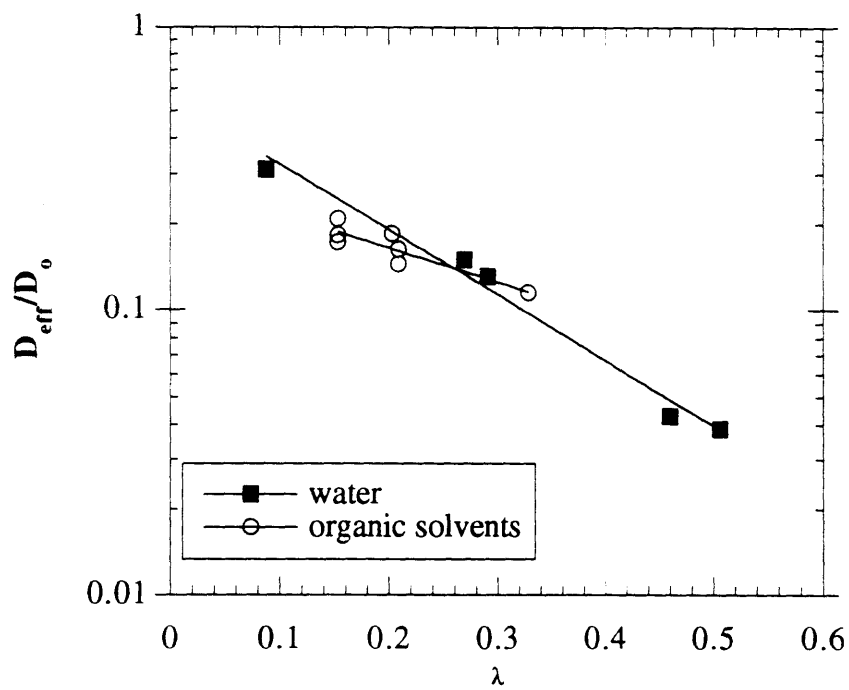
Etzler and Fagundus [13] compared the densities of different solvents in silica pores and found that water showed a 3% decrease in density in 14 nm diameter pores, but acetone and methanol did not, demonstrating the unique properties of water. Low [29] calculated the exponential increase in the viscosity of water as a function of interlayer distance in montmorillonite (i.e., pore size). Based on Low's Figure 1 we estimate an increase in water viscosity by a factor of 4 in pores of approximately 6 nm diameter. In

Table 3-6
Literature Vicinal Water Thicknesses

Reference	Property	δ_{vic} [Å]
Mulla and Low [32]	molar absorptivity [seven montmorillonites]	40
Ozeki [34]	dielectric relaxation [slit pores 1.04 nm diameter=ice-like]	5.2
Low [29]	viscosity [montmorillonite interlayer]	26
Etzler and Conners [12]	heat capacity [silica pores 242 Å diameter]	121
Etzler and White [14]	heat capacity [silica pores 2.4 to 24.2 nm diameter]	60
Etzler [11]	statistical thermodynamic model [vicinal self-diffusion coeff = 0.5 bulk value]	20-60
Etzler and Fagundus [13]	density [silica gel, porous glasses; 2.6 to 24.2 nm diameter pores]	30-50

δ_{vic} is best estimate of thickness of vicinal water layer based on the distance from the solid surface where the study reports a deviation in property value from the bulk water value.

Figure 3-14. Comparison of the constrictivity factor in water versus organic solvents based on the data of Satterfield et al. [44] for diffusion out of 3.2 nm pores in silica-alumina catalyst pellets.



pores of smaller diameter the increase in viscosity will be greater. Ozeki [34] measured the dielectric relaxation time of water in 1 nm slit-shaped pores and concluded that water adsorbed in these fine pores was "highly immobilized and behaved like ice at -32 °C". If ice-like conditions are obtained in micropores, the upper limit on water viscosity in fine pores will be the viscosity of ice. Barer et al. [2] examined the viscosity of nonfreezing water layers between ice and fused silica capillary tubes. They reported a viscosity of 0.4 to 0.5 poise at -2 °C for nonfreezing water layers of about 50 Å thickness. Thus, using the inverse relationship between diffusivity and viscosity [28, 29]:

$$\frac{D_{vic}}{D_{aq}} \approx \frac{\eta_{aq}}{\eta_{vic}} \approx \frac{0.8937}{40 \text{ to } 50} = 0.02 \quad (3-15)$$

and assuming that the viscosity reported by Barer et al. [2] represents vicinal water, the maximum effect vicinal water structure will have on PAH diffusivities is on the order of 0.02. In other words, the diffusivity in micropores will be about 1/50th the diffusivity in bulk water due to the structuring of water molecules near a solid surface! A correction of this magnitude for diffusion in fine pores could explain the discrepancy between our predicted and moment-derived effective diffusivities. Although this calculation is rough, it points to the possibility that an important diffusion-limiting mechanism has been missing from our pore diffusion/sorption models in aqueous systems.

Gregg and Sing [18] remark on the high interaction energy within micropores (pores of molecular dimensions) for gas adsorption systems and state that both pore shape and molecular size determine the limit at which pores begin to show increased interaction with solutes. They summarize that for slit-shaped pores the critical upper pore width is 1.5 times the molecular diameter and for cylindrical pores the limit is 2.5 times the molecular diameter (p. 209). These values translate into λ values of 0.67 and 0.4, respectively. For the PAH solutes we studied, these limits are reached at pore diameters of approximately 1.2 to 2 nm, respectively. Unfortunately, pores of this size are below the lower limit of the mercury porosimetry technique (3.5 nm), and assessment of micropore size distributions from gas adsorption isotherms (which give micropore total volume) is difficult [18].

Both N₂ adsorption and mercury porosimetry have been used in a few sorption studies to quantify the amount of internal porosity in aquifer sorbents [1, 15, 20]. However, no detailed investigation of the relative importance of micropores has yet been carried out. These studies have shown that, on a weight basis, intraparticle porosity (cm³/g) ranges from 0.015 to 0.05 in such sorbents as Borden and Moffett [1, 20],. These values are low but, as pointed out by Ball and Roberts [1], are sufficient to account for all

of the solute present in dilute aqueous solutions. Further, we surmise that the micropore mechanism referred to by Farrell and Reinhard [15] is due to both the structuring of water as well as the higher electrostatic potentials in micropores which could interact with both the double bond π -electrons of trichloroethylene and the polarizable carbon-chlorine bonds.

If vicinal water is abundant in natural sorbents, slow solute diffusion in micropores that are filled with structured water could explain the high effective tortuosity (=tortuosity/constrictivity) fitting parameter values reported by others [1, 15, 20]. In aquifer sorbents, effective tortuosity values of 170 to 11,000 were found for Borden sand [1], and Harmon et al. [20] fit Moffett aquifer sorption data with an effective tortuosity value of 350. Harmon and Dela-Barre [19] also reported high effective tortuosity values of 200-300 for larger size fractions and up to 10,000 for smaller size fractions of Moffett sorbent (personal communication, ACS conference). These values imply very small constrictivity values (i.e., extremely hindered diffusion) and/or highly tortuous diffusion paths within aquifer sorbents. In effect, the discrepancy we found between our predicted and moments-derived D_{eff} values translates into an effective tortuosity fitting parameter of about 900 ($=150 \cdot \tau_{\text{coat}}$). This value is within the range reported in the literature.

Intraorganic Matter Diffusion. Another possible explanation for the 100 fold discrepancy between measured and predicted D_{eff} values is that our predictor model is not quantifying the correct diffusion process. Equation 3-10 assumes that slow diffusion occurs in the water-filled pores of the coating which make up a tortuous diffusion regime. An alternative diffusion medium is the coating organic matter itself. Slow intraorganic matter diffusion has been proposed as the mechanism controlling sorption in aquifer materials by Brusseau and coworkers [4, 6]. Some of the difficulties associated with modeling such a diffusion process include: (1) the difficulty of predicting polymer diffusion coefficients that can vary greatly with temperature, pressure, penetrant size, shape and concentration as well as polymer rigidity and degree of polymer cross-linking [42], (2) difficulty of determining the size of the organic matter diffusion regime, and (3) possibility of microporosity within certain polymers that could increase solute diffusivities depending on the interconnectedness of these void spaces. Brusseau et al.[6] and Ball and Roberts [1] attempted to explain their sorption results using both pore diffusion and intraorganic matter diffusion models. At present there is no method for independently estimating intraorganic matter diffusion coefficients based on sorbent and sorbate properties. Thus, organic matter diffusion is a reasonable alternative to the coating diffusion model described here, but requires detailed information on organic matter composition and properties.

Summary and Conclusions

Sorption experiments using both batch and column techniques with a well-characterized sorbent and three PAH compounds indicated that (a) sorption kinetics is rate-limiting naphthalene, acenaphthene and phenanthrene transport in this low f_{oc} aquifer sorbent, (b) batch kinetics experiments were incapable of quantifying the rate of sorption due to sorbent degradation during batch mixing, (c) batch K_d values were not indicative of column K_d except for the largest compound, phenanthrene, possibly because of less sorbent abrasion at lower batch solid-to-water ratio, (d) a pore diffusion model based on retarded diffusion within the high f_{oc} , iron-oxide/kaolinite coatings on impermeable quartz grains was qualitatively able to predict the trend in sorption rate for the three PAHs studied.

The sorption rates we measured for naphthalene and phenanthrene support our earlier conclusion (Chapter 2) that a kinetic sorption model is required to accurately assess subsurface transport of these chemicals under natural gradient conditions. Our results using relatively high molecular weight hydrophobic organic compounds expands the range of HOCs for which sorption rate limitations have been documented. Furthermore, our use of flow rates that encompassed both natural gradient and pumping conditions extends the range of pore velocities over which sorption rate has been reported to be significantly slower than transport by advection. Use of a kinetic sorption model, rather than an equilibrium one in subsurface transport codes, should therefore provide more reliable estimates of both solute arrival times downgradient and the duration of pump-and-treat remediation schemes.

Using the coating diffusion model we identified that careful quantification of coating porosity, thickness and constrictivity are critical to the success of sorption rate prediction based on sorbent and sorbate properties. The abundance of such oxide coatings in natural sorbents suggests that such a model may have wider applicability. We postulate that discrepancies between measured and predicted diffusivities in the literature may reflect both our inability to easily characterize the diffusion media of the sorbent accurately and to the as yet unquantified processes associated with organic compound sorption in micropores of natural solids. Future work that focuses on detailed sorbent characterization should lead to greater understanding of the mechanism of HOC sorption in aquifer materials.

Literature Cited

1. Ball, W. P. and P. V. Roberts. (1991) Long-term sorption of halogenated organic chemicals by aquifer material. 2. Intraparticle diffusion. *Environ. Sci. Technol.*, 25: 1237-1249.
2. Barer, S. S., N. V. Churaev, B. V. Derjaguin, O. A. Kiseleva and V. D. Sobolev. (1980) Viscosity of nonfreezing thin interlayers between the surfaces of ice and quartz. *J. Colloid Interface Sci.*, 74: 173-180.
3. Beck, R. E. and J. S. Schultz. (1972) Hindrance of solute diffusion within membranes as measured with microporous membranes of known pore geometry. *Biochimica et Biophysica Acta.*, 255: 273-303.
4. Brusseau, M. L. (1992) Nonequilibrium transport of organic chemicals: the impact of pore-water velocity. *J. Contam. Hydrol.*, 9: 353-368.
5. Brusseau, M. L. (1993) The influence of solute size, pore water velocity and intraparticle porosity on solute dispersion and transport in soil. *Water Resour. Res.*, 29: 1071-1080.
6. Brusseau, M. L., R. E. Jessup and P. S. C. Rao. (1991) Nonequilibrium sorption of organic chemicals: elucidation of rate-limiting processes. *Environ. Sci. Technol.*, 25: 134-142.
7. Chantong, A. and F. E. Massoth. (1983) Restrictive diffusion in aluminas. *AIChE J.*, 29: 725-731.
8. Colton, C. K., K. A. Smith, E. W. Merrill and P. C. Farrell. (1971) Permeability studies with cellulosic membranes. *J. Biomed. Mater. Res.*, 5: 459-488.
9. Drost-Hansen, W. (1969) Structure of water near solid interfaces. *Ind. Eng. Chem.*, 61: 10-47.
10. Dullien, F. A. L. (1979) Porous Media: Fluid Transport and Pore Structure. Academic Press: New York, NY; 396 pp.
11. Etzler, F. M. (1983) A statistical thermodynamic model for water near solid interfaces. *J. Colloid Interface Sci.*, 92: 43-56.
12. Etzler, F. M. and J. J. Connors. (1990) Temperature dependence of the heat capacity of water in small pores. *Langmuir.*, 6: 1250-1253.
13. Etzler, F. M. and D. Fagundus. (1983) The density of water and some other solvents in narrow pores. *J. Colloid Interface Sci.*, 93: 585-586.
14. Etzler, F. M. and P. J. White. (1987) The heat capacity of water in silica pores. *J. Colloid Interface Sci.*, 120: 94-99.
15. Farrell, J. and M. Reinhard. (1994) Desorption of halogenated organics from model solids, sediments and soil under unsaturated conditions. 2. Kinetics. *Environ. Sci. Technol.*, 28: 63-72.

16. Garbarini, D. R. and L. W. Lion. (1986) Influence of the nature of soil organics on the sorption of toluene and trichloroethylene. *Environ. Sci. Technol.*, 20: 1263-1269.
17. Gauthier, T. D., W. R. Seitz and C. L. Grant. (1987) Effects of structural and compositional variations of dissolved humic materials on pyrene Koc values. *Environ. Sci. Technol.*, 21: 243-248.
18. Gregg, S. J. and K. S. W. Sing. (1982) Adsorption, Surface Area and Porosity. Academic Press: London; 303 pp.
19. Harmon, T. C. and B. K. D. Barre. (1994) The effect of temperature on the rate of desorption of halogenated alkenes from aquifer solids. 207th ACS National Meeting, San Diego, CA, 343-345.
20. Harmon, T. C., L. Semprini and P. V. Roberts. (1992) Simulating solute transport using laboratory-based sorption parameters. *J. Environ. Engineering.*, 118: 666-689.
21. Hayduk, W. and H. Laudie. (1974) Prediction of diffusion coefficients for nonelectrolytes in dilute aqueous solutions. *AIChE J.*, 20: 611-615.
22. Holmén, B. A. and P. M. Gschwend. (1994) Sorption kinetics of acenaphthene in an atlantic coastal plain aquifer sand. *Environ. Sci. Technol.*, submitted.
23. Hutzler, N. J., J. C. Crittenden and J. S. Gierke. (1986) Transport of organic compounds with saturated groundwater flow: experimental results. *Water Resour. Res.*, 22: 285-295.
24. Iversen, N. and B. B. Jorgensen. (1992) Diffusion coefficients of sulfate and methane in marine sediments: Influence of porosity. *Geochim. Cosmochim. Acta.*, 57: 571-578.
25. Johnson, R. L., J. A. Cherry and J. F. Pankow. (1989) Diffusive contaminant transport in natural clay: A field example and implications for clay-lined waste disposal sites. *Environ. Sci. Technol.*, 23: 340-349.
26. Karickhoff, S. W. (1981) Semi-empirical estimation of sorption of hydrophobic pollutants on natural sediments and soils. *Chemosphere.*, 10: 833-846.
27. Levenspiel, O. and W. K. Smith. (1957) Notes on the diffusion-type model for the longitudinal mixing of fluids in flow. *Chem. Eng. Sci.*, 6: 227-233.
28. Li, Y.-H. and S. Gregory. (1974) Diffusion of ions in sea water and in deep-sea sediments. *Geochim. Cosmochim. Acta.*, 38: 703-714.
29. Low, P. F. (1976) Viscosity of interlayer water in montmorillonite. *Soil Sci. Soc. Am. J.*, 40: 500-505.
30. McCarty, P. L., M. Reinhard and B. E. Rittman. (1981) Trace organics in groundwater. *Environ. Sci. Technol.*, 15: 40-51.
31. Miller, M. M., S. P. Wasik, G.-L. Huang, W.-Y. Shiu and D. Mackay. (1985) Relationships between octanol-water partition coefficient and aqueous solubility. *Environ. Sci. Technol.*, 19: 522-529.

32. Mulla, D. J. and P. F. Low. (1983) The molar absorptivity of interparticle water in clay-water systems. *J. Colloid Interface Sci.*, 95: 51-60.
33. Myrand, D., R. W. Gillham, E. A. Sudicky, S. F. O'Hannesin and R. L. Johnson. (1992) Diffusion of volatile organic compounds in natural clay deposits: Laboratory tests. *J. Contamin. Hydrol.*, 10: 159-177.
34. Ozeki, S. (1989) Dielectric properties of water adsorbed in slitlike micropores of jarosite. *Langmuir.*, 5: 181-186.
35. Parker, J. C. and A. J. Valocchi. (1986) Constraints on the validity of equilibrium and first-order kinetic transport models in structured soils. *Water Resour. Res.*, 22: 399-407.
36. Parker, J. C. and M. T. van Genuchten. (1984) Determining transport parameters from laboratory and field tracer experiments. Bulletin 84-3, Virginia Agricultural Experimental Station.
37. Pignatello, J. J. (1990) Slowly reversible sorption of aliphatic halocarbons in soils. II. Mechanistic aspects. *Environ. Tox. Chem.*, 9: 1117-1126.
38. Pignatello, J. J., F. J. Ferrandino and L. Q. Huang. (1993) Elution of aged and freshly added herbicides from a soil. *Environ. Sci. Technol.*, 27: 1563-1571.
39. Prasher, B. D. and Y. H. Ma. (1977) Liquid diffusion in microporous alumina pellets. *AIChE J.*, 23: 303-311.
40. Rao, P. S. C., R. E. Jessup, D. E. Rolston, J. M. Davidson and D. P. Kilcrease. (1980) Experimental and mathematical description of nonadsorbed solute transfer by diffusion in spherical aggregates. *Soil Sci. Soc. Am. J.*, 44: 684-688.
41. Rao, P. S. C., D. E. Rolston, R. E. Jessup and J. M. Davidson. (1980) Solute transport in aggregated porous media: theoretical and experimental evaluation. *Soil Sci. Soc. Am. J.*, 44: 1139-1146.
42. Rogers, C. E. (1965) Solubility and diffusivity. In *Physics and Chemistry of the Organic Solid State*. Fox, D., M. M. Labes and A. Weissberger (Ed.) Interscience: New York; pp. 509-635.
43. Ryan, J. N. and P. M. Gschwend. (1992) Effect of iron diagenesis on the transport of colloidal clay in an unconfined sand aquifer. *Geochim. Cosmochim. Acta.*, 56: 1507-1521.
44. Satterfield, C. N., C. K. Colton and J. Pitcher W.H. (1973) Restricted diffusion in liquids within fine pores. *AIChE J.*, 19: 628-635.
45. Schneider, P. (1986) Determination of effective diffusion coefficients for porous packings with an impermeable centre from peak moments. *Chem. Eng. Sci.*, 41: 1759-1764.
46. Schwarzenbach, R. P., P. M. Gschwend and D. M. Imboden. (1993) Environmental Organic Chemistry. John Wiley & Sons, Inc.: New York; 681 pp.

47. Schwarzenbach, R. P. and J. Westall. (1981) Transport of nonpolar organic compounds from surface water to groundwater. Laboratory sorption studies. *Environ. Sci. Technol.*, 15: 1360-1367.
48. Shackelford, C. D. and D. E. Daniel. (1991) Diffusion in saturated soil. II: Results for compacted clay. *J. Geotech. Engrg.*, 117: 485-506.
49. Ullman, W. J. and R. C. Aller. (1982) Diffusion coefficients in nearshore marine sediments. *Limnol. Oceanogr.*, 27: 552-556.
50. Valocchi, A. J. (1985) Validity of the local equilibrium assumption for modeling sorbing solute transport through homogeneous soils. *Water Resour. Res.*, 21: 808-820.
51. van Genuchten, M. T. (1985) A general approach for modeling solute transport in structured soils. *Memoires IAH.*, 17: 513-526.
52. Wu, S.-C. and P. M. Gschwend. (1986) Sorption kinetics of hydrophobic organic compounds to natural sediments and soils. *Environ. Sci. Technol.*, 20: 717-725.
53. Wu, S.-C. and P. M. Gschwend. (1988) Numerical modeling of sorption kinetics of organic compounds to soil and sediment particles. *Water Resour. Res.*, 24: 1373-1383.

Chapter 4

SORBENT COMPOSITION EFFECTS: ACENAPHTHENE SORPTION KINETICS IN THREE AQUIFER SANDS

Introduction

Few sorption studies with natural sorbents have thoroughly characterized the properties of the sorbent in great detail [1, 3, 21, 55]. In order to estimate the parameters in the retarded radial diffusion models presently being widely applied to sorption kinetics data, specific information on the texture and composition of the sorbent is required. Of particular interest for HOC sorption are such parameters as the distribution of organic matter within the solid, the required diffusive path lengths to the organic matter sorption "sites", and the tortuosity and constrictivity of the diffusion paths. Our approach was to compare the rate of acenaphthene sorption in three well-characterized sandy aquifer materials in order to elucidate the key sorbent parameters which govern sorption kinetics in these low organic carbon sediments. In particular, we examined how pore size distribution and iron oxide composition affect experimentally determined sorption parameters (K_d and sorption rate).

Background

Ball et al. [1] recognized the importance of thorough sorbent characterization in order to aid interpretation of sorption kinetics data in terms of a diffusion mechanism. Borden aquifer solids were characterized in terms of organic carbon content (f_{oc}), specific surface area, intraparticle porosity and petrographic mineral identification. With these independent measurements, Ball and Roberts [2] were able to model their tetrachloroethylene batch sorption experiments assuming diffusion lengths equal to particle radii and effective tortuosities ranging from 170 to 11,000. The effective tortuosity, defined as the ratio of tortuosity to constrictivity, amounted to a fitting parameter required to match experimental results and was not independently estimated.

Harmon et al. [21] determined f_{oc} , surface area and intraparticle porosity for aquifer solids from Moffett, CA. These authors also used batch kinetic experiments to quantify apparent intraparticle diffusivities and used intraparticle porosity measurements to quantify intraparticle retardation factors, assuming all the retardation occurred inside the porous particles. With these laboratory-based measurements, Harmon et al. [21] were able to simulate breakthrough fronts in a field test at the site using a two-region radial diffusion nonequilibrium model.

Other studies that have described sorbent properties in detail include Wood et al. [55] who focused on characterizing intragrain porosity in the Cape Cod aquifer material using some novel techniques (SEM, UV epifluorescence, mineral abrasion) in order to

identify the principal areas of ion-exchange capacity in this sorbent. These authors were able to show significant intragrain porosity ranging from 5 to 19% , depending on mineral composition, and that feldspar and mica alteration products inside the particles were responsible for a significant, diffusion-limited fraction of sodium adsorption. Barber et al. [3] also studied Cape Cod aquifer material and found higher polychlorinated biphenyl (PCB) sorption capacity in the silt-sized and magnetic mineral fractions which they attributed to the abundance of positively-charged mineral surfaces (i.e., iron-oxyhydroxides) in these fractions which sorb more organic matter. The sorption of dissolved organic matter by iron oxide and clay minerals has been studied by others [13, 23, 45]. In addition, Schwertmann [42] demonstrated that dissolved organic matter inhibited the formation of crystalline iron oxides from amorphous iron oxide.

Iron oxide coatings have been reported for many sandy aquifer materials. Stauffer [43] reports petrographic analyses for six aquifer materials in his thesis. Of particular importance to our study is that all six aquifer solids had significant iron-oxide coatings on quartz and feldspar grains. MacIntyre et al. [26] also report goethite and lepidocrocite coatings on quartz grains from alluvial terrace aquifer material from Columbus, MI. Other sorbents with appreciable iron oxide coatings include Borden [1], Cape Cod [55], the New Jersey Pine Barrens [38], Lula, OK, and Tampa, FL [8].

We suspected that differences in sorbent texture and mineralogy would affect the rate of acenaphthene sorption; thus three low organic carbon aquifer sands were studied. The Pine Barrens, New Jersey (PB) sand was previously studied (Chapter 2) and has been further characterized here in terms of pore size distribution and iron-oxide mineralogy. The Georgetown, South Carolina (GT) sand is an iron-oxide coated Atlantic Coastal Plain beach deposit like PB, but has very different handling characteristics and mineralogy, and the Aberjona, Massachusetts (AJ) sand is from a different type of depositional environment: glacial outwash. Both batch and column sorption experimental techniques were used to quantify sorption capacity and rate for these sands. Differences in sorption parameters (K_d , rate) were then correlated to sorbent properties in order to determine which sorbent properties are most critical for predicting sorption rates in aquifer sands.

Methods

Sorbent Characterization. The Georgetown (GT) sand was collected from the auger flights in the saturated zone at 2.4 to 3.0 meters depth in Baruch State Forest, Georgetown, South Carolina. The water-table aquifer at this site is composed predominantly of fine-grained sandy Coastal Plain terrace deposits approximately 100,000 years old underlain by

a 1-meter thick clay unit at 6-8 meters depth [53]. The sand is a bright, orange-brown color due to abundant iron-oxides.

The Aberjona sand (AJ) was collected with a hand auger from a depth of approximately 1.9 meters in the Aberjona watershed, Woburn, Massachusetts. The water table was intercepted at 0.65 meters in the hole. The AJ aquifer is a sand unit within a glacial valley that runs north-northeast underlain by bedrock at a depth of 20 meters. The sand unit comprises an unconfined glacial outwash aquifer up to 30 meters thick [18]. The sand used in this study was collected 50 meters east of a former municipal well (well "H") and approximately 15 meters north of a cluster of wells designated "S90".

The bulk sands were dried at 70°C, then sieved through 1000, 250, 105 and 53 micron screens to give five size fractions which were further characterized for organic carbon content, mineralogical composition and iron content. A second bulk sample was sonicated in distilled water for 30 min prior to wet sieving through the four screens. A Perkin-Elmer model 2400 CHN analyzer was used for fraction organic carbon (f_{oc}) determination on the dry-sieved size fractions after the larger fractions were ground with a mortar and pestle. Mineralogy and sediment texture were characterized using a Cambridge Stereoscan 240 scanning electron microscope (SEM) equipped with an energy dispersive X-ray (EDX) spectrometer (Link Analytical). Thin sections of the dry sand fractions were prepared by embedding the sand in low-viscosity Spurr's® epoxy, sectioning the samples with a diamond saw (Buehler, Isomet 54B), followed by grinding (240, 400 and 600 grit SiC paper) and polishing (0.05 micron alumina paste) the sections after bonding to glass slides with Crystalbond 509 (Aremco, Ossining, NY). The thin sections were carbon-coated prior to SEM analysis. Aqueous suspensions of the <53 micron wet-sieved size fraction were air-dried on glass slides for X-ray diffraction (XRD) analysis. The clay-sized fraction (<2 micron) was separated from the bulk sand by standard sedimentation techniques for further XRD characterization. XRD analysis was performed over a 2θ range of 4 to 72 degrees with a step size of 0.05 and a scan speed of 7.5 degrees per minute using a Diano XRD-5 diffractometer with the following operating conditions: 50kV, 200 mA, 0.5° divergence slit, 0.5° soller slit and 3 nm receiving slit. Identification of clay minerals was confirmed by glycerol and heat (above 550° C) treatments for the <2 micron fraction.

Pore size distribution was determined by Porous Materials Inc. (Ithaca, NY) using mercury intrusion on 2-3 g samples of three fractions (bulk, 250-1000 μm , sonicated 250-1000 μm) for each aquifer material. Pore diameters were calculated using the Washburn equation [25] for pressures up to 60,000 psi (approx 3.5 nm) assuming cylindrical pores, a contact angle of 140° and a surface tension of 480 dynes/cm.

Selected size fractions were also analyzed for total iron, Ti(III)-citrate-EDTA-bicarbonate (TiCEB) -extractable iron and oxalate-extractable iron. Total iron was measured by inductively coupled plasma (ICP) analysis of the diluted (1:200 or 1:250) extract from 0.1 g sediment digestions with HF-HCl-HNO₃ in teflon-lined bombs at 130°C for 45 minutes followed by 10 min at 130°C after boric acid addition to complex fluoride [44]. TiCEB extractions were performed following the method of Ryan and Gschwend [37] in order to characterize the fraction of surface iron (crystalline and amorphous iron oxides) in the sand subsamples. The amorphous iron content of the sand was determined using the ammonium-oxalate-in-the-dark (AOD) method of Jackson et al. [22] at pH 3 with 2 hour incubations on a wrist-action shaker followed by centrifugation at 4000 g and quantification of iron in the supernatant by ICP. ICP analyses of the total digestate, TiCEB and AOD extracts were performed using standard calibration curves for Fe solutions prepared in 5% HNO₃ (PlasmaPure, Leeman Labs, Lowell, MA) and a Thermo-Jarrell Ash Model Atomscan 25 Inductively Coupled Plasma spectrometer. A wavelength of 259.94 nm was used for Fe analysis. Method blanks consisting of the extracting solution were analyzed with each batch of samples. The reported iron values have an analytical error of less than 10%, based on a 6% relative standard deviation of standard counts over a day's run.

Solutions and Chemicals. Acenaphthene (Aldrich, 99%), acetone (EM Science, omnisolv[®]), methanol (EM Science, omnisolv[®]), and sodium nitrate (Johnson Matthey) were used in the sorption experiments. The log K_{ow} value for acenaphthene is 3.92, and its aqueous solubility is 25 μM [28].

Distilled water was 0.2 micron-filtered, prior to adding sodium acetate and glacial acetic acid (final concentrations of 10⁻⁴ M) to buffer the pH near the ambient groundwater value of 5.2 for Georgetown and 5.8 for Aberjona. The buffer also contained mercuric chloride at 10 mg/L to inhibit biological activity. Acenaphthene solutions were made up directly from the solid PAH and were mixed with a stirrer for 1 week prior to use.

Batch Experiments. All batch tests were designed to achieve final equilibrium aqueous concentrations equal to approximately 50% of the initial aqueous concentration using calculations based on K_{ocf_{oc}}. Wheaton v-vials (4.5 mL capacity) with foil-lined screw caps were used for all batch kinetics experiments with acenaphthene. One to two grams of the bulk GT or AJ sediment was tumbled end-over-end at ~2 rpm with a 2.6 μM acenaphthene solution made up in the appropriate acetate/HgCl₂ buffer (solid/water ratio = 0.25 for GT and 0.45 for AJ). The vials were removed from the tumbler at elapsed times

ranging from 30 to 41,000 min (29 days) and centrifuged for 20 min at 1400g. The supernatant was then pipetted into a quartz cuvet for fluorescence measurement (290 nm excitation/338 nm emission). Time of contact was recorded as ending when the cuvet was filled. Positive controls (acenaphthene solution without sand) were analyzed with each time point. Three negative controls (no acenaphthene added) were analyzed throughout the time course. Apparent K_d was calculated for each time point as:

$$K_d^{app} = \frac{(F_{ctrl} - F_{samp})}{F_{samp} r_{sw}} \quad (4-1)$$

where F_i is the fluorescence of the control or sample (F.U., fluorescence units) and r_{sw} is the solid/water ratio (g/mL). Fluorescence readings, made using a Perkin-Elmer LS-5 fluorescence spectrophotometer, were averaged over 16 sec for each sample. All experiments were conducted at room temperature (22 ± 4 °C).

A batch isotherm experiment was performed using five acenaphthene solutions at initial concentrations ranging from 0.1 to 16 μ M (about 0.4 to 60% of solubility). This range encompassed the concentrations used in the column experiments and the batch kinetics experiments. Isotherm vials had the same r_{sw} as the batch kinetics experiments and incubation times of 4 days were used. Sorbed concentrations were calculated by difference, based on fluorescence measurements, as described above.

Column Experiments. The experimental setup used for column experiments was assembled from high-pressure liquid chromatography (HPLC) components as described in Chapter 2. Briefly, the columns were 7 cm lengths of 22 mm i.d. (3.8 cm^2 cross-section) stainless steel mirror-finish tubing with low-dead-volume HPLC fittings (Alltech Associates; Deerfield, IL). The GT and AJ columns were packed with wet bulk sand by alternately adding buffer then sand to the column and tapping the column after every cm of sand filling. Column porosities for GT and AJ sands were determined gravimetrically by weight difference of saturated versus dried (90 °C) sand subcores of column material (GT) or saturated field samples (AJ). Column solid-to-water ratios were calculated assuming a solid density (ρ_s) of 2.5 g/cm^3 and using the calculated porosity (n) value:

$$r_{sw} = \frac{(1-n)\rho_s}{n} \quad (4-2)$$

The porosity was 0.27 for both the GT and AJ sands, and therefore the solid-to-water ratio was 6.8 g/mL in both columns. The columns were initially saturated from the bottom at a flow rate of 0.05 mL/minute. Effluent turbidity was monitored during the initial column flushing, and experiments were commenced after turbidity measurements stabilized at flow rates greater than the highest experimental rate. In contrast to previous experiments with the Pine Barrens sand, the GT and AJ column effluent turbidities were surprisingly low

and quickly achieved the distilled water blank value (within ~50 pore volumes). Experimental flow rates ranged from 0.007 to 0.5 mL/min which corresponds to linear velocities of 0.4 to 27 cm/hr. This range of velocities allowed us to evaluate sorption kinetics while operating under realistic aquifer flow conditions.

A Valco six-port valve was used to make pulse injections of the compound of interest using a 500 microliter sample loop. The Waters Model 484 UV absorbance detector was operated in difference mode as buffer was also pumped through the reference cell. The detector monochromator was set to various wavelengths for each analyte: acenaphthene (226 nm), acetone (264 nm), and nitrate (226 nm). Millivolt output from the UV detector was collected by a data acquisition board (12 bit, A/D converter PC-LABCARD 711B, Advantech Co.,LTD) and Labtech Notebook software (Laboratory Technologies, Inc., Wilmington, MA).

The absorbance output of the detector was occasionally checked by fluorescence analysis of column effluent during peak elution to confirm the presence of acenaphthene. Mass balance was also monitored on a few experiments by collecting column effluent fractions and analyzing them with the Perkin-Elmer spectrofluorimeter. Recoveries were consistently greater than ~85% but were generally higher for the higher velocity experiments. This dependence on flow rate was attributed to acenaphthene volatilization losses from the effluent reservoir over the longer duration, slow velocity experiments.

Data Analysis. In order to extract sorption rate constants from the column data, we employed the method of moments using a single sorption site first-order model as done previously for the Pine Barrens sand experiments (Chapter 2). The first absolute moment (μ'_1) and second central moment (μ_2) of the elution curves for acetone and acenaphthene were fit to the theoretical moment expressions in order to evaluate the model parameters: R = retardation factor, L = column length, α = dispersivity [cm], t_0 = input pulse duration [sec], and k_r = reverse sorption rate constant [sec^{-1}]. The appropriate moment expressions for the single-site model derived by Valocchi [47] were converted to dimensional form and simplified by assuming that the dispersion coefficient is linearly related to velocity (i.e., $D = \alpha v$):

$$\mu'_1 = \frac{L}{v} R + \frac{t_0}{2} \quad (4-3)$$

$$\mu_2 = \frac{2L\alpha R^2}{v^2} + \frac{2L(R-1)}{k_r v} + \frac{t_0^2}{12} \quad (4-4)$$

The first-order rate constant in this model is a lumped parameter that describes all sorption processes such as mass transfer with immobile water and the rate of sorption to organic matter or mineral surfaces. For the GT and AJ columns, we found appreciable

physical nonequilibrium (PNE) which expressed itself in the first moments of the nonsorbing tracer, acetone. Rather than resort to a two-region model as others have done for such sorbents (e.g., [34, 49]), we chose to model our data with the single-site model because it has only two sorption fitting parameters, K_d and k_r . In contrast, the two-site/two-region models have a third fitting parameter to describe the fractions of each site type (equilibrium or kinetic sites; mobile or immobile region), and there is no easy way to independently constrain this factor. We find no chemical or physical justification for dividing the sorbent into two types of sites, especially when the two-site model assumes a single partition coefficient applies to both sites. Further, the single-site model is better suited for making comparisons among different sorbents.

We interpret the retardation factor obtained with the single-site first-order model as a lumped parameter that describes retention of solutes both due to partitioning with stagnant water regions of the sorbent and with sorbent organic matter. In this sense, the total partition coefficient, K_d^{tot} , is the sum of the immobile water, K_d^{imm} , and the organic matter, K_d^{om} , partition coefficients:

$$K_d^{tot} = K_d^{imm} + K_d^{om} \quad (4-5)$$

where the partition coefficients are defined as:

$$K_d^{om} \left[\frac{mL}{g} \right] = \frac{C_{om} f_{om}}{C_m \theta_m} \quad \text{and} \quad K_d^{imm} \left[\frac{mL}{g} \right] = \frac{\theta_{im} C_{im}}{\theta_m C_m r_{sw}} \quad (4-6)$$

with C_{om} representing solute concentration in the sediment organic matter [mol/g_{om}]; f_{om} is the fraction of organic matter [g_{om}/g_{sed}], C_m is the mobile water concentration [mol/mL_m], θ_m is the fraction of mobile water [mL_m/mL_{tot}], θ_{im} is the fraction of immobile water [mL_{im}/mL_{tot}], C_{im} is the immobile water concentration [mol/mL_{im}], and r_{sw} is the solid-to-water ratio [g/mL_{tot}]. The total retardation factor is thus defined on the basis of the total partition coefficient as:

$$R = 1 + r_{sw} K_d^{tot} \quad (4-7)$$

Since the "nonsorbing" tracer, acetone, is assumed not to partition into organic matter, the retardation factor for acetone is defined solely on the basis of the immobile water partition coefficient. Therefore, assuming acenaphthene and acetone undergo similar exchange with immobile water due to their similar sizes, we can calculate the organic matter partition coefficients from the acenaphthene retardation factors and column r_{sw} .

All pore velocities ($v=Q/nA$) were calculated based on the gravimetrically-determined total column porosity (n), the measured flow rate (Q), and a column cross-sectional area (A) of 3.8 cm². Thus, the reported velocities will be smaller than the mobile-water velocity, v_m , which is based on the water content of the mobile zone only and is used by researchers employing the 2-site model.

As shown by many authors, the first-order model rate constant can be interpreted in terms of an effective diffusivity if k_r is regarded as a lumped mass transfer parameter [2, 33, 40, 48, 56]. For example, Wu and Gschwend [56] deduced the following empirical relationship between the first-order and radial diffusion model parameters to evaluate batch desorption data:

$$k_r = (10.56 r_{sw} K_d + 22.7) \frac{D_{eff}}{\delta^2} \quad (4-8)$$

where D_{eff} is the effective diffusivity [cm^2/sec] and δ is the diffusion path length. The effective diffusivity is defined as the ratio of pore diffusivity to internal retardation factor.

Results and Discussion

Sorbent Properties. There is a striking color difference between the Georgetown sand and both PB and AJ. The GT sand is a deeply colored reddish-brown fine-grained sand, while both PB and AJ are less intensely colored orangish to yellow-brown. The second property of the GT sand which distinguishes it from the other two is its high proportion of very fine-grained material. In contrast to the colloid fraction of the PB sand, this fine GT material, however, does not remain suspended when the sand is immersed in water. The AJ sand is distinct from the other two sands in that it has high proportions of feldspar and mica which are readily observed in hand specimen. The mineralogy of AJ reflects the younger age of this sand and its glacial depositional history relative to the older and more winnowed GT and PB beach deposits. Further information on the PB sand is presented below with the description of the GT and AJ sands.

Grain Size and Organic Carbon. The GT sand is highly aggregated when dried and composed of predominantly >1000 micron aggregates. Disaggregation by sonication and wet-sieving caused significant increases in the 105-250 and <53 micron size fractions (Table 4-1). The AJ sand particle size distribution, in contrast, had little fine-grained material and was less affected by sonication and wet-sieving. However, the <53 micron fraction wt % did increase by a factor of 3 after sonication, thus indicating the presence of fine-grained coatings on the 250-1000 micron grains which make up 70 wt % of this sand. The organic carbon content of all three sands generally increased with decreasing grain size below 250 microns. The bulk GT sand organic carbon is about 2 times higher than that for bulk AJ and PB, but the <53 micron AJ fraction has an f_{oc} that is twice as high as either the GT or PB <53 fraction. The low f_{oc} of the GT <53 fraction could be due to the aggregated state of the dry-sieved material that was analyzed by CHN such that some of the <53

Table 4-1
Sorbent Size Fractions and Organic Carbon Content

Size Fraction [microns]	PB	GT	AJ
<u>DRY SIEVING WT %</u>			
>1000	21.5	51.96	2.52
250-1000	66.45	36.93	72.83
105-250	11.34	9.84	23.42
53-105	0.42	1.14	0.88
<53	0.31	0.13	0.36
<u>SONICATION/WET SIEVING WT %</u>			
>1000	21.2	5.01	3.18
250-1000	64.2	46.79	69.29
105-250	11.58	35.71	25.69
53-105	0.99	0.39	0.66
<53	2.12	12.10	1.19
<u>FRACTION ORGANIC CARBON % (1σ) (dry sieved)</u>			
bulk	0.057 (.005)	0.109 (.025)	0.066 (.004)
>1000	0.061 (.009)	0.088 (.022)	0.062 (.017)
250-1000	0.048 (.003)	0.057 (.016)	0.059 (.002)
105-250	0.111 (.012)	0.072 (.012)	0.090 (.006)
53-105	0.528 (.005)	0.560 (.109)	0.266 (.012)
<53	0.784 (.096)	0.648 (.049)	1.645 (.024)

organic matter remained distributed in the larger size fractions as coatings on large grains. For the aggregated GT sand, the wet sieving data give a better representation of the true grain-size distribution and indicates that the GT sand is in general finer-grained than both the AJ and PB sands.

Iron Content. The total iron content correlated with grain size in the same way that f_{oc} did: higher total Fe was found in smaller size fractions below 250 microns. TiCEB- and AOD-

extractable iron analyses in four subsamples (bulk, 250-1000, sonicated 250-1000 micron, and wet sieved <53 micron) indicated: (1) GT had the highest TiCEB-extractable surface iron content, followed by PB and AJ, (2) appreciable amorphous iron oxide was present in the bulk GT and AJ sands but not in bulk PB, and (3) higher AOD-extractable Fe was found in the <53 micron size fraction for all three sands (**Table 4-2**). These observations are based on the assumption that AOD extracts only amorphous oxides and TiCEB extracts both crystalline and amorphous iron oxides. The principle by which the TiCEB method works is reductive dissolution and Fe^{+2} complexation at neutral pH such that all crystalline and amorphous iron oxides are extracted [37]. The principle behind the AOD method is less clear although it has been shown that exposure to light is critical to the success of the method (i.e., only in the dark can dissolution of goethite be avoided) [41]. McKeague and Day [27] demonstrated that complexation with oxalate is more important than acid dissolution in the AOD technique. Thus, the AOD technique has been shown empirically to dissolve amorphous iron oxides when the extraction time is short (few hours).

The TiCEB/Total iron ratio indicates that surface iron oxides make up approximately 70% of the bulk GT iron content and about 30% of the < 53 wet-sieved fraction. The remaining iron is probably distributed in heavy minerals and clays (i.e., vermiculite, see below). In contrast, for bulk PB sand, approximately 25% of the total iron occurs as extractable surface species and this ratio is lower still in the AJ sand (12%). Based on the ratio of AOD/TiCEB iron, the amorphous iron oxide fraction in each subsample was calculated. In the GT sand, amorphous iron oxides, which XRD analyses cannot detect, comprise approximately 8% of the surface iron in the bulk sand and 17% of the <53 wet-sieved fraction. These ratios are 1.5 and 14 percent for bulk PB and <53 micron PB, respectively. The agreement in AOD/TiCEB ratio between GT and PB for the <53 micron wet fraction, but not for the bulk or 250-1000 micron fractions probably indicates AOD extraction of oxides such as ilmenite or pseudorutile in PB (see Ryan and Gschwend, [38]). Borggaard [4] showed that 2-hr AOD extractions were capable of extracting both amorphous iron oxides and magnetite, but not the clay minerals he examined (chlorite, glauconite, nontronite). Furthermore, we suspect that the highly weathered oxide phases in PB would be more susceptible to the low pH AOD treatment than the relatively "clean" minerals used by Borggaard [4].

The bulk AJ sand iron content is much lower than that in either the GT or PB bulk sands. The near equivalence of the AOD and TiCEB extractable iron contents in the AJ bulk and 250-1000 micron fraction indicates that either (1) essentially all of the surface iron in AJ is amorphous iron oxide, or (2) the low pH of AOD extraction dissolved some of the Fe-rich clay and oxide minerals such as biotite, chlorite and magnetite. We found

Table 4-2
Sorbent Iron Concentrations ($\mu\text{mol/g}$)

Size Fraction [microns]	PB	GT	AJ
<u>Total Fe (digestion)</u>			
bulk	240	267	34
>1000	146	145	96
250-1000	119	178	22
105-250	384	131	67
53-105	1155	617	632
<53	1643	481	582
sonic >250	6	10.3	NA
sonic <53 wet	1238	1563	NA
<u>TiCEB-extractable</u>			
bulk	59	189	4.2
>1000	NA	65	NA
250-1000	36	103	3.7
105-250	NA	71	9
53-105	NA	531	12
<53	NA	713	71
sonic 250-1000	5	3.3	2.2
sonic <53 wet	430	490	132
<u>AOD-extractable</u>			
bulk	0.9	16	3.9
>1000	NA	16	NA
250-1000	0.6	11	2.4
105-250	NA	15	10
53-105	NA	71	18
<53	NA	88	103
sonic 250-1000	0.01	0.01	2.7
sonic <53 wet	61	85	305

NA= not analyzed.

Table 4-2 continued
Calculated Iron Fractions (%)

	PB			GT			AJ		
	bulk	250-1000	<53 wet	bulk	250-1000	<53 wet	bulk	250-1000	<53 wet
Total Surface Fe =(TiCEB/Total Fe)*100	25	30	35	71	58	31	12	17	23‡
Amorphous Total Fe = (AOD/Total Fe)*100	0.4	0.5	5	6.0	6.2	5	12	11	52‡
Amorphous Surface Fe = (AOD/TiCEB)*100	1.5	1.7	14	9	11	17	93	65	230

‡ <53 micron dry sieve fraction.

magnetite in our AJ 53-105 micron size fraction and believe that dissolution of magnetite during the AOD extractions explains why significantly higher AOD iron concentrations were found in AJ fraction < 53wet relative to TiCEB-extracted iron. Since XRD data on the AJ <53 wet and AJ <2 micron clay fractions lacked peaks for any crystalline iron oxide phases (see Figure 4-4 below), we believe that the abundant AJ iron oxide staining observed in thin section was amorphous iron oxide. The remaining non-surface iron measured in the total digestions of the AJ size fractions was probably from magnetite, ilmenite and clay minerals (chlorite and biotite).

Mineralogy and Texture.

PB. The bulk PB sand was thoroughly characterized by Ryan and Gschwend [38]. The Pine Barrens sand is composed of quartz (95%), kaolinite, goethite and trace ilmenite. Texturally, the predominantly 250-1000 micron diameter quartz grains are coated with kaolinite and goethite. The coatings are discontinuous and vary in thickness from 0 to 50 microns (**Figure 4-1**). Fine-grained matrix material, of similar composition to the coatings on quartz, occurs as patches between the quartz grains in the bulk PB sand. Ryan and Gschwend [38] estimated that coating and matrix made up 15% by volume of the bulk

sand. The experiments reported in Chapter 2, and reported here for comparison with the AJ and GT bulk sands, were performed on PB sand from which the fine-grained matrix was removed by sieving in order to give a more homogeneous sorbent with well-characterized path lengths. Thus, the coatings make up a much smaller volume percent (about 2%) of the PB size fraction we tested.

GT. SEM/EDX, XRD and petrographic observations show that the GT sand is composed predominantly of quartz (>95%; 100-1000 microns) with fine-grained kaolinite, vermiculite, gibbsite and goethite. The quartz grains are rimmed with abundant reddish-brown matrix/coatings which are discontinuous around a single grain but are up to 200 microns thick (**Figure 4-2**). SEM/EDX observation of the fine-grained coatings and matrix materials, defined as occurring around and between quartz grains, respectively, indicates that the grains within the matrix/coating are predominantly <1 micron in diameter and are composed of Fe, Al and Si, presumably a mixture of fine-grained kaolinite, gibbsite and goethite that could not be resolved with the SEM. The GT sand also contains minor large (250 micron) feldspar grains which have a dusty appearance in thin-section due to the presence of fine-grained alteration products (i.e., kaolinite). We also note that Fe was present in every EDX spectrum from the GT sand, indicating that iron oxide was coating even quartz surfaces that visually appeared to be free of coating material.

AJ. In contrast to the other two sands, the large grains in the Aberjona sand are more mineralogically heterogeneous and contain abundant feldspar (K-feldspar and plagioclase) in addition to quartz and mica (muscovite and biotite). Some of the sand grains are fragments of granite (**Figure 4-3**). In general, the plagioclase grains are highly altered, giving a dusty appearance in thin section. The feldspars are also fractured. Both quartz and feldspar grains have isolated fine-grained orange-brown coatings in the embayments of the larger grains. EDX analysis of these coatings shows they contain abundant Si, Al and Fe. In the <53 micron size fraction, XRD analysis identified quartz, mica, chlorite, and kaolinite. Ilmenite (AJ bulk), rutile (53-105 micron fraction) and weathered apatite (<53 micron fraction) were also identified by SEM/EDX. No crystalline iron oxide was identified by X-ray diffraction in the AJ sand, although both GT and PB had detectable goethite peaks in the < 53 wet fraction (**Figure 4-4**). The AJ <2 micron clay fraction XRD trace had chlorite, mica and kaolinite peaks, but no crystalline iron oxide either.

Porosity. For each sorbent three mercury porosimetry measurements were made. We analyzed the bulk sand, the 250-1000 micron size fraction and the 250-1000 micron size fraction after sonication and wet-sieving. The sonicated 250-1000 sample was compared to

Figure 4-1 (next page). Pine Barrens 250-1000 micron fraction SEM micrographs. Q=quartz, C=coating. (a) low magnification (145x). Large quartz grains with fine-grained coatings (surface pits on Q are due to poor polishing. (b) 709x. Surface of quartz grains after sonication showing surface pores up to 10 micron size and absence of fine-grained coating. (c) Back-scattered electron (BSE) image, 1500x. Close-up of 50 micron thick fine-grained coating composed of Fe, Al, and Si, on edge of quartz grain. (d) 994x. BSE image of coating on quartz.

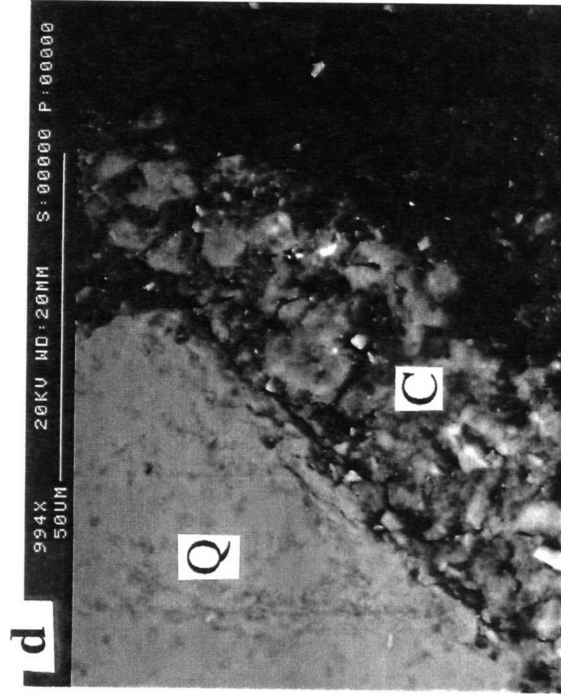
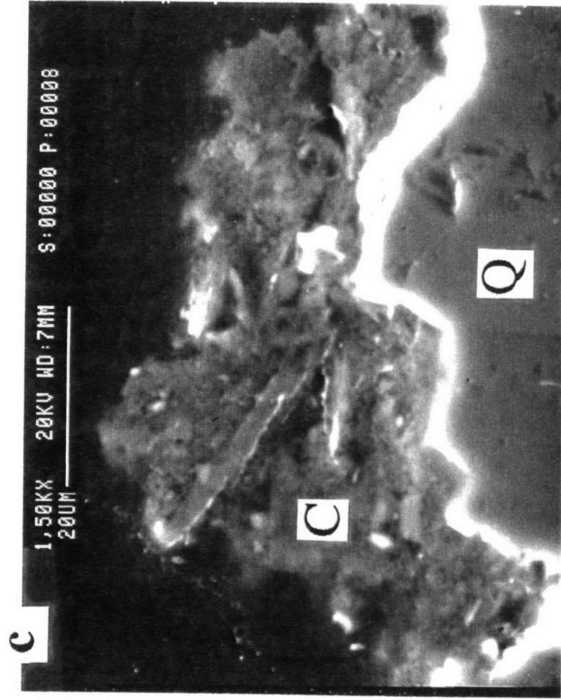
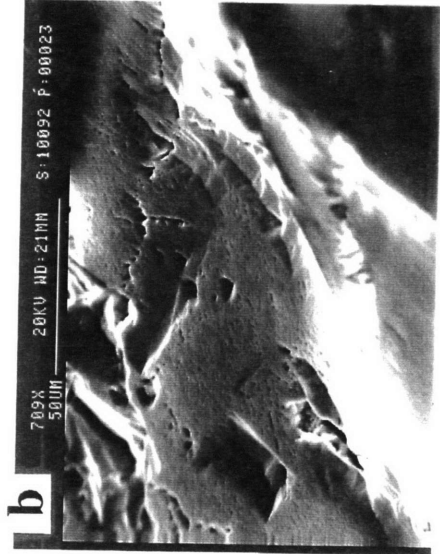
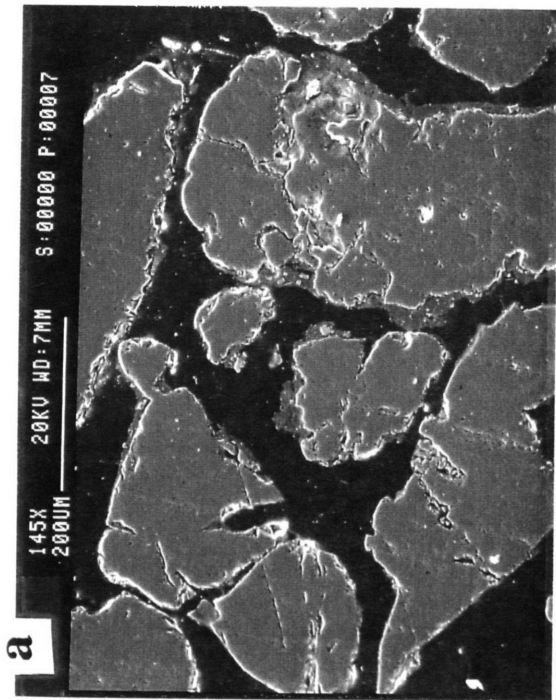


Figure 4-2 (next page). Bulk Georgetown sand micrographs. (a) 34.2x. BSE image of aggregates of bulk GT sand up to 1 mm diameter. (b) 133x. Close-up of aggregate showing large quartz grains and Fe, Al, Si-rich matrix between the quartz grains. (c) 412x. Matrix material that is >200 microns at widest point and includes many quartz fragments. (d) 1590x. Close-up of Spurr's-embedded matrix showing generally fine-grained nature of matrix material.

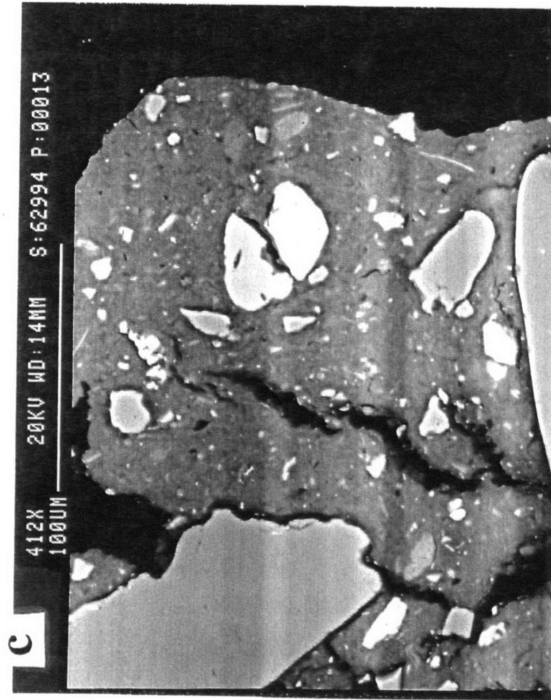
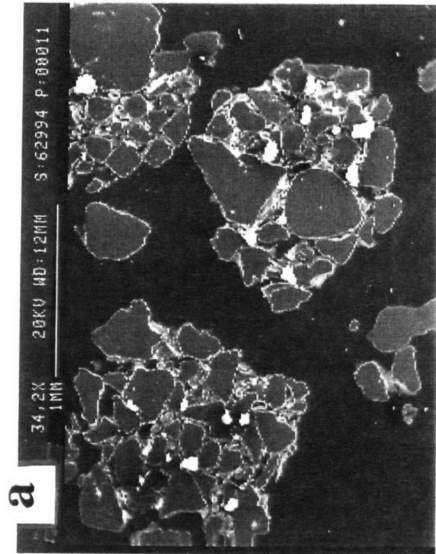
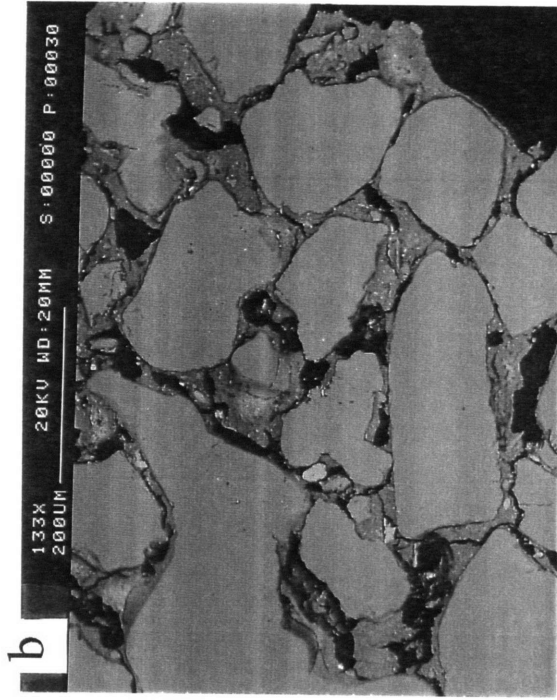


Figure 4-3 (next page). Bulk Aberjona sand micrographs. (a) 34.2x. Low magnification of bulk AJ sand shows lack of appreciable fine-grained material. (b) 443x. Fragment of granite is composed of quartz (**Q**), Ca-plagioclase (**P**) and biotite (**B**). Note the highly altered texture of the plagioclase relative to quartz. (c) 2970x. Fine-grained coating in K-feldspar (**K**) embayment up to 20 microns thick. (d) 632x. Surface of K-feldspar showing porous nature and abundance of fine-grained alteration products.

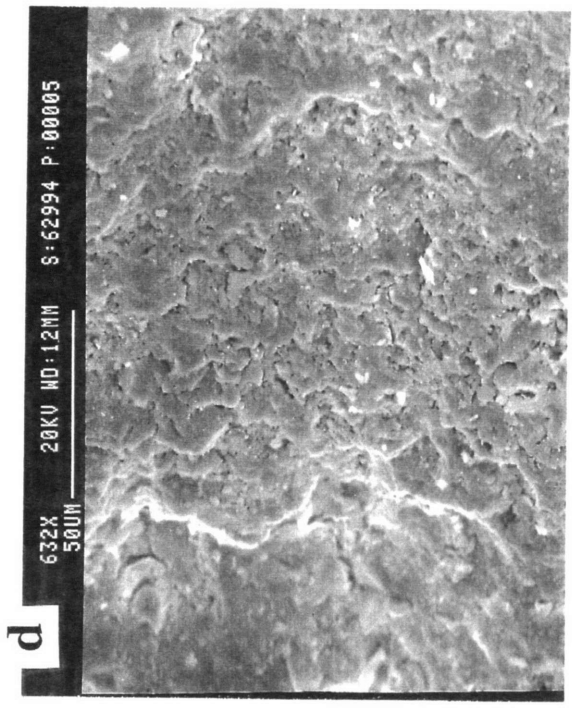
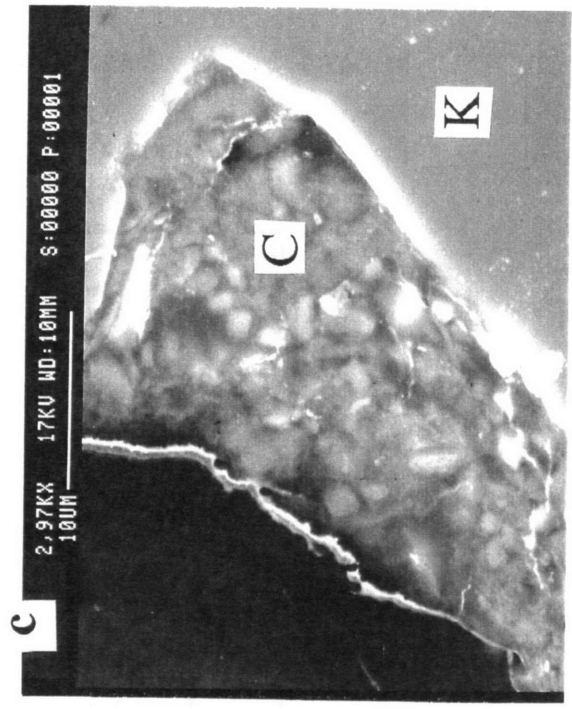
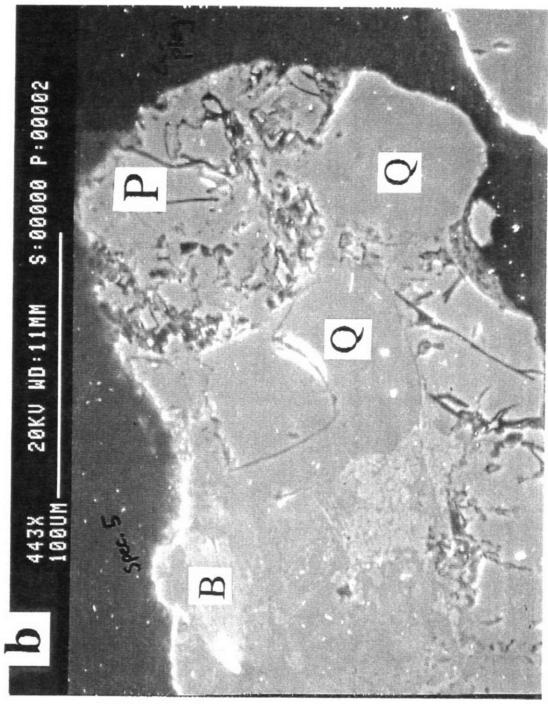
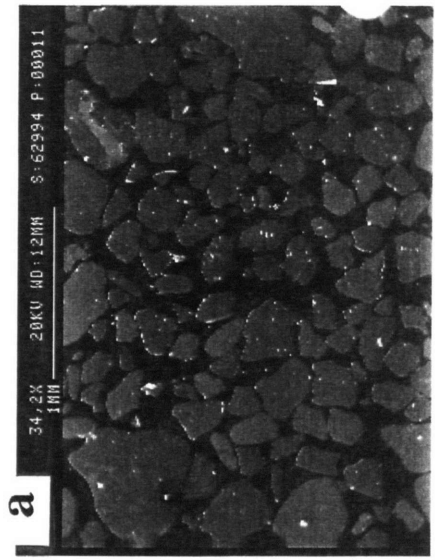
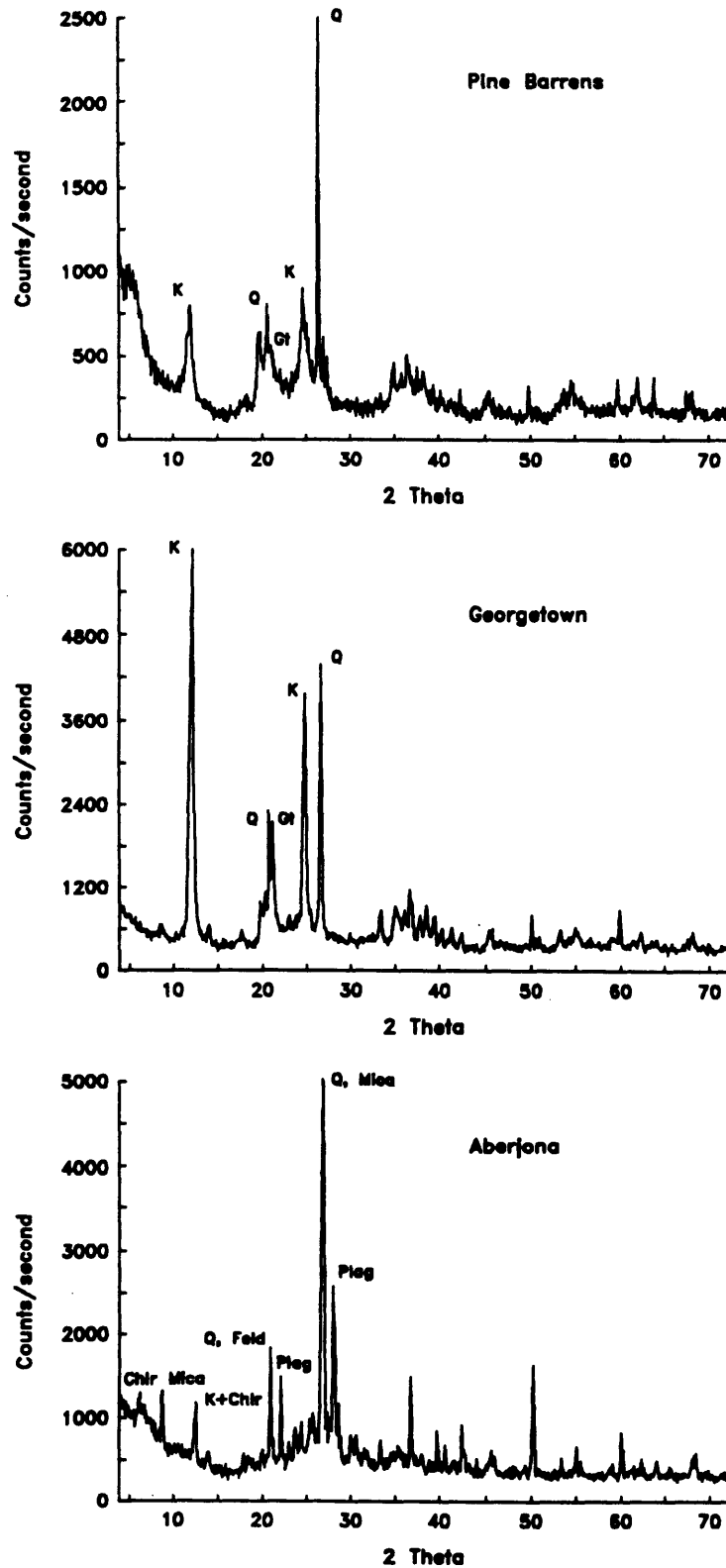


Figure 4-4. X-ray diffraction patterns for < 53 micron wet-sieved size fraction for the (a) PB, (b) GT and (c) AJ sands. Note the presence of goethite (Gt) peaks in the PB and GT sands but the absence of these peaks in AJ. Q=quartz, K=kaolinite, Chlr = chlorite, and Plag = plagioclase.



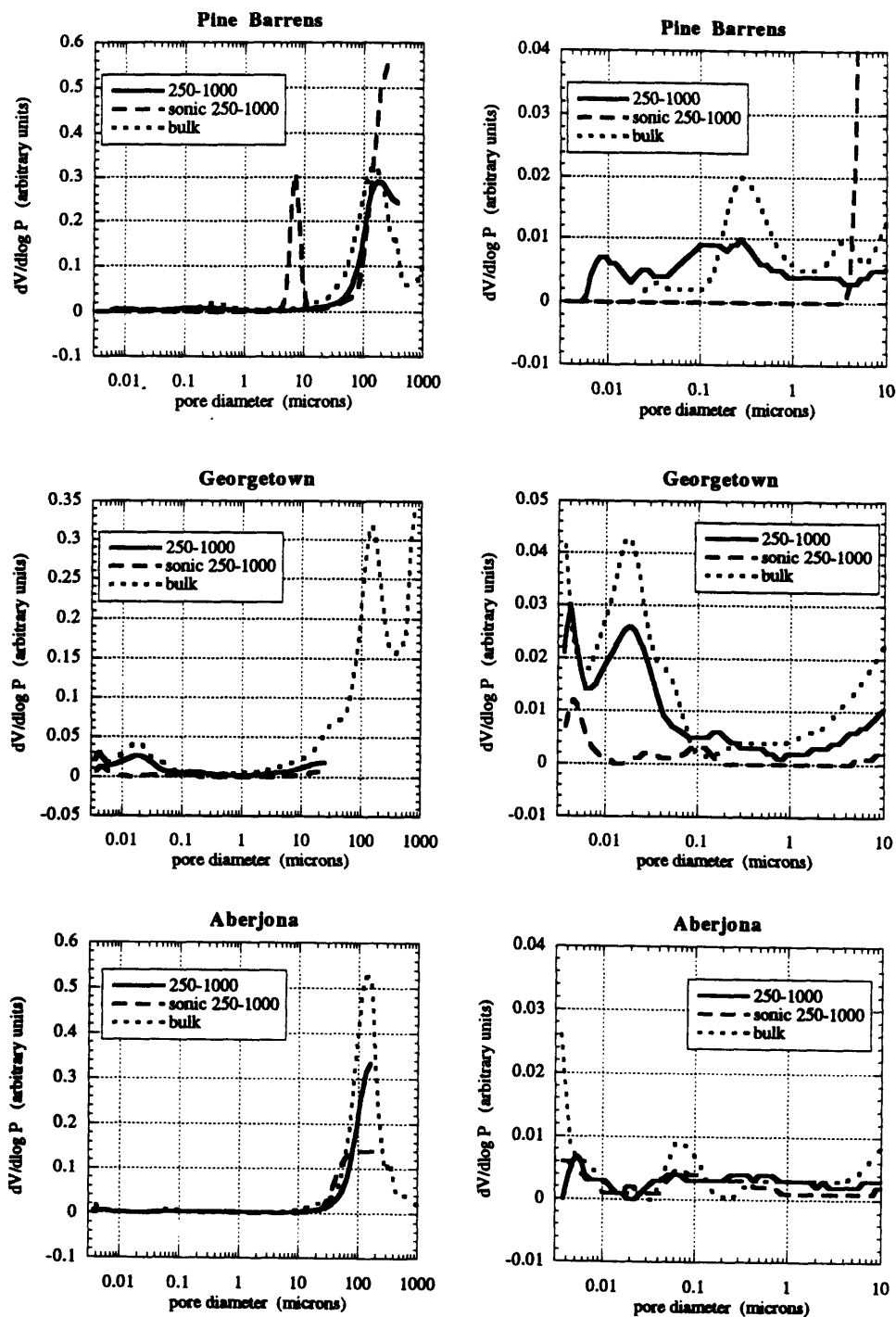
the unaltered 250-1000 sample to quantify both the porosity of the fine-grained iron-oxide coatings on the primary mineral grains and the internal porosity of the quartz and feldspar. The pore size nomenclature outlined in **Table 4-3** is based in part on Gregg and Sing [19]. Percent of pores within a certain size range were calculated from the cumulative mercury intrusion data. It is important to recognize that the sand sample used for Hg porosimetry analysis is air-dried prior to measurement. Thus, since drying could alter the pore sizes, the true pore diameters for aqueous conditions could be significantly different from those measured. Furthermore, the mercury intrusion technique quantifies the sizes of pore necks (narrow entrances to larger pore bodies) since larger pores are filled first (at low pressures) and smaller pores are intruded only under higher mercury pressures [14, 19]. Due to this limitation on determination of absolute *in situ* pore sizes, we focus on relative comparisons of pore size distributions among the three sorbents.

The three sands had very different pore size distributions which reflect their different textures and mineralogy. The PB sand (**Figure 4-5a**) had no internal pores in quartz, but had indentations on the quartz grain surfaces which contributed macroporosity (**Table 4-3**; see **Figure 4-1b**). We propose that the coated vs. uncoated PB results indicate that the kaolinite and goethite matrix filled these exterior pores in such a way that the fraction of macropores decreased from 27% to 8% in the presence of coatings.

Mercury porosimetry analyses indicated appreciable mesoporosity (20-500 Å) in the 250-1000 micron coated GT sand grains. There was also appreciable intragrain porosity in the sonicated GT sand which most likely occurs within the weathered feldspar grains and in some quartz grain fractures. The most abundant intragrain pores are between 0.003 and 0.005 microns diameter. The GT coating material increased the total porosity appreciably (50%), contributing to both the meso- and macropore fractions. The bulk GT sand had appreciable interparticle porosity due to the aggregated nature of the dried GT sand. The bulk also has an important 0.006 to 0.05 micron pore population due to pores in the fine-grained matrix material (**Figure 4-5b**).

Sonication had little effect on the AJ pore size distribution (**Figure 4-5c**), an observation which reflects either (1) the low abundance of fine-grained coating material, (2) the coatings were not removed by sonication, or (3) the coatings do not contribute significantly to the coated sample porosity, instead the primary grains are porous. Since the PB and AJ bulk sands showed similar changes in weight distribution after sieving, it is unlikely that the coating abundance was too low to see an effect in the porosity data. In addition, unlike the PB and GT sand 250-1000 micron fractions, the AJ fraction did not change color appreciably with sonication, thus we surmise that the AJ coatings were not completely removed by sonication. This may have been a function of the coatings being

Figure 4-5. Mercury porosimetry data for the 250-1000 micron sieve fraction, sonicated 250-1000, and bulk sample of the (a) PB, (b) GT and (c) AJ sands. Graphs on the left-hand side cover the entire pore size range and graphs on the right are close-ups of the 0.003 to 10 micron pore diameter range.



located in protected embayments in the AJ sand, or due to differences in iron oxide composition among the three sands. The amorphous iron oxide in the AJ sand may be more resistant to mechanical stresses than the more crystalline iron oxides in GT and PB. The observed fractures in quartz and feldspars probably also contributed significantly to the porosity in the AJ sand (see Figure 4-3b). The bulk AJ pore size distribution was very similar to the 250-1000 fraction's with the addition of very small diameter pores (0.003-0.006 and 0.03-0.15 microns). These pores probably reside within weathered mineral grains of the smaller sieve size fractions.

Table 4-3
250-1000 Micron Size Fraction Sorbent Porosity
Percent of Total Porosity in Pore Size Range

Pore Size Range [microns]	PB		GT		AJ	
	<u>sonic</u>	<u>coated</u>	<u>sonic</u>	<u>coated</u>	<u>sonic</u>	<u>coated</u>
<i>mesopores</i> 0.003-0.05	0	2.2	12.5	35.8	2.7	2.6
<i>macropores</i> 0.05-20	26.5	7.6	10.7	20.2	5.7	7.1
<i>interparticle</i> 20-400	73.5	90.1	76.8	44.0	91.6	90.4

Summary The three sands we examined are distinctly different in terms of (1) abundance of fine-grained, Fe- and organic carbon-rich, matrix material; (2) iron oxide composition, and (3) distribution of porosity; all factors which may influence the rate of sorption. The PB sand porosity is restricted to the iron-oxide coatings on quartz. In GT, much smaller pore sizes are present than found in PB and they are found in both the matrix/coatings and altered feldspar. For the AJ sand, we were unable to determine which type of sorption sites (coatings or intramineral) contributed more to the total porosity because, unlike PB and GT, the AJ coatings were not completely removed by sonication.

Based on the sorbent characterization we carried out, the sorption behavior of these three sands can be summarized in terms of a general aquifer sand sorption site model (Figure 4-6). There are three possible sorption regimes in the sand model:

- (I) high f_{oc} , iron-oxide and kaolinite coatings that rim the primary mineral grains (quartz and feldspar).
- (II) high f_{oc} , fine-grained matrix material found between the large grains.
- (III) intramineral voids and fractures within weathered primary silicates (feldspar, mica) and possibly weathered oxides (magnetite, rutile).

In terms of this sand model, the PB, GT and AJ sorption regimes are summarized in the following table (**Table 4-4**) on the basis of the sand descriptions. It is important to note that all three sands showed a strong correlation between organic matter content and iron content (**Figure 4-7**). This association of organic matter with iron-rich surface phases (i.e., TiCEB- and AOD-extractable) means that potential organic matter sorption sites will be located on the exterior surfaces of mineral grains in these coated aquifer materials. Thus, unless the organic matter is concealed within these oxide coatings, sorption to these sites should be rapid. Pignatello [30] pointed out, however, that shielding of organic matter by minerals can lead to sorption rate limitations. Thus, we expect sorption rate to be both a function of the pore structure of the sorption regime as well as the availability of organic matter within each regime. The pore structure will affect the ease of solute diffusion through the regime by affecting tortuosity and constrictivity properties, and the availability of organic matter sorption sites will affect the local retardation factor within each regime.

Table 4-4
Sorption Regimes Model Summary for 3 Sands

Sand	Description [†]	Type of Sorption Regimes
PB 250-1000	G and K coatings on Q; no internal Q porosity	I only
GT bulk	abundant G+Gb+K matrix; some weathered F	chiefly II, minor III
AJ bulk	coatings in embayments; weathered F and M	I, III

[†] G=goethite, K=kaolinite, Gb=gibbsite, Q=quartz, F=feldspar, M=mica. Sorption regime categories are depicted in Figure 4-6.

Figure 4-6. Aquifer Sand Sorption Regimes Model. Three distinct types of sorption sites are defined based on the texture of these iron-oxide coated sands.

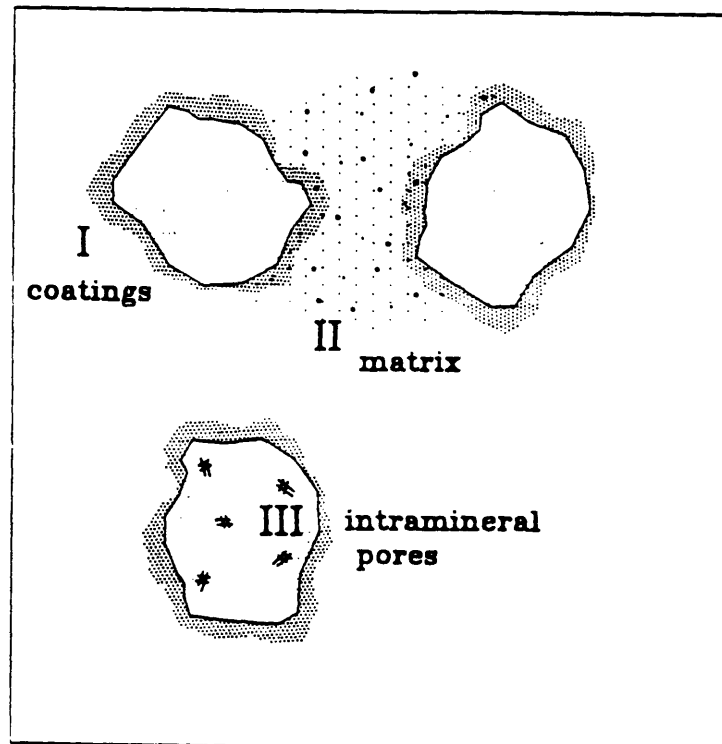
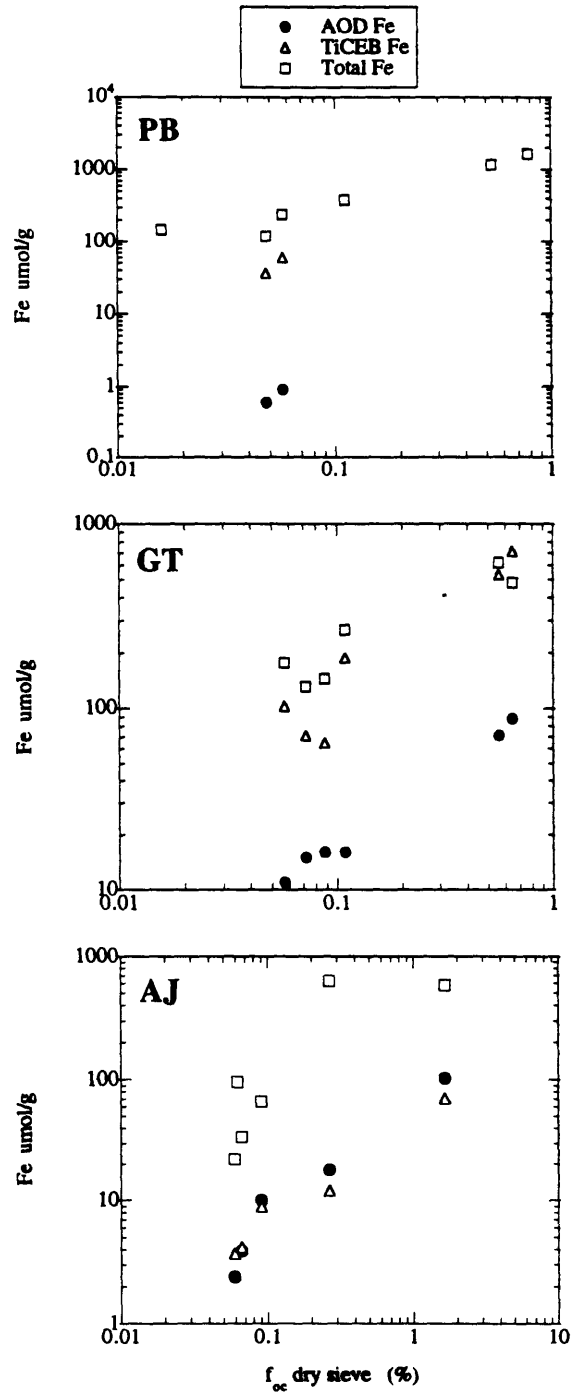


Figure 4-7. Iron ($\mu\text{mol/g}$) and organic carbon (f_{OC} of dry sieve size fractions) relationships in three sands. (a) PB, (b) GT, (c) AJ.



Batch Experiments

Georgetown. The GT batch kinetics experiment showed that equilibrium acenaphthene uptake was reached within 160 minutes and gave an apparent K_d value of 0.97 mL/g (\pm 0.07, 1σ) (Figure 4-8a). This K_d value is three times smaller than the K_d value of 3.7 one would predict from K_{oc} ($10^{3.53}$) and the sorbent f_{oc} (0.11%) using the organic partitioning model $K_d = K_{oc}f_{oc}$. These results may indicate that there was an organic carbon component that remained inaccessible to the sorbate over the 30-day incubation period, or the sand in the batch tubes had a lower f_{oc} than the subsample used for CHN analysis. Neither of these possibilities can be ruled out at present.

The batch isotherm for acenaphthene sorption to the GT sand was linear (Figure 4-8b) and the partition coefficient was 0.65 mL/g (SE = 0.03). Fitting the isotherm data with the nonlinear Freundlich model, $S = K_f C^n$, resulted in $K_f = 0.55$ (SE = 0.37) and $n = 1.03$ (SE = 0.11) thus confirming the linear nature of the isotherm.

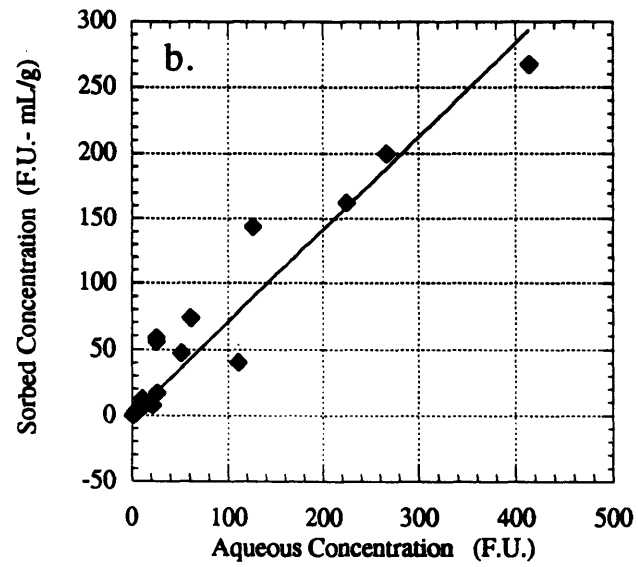
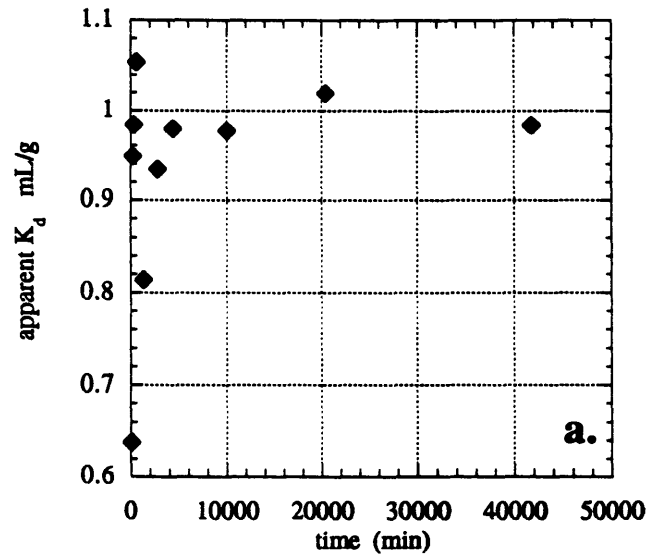
It should be noted that both of the GT batch experiments achieved a much lower fraction of sorbed acenaphthene (22-25%, relative to controls) than the experiments were designed to achieve (50%). The discrepancy between the batch kinetics and batch isotherm K_d values may reflect increased acenaphthene sorption to the vial walls during the isotherm experiment since positive controls showed appreciable (up to 10%) changes in acenaphthene concentration over the 4 day incubation period. This may have been caused by drying the isotherm vials in an oven at 100° C prior to use whereas all other batch test vials were air-dried.

We performed a second batch isotherm experiment with a sample of pulverized bulk GT sand that was also analyzed for organic carbon content. The K_d value for this isotherm was 0.86 ± 0.09 (SE) mL/g and the f_{oc} was 0.05%. This K_d is still 2 times lower than $K_{oc}f_{oc}$ (=1.7 mL/g). The K_d values of the pulverized isotherm and kinetics experiments give an average Georgetown sand K_d of 0.92 mL/g. Methanol extraction of the sediment in four vials of the pulverized isotherm experiment gave recoveries of 96 to 100%.

From the batch kinetics K_d value and the solid-to-water ratio in our column, we calculate an expected retardation factor for the column of 7.6. The pulverized isotherm K_d value gives an expected R of 6.8.

Aberjona. The batch kinetics experiment with the AJ sand showed an unusual behavior: at early times (<10000 min) the apparent K_d increased quickly and leveled off at a value of 0.52 ± 0.11 (1σ) mL/g. After 10,000 min the apparent K_d again increased and did not appear to reach equilibrium after 20 days (Figure 4-9a). The 20-day apparent K_d was 2.6 (1.39, 1σ , $n=2$) although there was appreciable scatter at this time point. Based on the

Figure 4-8. Georgetown batch (a) kinetics and (b) isotherm



organic carbon content of the AJ sand, the expected equilibrium partition coefficient is 2.2 and this value is approached by the 20 day time point. The 4-day AJ batch isotherm (**Figure 4-9b**) was linear with a slope of 3.2 (SE = 0.10). The calculated retardation factors we expect for acenaphthene in the Aberjona column are 4.5 based on the early plateau in the kinetics experiment and 22.6 based on the isotherm K_d .

In summary, acenaphthene batch uptake was slower in both GT and AJ than for PB. This could reflect the more fragile nature of the PB coatings which are easily dispersed in solution, or the presence of smaller pore sizes and intramineral porosity in GT and AJ. These issues will be discussed further in the Sorbent Comparison section.

Column Experiments.

Georgetown. Acetone was used as the conservative tracer with the GT sand because initial runs with nitrate showed some nitrate holdup relative to acetone for this sand, probably due to ion-exchange with clay minerals. Due to the pronounced tails on the conservative tracer elution curves at high velocities, the BTCs for the GT sand were not all truncated at the same pore volume. Instead, the acetone data represent collection of a minimum of 4 pore volumes of effluent up to 25 pore volumes at the highest flow rates. Similarly, at least 8 pore volumes of effluent was collected during the acenaphthene experiments at low velocities and up to 60 pore volumes were collected at the higher flow rates. The experiments were stopped when fluorescence measurements on the effluent indicated recovery of at least 85% of the injected acenaphthene.

a. BTC shape and flow rate. The acetone elution curves were asymmetric with long tails and the initial breakthrough pore volume decreased with increasing flow rate (**Figure 4-10**). Both of these observations indicate that appreciable physical nonequilibrium governed acetone transport in this sorbent. The texture of this sand as described above is consistent with the observed BTC characteristics. The abundant fine-grained matrix/coating patches with small diameter pores are likely immobile water domains. At high flow rates, water in the larger pores does not have time to equilibrate with these immobile water regions and the result is acetone elution at an early pore volume with a long tail due to slow mass transfer of some acetone molecules with the immobile water. The pore volume of elution of acetone's peak maximum, PV_{cmax} , decreased with increasing pore velocity and approached one pore volume for the slowest velocity experiment.

Additional evidence for slow mass transfer with immobile water regions in the GT sand was the presence of shoulders on acetone peaks for experiments conducted at higher flow rates (see **Figure 4-10** curve @ 0.078 mL/min). The shoulder presumably

Figure 4-9. Aberjona batch (a) kinetics and (b) isotherm.

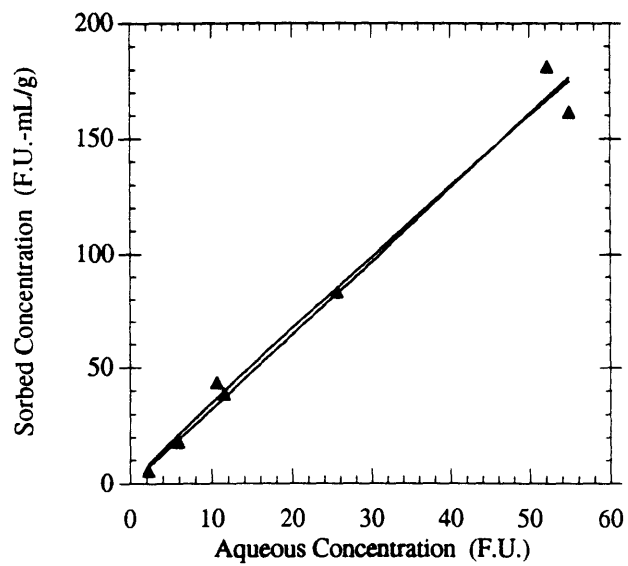
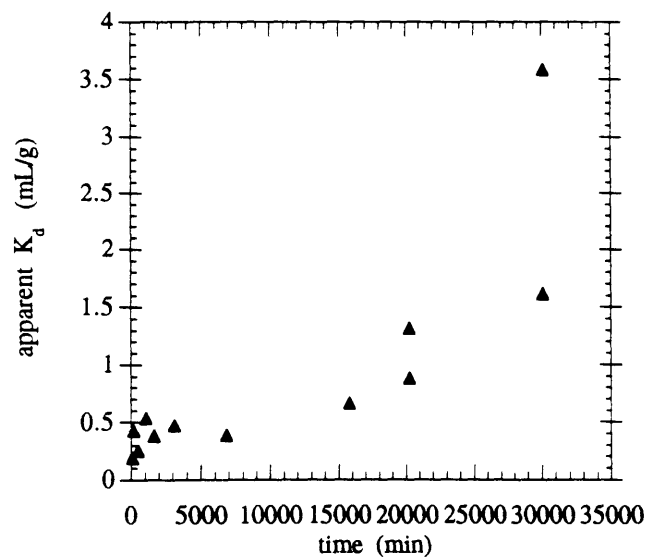
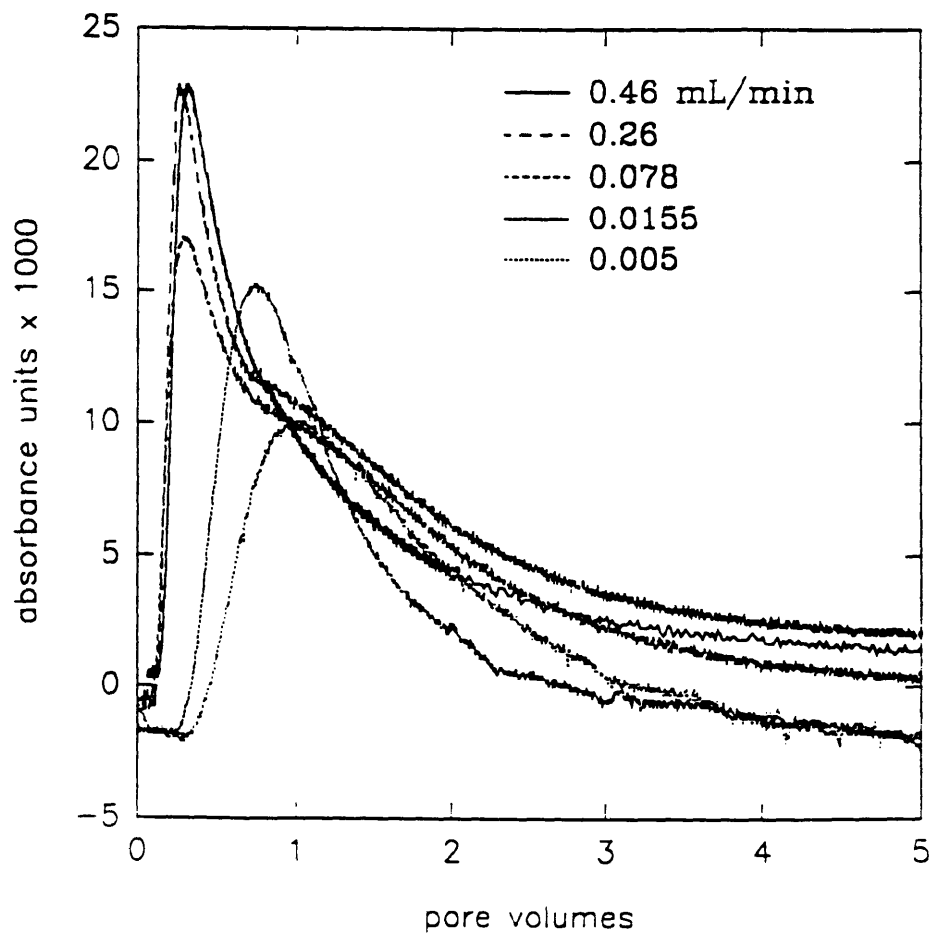


Figure 4-10. GT-acetone elution curves at 5 flow rates.

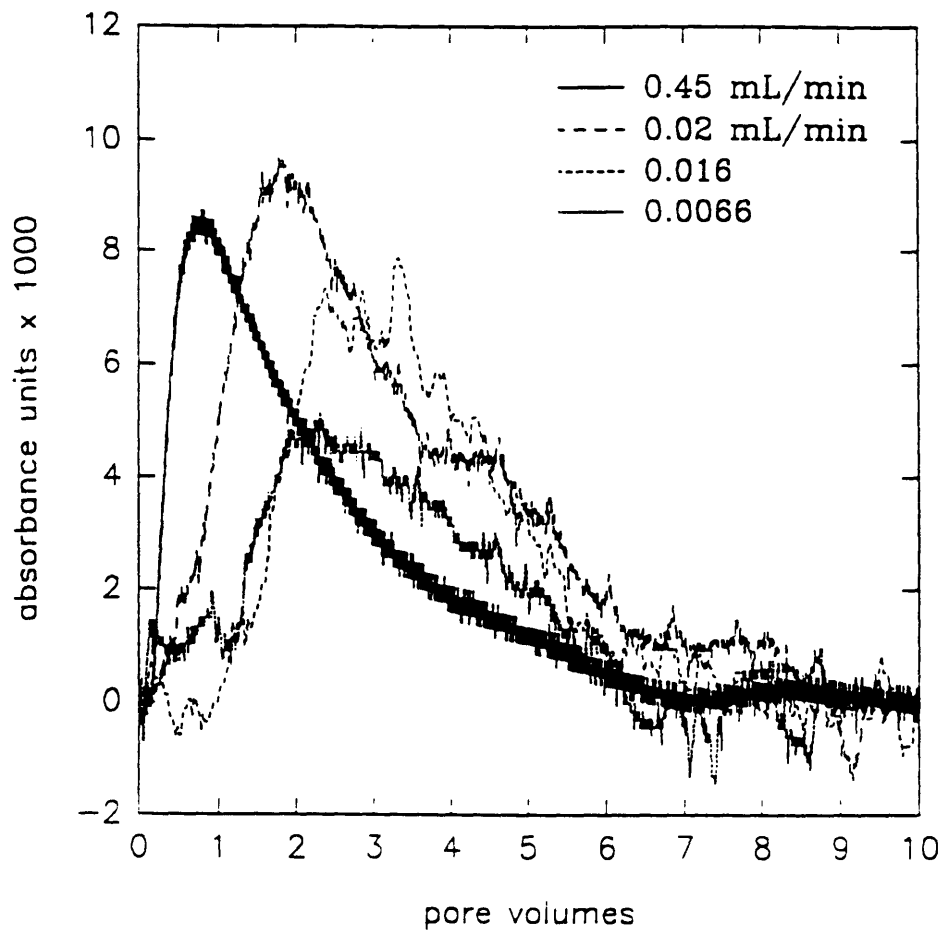


develops at a certain flow rate where the advection and mass transfer rates are of similar magnitude such that solute molecules distribute themselves between the two regions in a manner that allows some separation of the residence time distributions of the solute populations sampling each regime. At higher velocities, acetone transport is dominated by advection in the mobile zone and the peaks elute at less than one pore volume. At lower velocity, the immobile region contribution to the overall holdup increases and the shoulder merges with the mobile zone peak to give a broader peak that elutes later and closer to one pore volume. Villermaux [51] modeled such behavior for packed-column gas chromatography using a 2-site kinetic exchange model.

In the absence of immobile water, a conservative tracer peak should elute at one pore volume and its dimensionless first moment, PV_{u1} , should also occur at one pore volume. Neither of these criteria were met for acetone in the GT column, therefore we conclude that the asymmetrical acetone peak shape is due to the presence of abundant stagnant water in the GT sand. Other processes that could cause the peak asymmetry are channeling, preferential flow paths and slow sorption kinetics. Since it is unlikely that acetone sorbed to this sand and column repacking showed no change in elution curve shape, the observed asymmetry is attributed to slow exchange of acetone with the immobile water in the fine-grained matrix/coatings.

The GT-acenaphthene BTCs also shifted with pore velocity and were asymmetrical (**Figure 4-11**). The peak maximum approached 2 pore volumes as the flow rate decreased and the dimensionless first moment eluted at approximately 2.2 pore volumes at the slowest flow rates. The tailing on the acenaphthene BTC can result from both physical nonequilibrium and slow sorption. The rate parameter (k_r) derived from the acenaphthene second moment fit to the single-site model will quantify whichever mass transfer process is slower, diffusive mass transfer to immobile water or sorption kinetics. If the acetone and acenaphthene rate parameters are of the same magnitude (after correcting for differences in aqueous diffusivities), we conclude that the sorption "reaction" rate is fast relative to mass transfer. On the other hand, if the acenaphthene rate is much slower than that for acetone, we surmise that the sorption "reaction" step for the sorbate contributed to the slower overall transfer rate. The third possibility, that the acenaphthene rate is faster than the acetone mass transfer rate, is highly unlikely because the aqueous diffusivity of acenaphthene is smaller than that of acetone ($D_{\text{acetone}}/D_{\text{acenap}} = 1.66$), a fact that would make acenaphthene's rate of transfer to immobile water slower than that for acetone. Also, if retarded radial diffusion into the matrix material is the appropriate sorption mechanism in the GT sand, the effective diffusion coefficient for acenaphthene should be further reduced by a factor of R_{matrix} .

Figure 4-11. GT-acenaphthene elution curves at four flow rates.



b. Moment Curve Fits. The first absolute moments of the GT-acetone BTCs plotted against inverse velocity (**Figure 4-12a**) give a slope equal to LR. Assuming $L=7$ cm, the acetone data give an acetone retardation factor of 1.58 ± 0.09 . The acenaphthene first moment fit to inverse velocity (**Figure 4-12a**) gives an acenaphthene retardation factor of 2.16 ± 0.15 . This value is about 4 times smaller than the R value predicted from the batch kinetics K_d value.

For aggregated media such as GT, the dispersion coefficient may be significantly affected by axial diffusion in addition to hydrodynamic dispersion at low pore velocities [6]. We determined however that axial diffusion did not contribute significantly to dispersion in our experiments which were conducted over a range of flow velocities such that the velocity-dependent dispersion term was at least a factor of five greater than the molecular diffusion term. Assuming $D = \alpha v$, where α is the dispersivity in cm, the second moment fit for acetone (**Figure 4-12b**) gives a dispersivity value of 0.56 ± 0.09 cm, a value that is large compared to the mean grain size in the column, and indeed is equal to one-fifth of the column diameter. Large dispersivity values may indicate a wide range of pore velocities within the column or nonuniformity of pore diameters which contributes to increased dispersion [14]. Roberts et al. [35] observed that inhomogeneous aggregated soils may have a wide range in hydraulic conductivities (depending on variations in flow path) which contributes excess dispersional spreading relative to homogeneous sand packs. Han et al. [20] examined the effect of particle size distribution on dispersion. They found larger dispersion coefficients for wider particle size distributions when the maximum to minimum grain diameter ratio was about 7, but no difference in dispersion between a uniformly sized bed and one where $\text{max}/\text{min}=2$ for the same mean particle diameter in all three cases. Carbonnell [9] also noted that the "spread of the pulse is greatly magnified" as the pore size distribution standard deviation increases. Rao et al. [32] examined dispersion in aggregated media using a pore velocity distribution rather than an average velocity to model the behavior of tritium or methanol in two soils. They found that model BTCs based on a single average velocity showed less dispersion than the BTCs constructed using a wide range in pore velocities.

Therefore, we conclude that the large dispersion coefficient we determined for the GT sand is reasonable in light of the much wider pore size distribution in this column relative to that for the Pine Barrens column (see **Figure 4-5**) we studied previously.

The first-order model acetone rate parameter derived from the second central moment fit (**Figure 4-12b**) is $0.38 \pm 0.16 \text{ hr}^{-1}$. Similarly we calculated the first-order mass transfer rate for acenaphthene as $0.16 \pm 0.06 \text{ hr}^{-1}$, and a best-fit dispersivity value

Figure 4-12. Georgetown moments versus $1/\nu$. (a) First absolute moment, (b) second central moment.

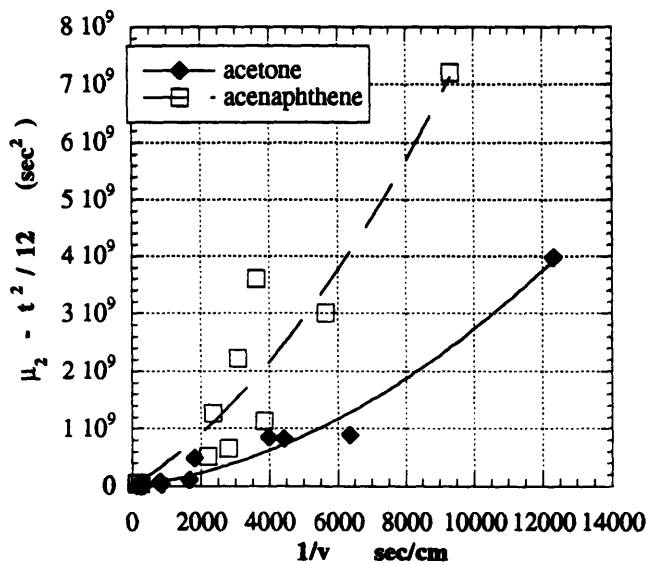
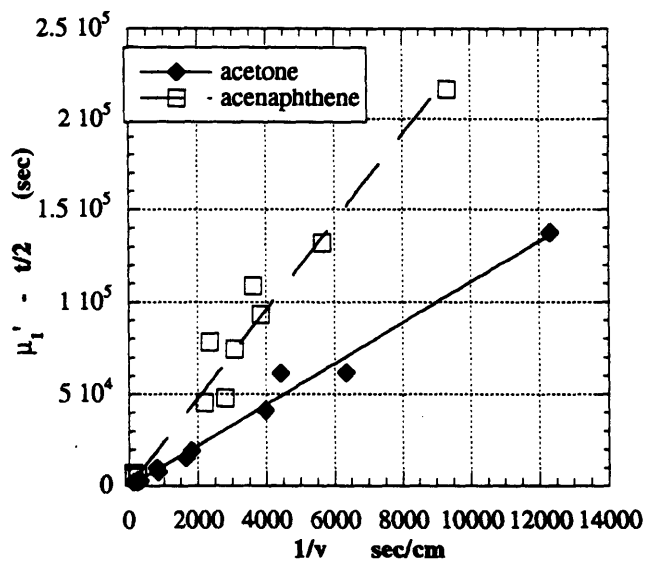
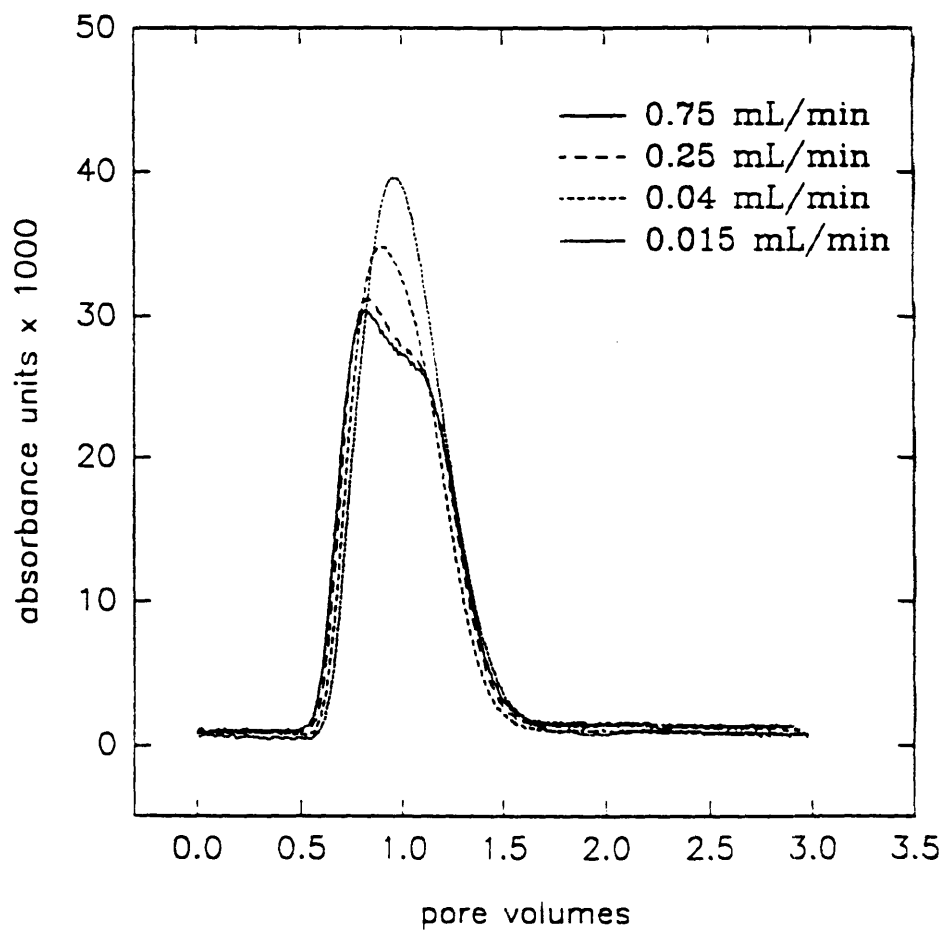


Figure 4-13. AJ-acetone elution curves at four flow rates.



derived from the acenaphthene data that agreed well with the acetone value (0.64 ± 0.31 cm). The acetone and acenaphthene k_r values are not significantly different from each other in this sand. We suspect that the small difference in aqueous diffusivity (40%) between acetone and acenaphthene cannot be distinguished by fitting the moments data. Due to the near equivalence in mass transfer rates, we also conclude that the rate of sorption is fast relative to diffusive mass transfer (i.e., physical nonequilibrium is rate-limiting). Alternatively, it is possible that acenaphthene was not sorbed significantly by the immobile regions and this explains why PNE controls acenaphthene transport. This possibility is discussed in more detail below (see Sand Comparisons).

We compared the mass transfer rate calculated for our acetone data with literature values for conservative tracers and found good agreement (Table 4-5). Also shown in this table are dispersivities calculated from the reported data (assuming $D = \alpha v$) which are of comparable magnitude to that we calculated for the GT sand.

Table 4-5
Two-Region Model Mass Transfer Rates and Dispersivities in Aggregated Media

Reference	tracer	α^* [hr ⁻¹]	α [cm]
Nkedi-Kizza et al. [29]	³⁶ Cl	0.008-0.13	0.39
van Genuchten et al. [50]	³ H ₂ O	.002-.015	0.7 - 2
Rao et al. [33]	³⁶ Cl, ³ H ₂ O	0.03-0.2	0.11 - 0.14
This Study	acetone	.4	0.6

Aberjona. We also used acetone as the conservative tracer with the AJ sand because nitrate eluted later than acetone in this sorbent. The acenaphthene retardation factor in this sand was significantly higher than that for the other two columns such that elutions required longer duration experiments which also led to increased detector drift. Thus, the acetone and acenaphthene elution curves were truncated at 3 and 15 pore volumes, respectively, at

all flow rates in order to minimize bias in calculated moments due to detector drift. As shown previously for the Pine Barrens experiments (Chapters 2 & 3), truncation at pore volumes greater than twice the retardation factor should not significantly affect the magnitude of the moment-derived sorption and transport parameters.

a. BTC shape and flow rate. In contrast to the GT sand, the AJ sand breakthrough curves for acetone were more symmetrical, and the acetone breakthrough pore volume was essentially invariant with flow rate (**Figure 4-13**). However, at the higher flow rates, the acetone peaks had shoulders which indicated either a column packing problem or distinct flow regimes in this bulk sand. We repacked the column and saw no change in the shape of the breakthrough curves at high velocities, thus the shoulders must indicate some inequality in flow velocity within the column. This could be due to the wide range of particle sizes in the AJ column relative to the PB column used previously. The pore size distribution data also support this hypothesis since three pore populations can be identified in the bulk AJ sand although the abundance of the smaller diameter pore populations is not as great as that for the Georgetown sand (**Figure 4-14**). The degree of communication between these various flow paths can be described using the one-site kinetic model in a manner similar to that employed for the aggregated GT sand.

The asymmetric shape of the acenaphthene breakthrough curves for the AJ column is indicative of either physical or sorptive nonequilibrium (**Figure 4-14**). Unlike the acetone BTCs, no shoulder was visible on the acenaphthene profiles probably because holdup of acenaphthene due to significant retardation allowed flow inequalities to be smoothed out.

In contrast to the GT sand, the acetone peak maximum did not vary significantly with flow rate, but the sorbing compound peak did elute at earlier pore volumes with increasing flow rate. Qualitatively, this indicates that sorption nonequilibrium was more important than physical nonequilibrium in controlling acenaphthene transport in the AJ column. A similar observation was made previously for the PB sand (Chapter 2).

b. Moment Curve Fits. The first absolute moment data for acetone vs. inverse velocity had a slope of 9.96 (**Figure 4-16a**). Assuming $L=7$ cm, the acetone retardation factor is 1.42 (± 0.07). The retardation factor determined from the acenaphthene first moment data (**Figure 4-16a**) is 4.83 (± 0.38) a value which is in excellent agreement with the value we predicted from the early-time plateau in the batch kinetics data!

Dispersivity and the mass transfer rates were calculated from the second central moments curve fits (**Figure 4-16b**). A dispersivity value of 0.14 cm (± 0.01) and mass

transfer rate of $41 \text{ hr}^{-1} (\pm 10.3)$ were calculated from the acetone data. Using this dispersivity, we fit the acenaphthene data with a mass transfer rate of $0.22 \text{ hr}^{-1} (\pm 0.06)$. The dispersivity is again fairly large and probably reflects the wide distribution of grain sizes in the AJ bulk material relative to the sieved PB sand fraction we used previously (Chapter 2). In contrast to the GT sand, the Aberjona mass transfer rates for the two test compounds were very different. The significantly higher k_r value for acetone relative to acenaphthene indicates that physical nonequilibrium was not controlling acenaphthene transport in this sand. Rather, the sorption rate was slower than the physical mass transfer rate in this sand. In the discussion below, we examine some of the properties of the three sorbents we have studied that explain the observed differences in the sorptive behavior of these aquifer sands.

Summary. The moment-derived single-site first-order model parameters for each of the three sorbents we studied are summarized in **Table 4-6**. Keep in mind that only two assumptions were made in deriving these parameters. Namely, (1) we assumed either $R=1$ (PB) or $L=7 \text{ cm}$ (GT, AJ) in order to calculate retardation factors, and (2) we assumed the dispersion coefficient was proportional to velocity in all three sands.

Table 4-6
Single-Site First-Order Model Parameters for 3 Sands

Model Parameter	PB 250-1000 micron	GT bulk	AJ bulk
L [cm]	6.2	7 assumed	7 assumed
R			
acetone	1.0 assumed	1.58 ± 0.09	1.42 ± 0.07
acenaphthene	4.04 ± 0.14	2.16 ± 0.15	4.83 ± 0.38
α [cm]	0.05 ± 0.01	0.56 ± 0.09	0.14 ± 0.01
k_r [hr^{-1}]			
acetone	∞	0.38 ± 0.16	41 ± 10.3
acenaphthene	0.4 ± 0.15	0.16 ± 0.06	0.22 ± 0.06

Errors are one standard deviation propagated from best-fit standard errors.

Figure 4-14. Mercury porosimetry data for the three sand column sorbents: PB 250-1000, bulk GT and bulk AJ.

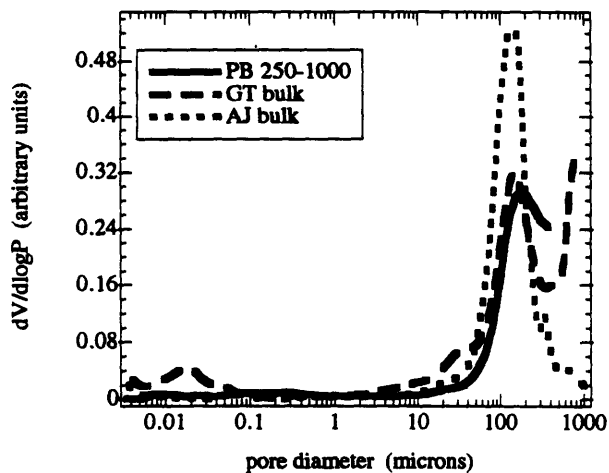
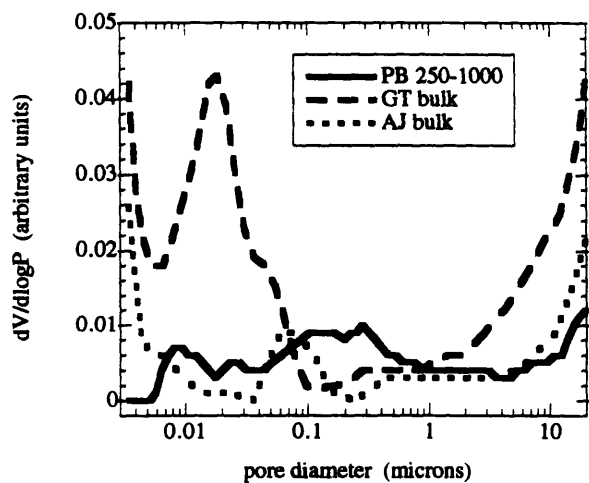


Figure 4-15. AJ-acenaphthene elution curves at four flow rates.

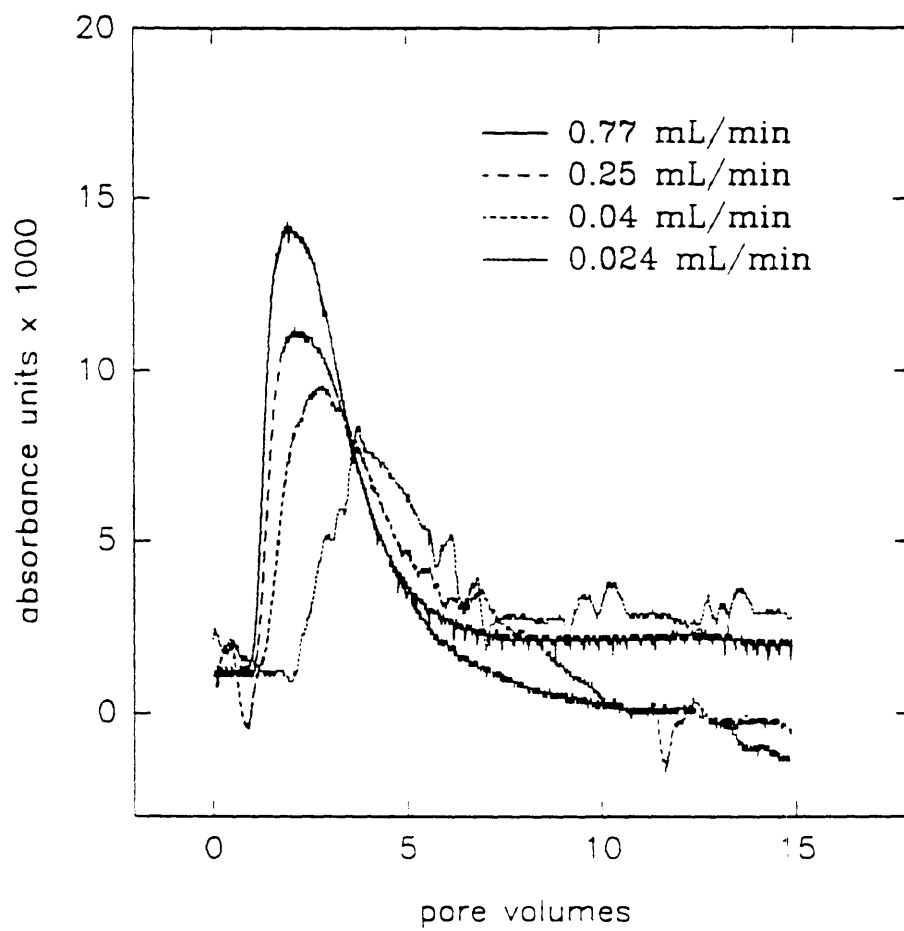
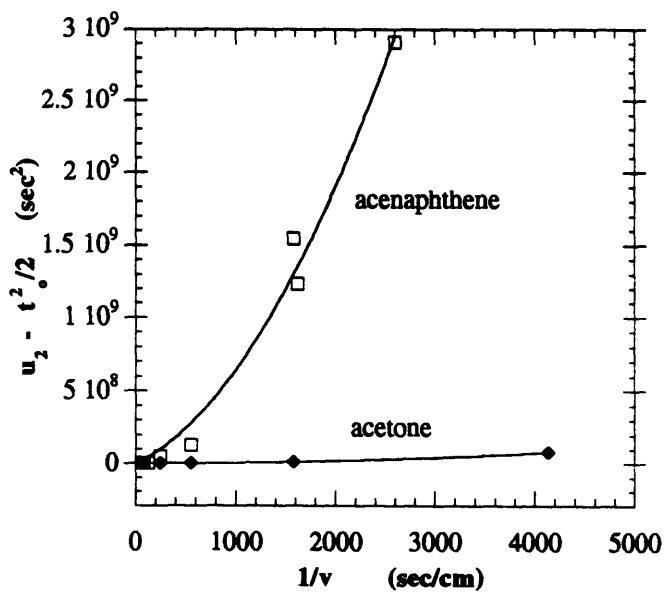
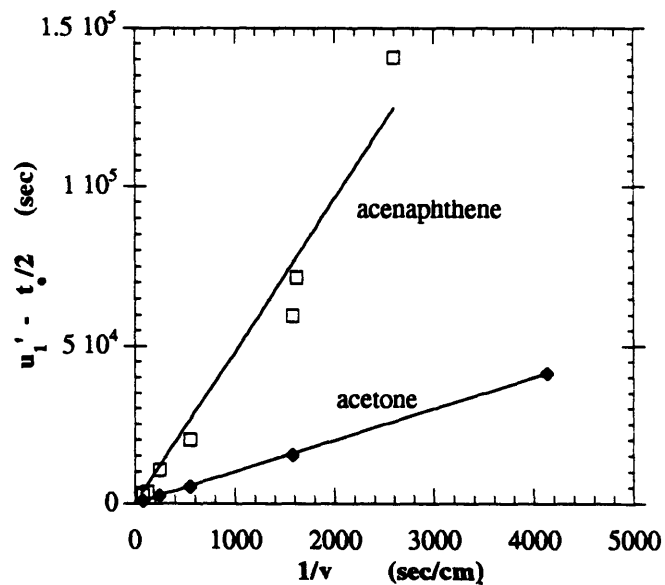


Figure 4-16. AJ moments versus $1/\nu$. (a) First absolute moment, (b) second central moment.



Sand Comparisons.

Batch vs. Column Acenaphthene Partitioning. There is a discrepancy between the batch and column K_d values for GT and AJ that is analogous to that seen previously in the Pine Barrens sand (Chapter 2). In all three sands, the batch sorption capacity is greater than that for the column. For the PB case, we had evidence for organic matter release and/or increased mineral surface exposure to sorbate under batch mixing conditions which we hypothesized was due to breakup of the high f_{oc} , kaolinite-goethite coatings. Also, in the PB case, the measured batch K_d agreed well (within a factor of 3) with $K_{oc}f_{oc}$. In the GT and AJ sands, the batch/ column K_d ratios are higher than for PB, and the AJ batch K_d agrees with $K_{oc}f_{oc}$, but the GT batch uptake capacity was about 4 times lower than $K_{oc}f_{oc}$ (Table 4-7).

Table 4-7
Acenaphthene Partition Coefficients¹

sand	Batch Kinetics	Batch Isotherm	Column		Partitioning Model
	K_d	K_d	K_d^{imm}	K_d^{om}	$K_{oc}f_{oc}$
Pine Barrens	2.5 (0.16)	2.6 (0.08)	na	0.82	1.63
Georgetown	0.97 (0.07)	0.86 (0.09)	0.086	0.086	3.69
Aberjona	2.6 (1.39)	3.2 (0.10)	.062	0.504	2.24

¹ Values in parentheses are standard errors (SE). Column K_d calculated from retardation factor and appropriate column r_{sw} . K_{oc} values based on regression of Karickhoff [24] for polycyclic aromatic hydrocarbons. na = not applicable.

We suspect that the batch - $K_{oc}f_{oc}$ discrepancy in the GT sand is due to either (a) an organic matter composition that is less sorptive than the organic matter upon which our f_{oc} correlations are based, or (b) to encasement of organic matter inside an impenetrable inorganic cement such as amorphous iron oxide or gibbsite. Organic matter composition has been shown to affect sorption capacity with the general observation that more polar organic matter sorbs less HOC than does organic matter with a high nonpolar content [11, 16, 17]. Gauthier et al. [17] remarked on the lower aromaticity of marine-derived

dissolved organic matter. Garbarini et al. [16] also pointed out that organic matter from marsh ecosystems may have a higher percentage of cellulose which would have lower sorptive capacity than organic matter dominated by lignin. These authors also commented on the low sorption capacity of dissolved organic matter in southeastern streams dominated by tannic acid. The geographic province of the Georgetown, SC, site could have contributed significantly to the discrepancy between K_d and calculated $K_{oc}f_{oc}$ for this sand relative to the other sites because of organic matter compositional variation. In addition, the younger age of the GT deposit relative to PB means there has been less diagenetic alteration of the GT organic matter, a factor which may also explain differences in sorption capacity. Further evidence for the relatively polar nature of the GT organic matter can be gained from comparing the organic matter partition coefficients, K_d^{om} , for the three sands. The organic matter partition coefficients for AJ and PB are both about an order of magnitude higher than that for GT. These column organic matter partition coefficients translate into K_{oc} values of 1700, 79 and 760 for PB, GT and AJ, respectively. All three sorbents, therefore, had low acenaphthene K_{oc} values relative to the value of about 3400 one would calculate from K_{ow} and Karickhoff's [24] K_{oc} - K_{ow} regression, but GT's value was significantly smaller than that for the other two sorbents.

Iron oxides have been shown to encase both dead and living bacteria cells in sediments from acidic environments [15], thus, it is conceivable that some of the GT organic matter was encased in the iron oxide of the coatings/matrix and was not available to acenaphthene in the batch tests. In contrast to the PB sand where quartz grains changed color after batch tumbling, the GT sand quartz grain surfaces were not significantly different after 30 days of tumbling. Thus, the GT iron oxides remained attached to the primary quartz grains during the batch tests, and we presume that the GT organic matter associated with the iron phases also remained encased during the tumbling. To test this organic matter-encasement hypothesis, we carried out a batch isotherm test on GT bulk sand that was first pulverized with a mortar and pestle. We also determined f_{oc} on this sand and found a value 2 times lower than for the sample reported in **Table 4-1**, 0.051%. As reported above, pulverization had no significant effect on the K_d value for this sorbent. Thus, either the GT organic matter is concealed within inorganic minerals of submicron dimensions or it is very hydrophilic relative to the PB and AJ organic material.

We presently have no additional data for determining which of these hypotheses is correct. The relative polarities of the organic matter in these three sands could be evaluated by detailed characterization using elemental analysis of the bulk sand (i.e., CHNOS), or UV absorbance [46] and ^{13}C -NMR on organic matter extracts [54]. Also, Weber et al. [52] used a low temperature vs. high temperature combustion method for evaluation of the

polarity of sorbent organic matter. Further, the iron-oxide minerals could be magnetically separated [3] and subjected to selective extractions followed by CHN analysis in order to determine where in the matrix the organic matter is located.

It is important to note that the AJ sand was the only sorbent which showed appreciable slow uptake in the batch kinetics experiment. Both PB and GT sands showed more rapid approaches to equilibrium: within 30 min for PB and 3 hours for GT. There are a few reasons this may have occurred. First, the young AJ sand may be less susceptible to tumbling artifacts than both the GT and PB sands because of its composition and texture. The iron oxides in the coatings on the primary grains in AJ are not crystalline iron oxides, but are amorphous. These may be a much better "glue" that holds the kaolinite to the quartz and feldspar grains. Evidence for the resistance of the AJ sand to disaggregation during tumbling is the observation that the primary grains did not lose their orange-brown staining during the batch tests, and did not even lose the iron oxide stain after sonication. (Both PB and GT lost their orange coloring after sonication). The second explanation for the slow batch kinetics observed for the AJ sand is that there are two distinctly different types or locations of sorptive sites in this sand, while the other sorbents only had one type of site. One type of sorption site could be the organic matter-rich iron oxide coatings and the second could be the weathered interiors of primary feldspar grains. The lag we observed between the two stages of batch uptake indicates that the second type of sorption site is somewhat inaccessible, thus the small diameter intramineral pores are ideal candidates. These intramineral sites may be restricted sites of either organic matter or mineral sorption. Wood et al. [55] showed the importance of weathered feldspar grains in a study of the slow uptake of lithium and sodium for the Cape Cod aquifer sand. The AJ sand is compositionally similar to the Cape Cod sand, however, we cannot extrapolate the sorption kinetics behavior of inorganic species to that of nonpolar organic compounds. Further work is required to identify the sorbent fraction responsible for the multi-stage batch uptake of acenaphthene by the AJ sorbent. Incidentally, the mercury porosimetry data for the AJ 250-1000 sonicated fraction indicated a significant population of pores less than 5 nm in diameter (see **Figure 4-5c**). These pores are either within the coatings that remained on the primary grains after sonication or within the primary grains. Since the coated AJ 250-1000 sample did not show these same small pore sizes, we presume that they represent chiefly intramineral (i.e., feldspar, mica) porosity.

Acetone Retardation Factors. As mentioned briefly above, the "nonsorbing" tracer, acetone, had a retardation factor greater than one in both the GT and AJ sands due to mass

transfer into the immobile water in these sands. GT, the sand with the highest abundance of fine-grained matrix material, had the highest acetone retardation factor. Examination of equation 4-6 shows that the immobile water partition coefficient is directly dependent on the volume ratio V_{im}/V_m . Therefore, sorbents such as GT with a large fraction of immobile water will have high K_d^{imm} values. AJ also showed some immobile water retention of acetone, probably in the finer-grained regions of the bulk sand as well as within the pores and fractures inside weathered mineral grains. In contrast, use of the 250-1000 micron sieve fraction in the PB column resulted in no appreciable immobile water in this sand and a nitrate retardation factor of 1.0 (the best fit value was 0.9 ± 0.05).

Acetone vs. Acenaphthene k_r . Comparing the acenaphthene and the acetone data for GT and AJ, we see that the rate constants measured for these two compounds were governed by different processes in these sands. In GT, the acetone mass transfer rate was equivalent to the acenaphthene rate within the scatter of the data; therefore, the sorbing solute did not experience a significantly slower transport rate due to any sorption-related mechanism. For AJ, however, the acetone mass transfer rate was significantly higher than the acenaphthene mass transfer rate, suggesting that a sorption-related process significantly slowed down acenaphthene's mass transfer. In the following discussion we examine possible explanations for these differences by interpreting the moment-derived k_r values as mass transfer parameters (i.e., proportional to effective diffusivities; see equation 4-8).

The GT data may not show sorption-related rate limitations due to (1) the relatively small amount of sorption capacity in this sand relative to the amount of immobile water, (2) because the organic matter sorption sites are not located in areas that have restricted access, or (3) acenaphthene was excluded from the immobile zone. The third hypothesis is unlikely since immobile water makes up such a large fraction of the GT sand's porosity. If acenaphthene was excluded from the matrix regions, acenaphthene should have eluted from the column earlier than acetone at the highest flow rates examined, and this was not observed. Acenaphthene eluted later than acetone at all flow rates, thus we doubt acenaphthene was excluded from the immobile water regions.

The first hypothesis implies that acenaphthene was retarded within the GT matrix, but to such a small extent that we were unable to detect significant holdup relative to acetone. As discussed previously, it is possible the organic matter was encased within the iron oxides of the matrix such that acenaphthene was not retarded in the immobile zone. This would result in equivalent effective diffusivities for acetone and acenaphthene, but requires zones of sorption capacity in the mobile region (i.e., on exteriors of matrix

patches) that preferentially retard acenaphthene. The high surface area of the matrix regions would make them ideal sites of dissolved organic matter sorption. Thus, it is conceivable that organic matter sorbed to the exteriors of the matrix was responsible for all of the retardation we observed in the GT sand.

Finally, the possibility exists that the locations of PNE resistance in the GT sand were not the same physical locations where organic matter is located. For example, if the observed physical nonequilibrium results from exchange with water in the pores of weathered feldspar grains, and not from exchange with water in the matrix pores, we would not expect acenaphthene to be retarded. This is because the mineral pores probably have very low organic matter contents relative to the matrix. Thus, we could have parallel uptake in two distinctly different types of sites and the slowest of these steps, mass exchange with immobile water, controlled the overall rate for both compounds. In order to evaluate this hypothesis, we note that the pore size distribution in the sonicated GT sample differed from the coated and bulk samples (Figure 4-5b) in that the coatings/matrix contain larger diameter pores than the mineral grains themselves. However, in the bulk sand, the mineral pores make up such a very small fraction of the total porosity it is unlikely they are responsible for the observed physical nonequilibrium.

The slow sorption process in AJ could be caused by a few factors: (1) the sorption reaction rate, in a chemical reaction sense, is slow relative to the rate of diffusion within the coatings, (2) the organic matter sorption "sites" are located in regions of the sorbent which are less accessible to the larger PAH molecule, (3) acenaphthene enters a different diffusion medium than acetone (i.e., organic matter diffusion) such that the rate of diffusion is reduced, and (4) acenaphthene is retarded as it diffuses through the coating pores but acetone is not. These hypotheses are discussed briefly below.

If organic matter partitioning is the correct local sorption mechanism, it is unlikely that the rate of this process will be slow relative to diffusion within the coating. Due to the unfavorable interactions between water molecules and nonpolar hydrophobic organic compounds, the energetics of sorption favor removal of the HOC from the coating pore water to the sediment organic matter. The rate of this partitioning process is generally considered to be instantaneous for nonpolar organic molecules such as acenaphthene, therefore it is unlikely that hypothesis (1) is rate-limiting in the AJ sorbent.

Accessibility of the sorption sites in the coatings (hypothesis 2) for acetone and acenaphthene is a function of the relative sizes of these molecules. If acenaphthene is significantly larger than acetone, its pore diffusivity will be smaller and, correspondingly, its sorption rate will be slower. Assuming molar volumes of 73.5 and 173 cm³/mol for

acetone and acenaphthene, respectively, equivalent spherical diameters of 6.2 and 8.2 Å were calculated using equation 3-9 (Chapter 3). We do not expect such small differences (30%) in molecular diameter to affect the relative pore diffusivities of these molecules by more than a factor of 2 to 5, based on constrictivity data from the chemical engineering literature (i.e., [10, 39]).

Slow intraorganic matter diffusion has been proposed by Brusseau and coworkers [5, 7] and Pignatello [31] to explain slow HOC sorption kinetics. Few environmental chemists have thoroughly examined the rates of organic compound diffusion in natural organic matter. Ball and Roberts [2] attempted to evaluate the sorption rate data they obtained for Borden aquifer solids in terms of an organic matter diffusion model and pointed out the difficulties of independently estimating organic matter diffusion path lengths and diffusion coefficients. Presently we have no way of assessing the feasibility of hypothesis (3). However, if organic matter diffusion was the only process limiting sorption in the AJ sand, and diffusivities within organic matter are constant, we would have expected the batch kinetics test to have shown only a single stage of uptake, rather than the two-stage uptake we observed. The batch AJ data suggest that there are either two types of sorption mechanisms operating or two different diffusion media in this sand. It is conceivable that one diffusion medium was the porous grain coatings and the other was within the organic matter of these coatings. If this is the case, the organic matter composition must be such that acetone's diffusivity was not significantly lowered, but acenaphthene's was decreased relative to the coating diffusivity. This situation could be explained by the relatively high polarity of soil organic matter relative to octanol [11], and the observation that diffusivity in polymers increases as the penetrant becomes more "like" the polymer in terms of hydrophobicity [36]. Equally plausible is the alternative discussed above that one medium is the iron-oxide coatings and the second is intramineral pores. In this case, the acetone rate of exchange would only be significantly faster than that for acenaphthene if acetone was excluded from some highly sorptive regions of the sorbent, possibly due to the higher polarity of acetone relative to acenaphthene.

At present, we suspect that the AJ data are best explained by slow retarded diffusion into the organic-matter rich coatings during the early stages of batch and column uptake (hypothesis 4). The agreement between the column K_d and the early plateau in the batch kinetics experiment support such an organic matter-controlled sorption mechanism to fairly accessible sites. The second stage of acenaphthene batch uptake was probably due to slow diffusion within confined (< 5 nm) pores of the weathered mineral grains (feldspars and mica) that take longer to reach. This second stage may reflect mineral surface sorption in addition to organic matter partitioning and results in a final batch K_d in excess of $K_{ocf_{oc}}$.

Also, the agreement between column K_d and the early batch plateau suggests that contact times in the column were not long enough to allow acenaphthene interaction to equilibrium with the second type of sites. Alternatively, the slow second stage could be due to diffusion through organic matter embedded deep within the coatings or mineral pores.

The most quickly sorbing sand, PB, showed an even larger difference between the conservative tracer's mass transfer rate and that for acenaphthene. This is most likely due to the negligible amount of immobile water that was present in the sieved fraction we studied. If we had examined the bulk PB sediment instead, we would expect the PB sorbent to also retard the "nonsorbing" tracer to a greater extent because of the presence of fine pores in the bulk PB sand (see mercury porosimetry data , **Figure 4-5**).

Sorption Time Constants. For any reversible first-order process, a time constant for the process can be defined as the inverse of the sum of the rate constants: $\tau = (k_f + k_r)^{-1}$ where k_f is the forward rate [sec^{-1}] and k_r is the reverse rate [sec^{-1}]. Using equation 2-10 (Chapter 2), k_f can be calculated from r_{sw} and K_d^{tot} . For the three sorbents we studied, both the acetone and acenaphthene sorption time constants increased from PB to AJ to GT (**Table 4-8**). Thus, the relative time constants agreed with the trend we observed in k_r values: solute transfer to the sorbent is slowest in GT and fastest in PB.

Table 4-8
Sorption Process Time Constants

	PB 250-1000 micron	GT bulk	AJ bulk
<i>acetone/nitrate</i>			
k_r [hr^{-1}]	∞	0.38	41
R	1.0	1.58	1.42
τ [hr]	0	1.7	0.02
<i>acenaphthene</i>			
k_r [hr^{-1}]	0.4	0.16	0.22
R	4.04	2.16	4.83
τ [hr]	0.6	2.9	0.9

The time constants for each sand can be compared to the time constants for advection, the competing transport process. Since we examined pore velocities from about 0.5 to 30 cm/hr, grain-scale advection time scales ranged from 0.1 to 0.002 hours, assuming an average particle size of 500 microns in these sands. Since the time constant for acenaphthene sorption is about 10 to 1000 times longer than the advection time, we conclude that acenaphthene transport in these three sorbents will be rate-limited by slow mass transfer to the available sorption sites (immobile water and/or organic matter).

Measured Sorbent Properties and Sorption Rate. We have identified two sorbent properties that showed general trends with the first-order model k_r values. These properties are the abundance of small diameter pores and the composition of the iron-oxide in each sand. The volume of immobile water is reflected in the mercury porosimetry data (**Table 4-3; Figure 4-14**). Both the GT and AJ bulk sands had significant pore populations in the range of 0.01 to 0.1 microns diameter which we interpret as chiefly matrix material in GT and both matrix and intramineral pores in AJ. The sand with the highest proportion of these small diameter pores, GT, had the slowest acenaphthene sorption rate. The sand with the lowest fraction of these 0.01 to 0.1 micron pores, PB, had the fastest measured k_r value. The total surface areas calculated from the mercury intrusion data also varied inversely with k_r : as TSA increased, k_r decreased. GT had the highest total surface area (15.2 m²/g), followed by AJ (4.0 m²/g) and PB had the lowest value at 1.9 m²/g. Since fine-grained minerals such as iron oxides and clays have high surface areas, the total surface area values quantify the abundance of matrix and coating materials in each sand. Thus, in general, we observe that as total surface area increased, the proportion of immobile water also increased in these sorbents, and the overall rate of acenaphthene exchange decreased.

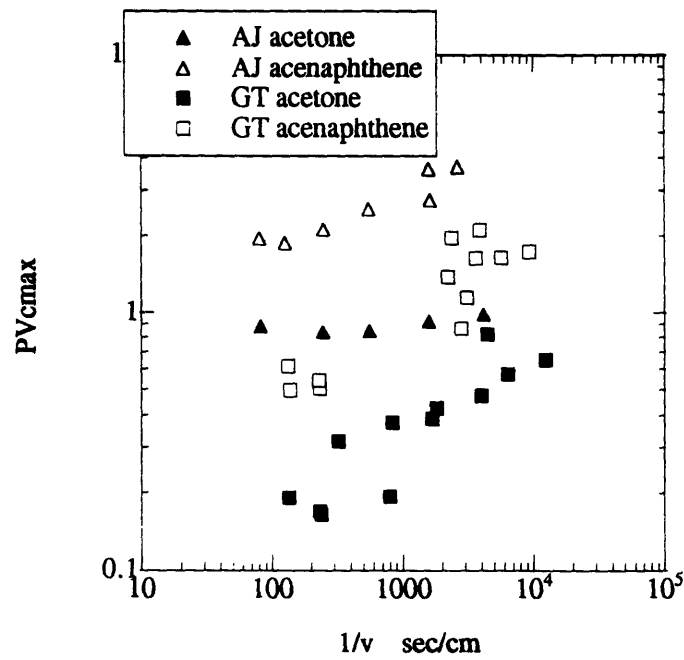
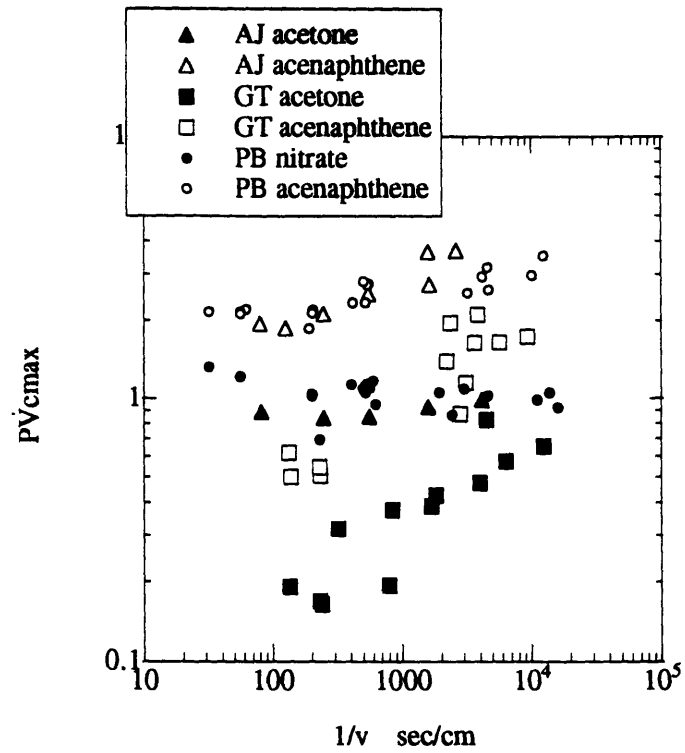
Iron oxide composition also showed a general relationship to the k_r value. The iron contents based on the TiCEB and AOD extraction methods were interpreted as indicators of the total amount of surface iron species (TiCEB) and the amount of amorphous iron (AOD). The GT sand had the slowest acenaphthene sorption rate and the highest fraction of surface iron (70%, see **Table 4-2**). The sands with the highest AOD/TiCEB iron ratios, AJ and GT, had lower k_r values than the PB sand, which had very little amorphous surface iron. Therefore, it appears that sorbents with more crystalline iron oxide compositions will have faster acenaphthene sorption rates. In the three sands we studied, the iron oxide composition also correlated with the strength of the oxide coatings on primary grains. The PB coatings were easily dispersed in the batch tests, whereas the GT coatings remained more intact in the batch and the AJ coatings were little affected even by

sonication. Crosby et al. [12] measured very different porosities and pore shapes in different iron oxide precipitates using nitrogen adsorption techniques. Therefore, we suspect that amorphous iron oxide composition affected the rate of acenaphthene mass transfer to the sorbent due to its control on coating/matrix pore structure. In addition, Schwertmann [42] observed that hydrous iron oxide crystallization was inhibited by the presence of dissolved organic matter. The slow AJ and GT sorption rates could therefore also be a function of the organic matter shielding effect described by Pignatello [30]. Perhaps the organic matter in these sorbents is enclosed within the amorphous iron precipitates making it much less accessible to acenaphthene. Further study of PAH sorption to different iron oxide compositions will help clarify the importance this factor has on sorption rate.

Peak Position and Flow Rate. We investigated whether the relative positions of the acenaphthene peaks at different flow rates could be used to give a qualitative understanding of the importance of mass transfer (PNE or sorption) rate limitations in these sands. Plots of PV_{cmax} versus inverse velocity showed striking differences between GT and the other two sands (**Figure 4-17**). Both the acetone and acenaphthene PV_{cmax} values increased with decreasing flow rate in the GT sand, while for PB and AJ only the acenaphthene peak maximum shifted significantly. As discussed previously, this behavior is attributed to significant physical nonequilibrium in GT due to the abundance of fine-grained matrix material. The second observation we make from **Figure 4-17** is that the acenaphthene peak position did not reach a plateau for any of the sands over the range of pore velocities we studied. Therefore, we conclude that equilibrium (physical or sorption) was not achieved even at the lowest flow rates we studied, which approached the range of natural groundwater velocities. This conclusion is also substantiated by our earlier work with the PB sorbent (Chapter 2) which demonstrated that, at the grain-scale, equilibrium was not achieved. Since PB showed the fastest acenaphthene mass transfer rate in the three sands, we expect both GT and AJ, which had lower k_r values, would be even further from equilibrium with acenaphthene than PB.

We hypothesized that sorbents which showed more rate limitations (i.e., slower sorption or mass transfer rate) would be expected to have a larger pore volume change in peak location over the velocity range examined than a sorbent with higher solute mass transfer rates (i.e., if close to equilibrium the peaks will not move as a function of velocity). Based on the differences in the relative positions of the conservative and sorbing tracer peaks (ΔPV_{cmax}) over the range of flow rates studied, we estimated that acenaphthene sorption/mass transfer kinetics was slowest in AJ, faster in PB and faster still

Figure 4-17. Pore volumes to peak maximum as a function of inverse velocity for three sands.



in GT. (Values of ΔPV_{cmax} for low velocity minus high velocity averages were 2.2, 1.6 and 0.98 pore volumes for AJ, PB and GT, respectively, based on visual estimates from **Figure 4-17**). This predicted trend agrees with that observed only for AJ and PB: acenaphthene transfer was about 2 times slower in AJ than in PB. The ΔPV_{cmax} trend does not correctly predict the relative rate of acenaphthene transfer in GT possibly because of the difference in controlling mechanism (i.e., PNE dominates in GT) in this sand relative to the other two sands.

Summary and Conclusions

We examined the rate of sorption of a single polycyclic aromatic hydrocarbon, acenaphthene, in three aquifer sands of different mineralogical composition and texture. All three sands had low organic carbon contents and primary mineral grains coated with iron-oxide and kaolinite. Two of the sands also contained appreciable intramineral porosity due to feldspar weathering. Sorption rates were quantified using the method of moments on elution curves collected over a wide range of pore velocities in each sand. For all three sands, we found that the single-site, first-order sorption model could be used to interpret the relative sorption effects of mass transfer to immobile water (i.e., physical nonequilibrium) and organic matter partitioning. Thus, we interpret the "sorption" process as encompassing retention by both stagnant water pores in the sand and by sorbent organic matter. The key to our analysis of the model parameters was to let the conservative tracer retardation factor quantify the amount of immobile water, and the conservative tracer k_r value quantify the rate of immobile water mass transfer. Use of this simple model with only two sorption fitting parameters for all three sands allowed us to directly compare the acenaphthene k_r values and interpret them in terms of measured sorbent properties.

For all three sands, the rate of sorption was significantly slower than the grain-scale advection rate. Therefore, acenaphthene subsurface transport in these sands will be rate-limited by the sorption rate. Successful modeling of acenaphthene transport in these sorbents will thus require a sorption kinetic model rather than use of the equilibrium sorption model.

We measured acenaphthene sorption time constants which varied by a factor of 3 among the three sorbents. The mechanism controlling sorption varied with the amount of immobile water in each sorbent. In the sand with the highest immobile water fraction, acenaphthene transport was governed by physical nonequilibrium as evidenced by equivalent acetone and acenaphthene k_r values. This rate of immobile water exchange was slow due to the abundance of small diameter pores in the fine-grained matrix between primary grains. In the other sands, acenaphthene transport was controlled by sorption to

organic matter located within the high- f_{oc} , iron-oxide coatings. In general, the acenaphthene sorption rate was highest in the sand with the more crystalline iron oxide composition, negligible intramineral porosity, and lowest total surface area (~ lowest proportion of immobile water).

Further investigation of the sorption kinetic characteristics of the ubiquitous organic matter-rich, iron-oxide and clay coatings that occur on aquifer sand grains is warranted. Since these coatings are located on the exteriors of aquifer sand grains, they represent primary sorption sites to pore water solutes. Further, the high f_{oc} of these coatings makes them potential sites of high organic matter sorption capacity. Based on our results, we speculate that one of the key sorbent properties which controls the rate of acenaphthene sorption is degree of iron oxide crystallinity. We found slower sorption rates in the sorbent with the highest proportion of amorphous iron oxide coatings. The intimate association of organic matter with precipitating iron oxides and the effect this organic matter has on the structure of the oxide must affect the accessibility of the organic matter sorption sites. More detailed studies of the pore structure and organic matter relationships in these iron-oxide coatings will lead to improved predictions of sorption rate in coated aquifer sands. We suspect that detailed investigations of sorbent pore structure by NMR and N_2 isotherm analysis will improve our understanding of the sorbent diffusion regime.

Literature Cited

1. Ball, W. P., C. H. Buehler, T. C. Harmon, D. M. Mackay and P. V. Roberts. (1990) Characterization of a sandy aquifer material at the grain scale. *J. Contamin. Hydrol.*, 5: 253-295.
2. Ball, W. P. and P. V. Roberts. (1991) Long-term sorption of halogenated organic chemicals by aquifer material. 2. Intraparticle diffusion. *Environ. Sci. Technol.*, 25: 1237-1249.
3. Barber, L. B., II, E. M. Thurman and D. D. Runnells. (1992) Geochemical heterogeneity in a sand and gravel aquifer: Effect of sediment mineralogy and particle size on the sorption of chlorobenzenes. *J. Contam. Hydrol.*, 9: 35-54.
4. Borggaard, O. K. (1982) Selective extraction of amorphous iron oxides by edta from selected silicates and mixtures of amorphous and crystalline iron oxides. *Clay Minerals.*, 17: 365-368.
5. Brusseau, M. L. (1992) Nonequilibrium transport of organic chemicals: the impact of pore-water velocity. *J. Contam. Hydrol.*, 9: 353-368.
6. Brusseau, M. L. (1993) The influence of solute size, pore water velocity and intraparticle porosity on solute dispersion and transport in soil. *Water Resour. Res.*, 29: 1071-1080.

7. Brusseau, M. L., R. E. Jessup and P. S. C. Rao. (1991) Nonequilibrium sorption of organic chemicals: elucidation of rate-limiting processes. *Environ. Sci. Technol.*, 25: 134-142.
8. Brusseau, M. L., T. Larsen and T. H. Christensen. (1991) Rate-limited sorption and nonequilibrium transport of organic chemicals in low organic carbon aquifer materials. *Water Resour. Res.*, 27: 1137-1145.
9. Carbonell, R. G. (1979) Effect of pore distribution and flow segregation on dispersion in porous media. *Chem. Eng. Sci.*, 34: 1031-1039.
10. Chantong, A. and F. E. Massoth. (1983) Restrictive diffusion in aluminas. *AIChE J.*, 29: 725-731.
11. Chiou, C. T. and D. E. Kile. (1994) Effects of polar and nonpolar interactions on the partition of organic compounds in soil organic matter. 207th ACS, San Diego, CA, 327-330.
12. Crosby, S. A., D. R. Glasson, A. H. Cuttler, I. Butler, D. R. Turner, M. Whitfield and G. Millward. (1983) Surface areas and porosities of Fe(III)- and Fe(II)-derived oxyhydroxides. *Environ. Sci. Technol.*, 17: 709-713.
13. Davis, J. A. (1982) Adsorption of natural dissolved organic matter at the oxide/water interface. *Geochim. Cosmochim. Acta.*, 46: 2381-2393.
14. Dullien, F. A. L. (1979) Porous Media: Fluid Transport and Pore Structure. Academic Press: New York, NY; 396 pp.
15. Ferris, F. G., K. Tazaki and W. S. Fyfe. (1988) Iron oxides in acid mine drainage environments and their association with bacteria. *Chem. Geol.*, 74: 321-330.
16. Garbarini, D. R. and L. W. Lion. (1986) Influence of the nature of soil organics on the sorption of toluene and trichloroethylene. *Environ. Sci. Technol.*, 20: 1263-1269.
17. Gauthier, T. D., W. R. Seitz and C. L. Grant. (1987) Effects of structural and compositional variations of dissolved humic materials on pyrene Koc values. *Environ. Sci. Technol.*, 21: 243-248.
18. GeoTrans, Inc. (1994) Wells G & H site central area remedial investigation. Phase IA. Vol. 1, February 1994.
19. Gregg, S. J. and K. S. W. Sing. (1982) Adsorption, Surface Area and Porosity. Academic Press: London; 303 pp.
20. Han, N., J. Bhakta and R. G. Carbonell. (1985) Longitudinal and lateral dispersion in packed beds: effect of column length and particle size distribution. *AIChE J.*, 31: 277-288.
21. Harmon, T. C., L. Semprini and P. V. Roberts. (1992) Simulating solute transport using laboratory-based sorption parameters. *J. Environ. Engineering.*, 118: 666-689.
22. Jackson, M. L., C. H. Lim and L.W.Zelazny. (1986) Oxides, hydroxides, and aluminosilicates. In Methods of Soil Analysis, Part 1- Physical and Mineralogical

- Methods. Klute, A. (Ed.) American Society of Agronomy, Inc.: Madison, WI; pp. 101-150.
23. Jardine, P. M., N. L. Weber and J. F. McCarthy. (1989) Mechanisms of dissolved organic carbon adsorption on soil. *Soil Sci. Soc. Am. J.*, 53: 1378-1385.
 24. Karickhoff, S. W. (1981) Semi-empirical estimation of sorption of hydrophobic pollutants on natural sediments and soils. *Chemosphere.*, 10: 833-846.
 25. Lowell, S. and J. E. Shields. (1984) Interpretation of mercury porosimetry data. In *Powder Surface Area and Porosity*. Chapman & Hall: London; pp. 97-120.
 26. MacIntyre, W. G., T. B. Stauffer and C. P. Antworth. (1991) A comparison of sorption coefficients determined by batch, column, and box methods on a low organic carbon aquifer material. *Ground Water.*, 29: 908-913.
 27. McKeague, J. A. and J. H. Day. (1965) Dithionite- and oxalate-extractable Fe and Al as aids in differentiating various classes of soils. *Can. J. Soil Sci.*, 46: 13-22.
 28. Miller, M. M., S. P. Wasik, G.-L. Huang, W.-Y. Shiu and D. Mackay. (1985) Relationships between octanol-water partition coefficient and aqueous solubility. *Environ. Sci. Technol.*, 19: 522-529.
 29. Nkedi-Kizza, P., J. W. Biggar, H. M. Selim, M. T. van Genuchten, P. J. Wierenga, J. M. Davidson and D. R. Hielsen. (1984) On the equivalence of two conceptual models for describing ion exchange during transport through an aggregated oxisol. *Water Resour. Res.*, 20: 1123-1130.
 30. Pignatello, J. J. (1990) Slowly reversible sorption of aliphatic halocarbons in soils. II. Mechanistic aspects. *Environ. Tox. Chem.*, 9: 1117-1126.
 31. Pignatello, J. J., F. J. Ferrandino and L. Q. Huang. (1993) Elution of aged and freshly added herbicides from a soil. *Environ. Sci. Technol.*, 27: 1563-1571.
 32. Rao, P. S. C., R. E. Green, L. R. Ahuja and J. M. Davidson. (1976) Evaluation of a capillary bundle model for describing solute dispersion in aggregated soils. *Soil Sci. Soc. Am. J.*, 40: 815-820.
 33. Rao, P. S. C., R. E. Jessup, D. E. Rolston, J. M. Davidson and D. P. Kilcrease. (1980) Experimental and mathematical description of nonadsorbed solute transfer by diffusion in spherical aggregates. *Soil Sci. Soc. Am. J.*, 44: 684-688.
 34. Rao, P. S. C., D. E. Rolston, R. E. Jessup and J. M. Davidson. (1980) Solute transport in aggregated porous media: theoretical and experimental evaluation. *Soil Sci. Soc. Am. J.*, 44: 1139-1146.
 35. Roberts, P. V., M. N. Goltz, R. S. Summers, J. C. Crittenden and P. Nkedi-Kizza. (1987) The influence of mass transfer on solute transport in column experiments with an aggregated soil. *J. Contamin. Hydrol.*, 1: 375-393.
 36. Rogers, C. E. (1965) Solubility and diffusivity. In *Physics and Chemistry of the Organic Solid State*. Fox, D., M. M. Labes and A. Weissberger (Ed.) Interscience: New York; pp. 509-635.

37. Ryan, J. N. and P. M. Gschwend. (1991) Extraction of iron oxides from sediments using reductive dissolution by titanium (III). *Clays Clay Mins.*, 39: 509-518.
38. Ryan, J. N. and P. M. Gschwend. (1992) Effect of iron diagenesis on the transport of colloidal clay in an unconfined sand aquifer. *Geochim. Cosmochim. Acta.*, 56: 1507-1521.
39. Satterfield, C. N., C. K. Colton and J. Pitcher W.H. (1973) Restricted diffusion in liquids within fine pores. *AIChE J.*, 19: 628-635.
40. Schuth, C. and P. Grathwohl. (1994) Nonequilibrium transport of PAHs: A comparison of column and batch experiments. In *Transport and Reactive Processes in Aquifers*. Dracos, Th. and F. Stauffer (Eds.) Balkema: Rotterdam; pp. 143-148.
41. Schwertmann, U. (1964) Differenzierung der Eisenoxide des Bodens durch Extraktion mit Ammoniumoxalat-Lösung. *Z. Pflanzenern. Dgg. Bodenkde.*, 194-202.
42. Schwertmann, U. (1966) Inhibitory effect of soil organic matter on the crystallization of amorphous ferric hydroxide. *Nature.*, 21: 645-646.
43. Stauffer, T. B. (1987) Sorption of nonpolar organics on minerals and aquifer materials. Ph.D. thesis, College of William and Mary.
44. Thompson, M. and J. N. Walsh. (1989) Handbook of Inductively Coupled Plasma Spectrometry. Blackie: London; 95-99 pp.
45. Tipping, E. (1981) The adsorption of aquatic humic substances by iron oxides. *Geochim. Cosmochim. Acta.*, 45: 191-199.
46. Traina, S. J., J. Novak and N. E. Smeck. (1990) An ultraviolet absorbance method of estimating percent aromatic carbon content of humic acids. *J. Environ. Qual.*, 19: 151-153.
47. Valocchi, A. J. (1985) Validity of the local equilibrium assumption for modeling sorbing solute transport through homogeneous soils. *Water Resour. Res.*, 21: 808-820.
48. van Genuchten, M. T. (1985) A general approach for modeling solute transport in structured soils. *Memoires IAH.*, 17: 513-526.
49. van Genuchten, M. T. and P. J. Wierenga. (1976) Mass transfer studies in sorbing porous media I. Analytical solutions. *Soil Sci. Soc. Am. J.*, 40: 473-480.
50. van Genuchten, M. T. and P. J. Wierenga. (1977) Mass transfer studies in sorbing porous media:II. Experimental evaluation with tritium. *Soil Sci. Soc. Am. J.*, 41: 272-278.
51. Villiermaux, J. (1974) Deformation of chromatographic peaks under the influence of mass transfer phenomena. *J. Chromat. Sci.*, 12: 822-831.
52. Weber, W. J., Jr., P. M. McGinley and L. E. Katz. (1992) A distributed reactivity model for sorption by soils and sediments. 1. Conceptual basis and equilibrium assessments. *Environ. Sci. Technol.*, 26: 1955-1962.

53. Williams, T. M. and J. C. McCarthy. (1991) Field-scale tests of colloid-facilitated transport. National Research and Development Conference on Control of Hazardous Materials, Greenbelt, MD, 179-184.
54. Wilson, M. A., A. M. Vassallo, E. M. Perdue and J. H. Reuter. (1987) Compositional and solid-state nuclear magnetic resonance study of humic and fulvic acid fractions of soil organic matter. *Anal. Chem.*, 59: 551-558.
55. Wood, W. W., T. F. Kraemer and J. Hearn P.P. (1990) Intragranular diffusion: an important mechanism influencing solute transport in clastic aquifers? *Science.*, 247: 1569-1572.
56. Wu, S.-C. and P. M. Gschwend. (1988) Numerical modeling of sorption kinetics of organic compounds to soil and sediment particles. *Water Resour. Res.*, 24: 1373-1383.

Chapter 5. CONCLUSIONS

Summary

This work focused on understanding the mechanism of rate-limitation in the sorption of hydrophobic organic compounds by low organic matter aquifer solids. We began by addressing the question of whether or not the rate of sorption of a high molecular weight PAH, acenaphthene, was slow relative to the rate of groundwater advection (Chapter 2). Using the method of moments to quantify the rate of sorption in an iron-oxide- and kaolinite-coated quartz sand, sorption rates were found to be significantly slower than the particle-scale advection rates even at the natural groundwater velocity.

We also found that the batch experiment K_d value overestimated the column retardation factor by a factor of about 3. We suspect the batch mixing conditions led to disaggregation of the coating sorption sites in this sand and subsequently allowed increased sorption by either mineral surfaces or newly exposed organic matter. The higher solid-to-water ratio and quiescent conditions in the column did not allow a similar increase in sorption site exposure during the column tests.

The next phase of our investigations involved examination of how the rate of sorption in this sand varied with sorbate hydrophobicity (Chapter 3). We chose two additional PAH for comparison with our acenaphthene results: naphthalene and phenanthrene. These three compounds span a log K_{ow} range from 3.35 to 4.57, but have molecular diameters that are within 10% of one another. Thus, any differences in sorption rate that we observed were not due to differences in physical factors among the sorbates (i.e., size exclusion phenomena). We found the rate of sorption to vary inversely with log K_{ow} for the Pine Barrens sand. Since organic matter partition coefficients increase with increasing hydrophobicity, and because the grain coatings were sites of high organic carbon content, we hypothesized that the sorption rate was controlled by the rate of retarded diffusion within the goethite and kaolinite coatings on the quartz grains. We used a diffusion model based on the porous coating/impermeable core sorbent geometry to convert the first-order sorption rates to effective diffusivities. In this way we were able to compare the moment-derived diffusivities to those we predicted using an intra-coating retarded diffusion model. The predicted effective diffusivities were two orders of magnitude higher than the moment-derived effective diffusivities. The simplest explanation for this divergence was that our coating model predictions of coating thickness and coating porosity were too high. We explored other possible explanations for this discrepancy and found

that hindered diffusion could not explain the data, but the presence of mineral micropores containing structured water could account for the 100 fold variation.

The final phase of our investigation involved a study with two other aquifer sands in order to determine whether the slow acenaphthene sorption rate found in the Pine Barrens sand was peculiar to that sorbent. In addition, if sorption was similarly slow in these new sands, we wanted to pinpoint the sorbent properties that influence the rate of sorption. The two sands we chose to study were also iron-oxide coated sands, but they had very distinct properties from the Pine Barrens as well. Both of the new sands were studied as bulk material in contrast to our use of the 250-1000 micron sieve fraction of the Pine Barrens sand. The addition of the finer material to these columns resulted in appreciable stagnant water zones and thus two types of sorption "sites" existed: immobile water and organic matter in iron-rich coatings/matrix. We used the conservative tracer, acetone, to quantify the abundance of the immobile water sites and the rate of mass transfer to these sites, again using a single-site sorption model.

The rate of acenaphthene sorption was significantly slower than the groundwater advection rate in the Aberjona and Georgetown sands as well. The Georgetown sand, which had the highest proportion of immobile water zones, had the slowest sorption rate, and this rate was controlled by a physical nonequilibrium mechanism. In the Aberjona sand, acenaphthene sorption was controlled by intrasorbent partitioning to organic matter rather than the rate of exchange with immobile water. We inferred that a retarded diffusion mechanism within the high f_{oc} iron oxide coatings was responsible for the slow rate of acenaphthene sorption in both the Aberjona and Pine Barrens sand. Thus, the faster rate of sorption in the Pine Barrens sand must have been due to its lack of amorphous iron oxides in the coatings and lack of intramineral porosity. We identified the occurrence of amorphous iron oxide phases and the presence of porous weathered mineral grains with the more slowly sorbing sands. The sands with these properties also showed slower batch uptake of acenaphthene.

Accomplishments

This work has shown that measurement of a batch partition coefficient cannot always be used to predict the retardation factor in a sand column. The fact that we found sorption rates to be at least an order of magnitude slower than the grain-scale advection rate in three sandy aquifer materials and for three PAH compounds means that prediction of solute arrival downgradient of a chemical spill will depend on the sorption rate. We demonstrated that the rate of sorption in these aquifer solids was dependent on solute

hydrophobicity and sorbent properties. Therefore, characterization of sorbate and sorbent will be required for successful prediction of intrasorbent diffusion model parameters.

In our efforts to identify the key sorbate and sorbent properties that control sorption in sandy aquifer materials, we found that, for hydrophobic organic chemicals such as PAHs, sorbent regions of high organic matter content were important sites of sorption. These regions were the iron-oxide coatings on quartz and feldspar grains in the sands we studied. Thus, partitioning to organic matter is an important part of the sorption mechanism even when the bulk sorbent f_{oc} is less than 0.1%.

Since these coatings are primary sorption sites, we found that detailed characterization of the coating properties aided in predictions of sorbate effective diffusivities. Of particular importance are the f_{oc} , porosity and geometry (i.e., coating thickness) of the sorption regime. Furthermore, we showed that slow diffusion within sorbent micropores filled with vicinal water is a potential sorption mechanism that has been overlooked in intrasorbent diffusion studies to date.

By examining the rate of acenaphthene sorption to three iron-oxide coated aquifer sands we identified two sorbent factors that varied with sorption rate: the abundance of immobile water and the composition of the iron oxide. Sorption rates decreased with increasing fraction of immobile water and increasing amorphous iron content of the coatings. Although studies with a wider range of sorbates and sorbents is required, our research highlights the importance of characterizing the abundance of iron-oxide coatings on sand grains and the composition of the iron-oxide, as well as the abundance of intramineral pores.

The key sorbate properties required to predict sorption rate in these solids are K_{oc} and aqueous diffusivity, parameters that are generally easily estimated. We found that molecular size had little effect on sorption rate compared to the effect hydrophobicity had on intrasorbent retardation. However, if sorbents with pore diameters approaching 1 nm are present in the sorption regime, hindered diffusion of PAH solutes may significantly slow the rate of sorption.

Implications

Modeling Solute Transport. We identified slow sorption as an important mass transfer process in aquifer sands even at natural groundwater flow velocities. Thus, one of our primary goals has been accomplished. This finding has important repercussions for the modeling of contaminant transport in groundwater. It is clear that an equilibrium sorption model will not satisfactorily predict solute transport in these media at the laboratory scale.

Thus, the task before us is to develop the best sorption kinetics model to accurately predict solute transport, but without incorporating physically-meaningless fitting parameters. A diffusion model that is based on measurable physical properties of the sorbent is probably the best choice for accurate prediction of sorption rates. However, detailed sorbent characterization will be required in order to determine the appropriate sorption medium and to make realistic estimates of the diffusion model parameters.

Our research has focused on laboratory-scale sorption processes. Burr et al. [2] have recently simulated sorption kinetics in a heterogeneous aquifer modeled after Borden and concluded that local equilibrium sorption coupled with spatial variations in hydraulic conductivity and K_d can produce solute transport behavior similar to what one would attribute to sorption kinetics (i.e., retardation factors that increase with time/transport distance). They concluded that, for the set of kinetic parameters they chose, large-scale aquifer heterogeneity affected plume velocity and dispersion significantly more than small-scale sorption kinetics. A similar finding was reported by Brusseau and Rao [1] who compared the relative magnitudes of the terms contributing to field-scale solute dispersion.

Thus, we must recognize that laboratory studies such as reported here are critical to identifying the mechanism of sorption, but may not be directly applied to field-scale solute transport where other factors contribute to transport nonequilibrium (i.e., aquifer heterogeneity). Once the fundamentals of the sorption process are understood, we will be able to quantify the sorbent properties which are most critical to determination of sorption capacity and rate. These particle-scale properties can then be used to quantify spatial variations in sorption properties at larger scales. For example, identification of the importance of high f_{oc} coatings as important sorption sites suggests that field-scale distributions of such coatings could be important indicators of aquifer heterogeneity. Furthermore, since coating abundance (and f_{oc}) correlates with iron oxide content, simple measurement of Fe content in aquifer materials across a field site could be used to calibrate aquifer heterogeneity in solute transport models.

Pump-and-Treat Remediation Schemes. Remediation techniques such as pump-and-treat which employ very high advection rates will be greatly affected by slow sorption and desorption of organic contaminants. The primary significance of the present work with respect to these cleanup techniques is the magnitude of the sorption rate constants we measured. Assuming the laboratory-derived, particle-scale sorption rates also apply to the local-scale in the field, the first-order rates we determined can serve as a starting point for designing more effective remediation schemes. For example, an initial estimate of the desorption rate in a sandy aquifer would be on the order of 0.3 hr^{-1} for a compound like

acenaphthene. Based on this value, and some knowledge of the hydraulic characteristics of the contaminated site, preliminary calculations of the most efficient pumping rate could be made. From this starting point, adjustments could be made to fine-tune the remediation project to meet the cleanup goals in the most economical way. Of course, as discussed above, the field-scale transport will also be complicated by larger-scale processes such as site heterogeneity.

Laboratory Sorption Studies. Our finding that batch K_d s did not reflect the K_d measured in the column environment suggests that for some sorbents column studies will be the only way to determine the "true" field K_d value. Also, the rate of uptake we observed in the batch experiments was rapid relative to the column rate for our sands. These results imply that the more difficult column technique is the only way to accurately quantify sorption properties of subsurface environments.

Future Work

This study has failed to develop a successful tool for prediction of sorption rate that can be widely applied to a variety of sorbents. Many more sorbent compositions need to be tested in order to identify the microscale properties that control the grain-scale sorption mechanism. We have identified a few possible areas of productive research as outgrowths of this work. These are briefly described below.

The ubiquitous occurrence of iron-oxide coatings on mineral grains in different environments (soils, aquifer sediments, river sediments) and the observation that organic matter is associated with the iron oxides makes them important sites of hydrophobic organic compound sorption. More research needs to be done to quantify the rate of sorption to these materials. In addition, detailed characterization of these coatings with techniques such as nitrogen adsorption isotherms and NMR (which gives *in situ* pore sizes; see [3]) will improve our understanding of the porosity and pore structure of these diffusion media. We also need to examine in more detail how simpler analytical techniques such as selective oxide extractions can be correlated with the porosity and sorption characteristics in order to develop simple analytical tools for estimating sorption rate. We identified crystallinity of the iron oxide as one potential candidate requiring further investigation.

Methods need to be developed to characterize the location of the organic matter sorption sites in aquifer sorbents. Possible avenues to be explored are fluorescent staining and epifluorescence or microradiography. If we identify where the organic matter is located, we gain important information concerning the diffusion path lengths in the sorbent.

The final area of future work is investigation of the abundance and role micropores play in slow organic compound diffusion. Careful quantification of these nm-sized pores in natural sorbents may be beyond our present analytical capabilities, however, there is preliminary evidence which suggests they may play an important role in intraparticle diffusion.

Literature Cited

1. Brusseau, M. L. and P. S. C. Rao. (1989) Nonequilibrium and dispersion during transport of contaminants in groundwater: Field-scale processes. International Symposium on Contaminant Transport in Groundwater, Stuttgart, Germany, 237-244.
2. Burr, D. T., E. A. Sudicky and R. L. Naff. (1994) Nonreactive and reactive solute transport in three-dimensional heterogeneous porous media: Mean displacement, plume spreading, and uncertainty. *Water Resour. Res.*, 30: 791-815.
3. Hinedi, Z. R., Z. J. Kabala, T. H. Skaggs, D. B. Borchardt, R. W. K. Lee and A. C. Chang. (1993) Probing soil and aquifer material porosity with nuclear magnetic resonance. *Water Resour. Res.*, 29: 3861-3866.

APPENDICES

Appendix A: Fortran Programs

The following listings of the Fortran programs used in this research are preceded by a brief description of each program.

Program SUBSLOPE

- program to subtract sloping baselines from elution curves prior to determination of curve moments. Input file contains one column of time, second column of concentration data. Program queries user for number of data points.

```
c subslope.for 7/19/93 Britt Holmen
c uses data files with time in seconds
c subtracts a sloping baseline from data files
c
  real c,t,base
  real initbase,finalbase
  real sumc,encd,slope
  integer ndata
  dimension t(28000), c(28000),base(28000)
  character*12 filename

  write(*,5)
5  format(3x,'Enter Filename:')
  read(*,6) filename
6  format(a12)
  write(*,7)
7  format(3x,'Enter Number of Data Points:')
  read(*,8) ndata
8  format(I10)

c
c open the output file and print column headers
c
  open(11,file='output',status='unknown')

c read data from the data files
c
  open(7,file=filename,status='old')
c
  write(*,*) filename,ndata
  do 100 i = 1, ndata
    read(7,*) t(i), c(i)
100 continue
  close(7)
  write(*,333) t(1),c(1)
333 format(2x,'data read into arrays',3x,'t(1)='F13.4,3x,
1    'c(1)='F13.4)
c
```

```

c calculate base for each point based on overall slope
  sumc=0.0
  endc=0.0
  do 99 k=1,25
    sumc = sumc + c(k)
99  continue
    initbase = sumc/25
    do 88 k=ndata-25,ndata
      endc =endc +c(k)
88  continue
    finalbase = endc/26
    slope = (finalbase-initbase)/(t(ndata)-t(1))

    write(*,66) initbase,finalbase
66  format(5x,'initbase:',F14.4,3x,'finalbase:',F14.4)
    do 77 j=1,ndata
      base(j) = initbase + slope*(t(j)-t(1))
      c(j) = c(j) - base(j)
77  continue

c write results to previously opened data file
c

    do 300 m=1,ndata
      write(11,298) t(m),c(m)
298  format(1x,F12.4,1x,F12.4)
300  continue
      close(11)

    stop
    end

```

Program MOMENT13

- program calculates the zeroth to fourth ordinary moments of an ASCII input file containing one column of time, second column of concentration data. Program also calculated weighted moments, but these were not used in this work. From the ordinary moments, the absolute first moment, central second moment and skew are calculated by the program.

```

c moment13.for 5/12/93 Britt Holmen
c uses data files with time in seconds
c calculates dimensional moments!
c
  real c,t,base,s,p,key,cmax,tmode,tsum, w0,w1,w2,w3,w4
  real q,v,flow,vel,poros,col_leng
  real loop,pulse,Tnot,r
  integer ndata
  dimension t(50000), c(50000)
  parameter(poros=0.3)
  character*12 filename

  dimension p(5), q(5), s(5), nw(3), v(5),r(5)

```

```

c   read the INPUT file parameters
c
    write(*,5)
5   format(3x,'Enter Filename:')
    read(*,6) filename
6   format(a12)
    write(*,7)
7   format(3x,'Enter Number of Data Points:')
    read(*,8) ndata
    write(*,9)
9   format(3x,'Enter base:')
    read(*,10) base

8   format(I10)
10  format(F6.2)
c
c   open the output file and print column headers
c
    open(11,file='output',status='unknown')
    write(11,200)
200  Format(1x,' file',7x,'base', nw ',7x, 'Oth',7x,
C     '1st',6x,'2nd',8x, '3rd',6x,'4th',10x,'absl',10x,'var',
C     10x,'skew')
    write(11,222)
222  format(1x,'-----
c-----')

    write(*,900)
900  format(5x,'Enter Column Flow Rate in mL/min:')
    read(*,901) flow
901  format(F8.4)
    write(*,902)
902  format(5x,'Enter Loop size in microliters:')
    read(*,903) loop
903  format(F9.4)

    col_leng = 7.0
c   velocity in cm/sec; Tnot in seconds
    vel = flow/(60*poros*3.8)
    pulse = loop*0.06/flow
    Tnot = pulse
    write(*,223) loop
223  format('loop=', F9.4)

c   read data from the data files
c
    open(7,file=filename,status='old')
c
    do 100 i = 1, ndata
        read(7,*) t(i),c(i)
100  continue
    close(7)
    write(*,333)
333  format(2x,'data read into arrays')
c
c   loop to calculate weighting factor
c

```

```

    key = 0.0
    tsum = 0.0

do 101 i = 1, ndata
  if (c(i).gt.key) then
    key = c(i)
    tmode = t(i)
    cmax = c(i)
  endif
  tsum = tsum + t(i)
101 continue

    s(0) = ndata/tsum
do 102 n = 1,4
  s(n) = n/tmode
102 continue
write(*, 444) s(0), s(1), s(2), s(3), s(4)
444 format(2p,1x,5E12.3, 'weighting factors')

c calculate the (weighted) moments
c
nw(0) = 0

do 103 l=1,2
  nw(l) = nw(l-1) +1

sum0=0.
sum1=0.
sum2=0.
sum3=0.
sum4=0.
abs1=0.
cent1=0.
cent2=0.
cent3=0.
cent4=0.

do 110 i = 2, ndata
  w0=1.0
  w1=1.0
  w2=1.0
  w3=1.0
  w4=1.0
  if (nw(l).ne.1) then
    w0=exp(-s(0)*t(i))
    w1=exp(-s(1)*t(i))
    w2=exp(-s(2)*t(i))
    w3=exp(-s(3)*t(i))
    w4=exp(-s(4)*t(i))
  endif
  dt = t(i)-t(i-1)
  cave = (c(i)+c(i-1))/2.0 - base
  tave = (t(i)+t(i-1))/2.0
  sum0 = sum0 + w0*cave*dt
  sum1 = sum1 + w1*cave*tave*dt
  sum2 = sum2 + w2*cave*tave**2*dt

```

```

        sum3 = sum3 + w3*cave*tave**3*dt
        sum4 = sum4 + w4*cave*tave**4*dt
110    continue

        write(*,555)
555    format(1x,'ordinary moment loop OK')
c
c    calc central moments
c
    DO 120 i=2, ndata
        dt = t(i)-t(i-1)
        cave = (c(i)+c(i-1))/2.0 - base
        tave = (t(i)+t(i-1))/2.0

        abs1= sum1/sum0
        cent1 = cent1 + (tave - abs1)*cave*dt
        cent2 = cent2 + (tave - abs1)**2*cave*dt
        cent3 = cent3 + (tave - abs1)**3*cave*dt
        cent4 = cent4 + (tave - abs1)**4*cave*dt
120    continue
        var = (sum2/sum0) - (sum1/sum0)**2
        u1 = cent1/sum0
        u2 = cent2/sum0
        u3 = cent3/sum0

        skew = u3/(u2)**1.5

        write(*,666) nw(l)
666    format(1x,'finished central loop', 'nw=', I2)

c    set aside absolute 1st moment
        p(l) = abs1
c    set aside u2
        q(l) = u2
c    set aside u3
        v(l) = u3
c    set aside skew
        r(l) =skew

c    write results to previously opened data file
c
        write(11,295) filename,base,nw(l),sum0, sum1, sum2
C        , sum3, sum4,abs1,var,skew
295    Format(2p,1x,A12,1x,E8.1,2x,I2,3x,8(E10.3,1x))
        if(nw(l).ne.1) then
            write(11,300) s(0),s(1),s(2),s(3),s(4)
        else
            write(11,301)
        endif
300    Format(2P,10x,'weighting factors:', 10x, 5E12.3)
301    Format(10x,'unweighted moments')
        write(11,303)
303    format(' ')
103    CONTINUE

c
        write(11,288) Tnot

```

```

288  Format(/,10x,'pulse duration in sec = ',E13.2,/)
c
c
      write(11,399) tmode
399  format(2P,10x,'tmode=',E13.4)
      write(11,499) cmax
499  format(2P,10x,'cmax=',E13.4)
      write(11,599) tsum
599  format(2P,10x,'tsum=',E13.4)
      write(11,699) ndata
699  format(2p,10x,'ndata=',I12)
      write(11,700) v(1)
700  format(2P,10x,'u3:',3x,'v(1)=',E13.4)
      write(11,800) q(1)
800  format(2P,10x,'u2:',3x,'q(1)=',E13.4)
      write(11,801) p(1)
801  format(2P,10x,'abs1:',3x,'p(1,1)=',E13.4)
      write(11,802) r(1)
802  format(2P,10x,'skew:',3x,E13.4)

c

      vel = vel*3600

      write(11,909) col_leng,vel,flow,poros
909  format(/,5x,'COL length=',4x,F4.2,3x,'Velocity(cm/hr)=',4x,F10.3,
c    /,'flow rate=', 3x,F9.3,' mL/min',10x,'porosity=',2x,F8.4)

      write(11,910)
910  format(///,'moment13.for')
      close(11)

      stop
      end

```

Program CXTFIT (not listed)

- program was obtained from J. Parker (Virginia Polytech.) and is described in detail in the following reference:
Parker, J. C. and M. Th. van Genuchten. (1984) Determining transport parameters from laboratory and field tracer experiments. Virginia Agricultural Experimental Station: Bulletin 84-3, Virginia Polytechnic Institute and State University, Blacksburg, VA 24061.
- I modified CXTFIT to take files up to 500 data points in length. This program is called 500CXT.
- A previous version of CXTFIT, CFITIM, was obtained from the U.S. Salinity Lab, Riverside, CA and was modified to accept 200 data points. This program is called CFIT200.

Program 200COUNT

- program reduces large data files to files of 200 data points for use with CFIT200.

```

c 200count.for 5/09/94 Britt Holmen
c reduces data files to 200 points for use with CFITIM20 or CFIT200
c
      real c,t,cout,tout
c vars:conc,time

```



```

c      integer numout,ndata,sampint,point
c vars:#output data pts, # input data pts,sampling interval
      dimension t(20000), c(20000),tout(200),cout(200)
      dimension point(20000)
      character*12 filename, fileout
c
      write(*,799)
799  format(4x,'200count.for',/,4x,'Enter filename:')
      read(*,800) filename
      write(*,798)
798  format(4x,'Enter number of data points:')
      read(*,801) ndata
      sampint=ndata/200
      numout=200
      write(*,797) sampint
797  format(4x,'sampling interval is every ',I10,2x,'points')

800  format(A12)
801  format(I10)

c      read data from the data files
c
      open(7,file=filename,status='old')
c
      do 200 i = 1, ndata
      read(7,*) t(i),c(i)
200  continue
      close(7)
      write(*,333)
333  format(2x,'data read into arrays')
c
c
c      the k-loop controls the output array
c
      point(1) = 1
      tout(1)=t(1)
      cout(1)=c(1)

      do 600 k = 2,numout

      point(k) = point(k-1) + sampint
      j=point(k)
      tout(k) = t(j)
      cout(k) = c(j)
      write(*,888) tout(k),cout(k)
888  format(10x,F12.4,2x,F12.4)

600  continue

c
c      write to the output file
c
      write(*,777)
777  format(5x, 'Enter output filename: ',/)
      read(*,701) fileout

```

```
701 format(A12)
    open(12,file=fileout,status='unknown')

    do 100 i=1,numout
      write(12,222) tout(i),cout(i)
100  continue
222  Format(1x,F12.4,3x,F12.4)

    close(12)
    stop
    end
```

Appendix B: Error Propagation Expressions

The following equations were used to calculate the reported one standard deviation errors for all moment-derived model parameters. The equations are based on propagation-of-error techniques and the single-site, first-order moment expressions of Valocchi (1985) as outlined in equations (2-1) to (2-5') in Chapter 2.

Equations (2-4) and (2-5') were recast into the following general forms:

$$\mu_1' - \frac{t_0}{2} = \frac{A}{v}; \quad \text{where } A = LR$$

$$\mu_2 - \frac{t_0^2}{12} = \frac{A}{v^2} + \frac{B}{v}; \quad \text{where } A = 2L\alpha R^2, B = 2L(R-1)/k_r$$

For all calculations, it was assumed that variances (V) of fit values = (SE)² where SE = standard error as determined by SigmaPlot curve-fitting. We assumed one standard deviation of the model parameter was equal to the square root of the calculated variance.

A_i = curve – fit A (or B) value for i^{th} moment expression

V_j = variance of j^{th} parameter

column length, L: error given by SE of curve-fit.

retardation factor, R:
$$V_R = \left(\frac{R}{A_{\mu 1}}\right)^2 V_{A_{\mu 1}} + \left(\frac{-R}{L}\right)^2 V_L$$

dispersivity, α :
$$V_\alpha = \left(\frac{\alpha}{A_{\mu 2}}\right)^2 V_{A_{\mu 2}} + \left(\frac{-\alpha}{L}\right)^2 V_L$$

sorption rate constant, k_r :
$$V_{k_r} = \left(\frac{-k_r}{B_{\mu 2}}\right)^2 V_{B_{\mu 2}} + \left(\frac{k_r}{L}\right)^2 V_L + \left(k_r - \frac{2L}{B_{\mu 2}}\right)^2 V_R$$

Appendix C: Breakthrough Curves

Raw Data. All of the column elution curves used to calculate the model parameters in this research are shown here as plots of absorbance (NO_3^- , acetone, naphthalene, acenaphthene) or fluorescence (phenanthrene) signal on the y-axis and elapsed time in seconds on the x-axis. The curves are labelled by sorbent (PB,GT or AJ), compound (ACE = acenaphthene; acet = acetone, NAP = naphthalene, PHEN = phenanthrene, and NO_3 = nitrate), and date of measurement (month,date,year). The corresponding flow rates can be found using the following table which identifies all the experimental runs, sorted by flow rate. The BTCs were truncated as described in the text of this thesis.

Simulated BTCs. Following the data curves are sixteen BTCs and the corresponding simulated BTCs generated using CXTFIT and the single-site, first-order model parameters described in the text. The simulations were performed using the moment-derived model parameters for R , α and k_r found in Tables 3-3 and 4-6. Velocity was calculated from flow rate (Q) using the appropriate sorbent porosity values (0.42 for PB and 0.27 for GT and AJ). CXTFIT was run as a BTC generator using the constraint that $\beta = 1/R$ in order to convert the 2-site CXTFIT model into a single-site sorption model. Some simulated BTCs appear to have much smaller R values than the data (i.e., PBACE_FAST, PBPEN_FAST), however, the long near-zero tails on the simulated BTCs extend to very long elution times and account for the apparent discrepancy in R . The early breakthrough of some simulated BTCs relative to the data, particularly at the higher flow velocities (i.e., PBPHEN_FAST, AJACE_FAST) may indicate that we have underestimated the value of k_r . The particularly poor fits for the fast runs of PBPHEN and AJACE are a result of the very low β values for these sorbate-sorbent pairs due to the relatively high R values. For example, the β value for PBPHEN simulations is 0.04, indicating that, in terms of a 2-site model, only 4% of the sorption sites are readily available for instantaneous sorption. The result is early elution of the peak and a long low concentration tail when the sorption rate is slow relative to the flow rate.

One high velocity and one low velocity experimental run were simulated for each sand/sorbate pair studied. The runs that were simulated are marked with an asterisk in the following table.

Column Experiment Information and Moments

Sand-Cpd	Date	Q [mL/min]	u_1' [sec]	u_2 [sec ²]
PB-Nitrate				
	4/12/1993	0.006	97000	1.2000e+08
	9/17/1993	0.009*	70586	9.6005e+07
	2/1/1993	0.022	30151	4.8754e+07
	12/19/1993	0.023	28955	5.8001e+07
	4/27/1993	0.032	25000	8.1000e+07
	11/6/1992	0.05	13071	4.1141e+06

12/10/1992	0.04	13812	9.8371e+06
11/19/1992	0.2	4776.2	1.2100e+06
11/22/1992	0.15	4288.3	1.2912e+06
11/20/1992	0.17	4168.4	6.9776e+05
1/12/1993	0.17	4125.7	2.1301e+06
1/22/1993	0.18	3980.2	1.6430e+06
4/2/1993	0.18	3600.0	5.5000e+05
4/5/1993	0.186	3800.0	6.9000e+05
1/13/1993	0.19	3417.4	3.8203e+05
12/31/1992	0.24	2915.9	5.1444e+05
3/19/1993	0.42	1457.7	5.4765e+05
3/29/1993_1	0.48*	1300.0	36000
3/29/1993_2	0.48	1300.0	41000
3/29/1993_3	0.48	1400.0	66000
3/29/1993_4	0.48	1300.0	7000.0

PB-Acenaphthene

5/7/1993	0.008	3.4 e+05	6.3000e+09
5/29/1993	0.01*	2.2 e+05	4.5000e+09
9/4/1993	0.021	1.38 e+05	3.7308e+09
2/3/1993	0.021	1.16 e+05	1.3895e+09
12/16/1992	0.023	89205	4.2308e+08
4/28/1993	0.030	51000	1.5000e+08
11/21/1992	0.175	11033	1.3243e+07
1/22/1993	0.178	9818.9	5.0080e+06
4/5/1993	0.185	9200.0	5.4000e+06
1/12/1993	0.19	11164	1.4779e+07
5/21/1993	0.232	7700.0	9.1000e+06
3/31/1993	0.466*	3500.0	2.0000e+06
5/20/1993	0.467	3600.0	1.8000e+06
3/31/1993	0.471	3500.0	1.8000e+06
3/19/1993	0.50	3537.9	2.4214e+06

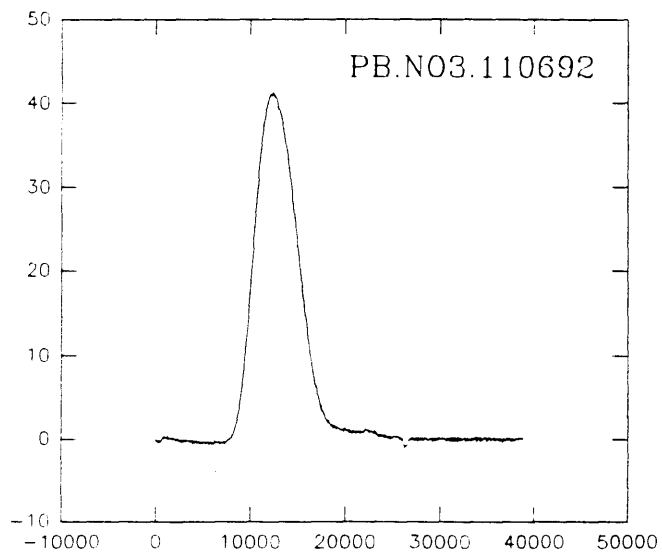
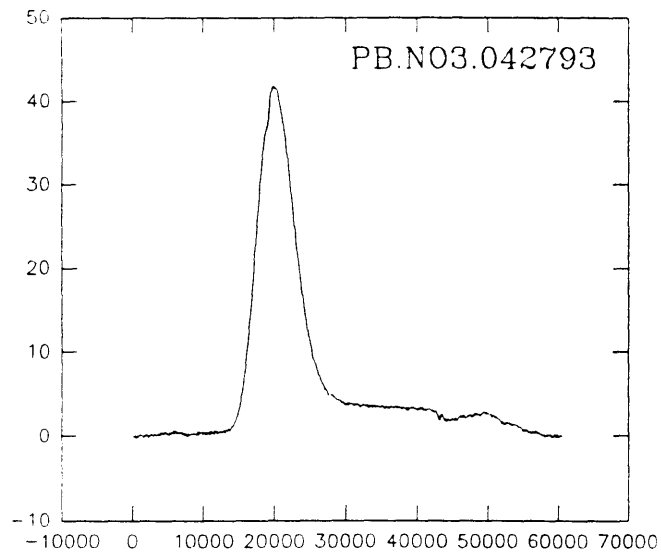
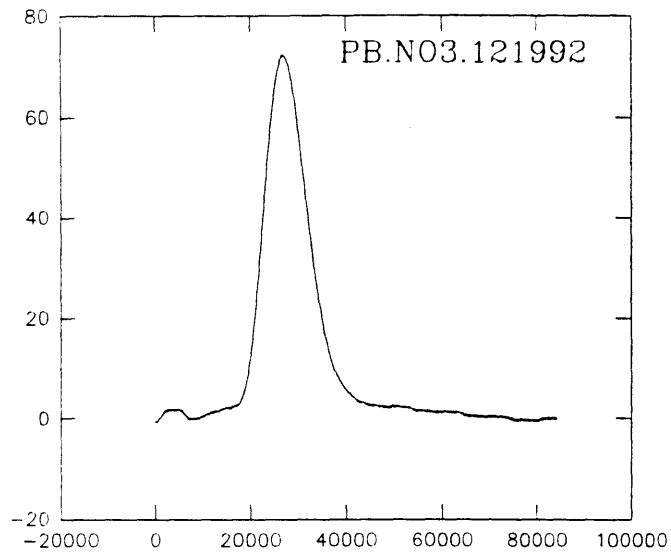
PB-naphthalene

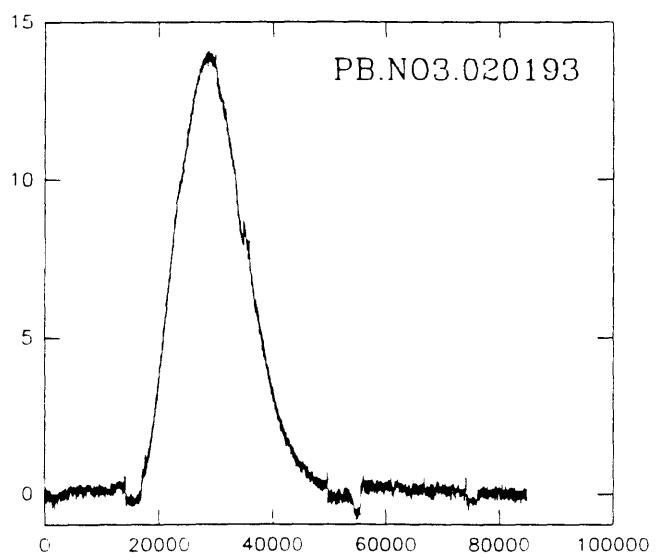
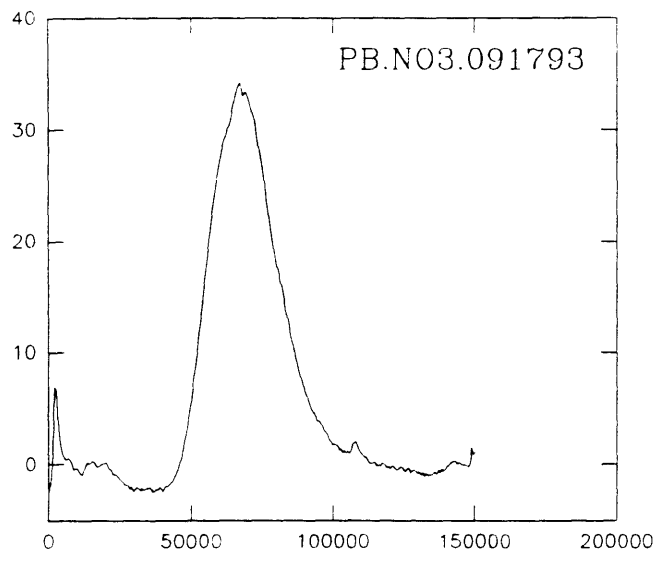
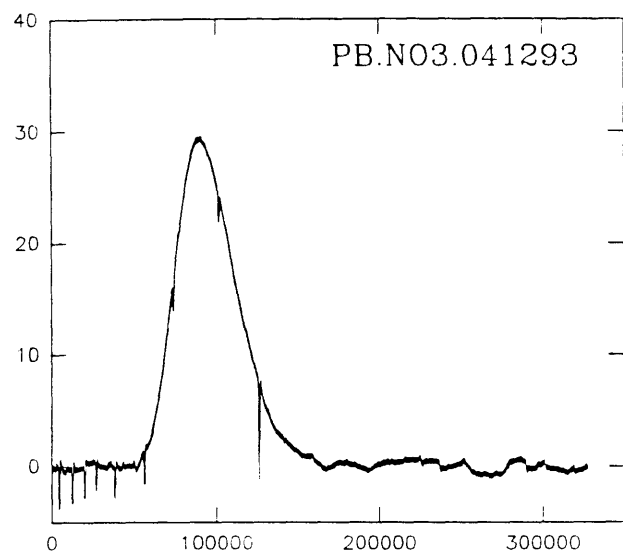
9/29/1993	0.0091	87010	3.9440e+08
11/5/1993	0.0104*	86640	1.7740e+08
11/12/1993	0.0122	76620	8.7940e+07
12/5/1993	0.013	71910	1.6230e+08
11/30/1993	0.013	73260	4.0580e+08
10/4/1993	0.021	28930	2.0790e+08
11/18/1993	0.026	36820	4.4100e+07
10/26/1993	0.092	9001.0	4.9470e+06
11/2/1993	0.173	5598.0	9.6800e+05
5/22/1993	0.231	3969.0	1.4580e+06
11/3/1993	0.426	2111.0	3.5580e+05
11/3/1993	0.434	2150.0	4.3600e+05
5/19/1993	0.468	1941.0	3.3030e+05
11/4/1993	0.663*	1436.0	1.8530e+05

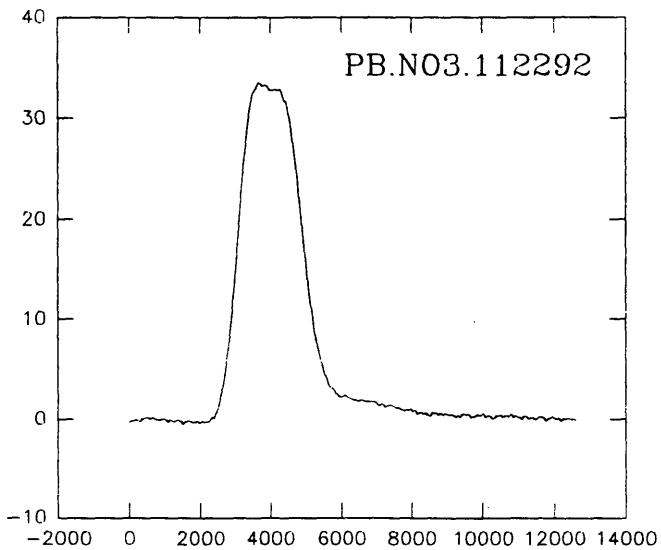
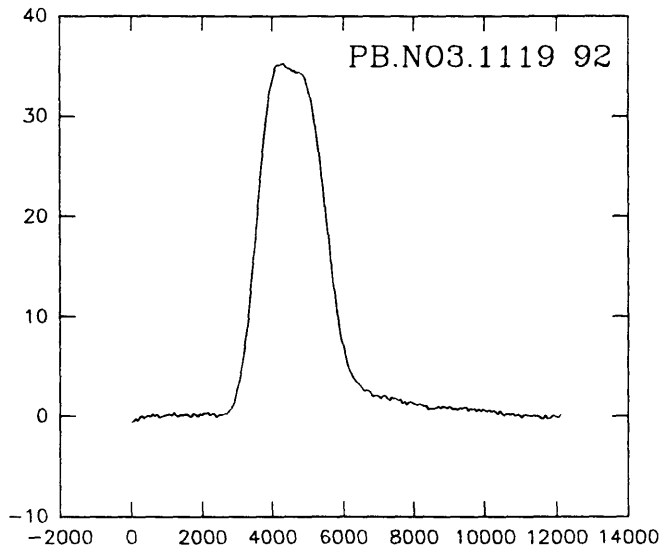
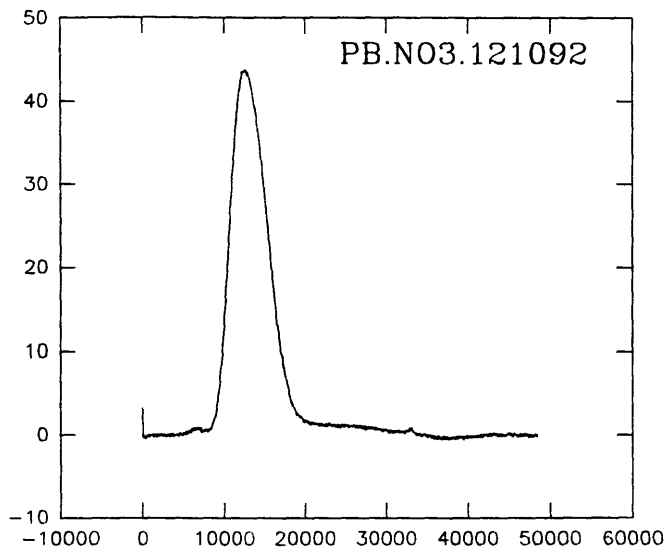
PB-phenanthrene

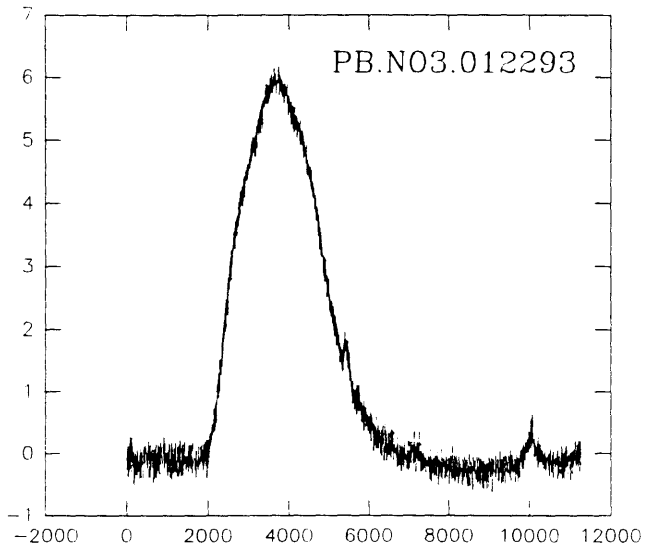
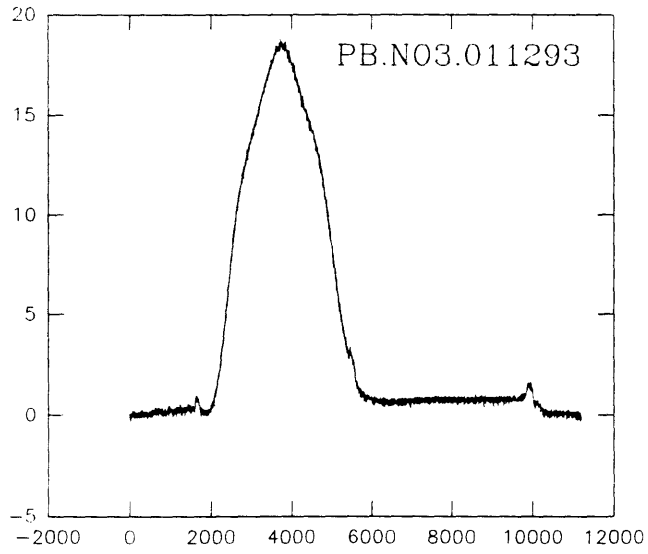
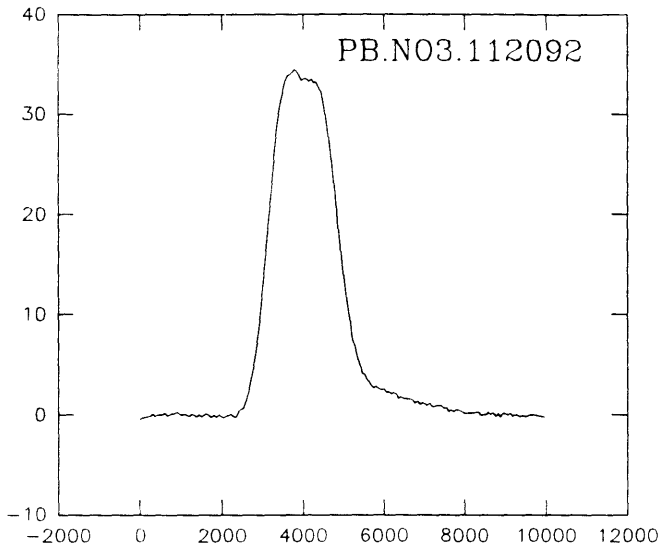
11/2/1994	0.009*	1.7240e+06	2.5876e+11
5/2/1994	0.019	7.4175e+05	6.6591e+10

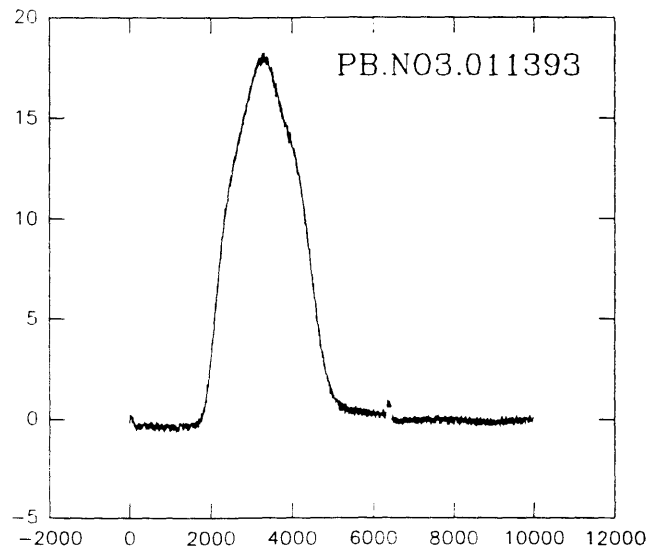
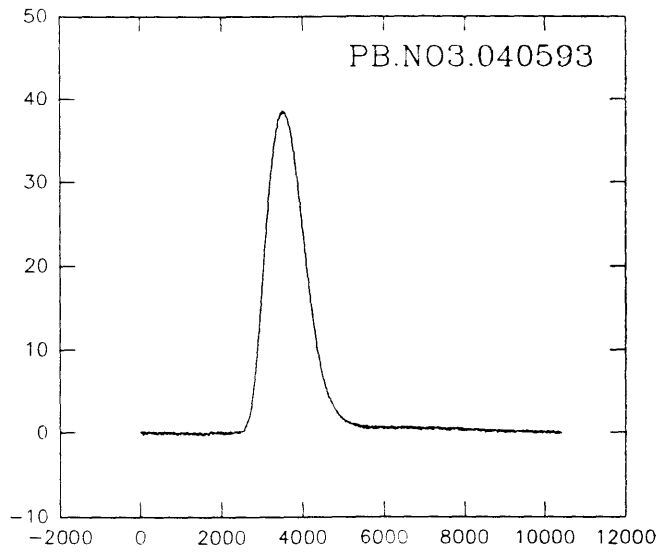
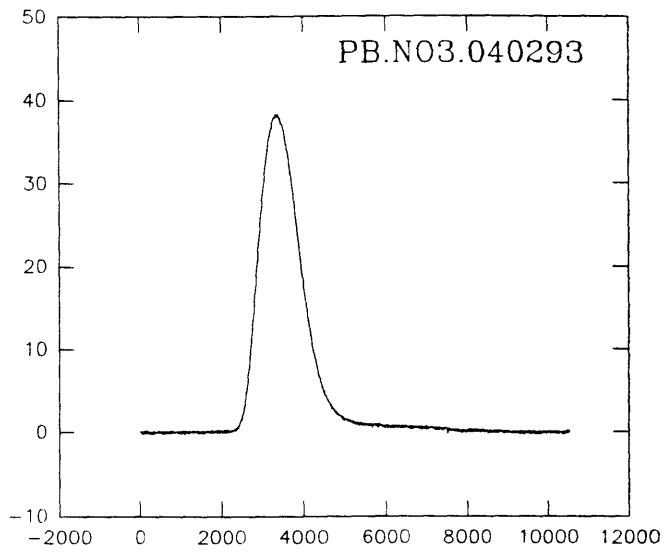
	4/21/1994	0.040	3.4970e+05	1.8624e+10
	4/11/1994	0.080	1.1442e+05	9.4136e+08
	4/16/1994	0.080	1.5073e+05	4.7311e+09
	4/7/1994	0.280	37131	3.2104e+08
	5/26/1994	0.386	28528	2.0436e+08
	5/25/1994	0.98*	9946.8	2.9105e+07
GT-acetone				
	5/1/1994	0.005*	1.4067e+05	3.9782e+09
	4/10/1994	0.0097	63217	8.9647e+08
	4/7/1994	0.0139	62455	8.1801e+08
	4/12/1994	0.0155	42294	8.5024e+08
	3/5/1994	0.0341	19841	4.8623e+08
	2/28/1994	0.037	15781	1.0709e+08
	2/22/1994	0.074	7790.2	3.4474e+07
	5/26/1994	0.078	10067	8.0723e+07
	2/19/1994	0.194	2677.3	3.7712e+06
	5/27/1994	0.260	2236.1	2.7792e+06
	5/29/1994	0.268	3226.0	9.2516e+06
	5/31/1994	0.460*	1939.4	4.7460e+06
GT-Acenaphthene				
	4/23/1994	0.0066	2.1914e+05	7.2110e+09
	4/18/1994	0.0109	1.3346e+05	3.0051e+09
	3/11/1994	0.016	94242	1.1286e+09
	4/14/1994	0.017	1.0966e+05	3.6065e+09
	4/2/1994	0.020*	75309	2.2205e+09
	3/21/1994	0.022	48542	6.4895e+08
	6/8/1994	0.0262	78786	1.2679e+09
	5/11/1994	0.0280	45928	5.1448e+08
	5/28/1994	0.266	5994.6	4.6493e+07
	5/29/1994	0.27	5514.8	3.7902e+07
	5/30/1994	0.45	6864.8	4.1294e+07
	5/31/1994	0.463*	4899.9	5.5243e+07
AJ-acetone				
	7/3/1994	0.0149*	42379	8.0502e+07
	6/20/1994	0.039	15604	1.0599e+07
	6/17/1994	0.111	5479.0	1.5076e+06
	6/15/1994	0.252	2458.1	3.6347e+05
	6/14/1994	0.754*	869.84	869.84
AJ-Acenaphthene				
	7/6/1994	0.0237	1.4124e+05	2.9094e+09
	6/21/1994	0.038*	71903	1.2345e+09
	6/17/1994	0.039	60075	1.5459e+09
	6/15/1994	0.112	20267	1.2940e+08
	6/14/1994	0.251	10555	5.0951e+07
	7/18/1994	0.49	3672.6	1.8999e+06
	6/14/1994	0.769*	2817.7	3.6845e+06

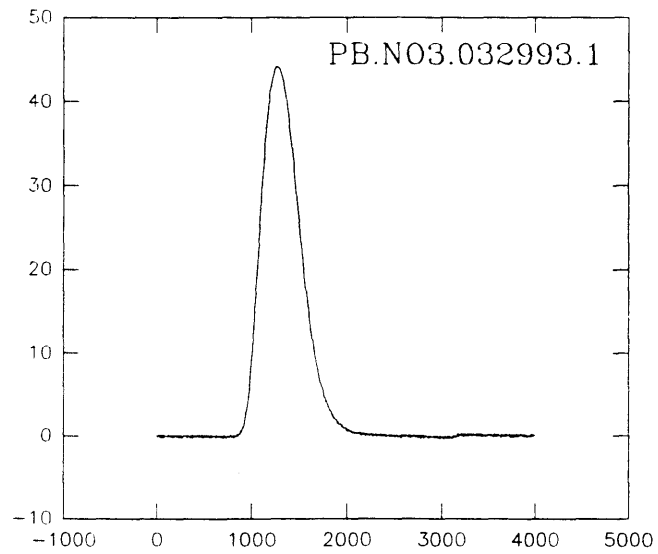
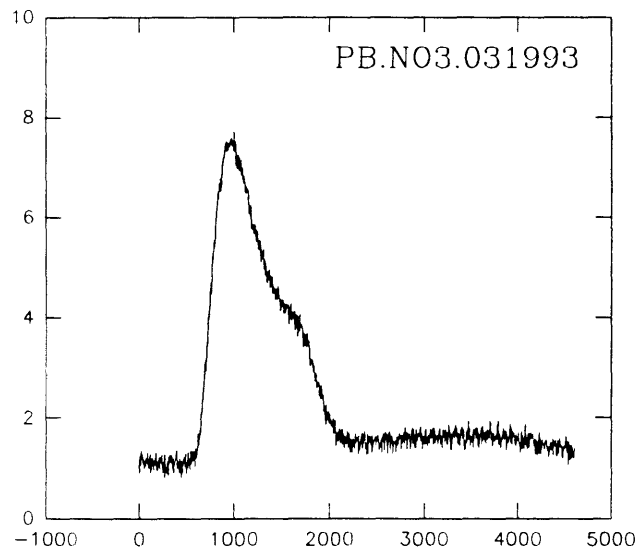
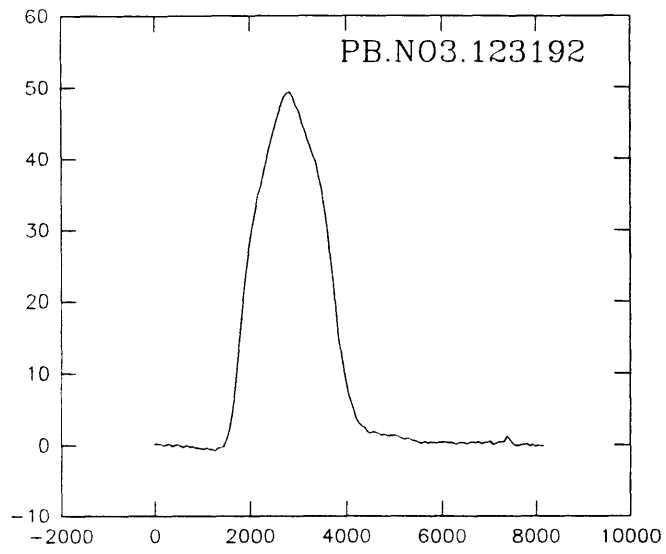


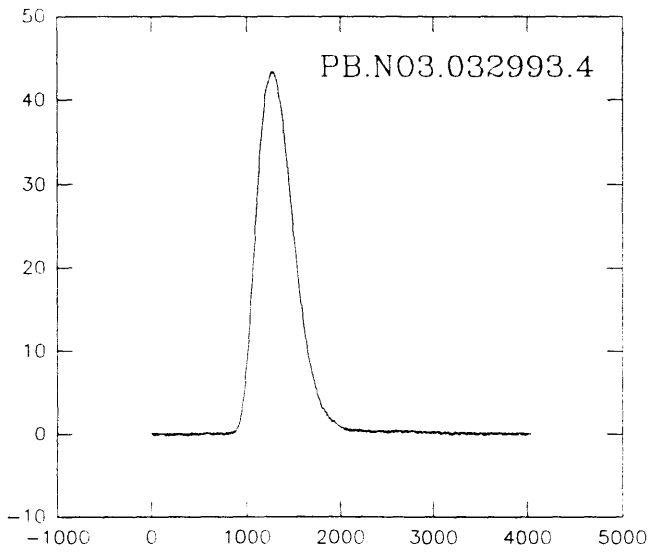
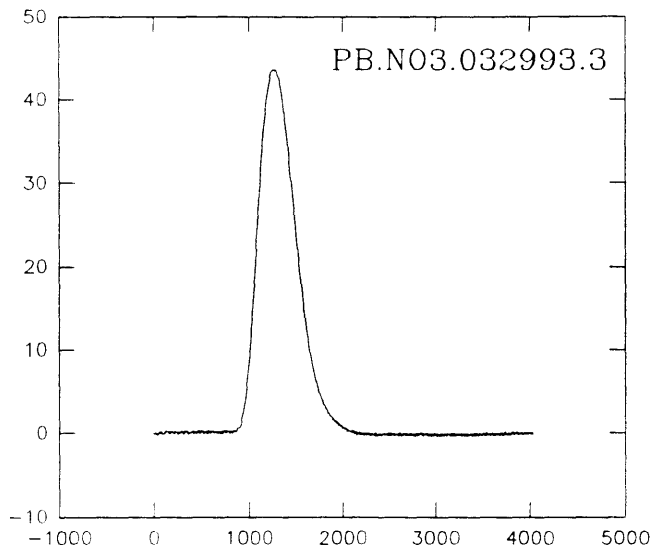
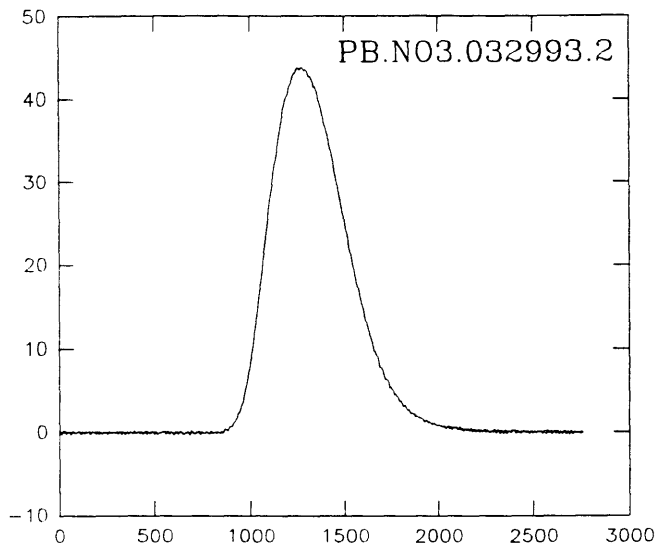


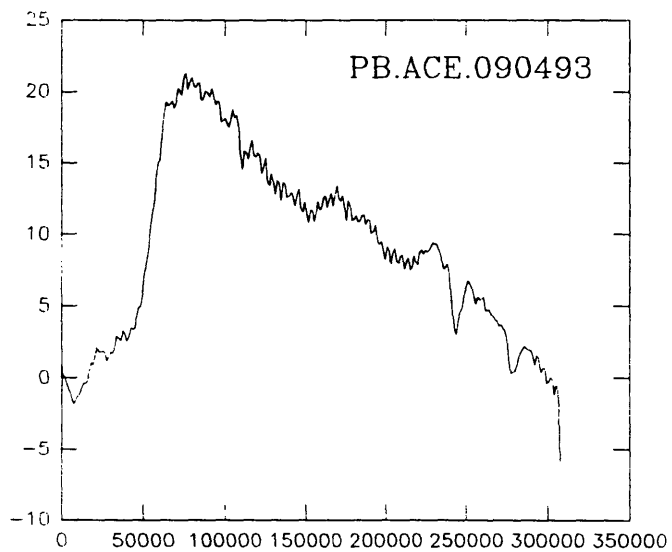
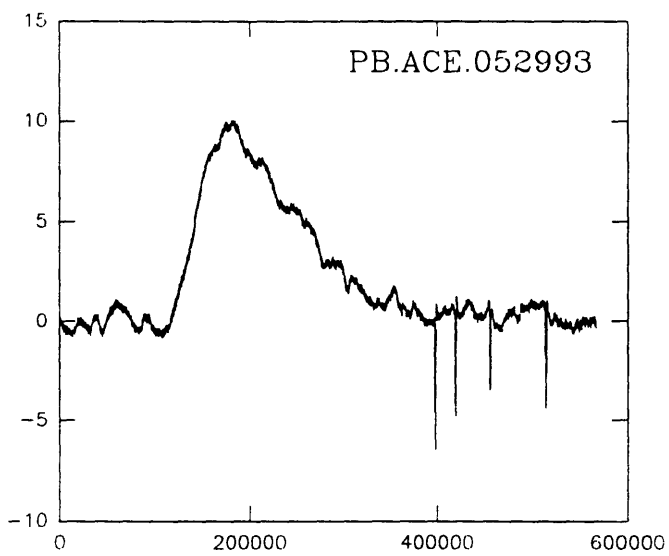
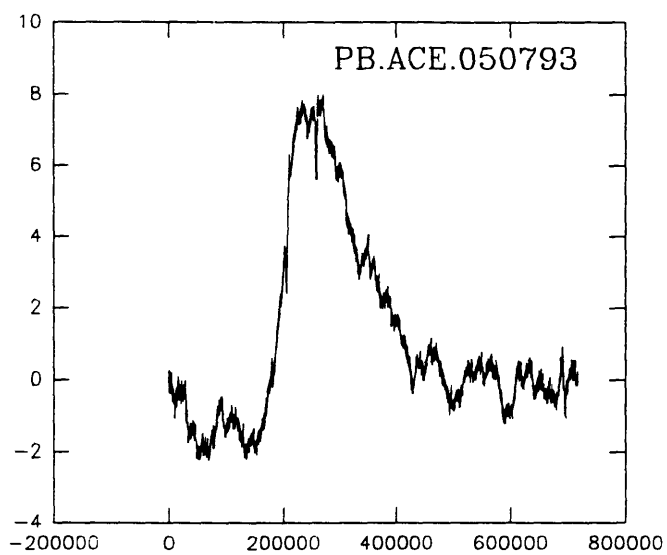


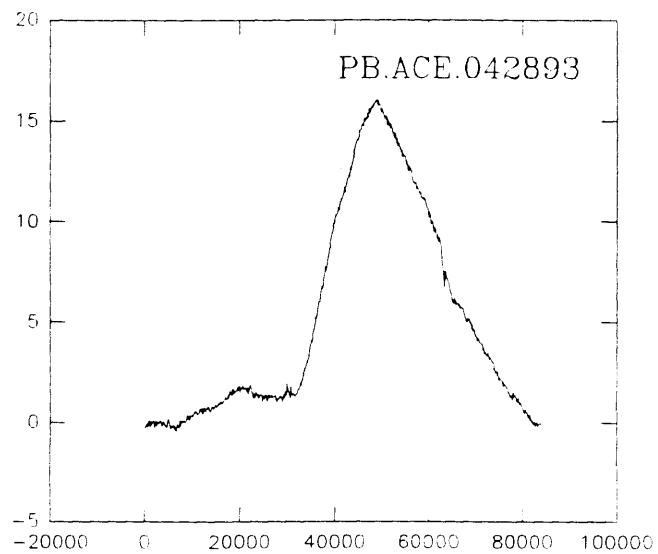
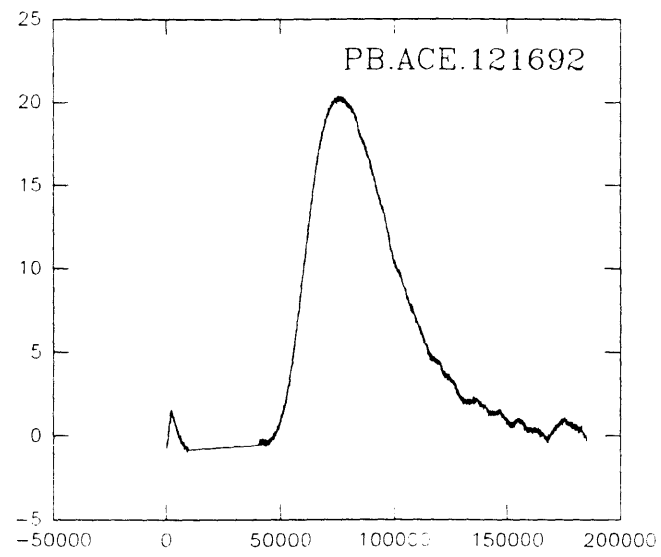
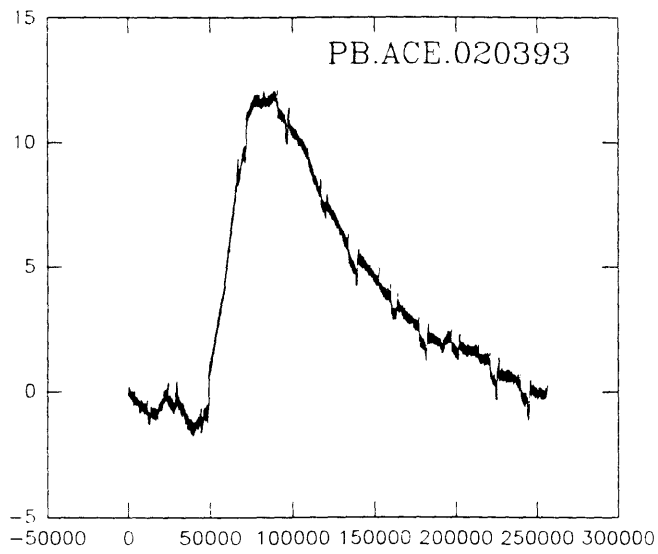


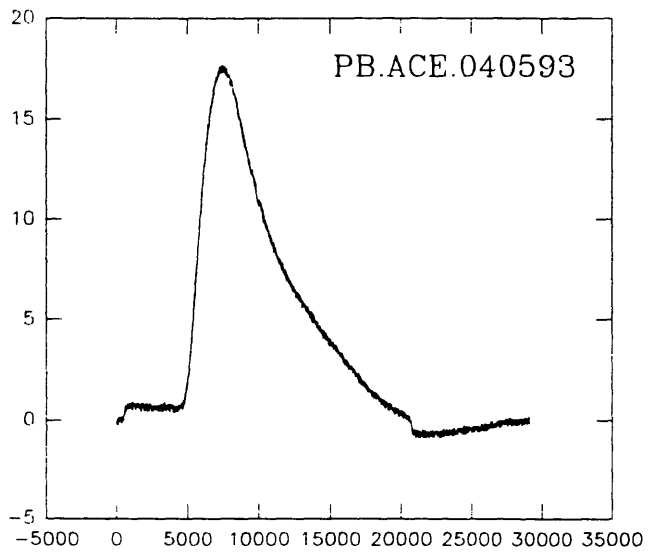
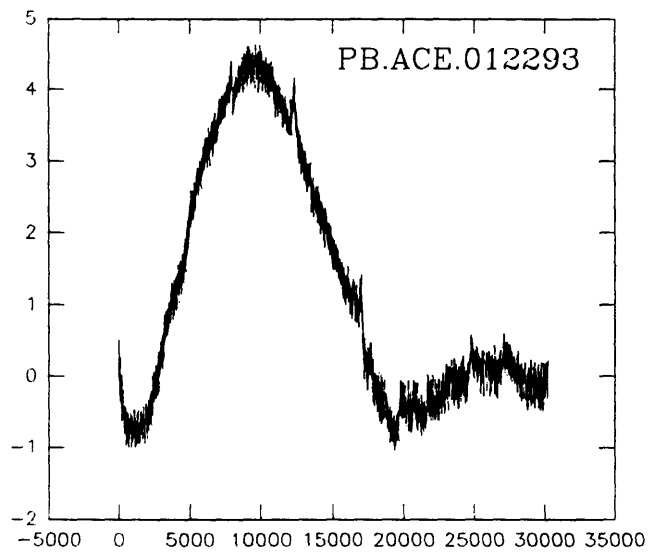
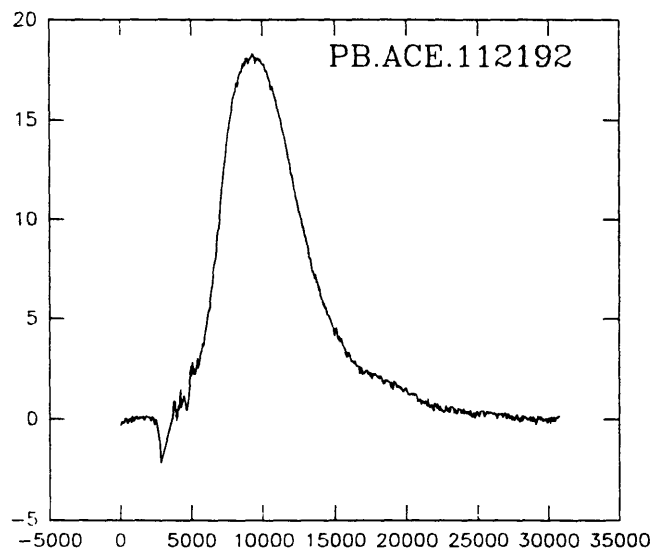


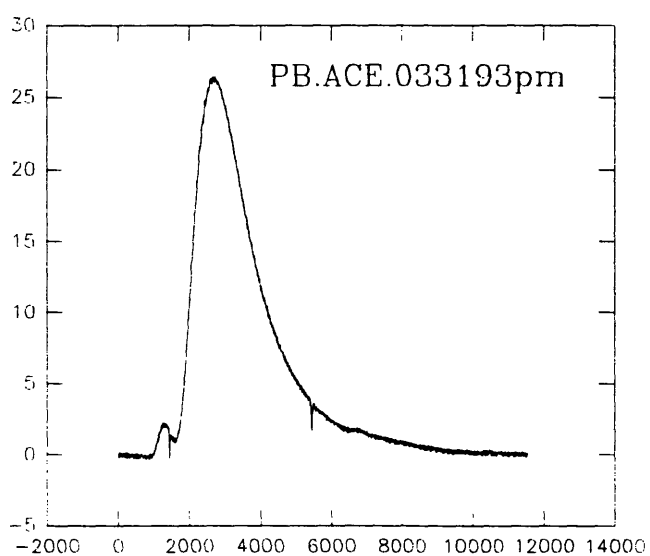
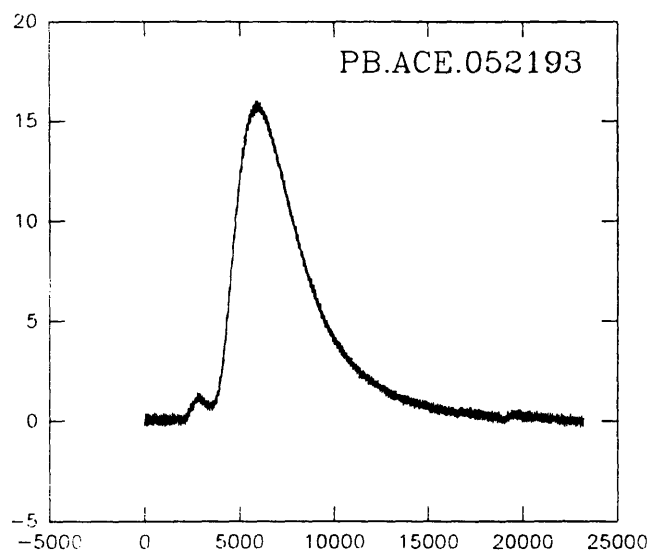
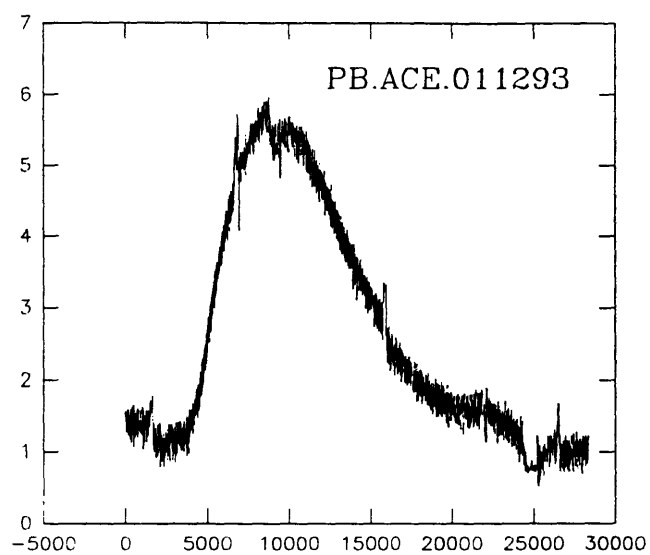


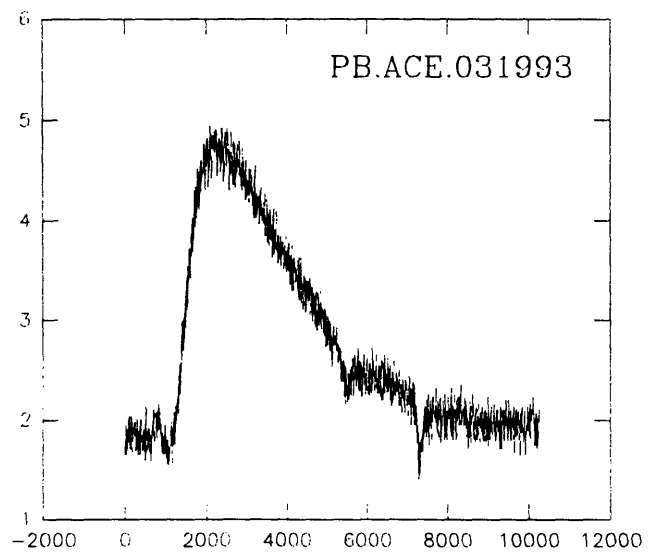
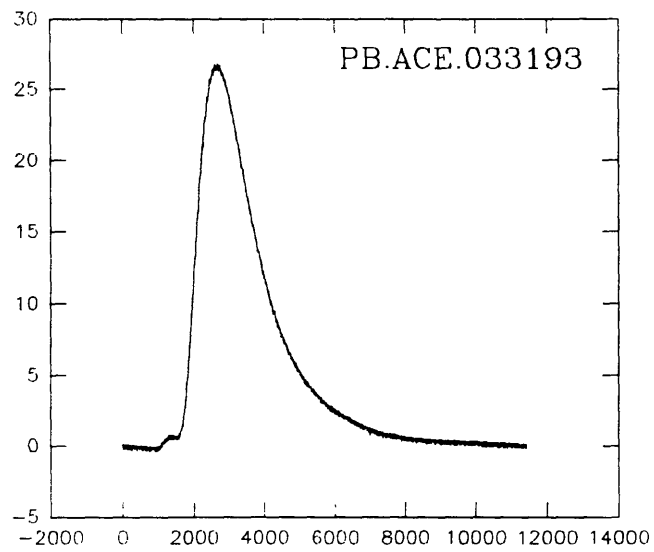
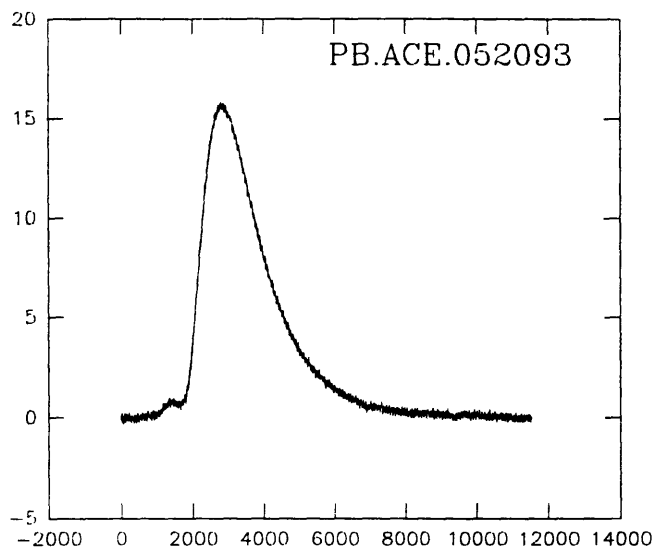


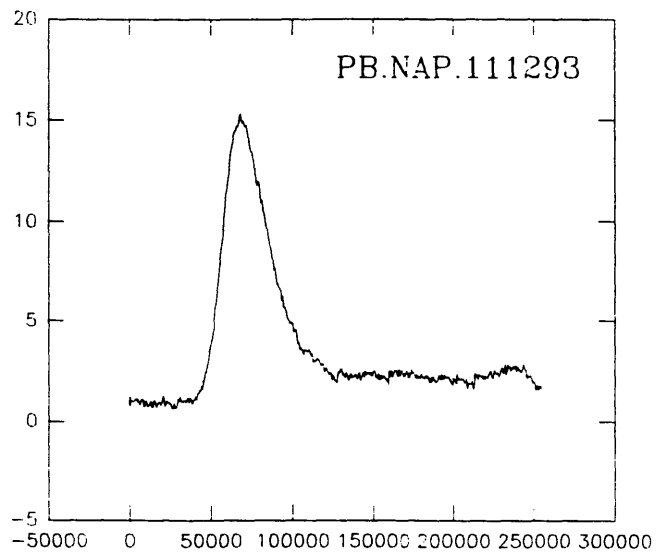
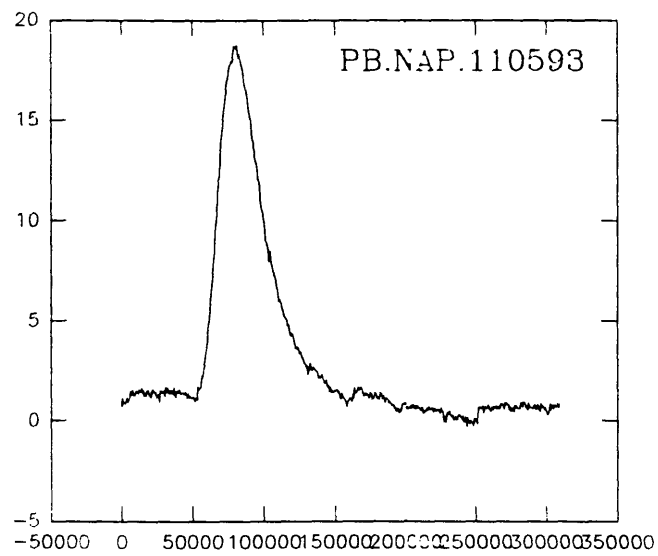
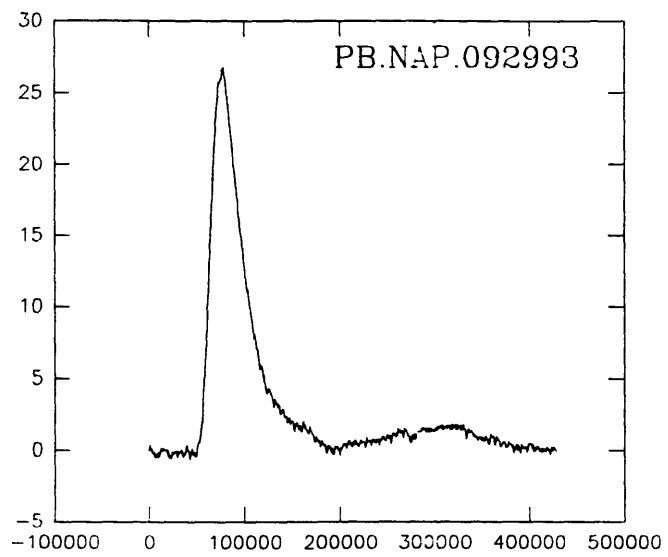


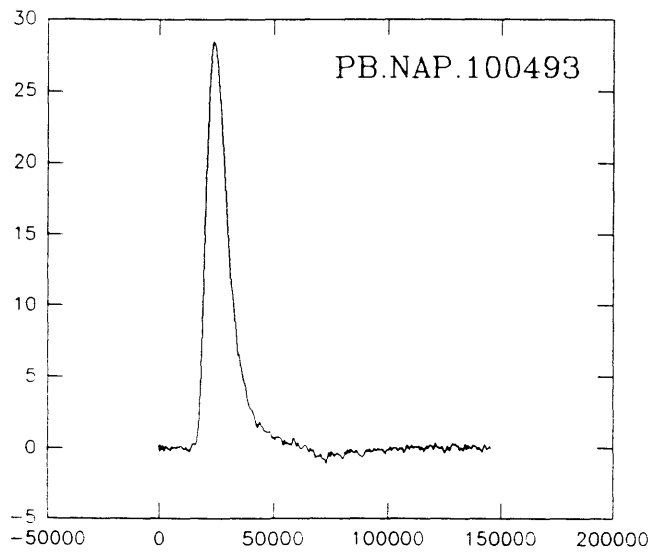
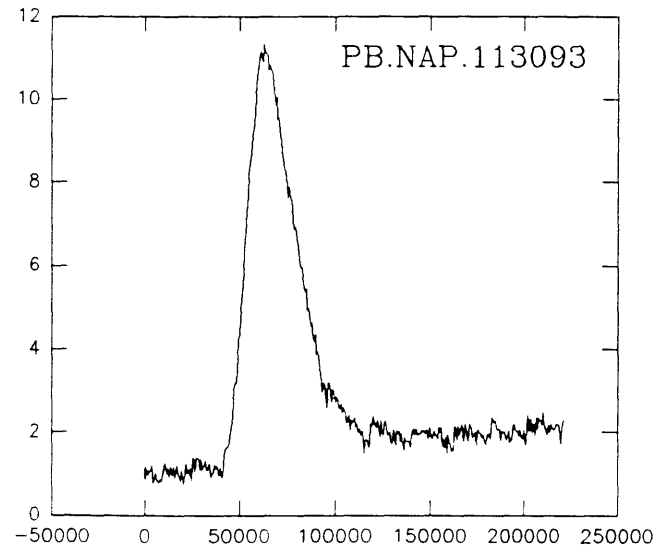
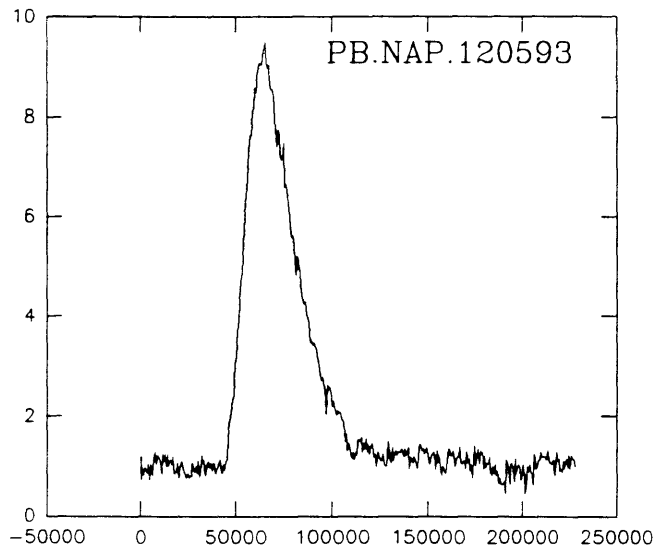


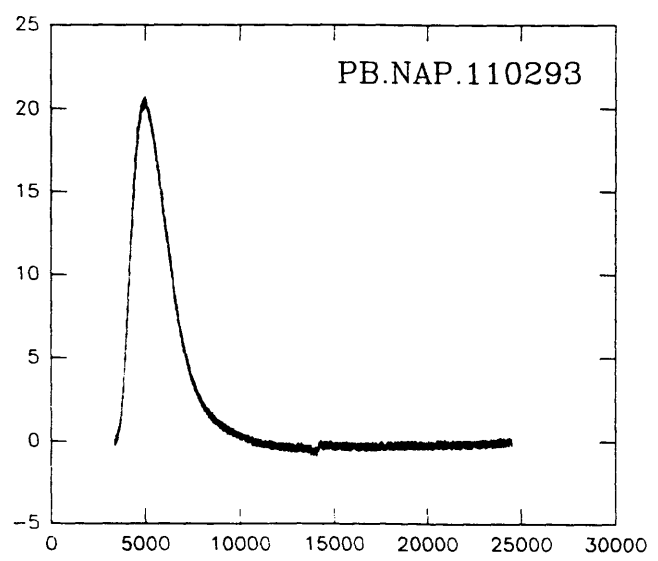
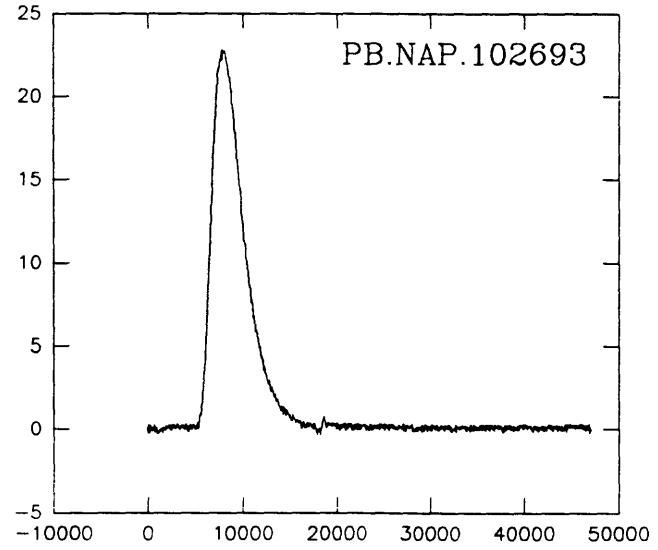
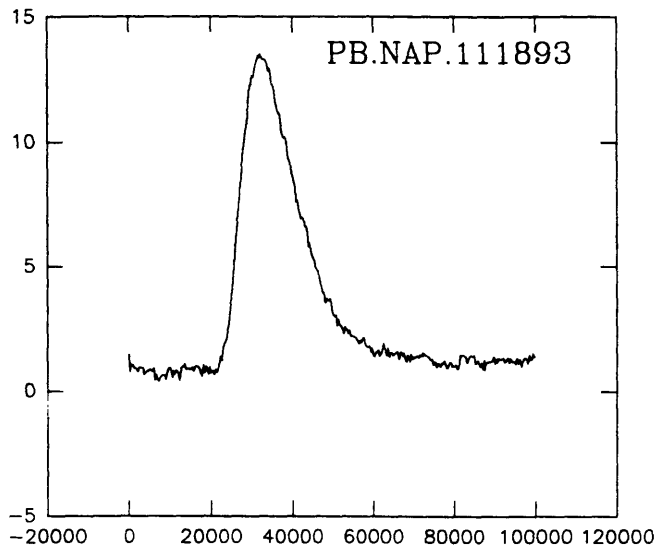


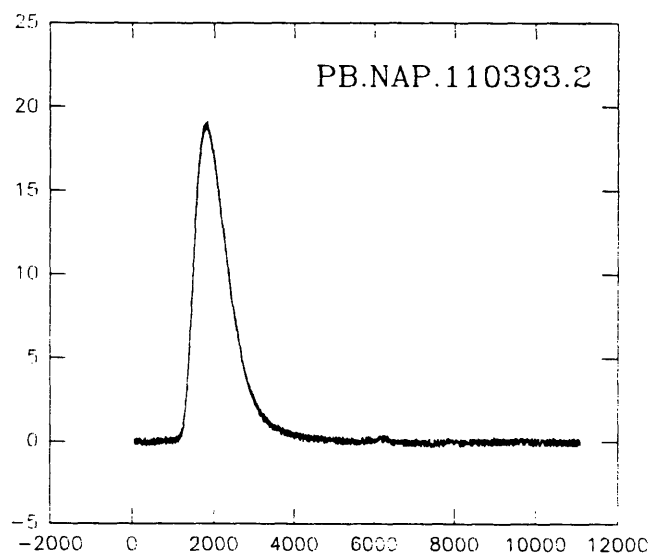
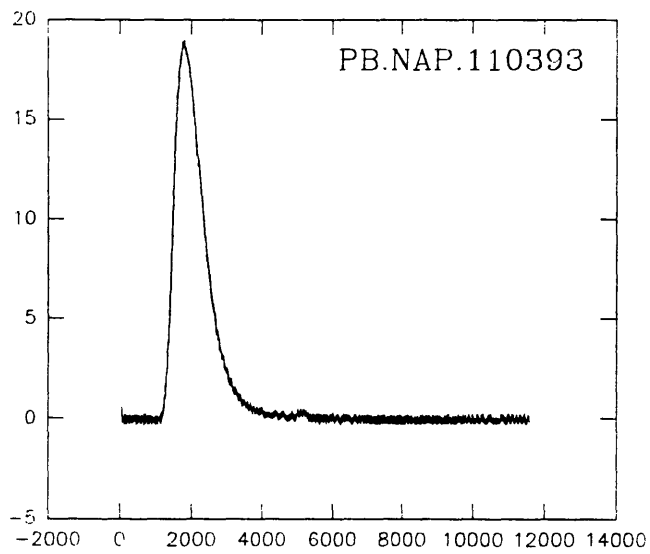
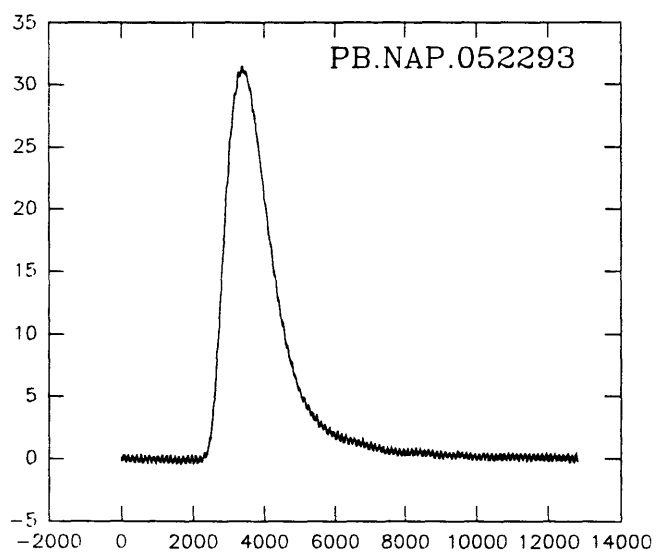


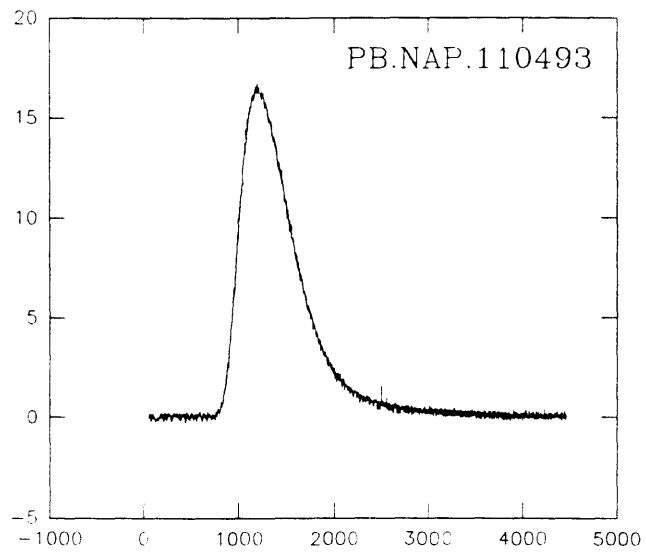
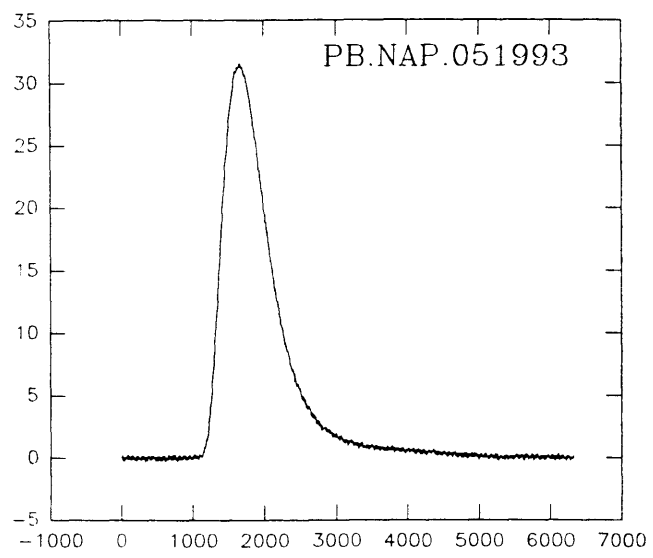


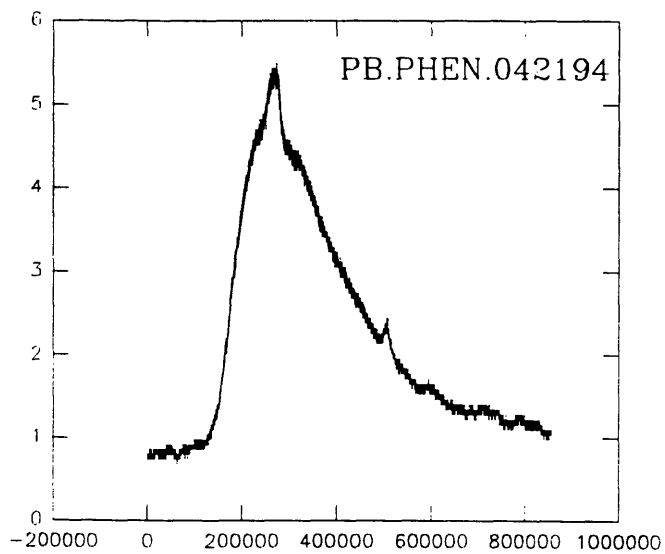
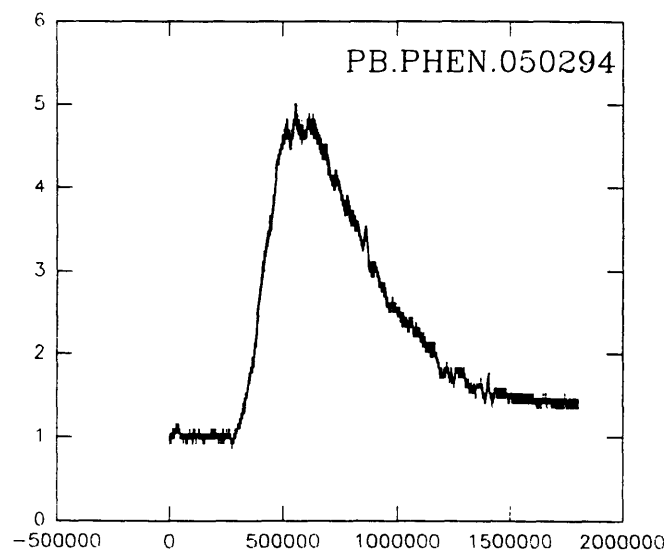
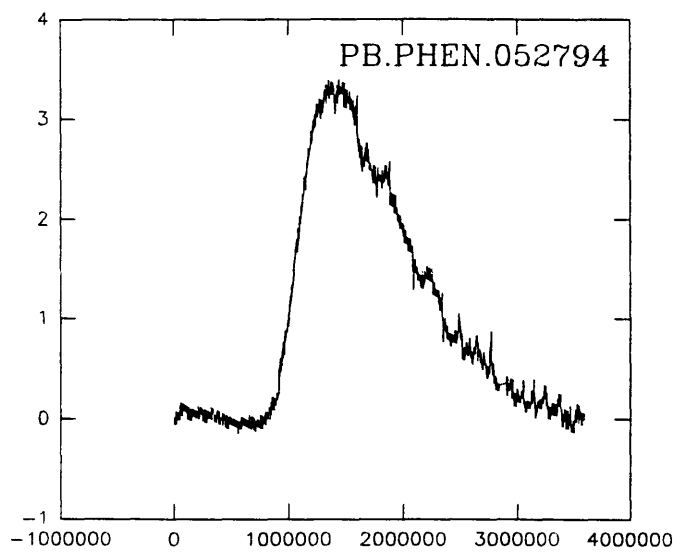


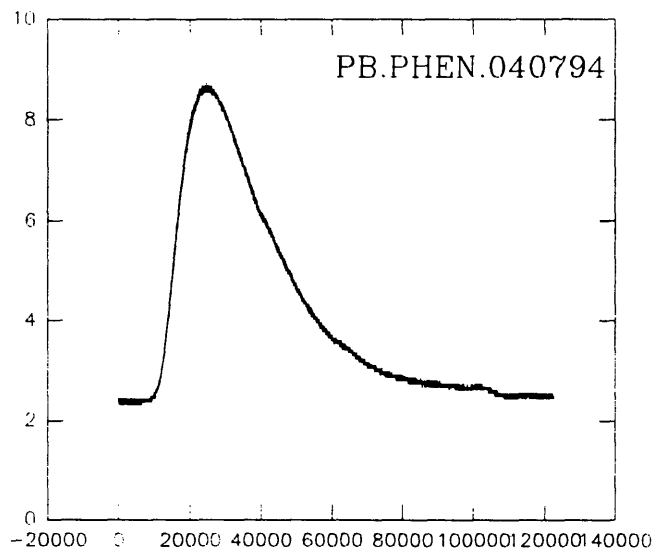
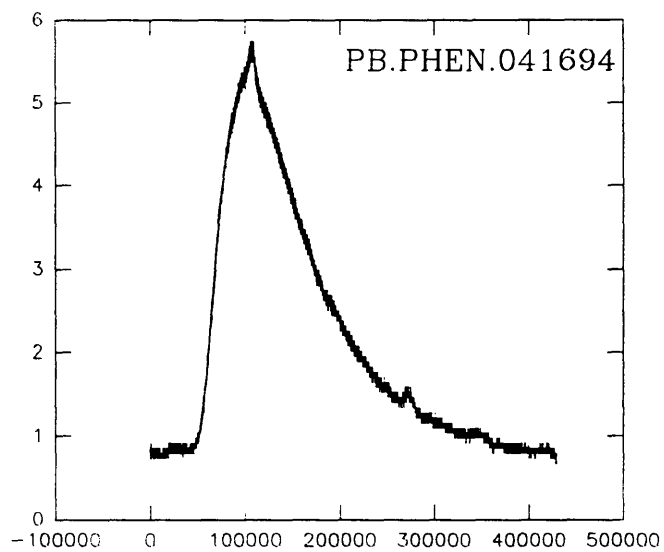
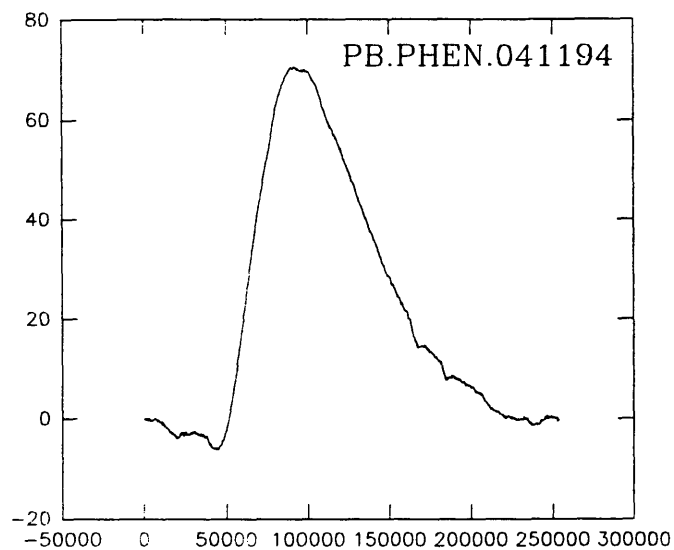


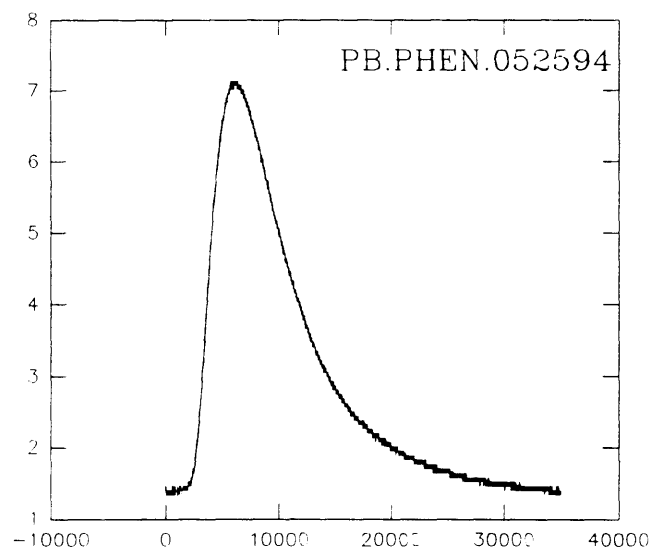
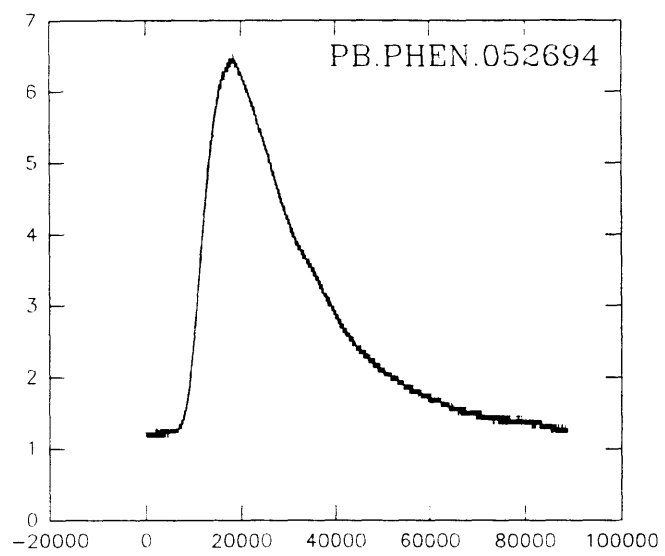


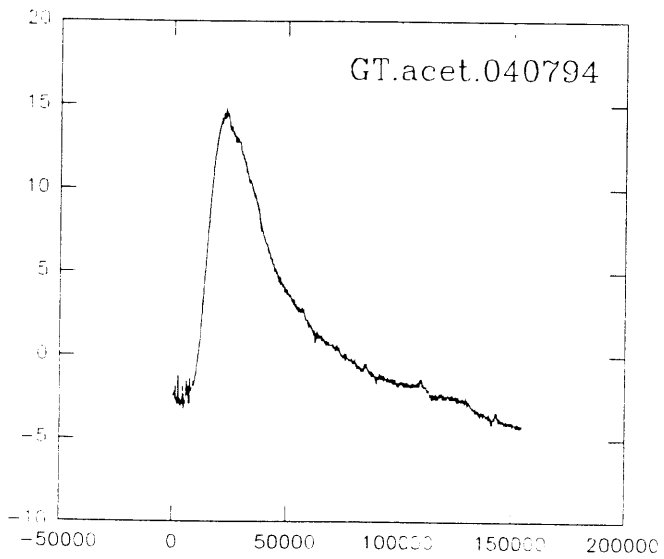
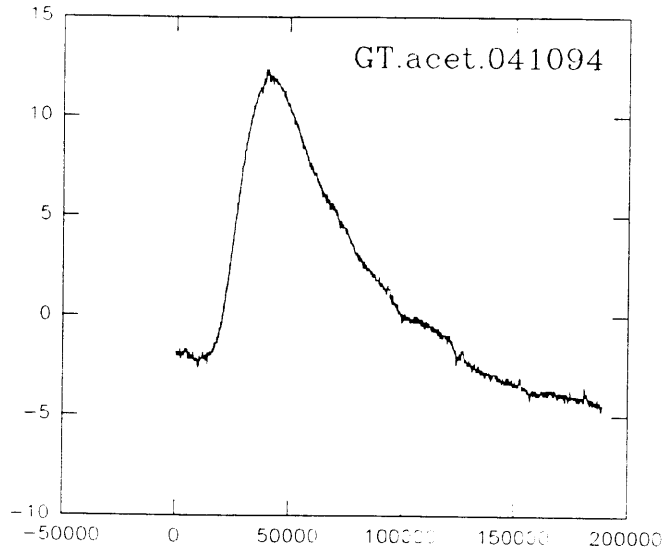
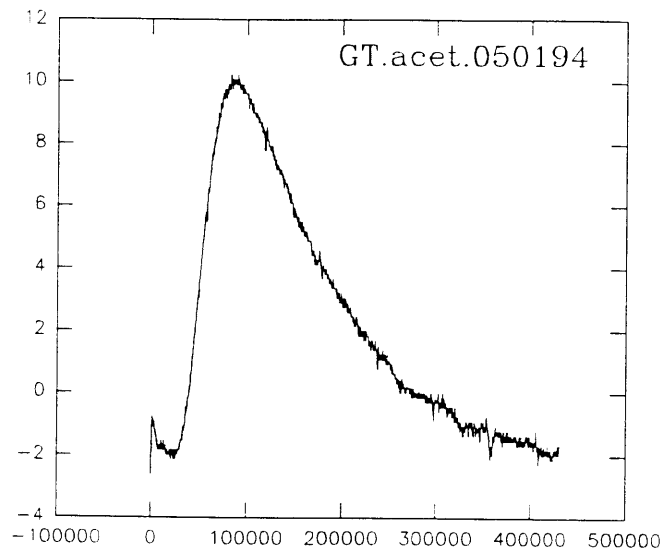


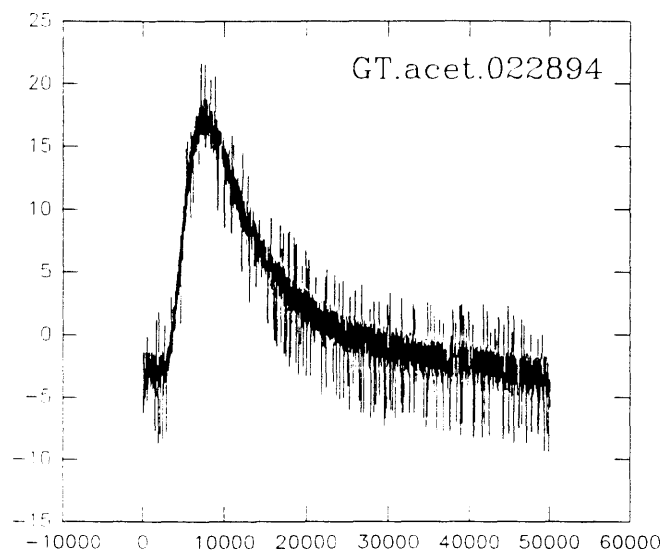
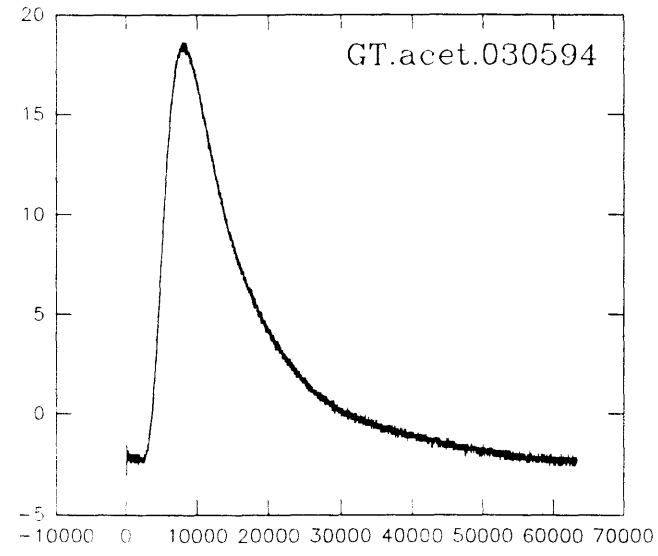
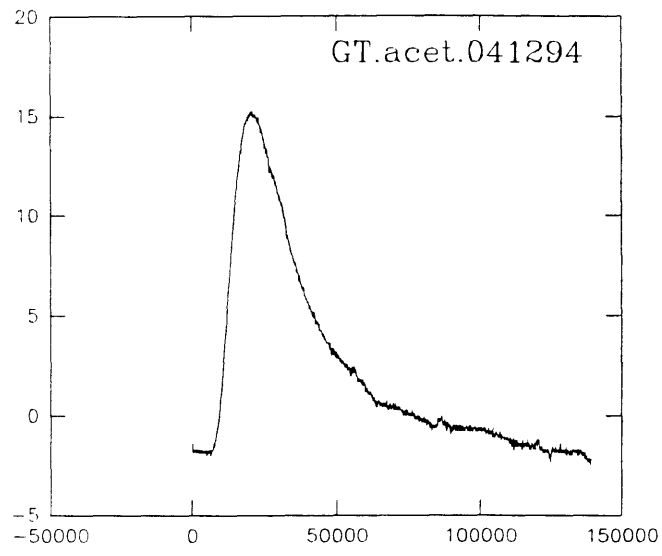


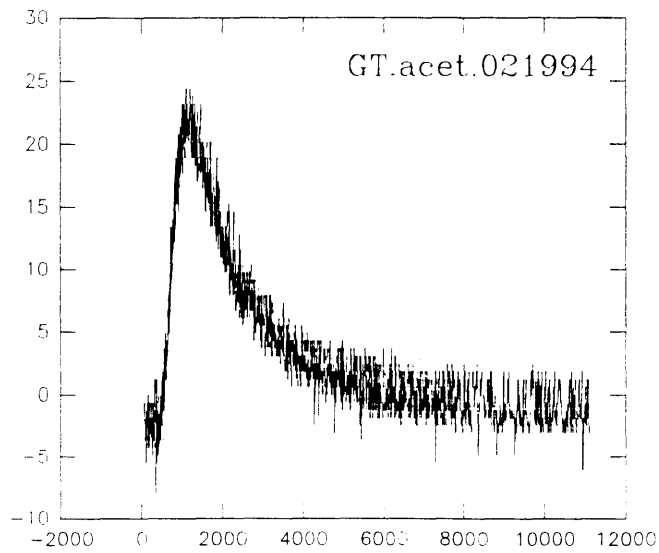
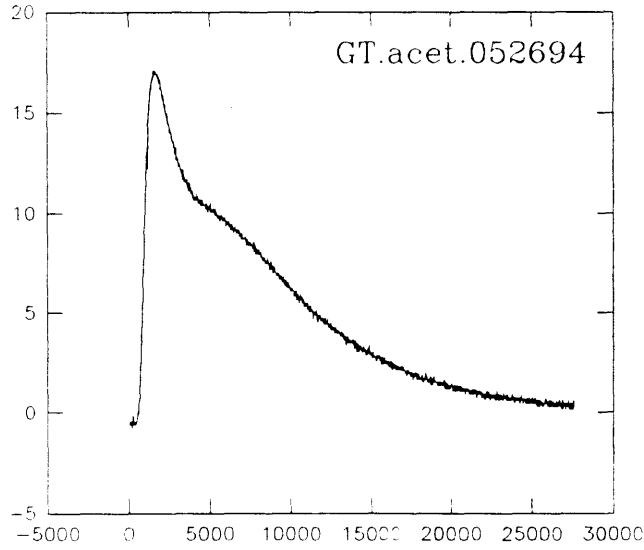
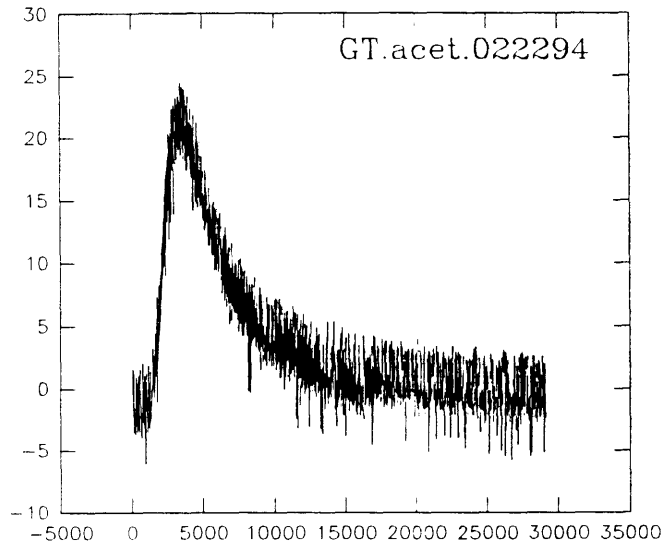


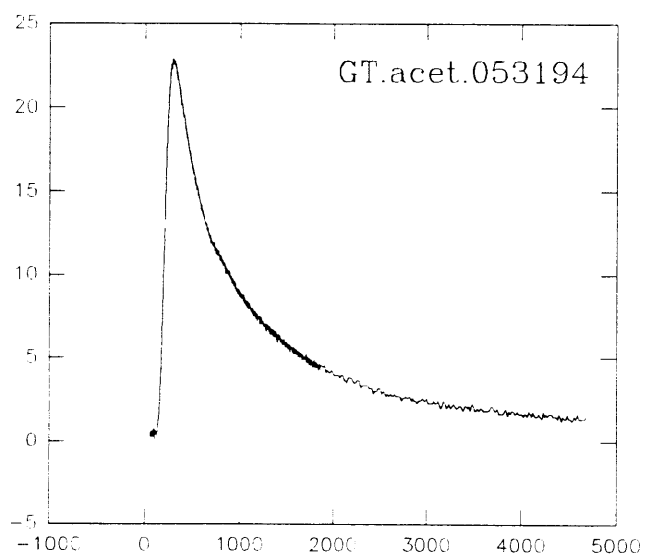
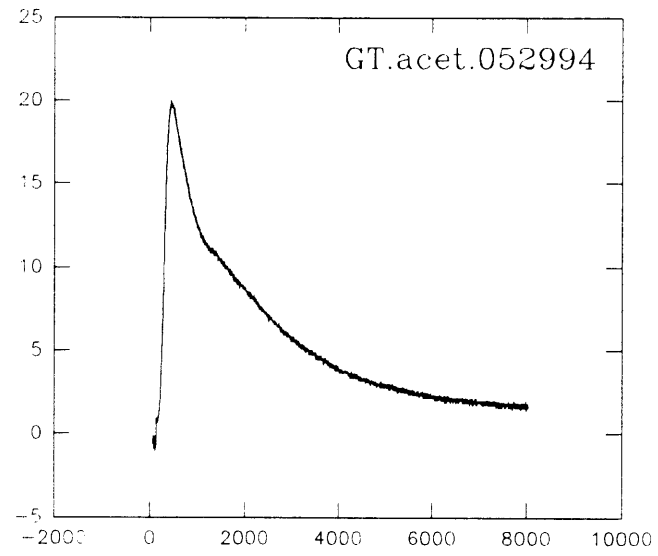
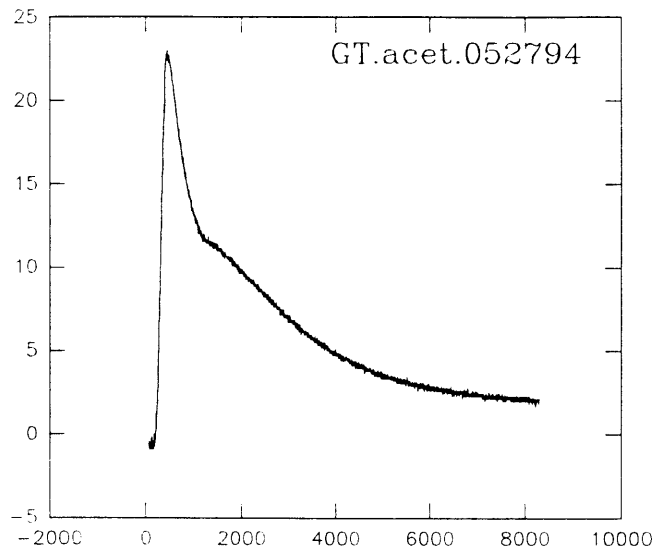


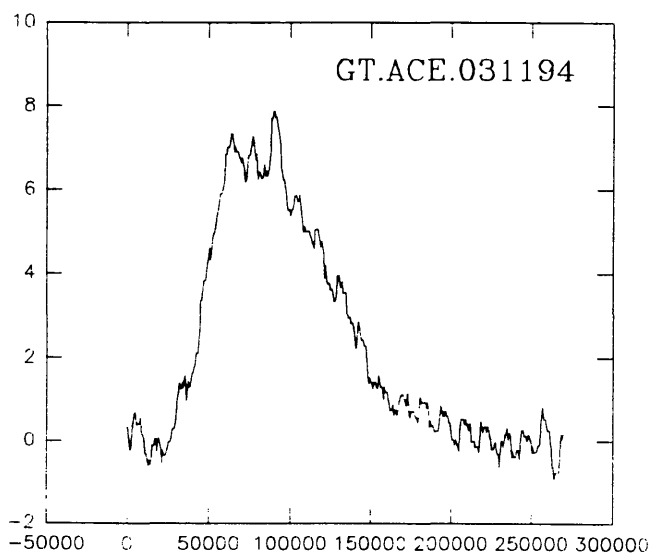
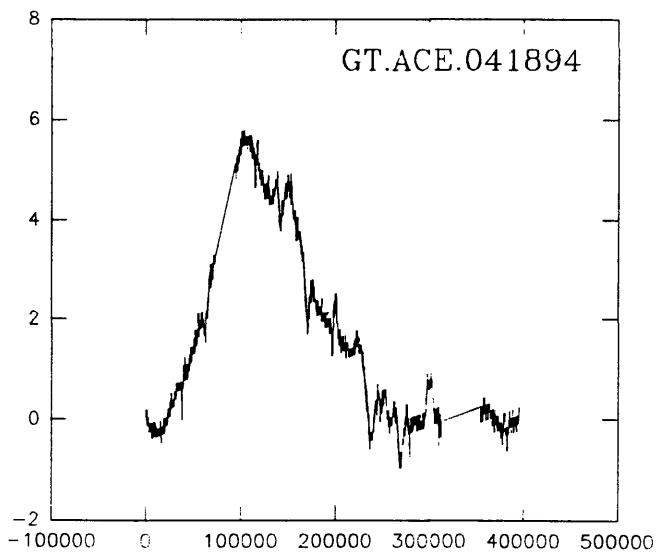
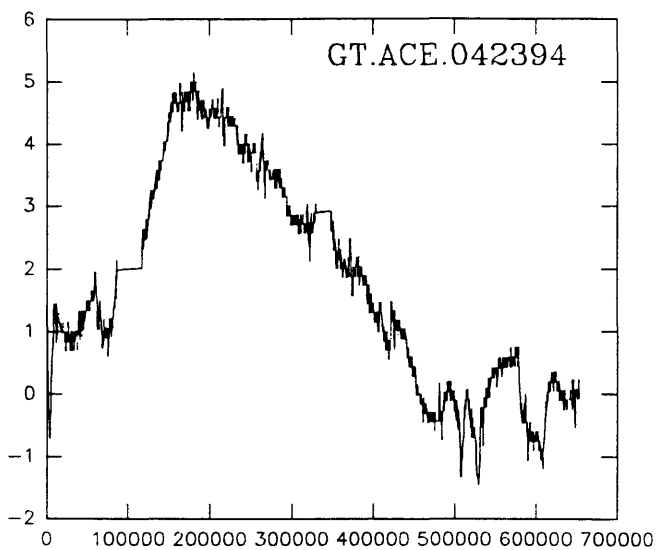


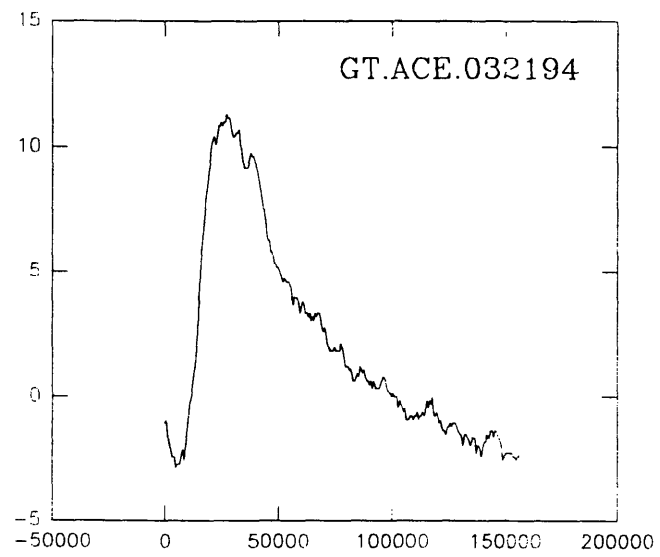
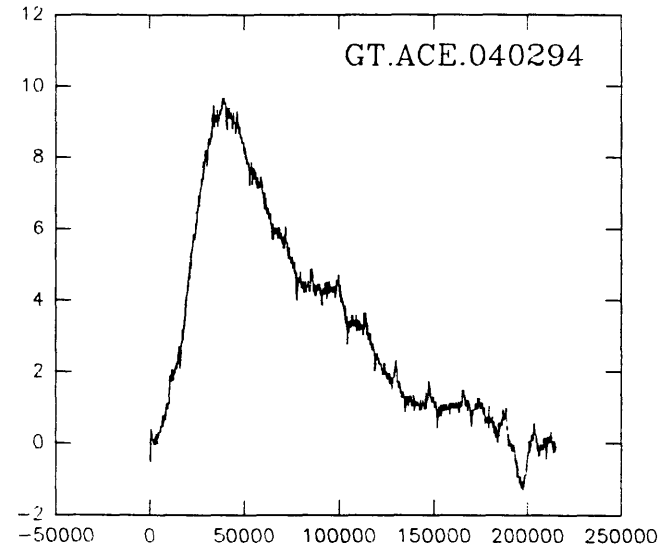
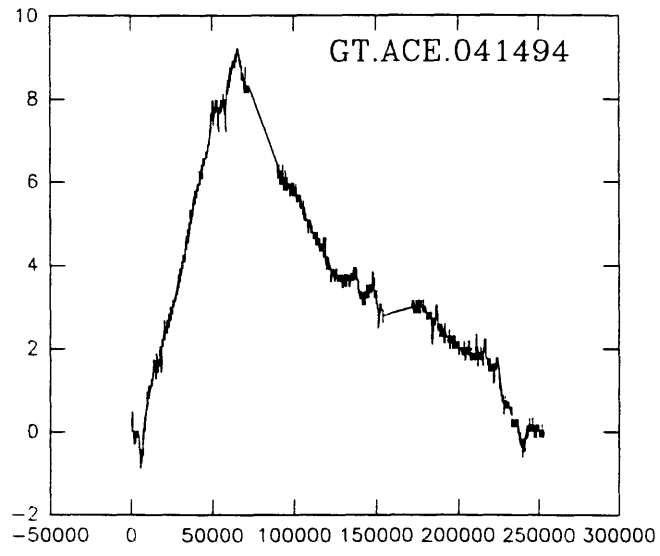


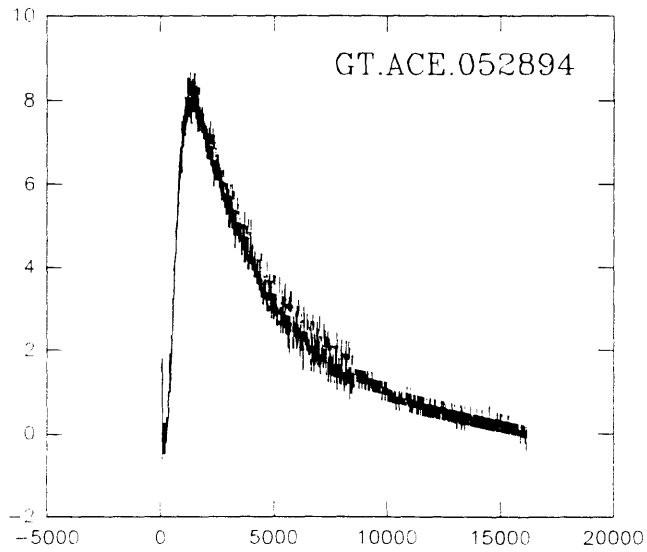
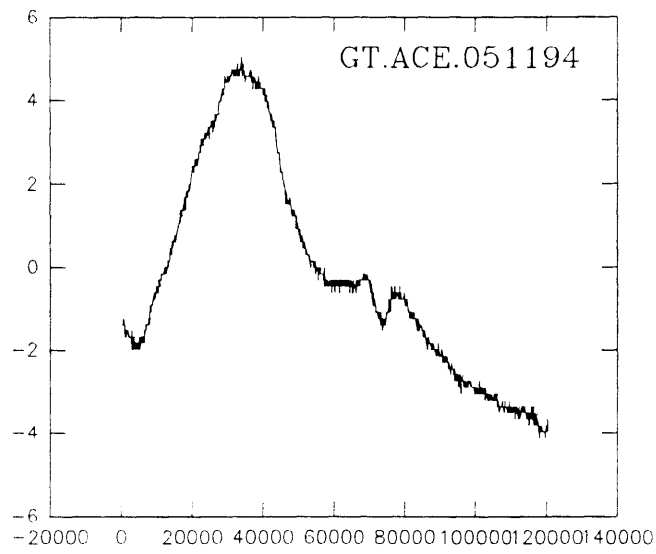
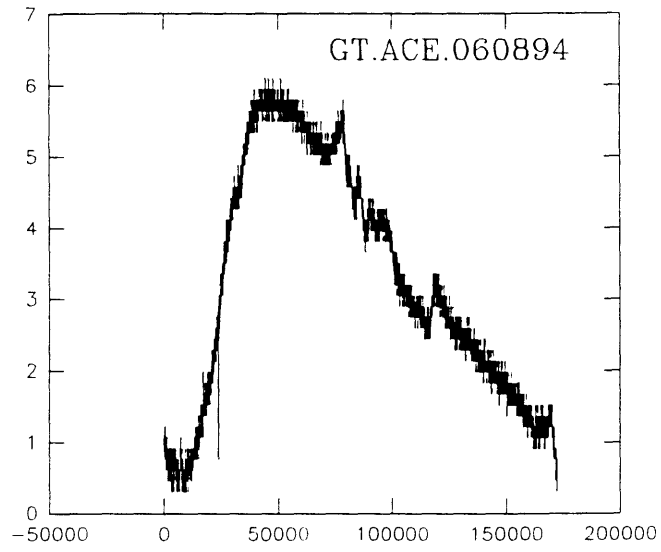


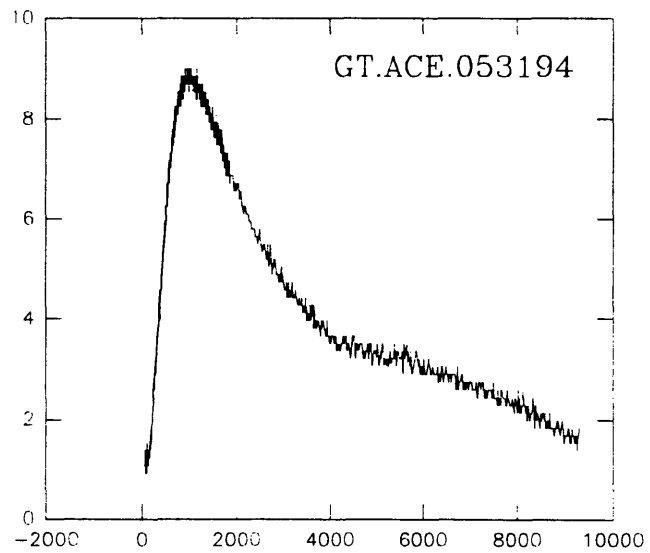
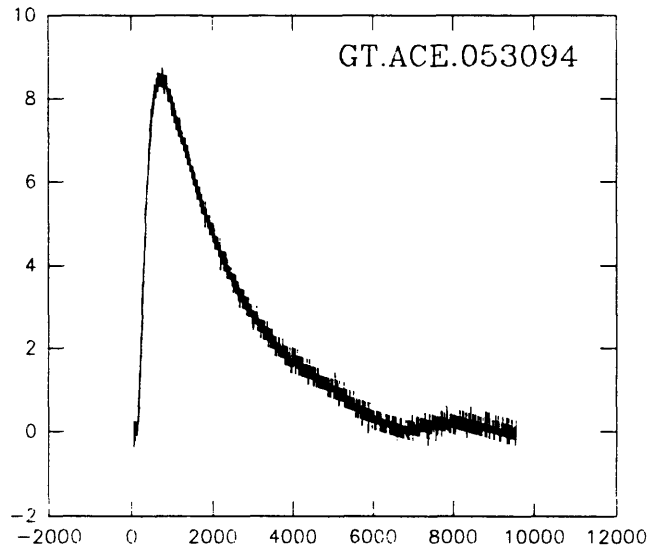
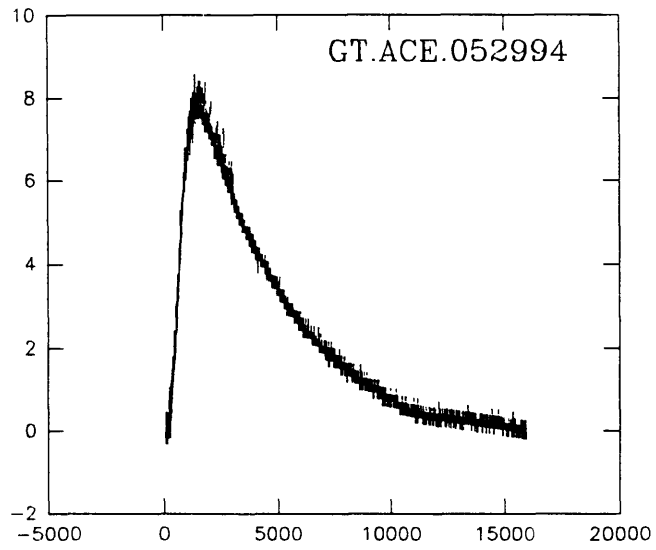


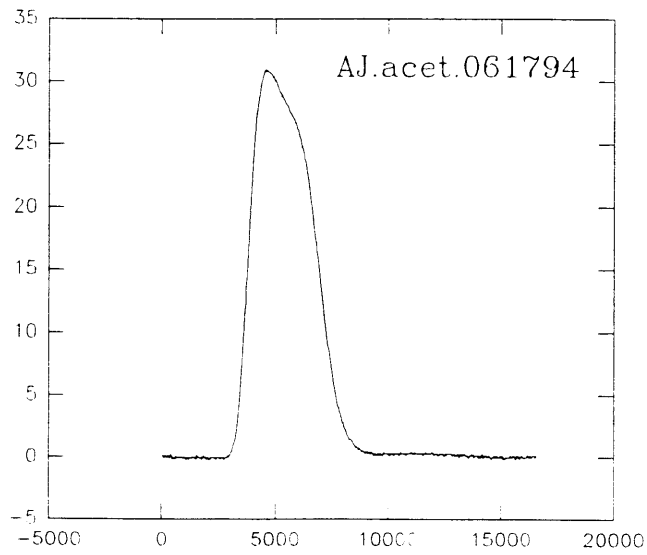
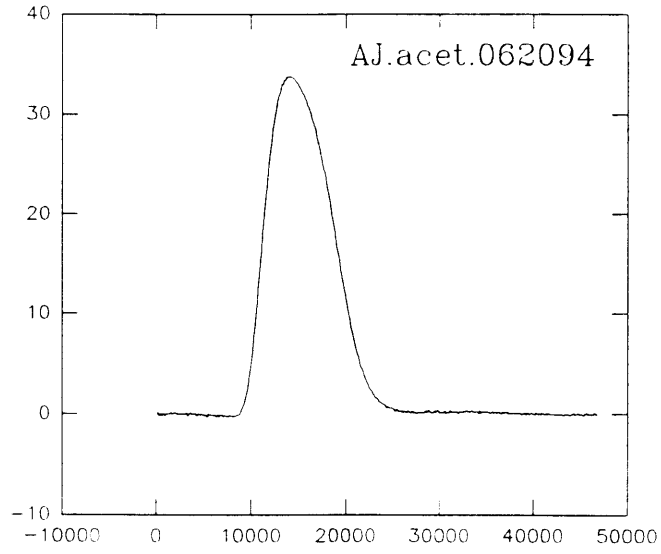
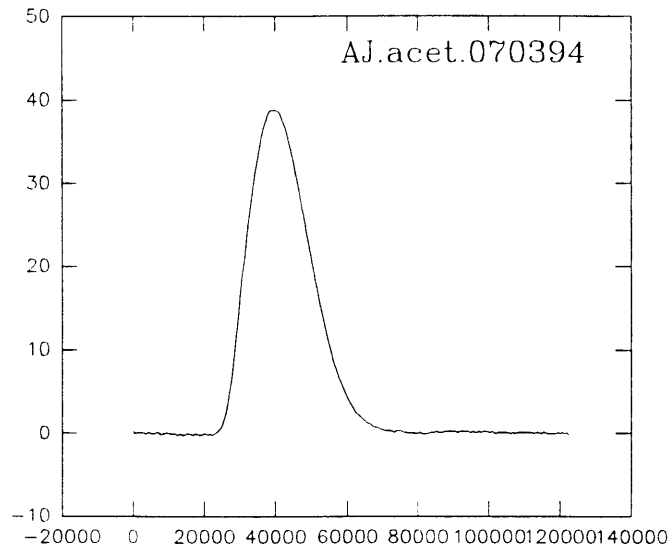


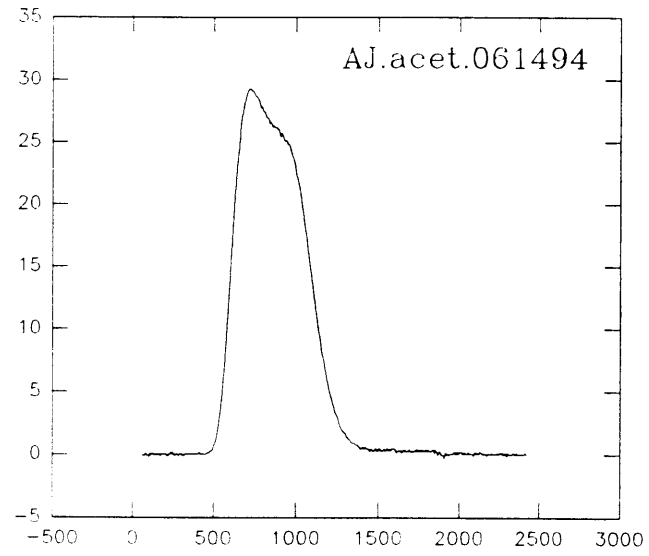
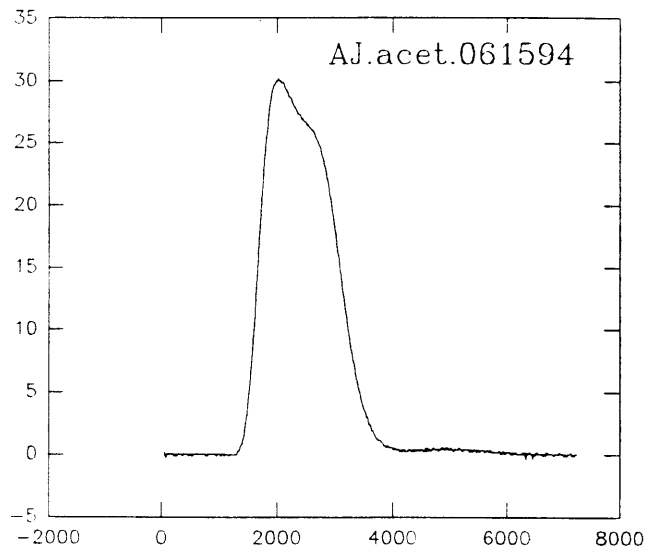


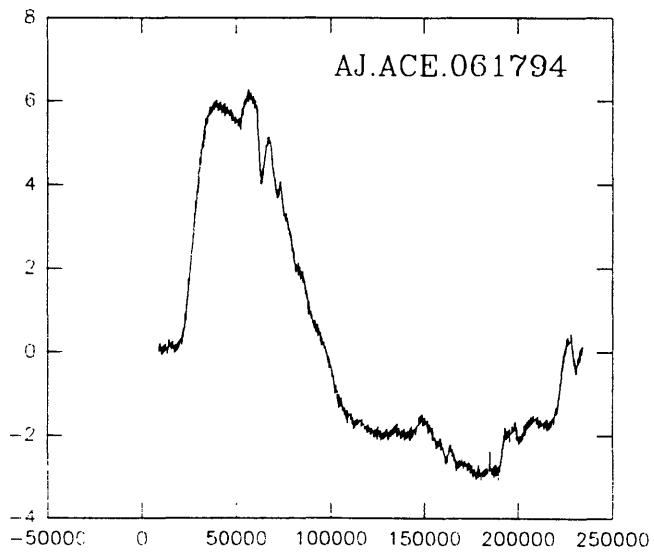
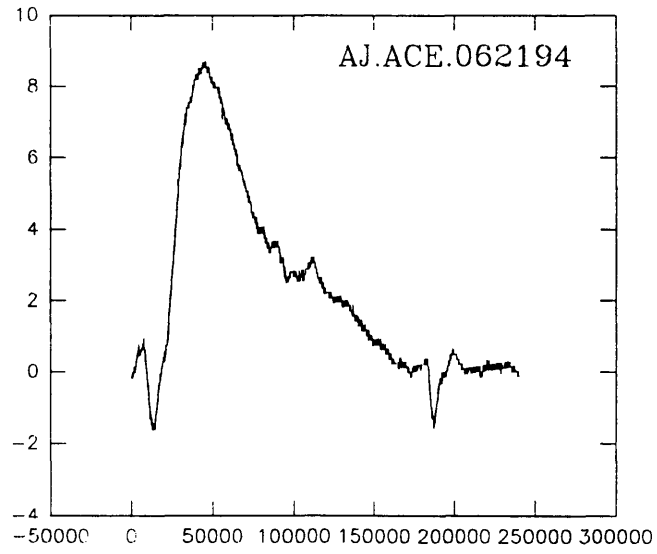
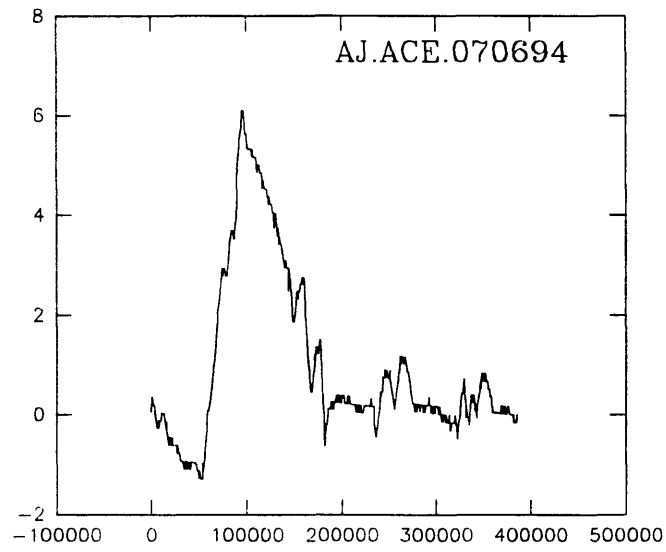


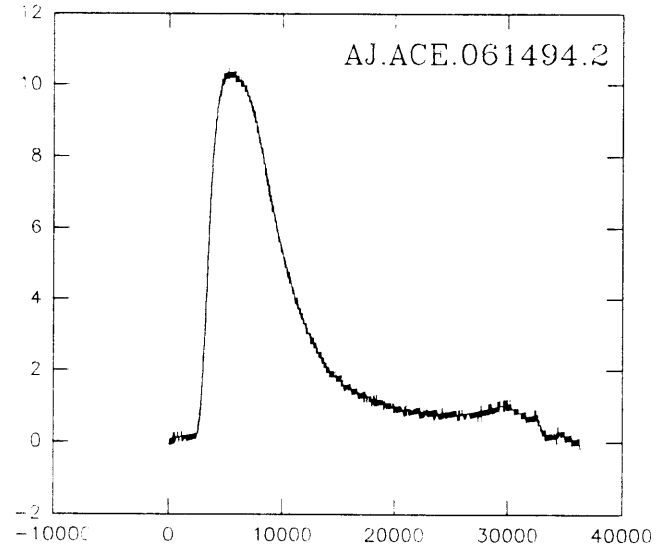
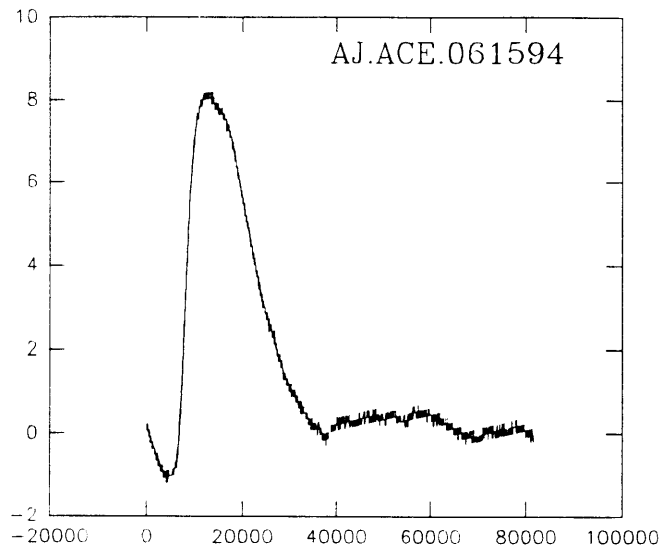


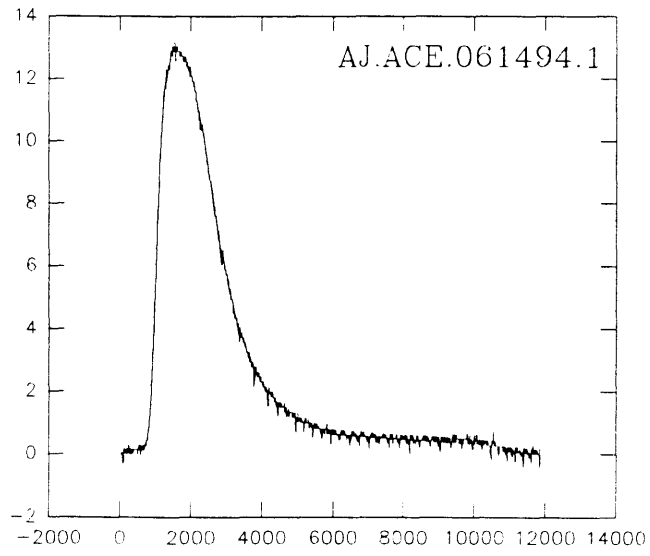
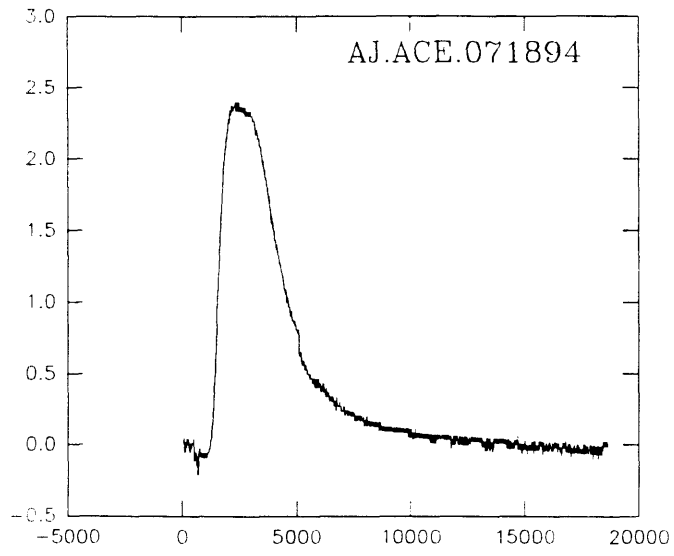




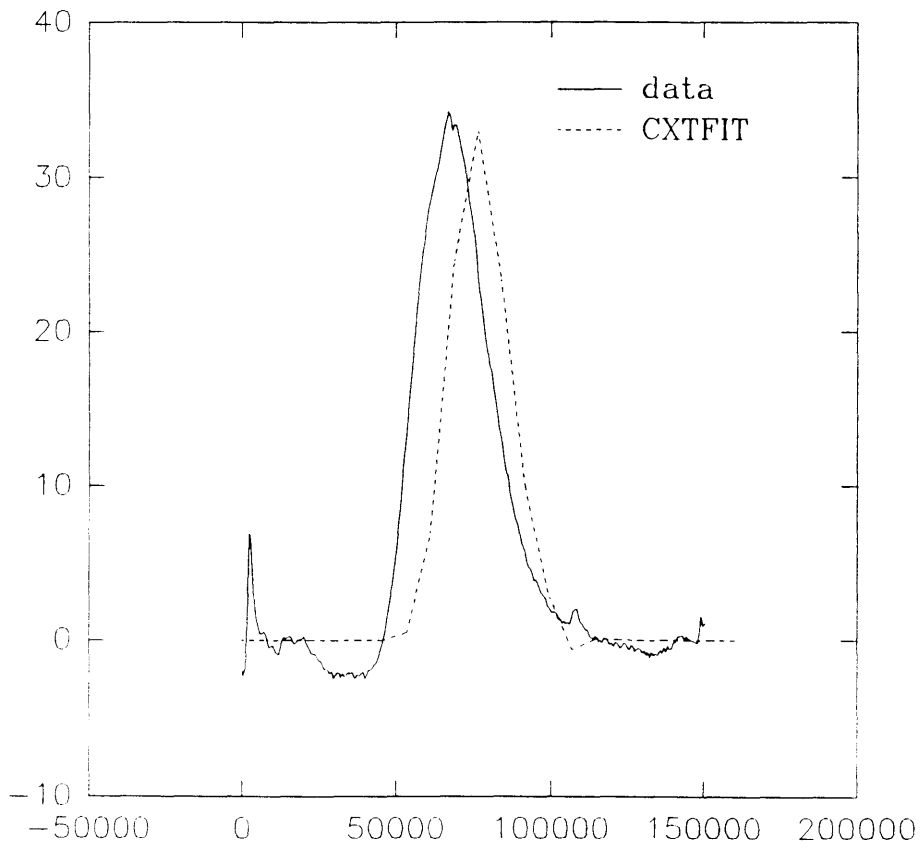




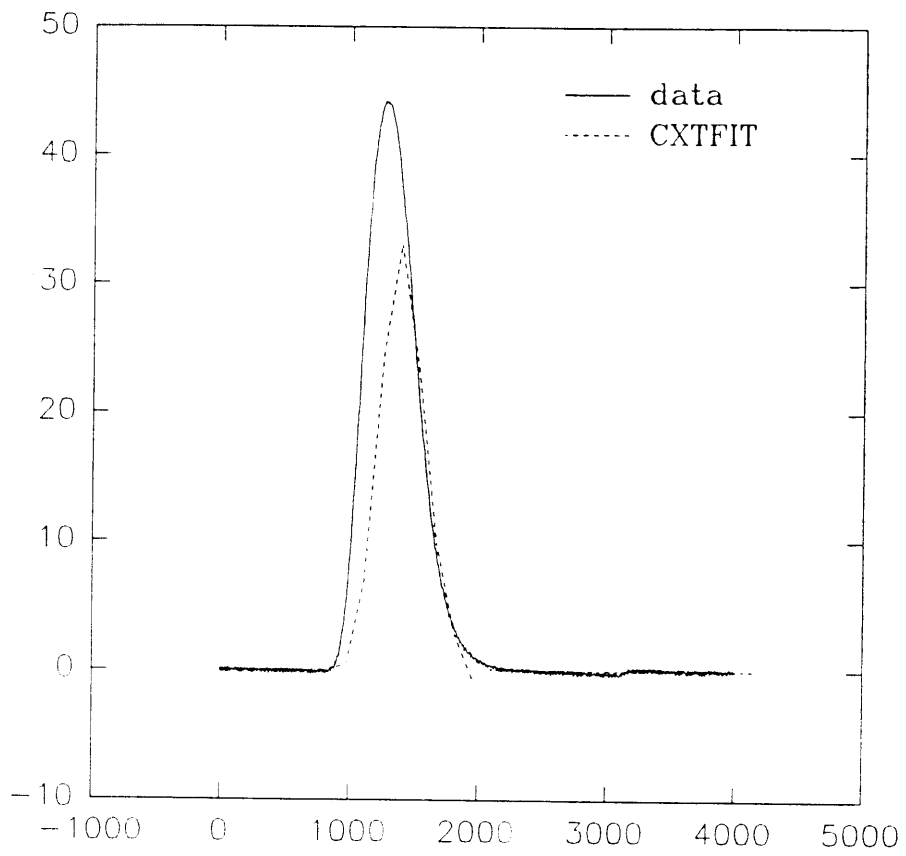




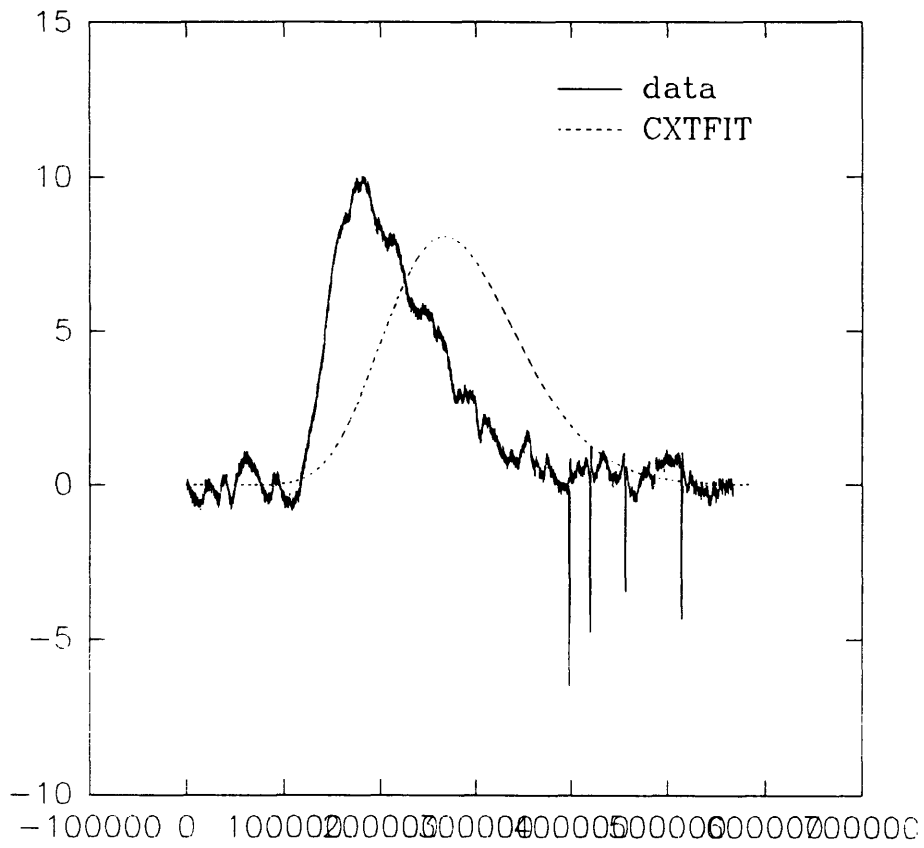
PBNO3_SLOW



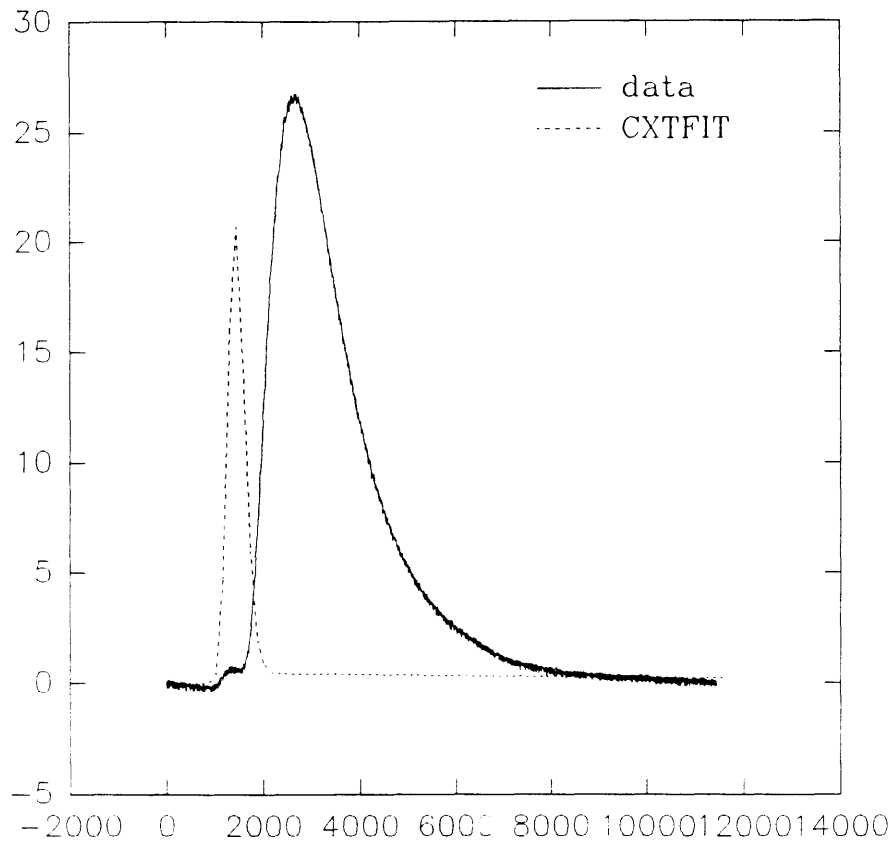
PBN03_FAST



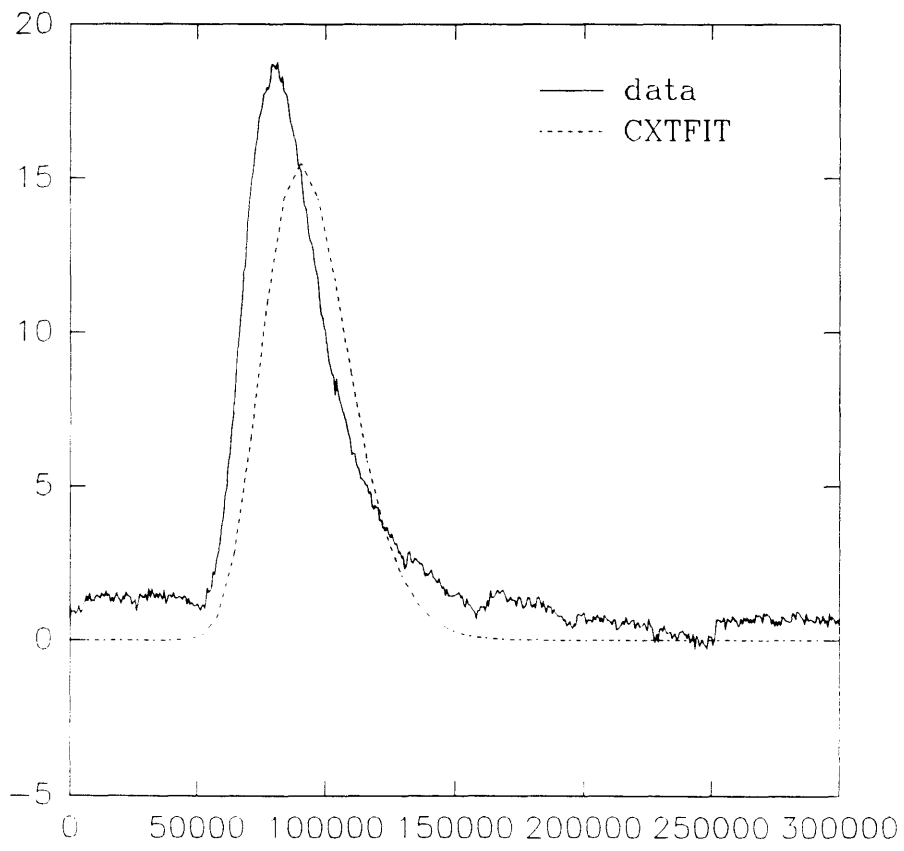
PBACE_SLOW



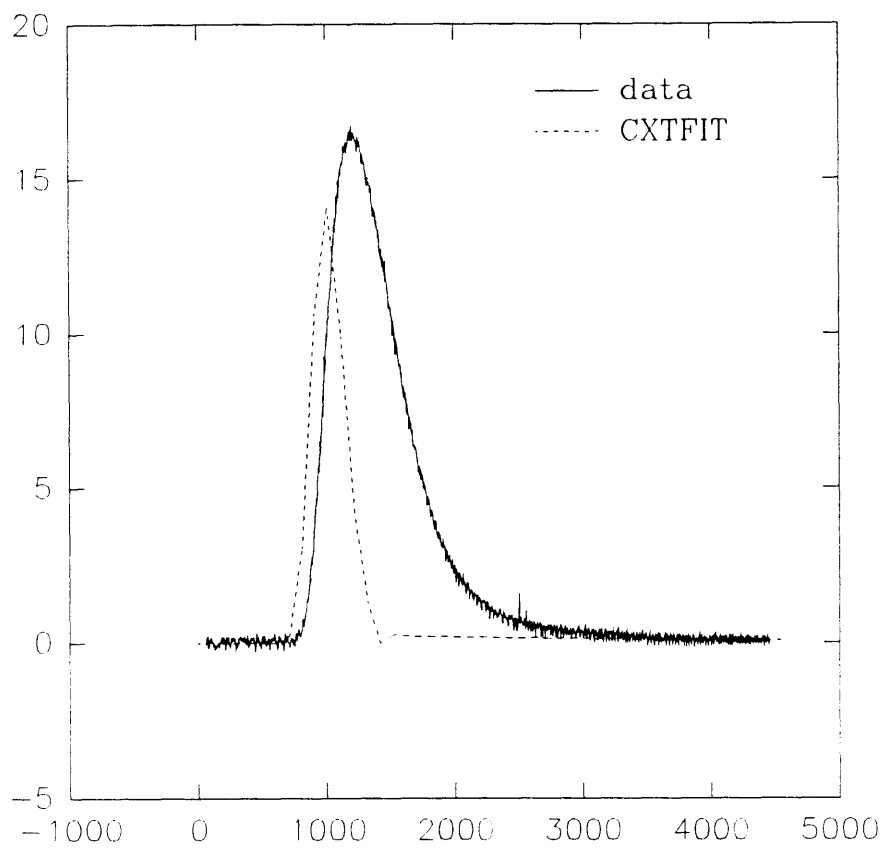
PBACE_FAST



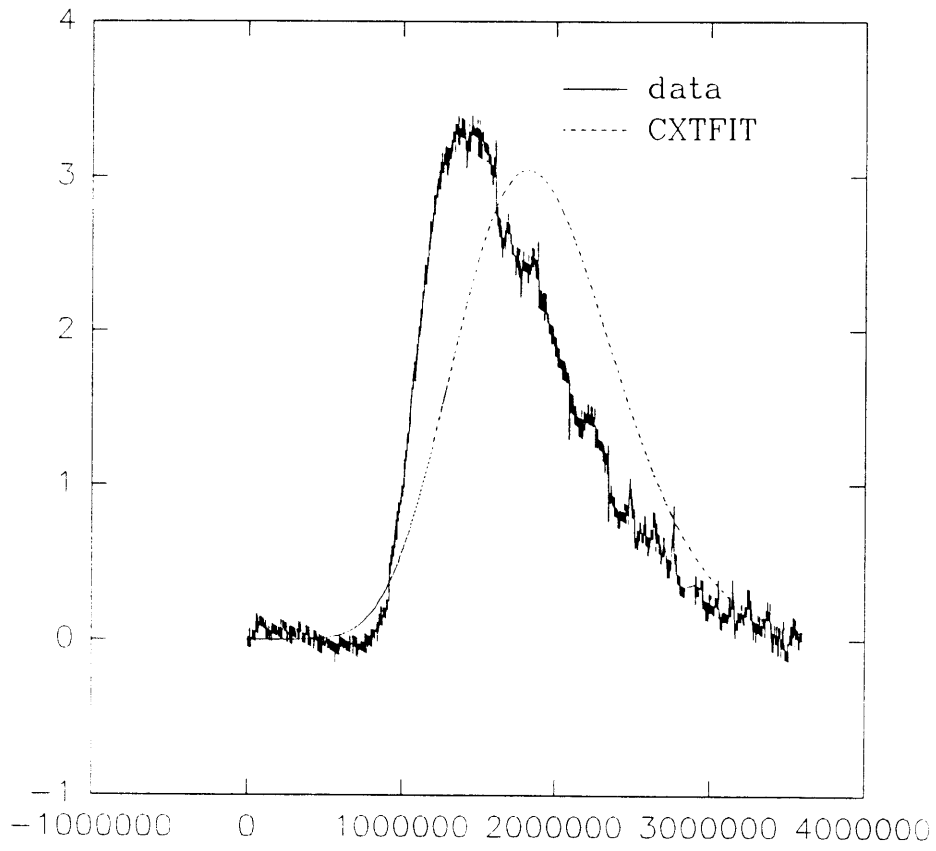
PBNAP_SLOW



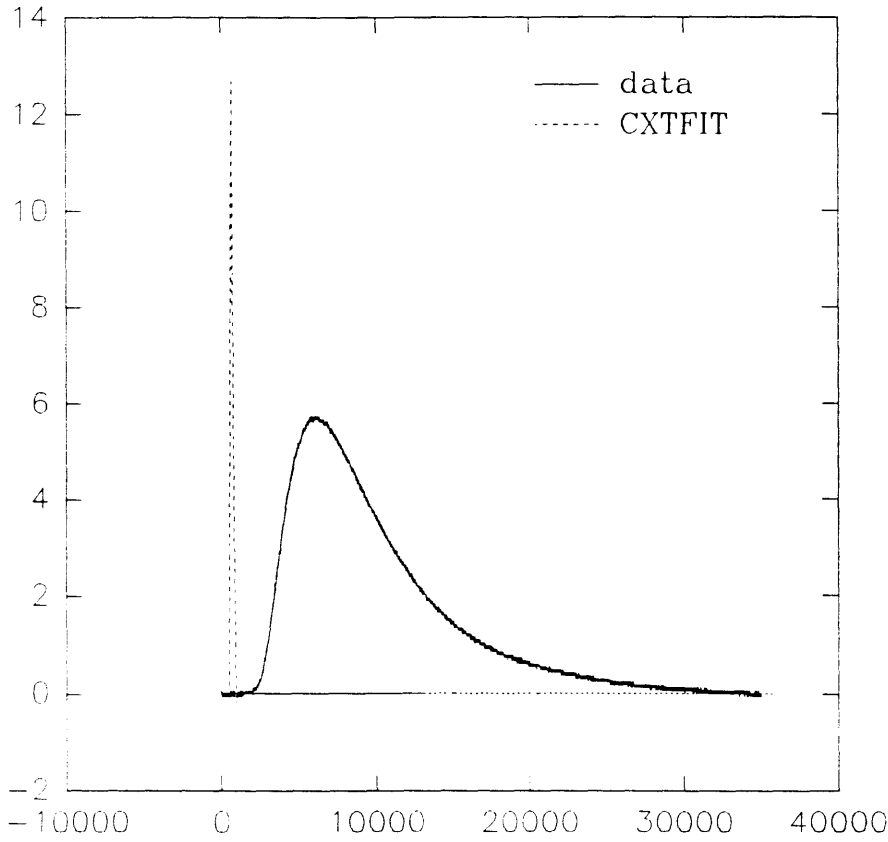
PBNAP_FAST



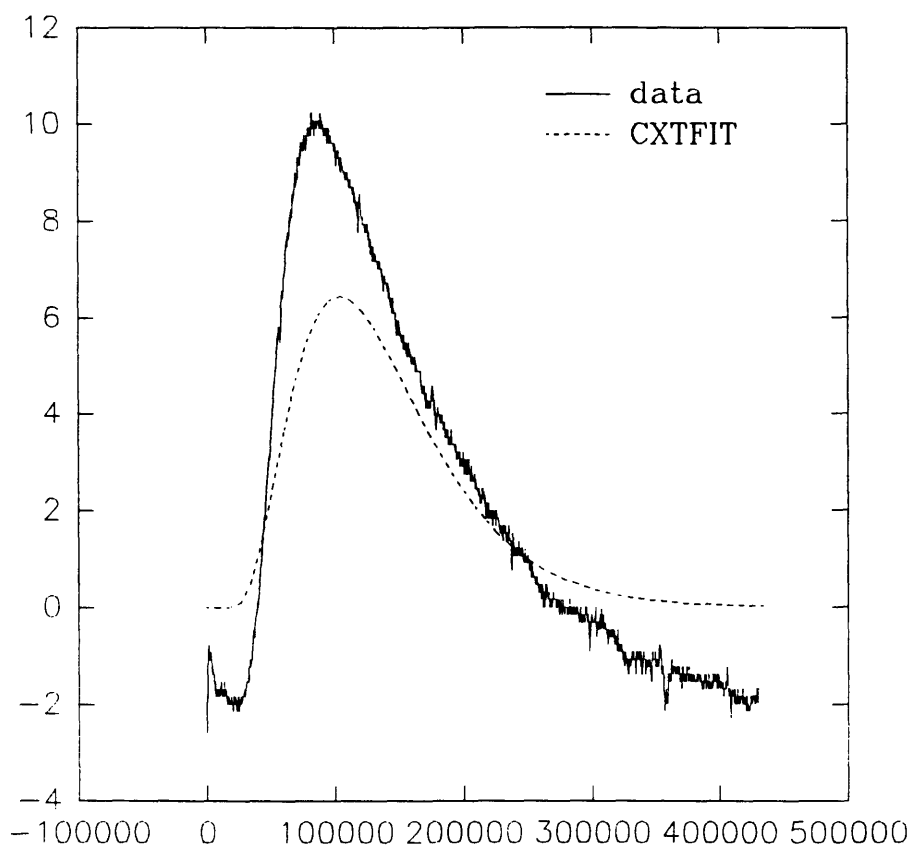
PBPHEN_SLOW



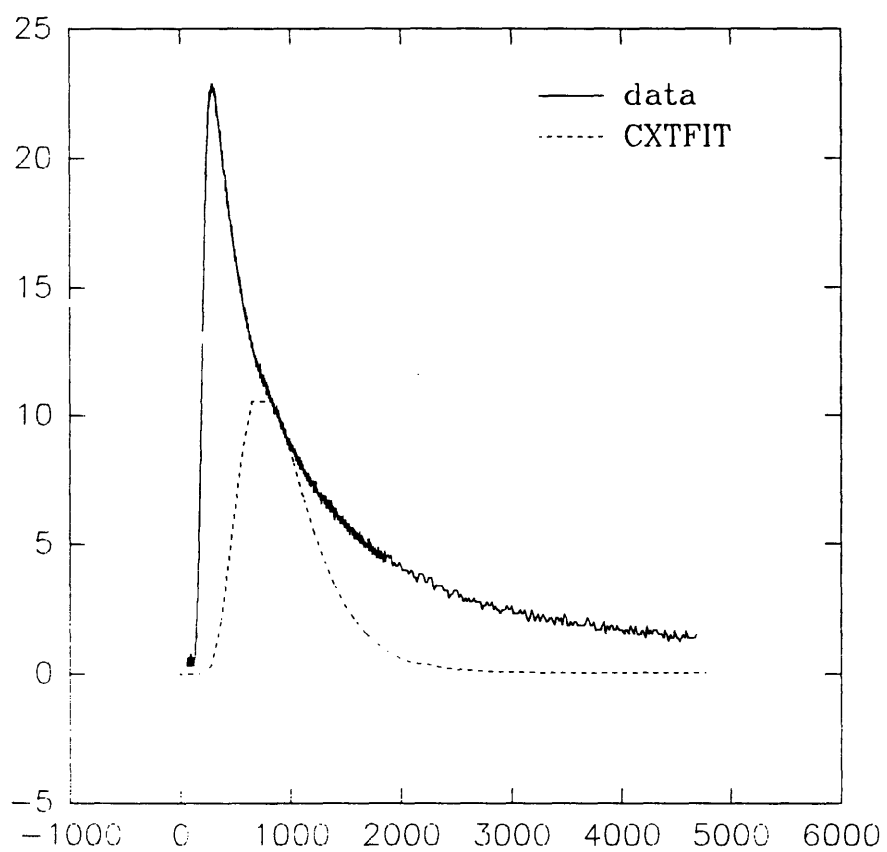
PBPHEN_FAST



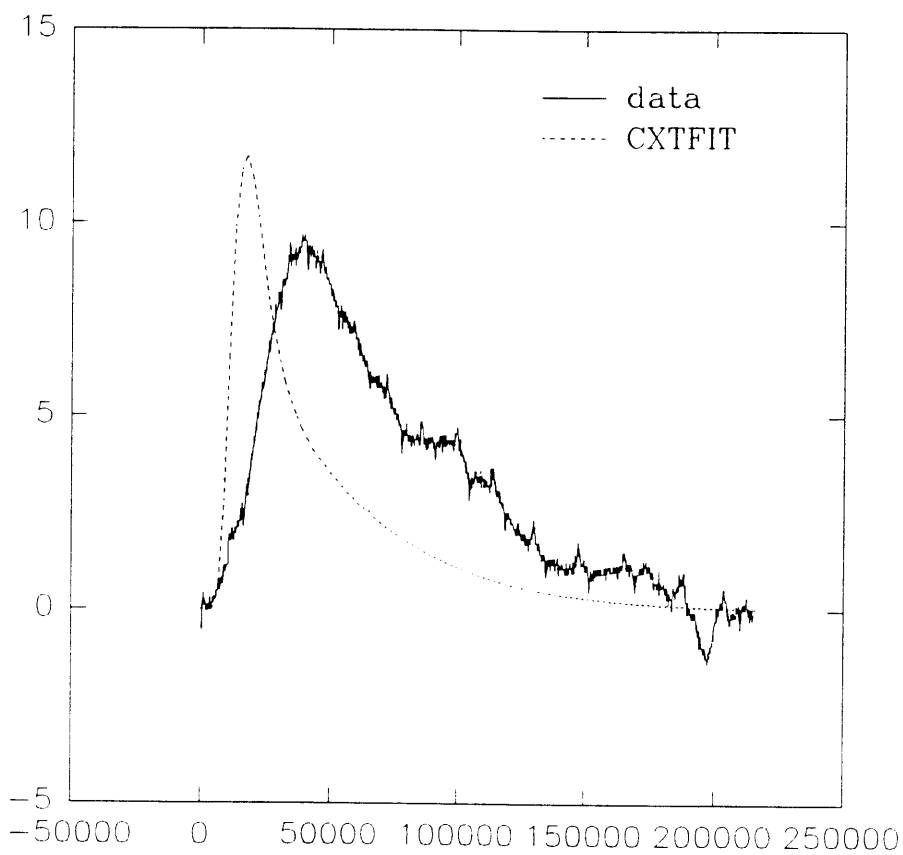
GTACETONE_SLOW



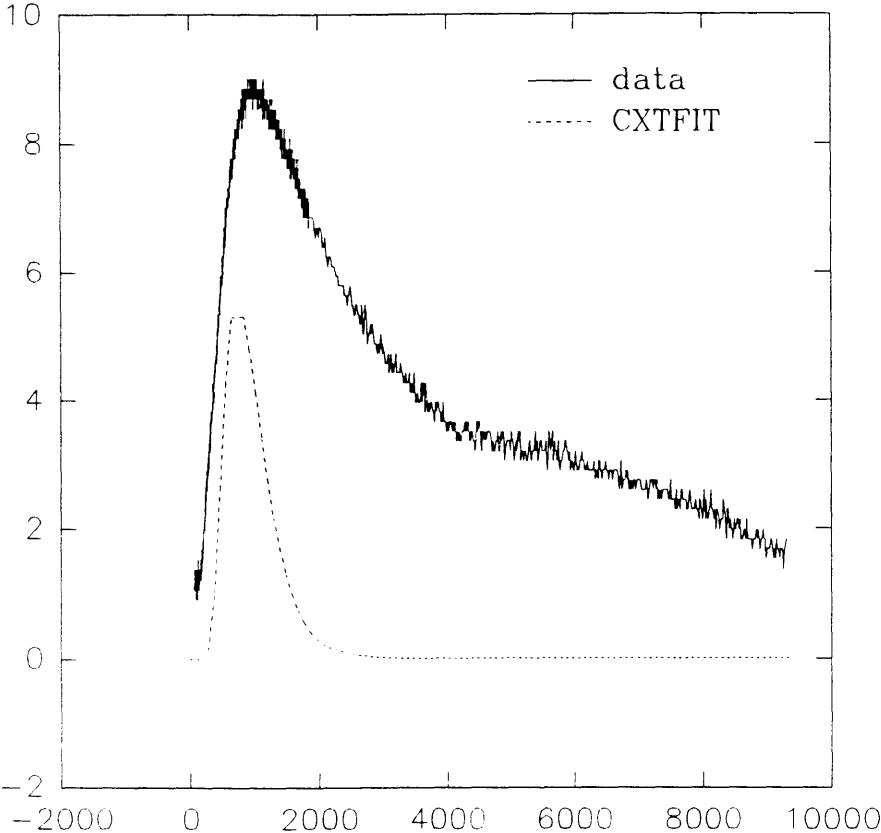
GTacetone_FAST



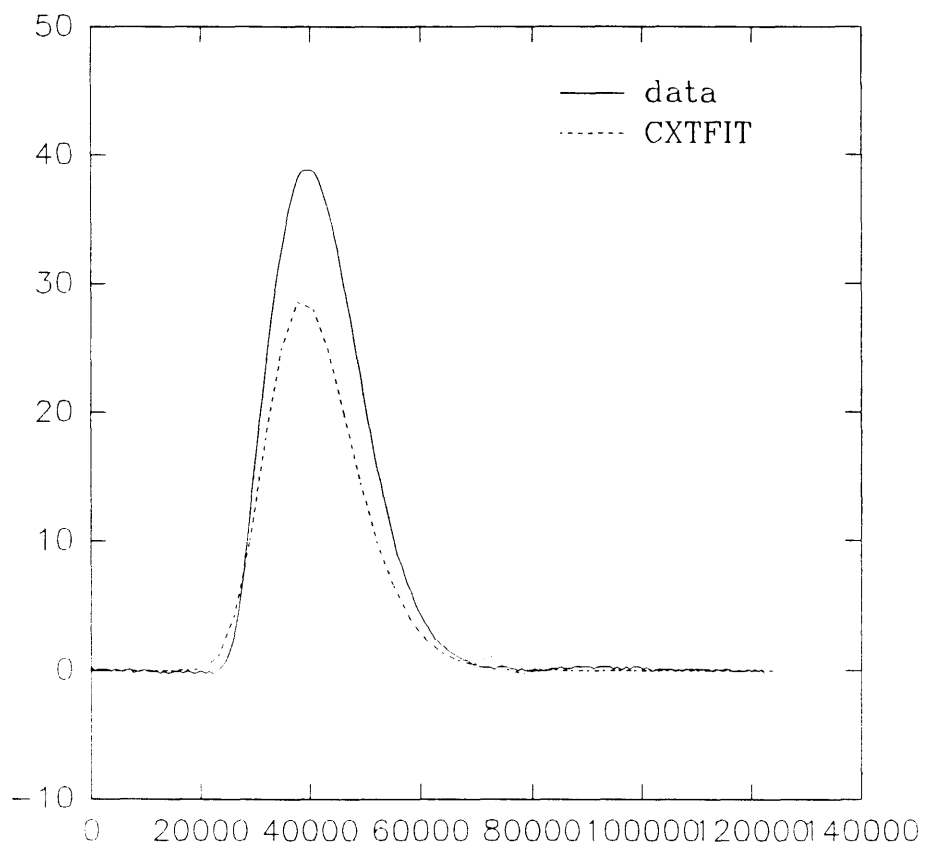
GTACE_SLOW



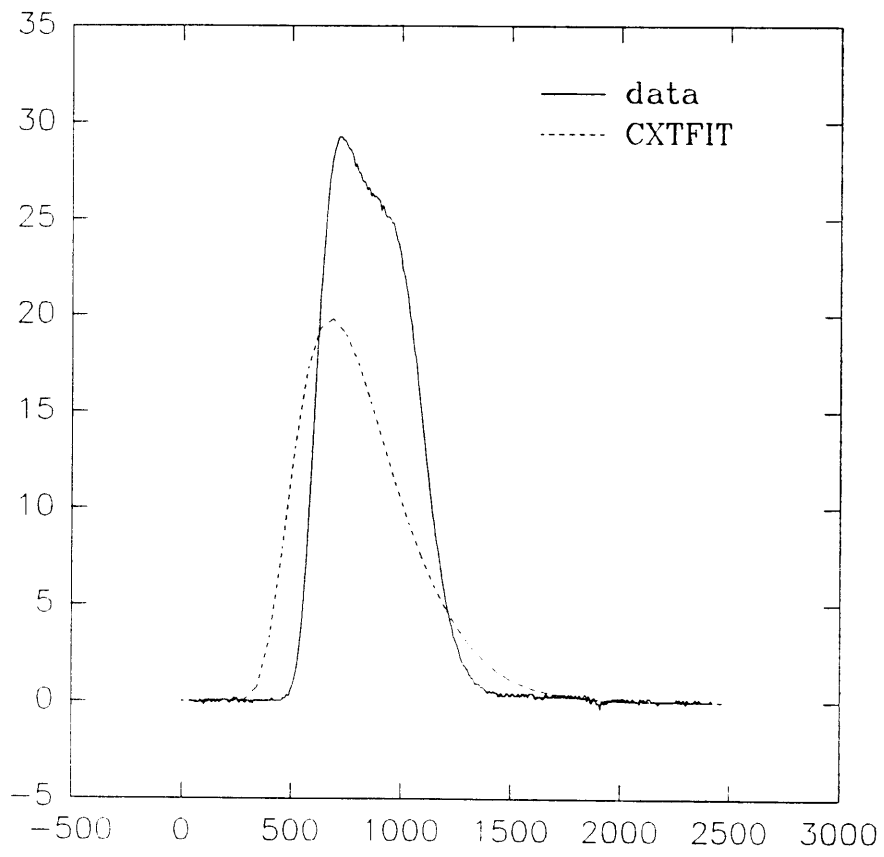
GTACE_FAST



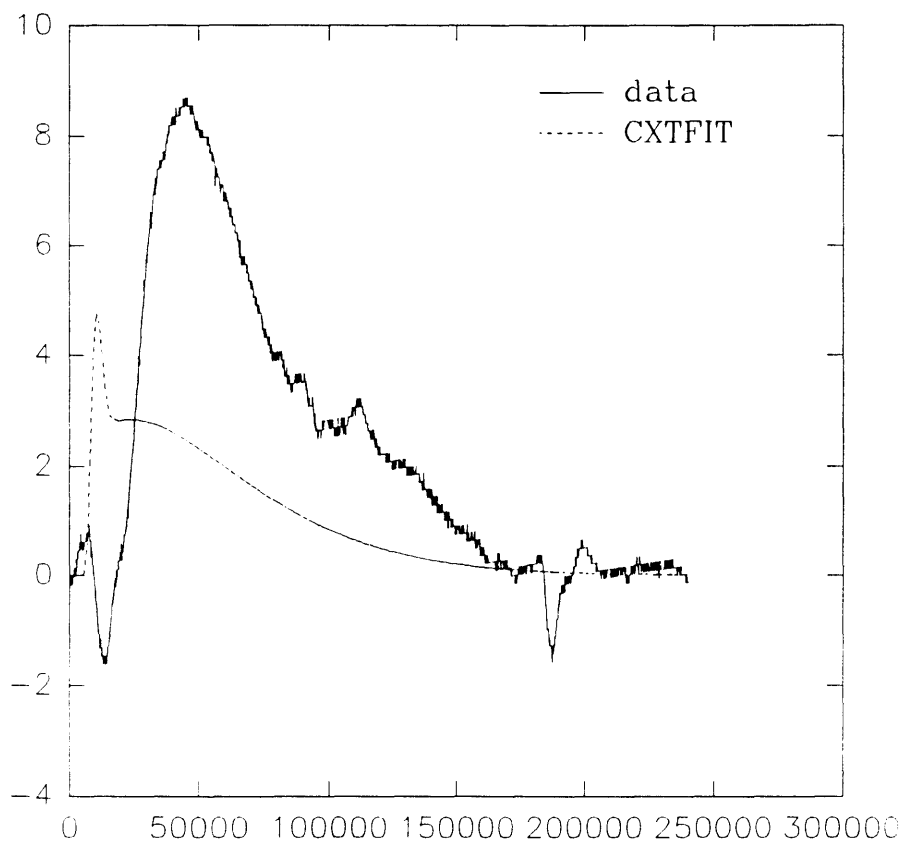
AJacetone_SLOW



AJacetone_FAST



AJACE_SLOW



AJACE_FAST

